NRL Report 8261

A New Theory for Striations with Experimental Verifications

E. E. KEMPE

Advanced Techniques Branch
Tactical Electronic Warfare Division

October 14, 1980

NAVAL RESEARCH LABORATORY
Washington, D.C.

REPORT DOCUMENTATION PAGE

READ INSTRUCTIONS BEFORE COMPLETING FORM

1. REPORT NUMBER NRL Report 8261	2. GOVT ACCESSION NO.	3. RECIPIENT'S CATALOG NUMBER
4. TITLE (and Subtitle) A NEW THEORY FOR STRIATIONS WITH EXPERIMENTAL VERIFICATIONS		5. TYPE OF REPORT & PERIOD COVERED Interim report on a continuing NRL Problem 6. PERFORMING ORG. REPORT NUMBER
7. AUTHOR(s) E. E. Kempe		8. CONTRACT OR GRANT NUMBER(s)
9. PERFORMING ORGANIZATION NAME AND ADDRESS Naval Research Laboratory 4555 Overlook Avenue Washington, D.C. 20375		10. PROGRAM ELEMENT, PROJECT, TASK AREA & WORK UNIT NUMBERS NRL Problem R16-09 Program Element 61153N Project RR021-05-41
11. CONTROLLING OFFICE NAME AND ADDRESS Office of Naval Research Arlington, VA 22217		12. REPORT DATE October 14, 1980 13. NUMBER OF PAGES 147
14. MONITORING AGENCY NAME & ADDRESS(if different from Controlling Office)		15. SECURITY CLASS. (of this report) Unclassified 15a. DECLASSIFICATION/DOWNGRADING SCHEDULE

16. DISTRIBUTION STATEMENT (of this Report)

Approved for public release; distribution unlimited.

17. DISTRIBUTION STATEMENT (of the abstract entered in Block 20, if different from Report)

18. SUPPLEMENTARY NOTES

19. KEY WORDS (Continue on reverse side if necessary and identify by block number)

Gas discharges
Moving striations
Ionization waves
Glow discharge plasmas
Plasma instabilities

20. ABSTRACT (Continue on reverse side if necessary and identify by block number)

A new general theory for striated positive columns containing atomic or molecular fill gases is elaborated that gives a unified explanation of both standing striations and cathode-directed and anode-directed moving striations along with the significance of the Novak potential. The *p*, *r*, and *s* striation varieties in neon are explained according to this new theory, including the ionization mechanisms associated with their generation, and the results are experimentally verified via measurements in neon discharges and Penning discharges of neon with argon admixtures. The mathematical model of the positive column derived for this theory shows how an open-loop instability that is an

(Continued)

DD FORM 1473, 1 JAN 73 EDITION OF 1 NOV 65 IS OBSOLETE
S/N 0102-014-6601

20. ABSTRACT (Continued)

inherent feature of the process maintaining the charged particle density along the column sustains self-excited striations. To illustrate the basic nature of the open-loop instability leading to self-excited striations, a simple analog of the positive column is presented. This new theory therefore contrasts with the widely accepted viewpoint of Pekarek that self-excited striations are caused by closed-loop feedback paths consisting of propagating "ionization waves" which couple disturbances back to their point of origin with sufficient amplitudes to excite successive ionization waves. Standing striations in RF-excited columns are also explained.

CONTENTS

ACKNOWLEDGMENTS

I am grateful to Dr. Hochuli for suggesting this problem and for providing guidance throughout the course of this research. I also thank Paul Haldemann for his help with the experimental aspects of this research. A NSF Fellowship helped to make possible my full time pursuit of graduate studies during the years 1969-1972. Also, during this period this research was partially supported by the Office of Naval Research under Grant N00014-67-A-0239-0016. From 1972 to the present I have been employed at the Naval Research Laboratory, and I wish to thank my supervisor Dr. G. E. Friedman for his cooperative attitude regarding this work and for his technical suggestions and discussions.

A NEW THEORY FOR STRIATIONS WITH EXPERIMENTAL VERIFICATIONS

INTRODUCTION

Striations are stationary or traveling-wave variations of the glow plasma parameters along the longitudinal axis of a positive column. The first observations of standing striations are attributed to Abria in 1843 [1], and moving striations were detected nearly 100 years ago via a rotating-mirror technique [2]. Over the years many researchers have made measurements with the objectives of discovering the basic nature of striation phenomena and formulating a theory which explains how the parameters that characterize the striated positive column such as striation wavelength and frequency depend on the parameters that characterize the discharge such as the type of fill gas, its pressure, the tube current, and the positive-column radius. These early researchers included such well-known names as J. J. Thomson, F. M. Penning, J. S. Townsend, J. J. Druyvesteyn, I. Langmuir, and L. B. Loeb.

As an understanding of the various glow plasma processes evolved, many theories incorporating these processes were put forth in attempts to explain striations. Some of these theories contained variations on the theme of electrons cyclicly acquiring energy from the longitudinal electric field at one position and losing it via ionization and or excitation at another as they drifted along the length of the positive column. For example, Penning [3] found that for the few standing striations that occur at the cathode end of positive columns containing rare gases the potential $E_0\lambda_s$ across a striation wavelength approximately equals certain excitation potentials of the fill-gas ground-state atoms such as the 18.5-volt excitation potential of the 2p state in neon.

With regard to moving striations, calculations by Druyvesteyn [4] link the cathode-directed striation velocity to the velocity of the positive ions. Other earlier hypotheses advanced to explain moving striations are based on such diverse plasma mechanisms as the propagation of acoustic waves in the neutral-gas component of the plasma [5], ion plasma oscillations [6], the propagation of ion acoustic waves [7], ion oscillations in a potential minimum in the negative glow region [8], and anode spot oscillations [9]. In every instance subsequent experimental data disproved these explanations.

In 1954 Pekarek observed that a so-called wave of stratification could be excited by applying a pulse disturbance to the positive column of a neon glow discharge tube operating in a regime of limited current and pressure in which spontaneously excited moving striations do not occur [10]. Pekarek [11] states: "A direct analogy to the process of the wave of stratification in other physical media has not been found. It seems, therefore, that phenomena, which are specific only for discharge plasma, assert themselves in the production of a wave of stratification. .... Phenomenologically the wave of stratification resembles the transient process of the production of waves on a water surface after a local aperiodic (impulse) disturbance, e.g.,

Manuscript submitted June 20, 1978

after throwing a stone." On the basis of this notion that the wave of stratification is a generic phenomenon in glow discharge plasmas of fundamental physical significance, Pekarek has over the past 20 years formulated a theory which explains striations as being a succession of waves of stratification that are self-excited by feedback mechanisms that couple disturbances back to their point of origin.

Pekarek [12] further states: "self-excitation of low-frequency oscillations connected with moving striations can come about in two different ways [10]. With both these mechanisms the wave of stratification plays the role of a necessary link in a chain of processes by which the feedback loop is closed." The two feedback mechanisms advanced by Pekarek involve the external circuit and the arrival of a striation in the cathode region [12].

The wave of stratification is currently called an ionization wave, and Pekarek has formulated a wave equation that characterizes its propagation in the glow plasma medium [13]. Pekarek's hypotheses that the ionization wave is a generic wave type in glow plasmas of fundamental physical significance such as an ion-acoustic wave and that self-excited striations are the superposition of propagating ionization waves are currently widely accepted [14]. Given in the next section is the background leading to the viewpoint that backcoupled ionization waves explain self-excited striations.

In the third section it is shown how striations are self-excited via an open-loop mechanism that is an inherent feature of the processes maintaining the charged-particle density along the column. An analog for the positive column is conceptualized in terms of a trough into which moving hoppers drop sand. The analog illustrates the basic nature of the open-loop instability that sustains self-excited striations and shows that the striation phenomenon under consideration does not depend on a glow plasma media per se.

In the fourth section striations are interpreted via a steady-state mathematical model for the positive column. The model shows how both standing striations and cathode-directed and anode-directed moving striations can be self-excited via the same open-loop mechanism. The significance of the Novak potential, the *p*, *r*, and *s* striation varieties, and the quiet regions of pressure and current values requiring artificial generation of striations is also explained via the model.

In the fifth section a novel engineering approach is used to formulate a mathematical model for the striated positive column. The analytical formalism uses a phasor algebra and calculus which is explained in Appendix A and is tantamount to solving the Boltzmann equation in that the detailed variations in the shape of the electron energy distribution function are taken into account. The model incorporates parameters that are readily measured by experiment, such as the quiescent values of Novak's potential, the mean electron energy, the relative fraction of the discharge input power that is dissipated via electronic and vibrational excitations, and the relative number of electrons with energy in excess of the first electronic excitation potential. The model applies to both atomic and molecular fill gases and is amenable to numerical predictions, thereby facilitating its experimental verification. In Appendix B the model is extended to RF-excited positive columns.

In the sixth section the model is used to derive general formulations which predict striation properties such as frequency and wavelength.

It is well known that self-excited striations occur only when the discharge current and pressure are less than certain limiting values. Pupp found that in pure rare gases the threshold currents and pressures are such that $I_t p_t = C$, where C is a constant that depends on the fill gas [15]. In the seventh section general expressions are derived for I_t and p_t based on two relaxation time constants of the electron energy distribution function, one stemming from elastic energy exchange via electron-electron collisions and the other stemming from elastic energy exchange via electron-neutral collisions.

The properties of the *p, r,* and *s* striation varieties in neon are also predicted via the model, and the results are compared with experiment. In Appendix C the experimental techniques and apparatus are discussed. Several state-of-the-art measuring techniques in plasmas were incorporated into an automated facility for measuring striation parameters that was used to generate spectral-raster and space-time photographic displays of the dependencies of the striation parameters on two continuous variables: discharge-tube current and pressure.

The neon discharge was extensively investigated throughout the entire plane of reduced current and pressure in which the *p, r,* and *s* varieties of striations are spontaneously generated and in the quiet regions of pressure and current values, in which regions the *p, r,* and *s* varieties of the wave of stratification were artificially generated and their parameters measured. The experimental data are presented in Appendix D.

In the eighth section striation phenomena in a Penning discharge of neon with an argon admixture are discussed. In such a discharge it was found that the values of the Novak potentials for the *p* and *s* waves increase continuously as a function of argon concentration and that the striations are quenched for argon amounts in excess of approximately 0.2%. These observations are also accurately predicted by the model.

In the final section the model is used to explain the nature of the higher order frequency spectra of striations.

BACKGROUND OF THE CURRENT THEORY FOR SELF-SUSTAINED STRIATIONS

As depicted in Fig. 1, self-excited striations are standing-wave or traveling-wave variations in light intensity and other plasma parameters such as charged-particle density, electric field, and electron energy along the positive column of a glow discharge. Stationary, or standing, striations are readily discerned by the unaided eye and were first observed over 130 years ago [1]. The velocities of moving striations are large enough that to the unaided eye a positive column containing them appears to be uniformly illuminated. Moving striations were first detected nearly 100 years ago by viewing a positive column in a rotating mirror whose rotation rate was synchronized to the striation velocity [2]. Self-excited striations spontaneously occur unless the discharge-tube pressure and current are within the ranges of values called quiet regions.

As depicted in Fig. 2, if a transient perturbation is applied to a positive column operating in a quiet region, a striation phenomenon is excited that consists of localized moving striations whose amplitudes define a wave-packet-like envelope along a portion of the column. The wave packet spreads as it moves along the column, and in the case of the rare gases the striations that delineate the packet envelope move in the opposite direction of the anode-directed wave

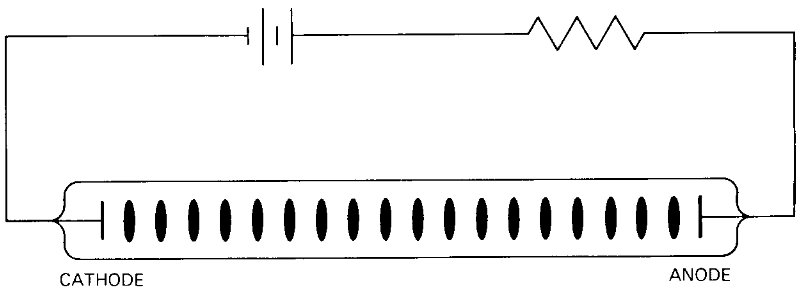

Fig. 1 — Self-excited striations

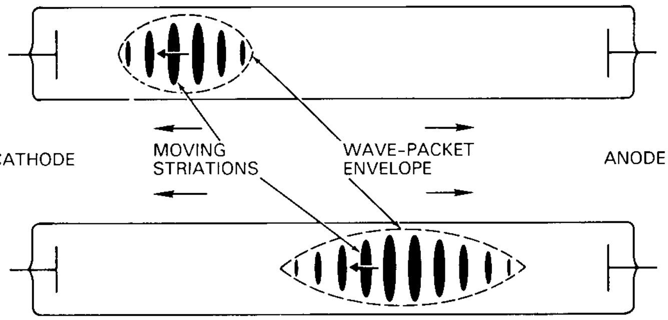

Fig. 2 — Artificially excited anode-directed ionization wave in a column containing a rare gas. The bottom sketch shows the same wave packet shown in the top sketch but at a later time.

packet. After the wave packet reaches the end of the positive column and transient effects dissipate, the column regains its initial longitudinally homogeneous state. This wave-packet-like transient response of a discharge operating in a quiet region was originally called a wave of stratification by Pekarek [10] and is now called an ionization wave [14].

Except for their position-dependent amplitudes the artificially excited moving striations whose amplitudes delineate the ionization wave-packet envelope are essentially identical to the constant-amplitude self-excited moving striations that are spontaneously generated when the discharge is operated outside the quiet region. Over the past 20 years a theory for self-excited striations has evolved that is based on the notion that the artificially excited ionization wave is the fundamental striation phenomenon in the positive column and that constant-amplitude self-excited striations are a succession of ionization waves whose wave-packet envelopes have spread to the extent that they encompass the entire length of the positive column.

According to Pekarek a succession of ionization waves is self-excited by a closed-loop process consisting of amplified ionization waves that are backcoupled to their point of origin. Pekarek [12] advances the viewpoint (Fig. 3) that the propagation of the ionization wave along the column provides a feed-forward path and that external backcoupling through the circuit or

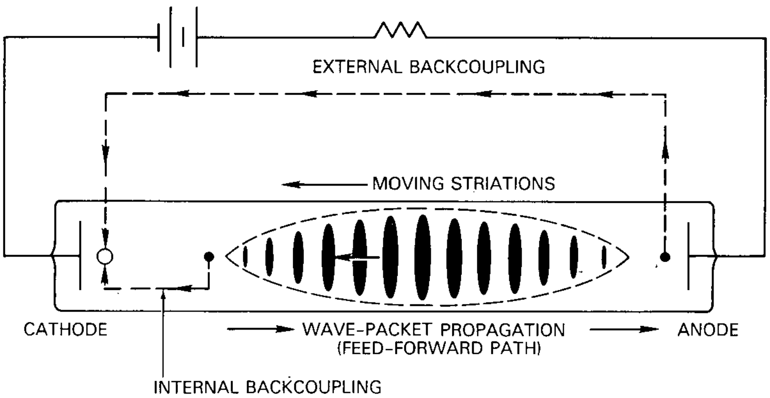

Fig. 3 — Current-theory concept of backcoupling mechanisms for exciting successive ionization waves

internal backcoupling in the cathode region caused by the oppositely directed motion of the striations within the wave packet provide feedback mechanisms that couple disturbances back to the point of origin of the ionization waves with sufficient intensity to excite successive ionization waves. Pekarek [16] discusses the amplification of the ionization wave as it propagates along the positive column and concludes that for striations to be self-excited this amplification must be so effective that it is sufficient to overcome losses not only in the positive column itself but also in the other links in the chain of backcoupling (external circuit, cathode region, etc.).

Lee, Bletzinger, and Garseadden [17] examine the gain of the positive column with regard to propagating ionization waves. They refer to a model by Achterberg and Michel [18] that represents a discharge with moving striations by an electrical circuit consisting of an amplifying component (the striating positive column) and a current feedback and point out that the gain of the column and the amount of feedback which determines the oscillation conditions for such a circuit depends on the discharge parameters.

A distinguishing feature of the existing theory for striations is that striations are self-excited by a closed-loop feedback path consisting of propagating ionization waves that couple disturbances back to their point of origin with sufficient amplitudes to excite successive ionization waves. In addition to difficulties concerning the nature of the postulated backcoupling mechanisms [19], the backcoupled ionization wave theory does not satisfactorily explain such fundamental striation properties as anode-directed striations, standing striations, Novak's law, and the *r*, *s*, and *p* striation varieties in neon. The new theory being reported here shows that backcoupling mechanisms such as Pekarek's are not necessary to explain how striations are self-excited, and it also provides a unified explanation for all types of striations and their properties.

THE NEW THEORY BASED ON AN OPEN-LOOP MECHANISM FOR SUSTAINING STRIATIONS

The new theory shows how resonant-wavelength striations are self-sustained by an open-loop mechanism that consists of a transport delay between changes in ion density along a positive column and the induced changes in the net rate at which ions accumulate in a unit volume along the column. This delay is an inherent feature of the glow plasma processes that maintain the ion-density along the column, and it arises as follows.

Figure 4 depicts a constant-amplitude sinusoidal variation in ion density along an unbounded length of positive column and represents the drifting electron gas by a reference frame that moves along the column with the electron drift velocity. As the electron gas drifts past positions such as 1 where a relative deficiency in ion density exists, its energy distribution begins to evolve toward one that increases the net ion accumulation rate so as to restore the ion density at these positions to its equilibrium value. Time delays for the redistribution of electron energies coupled with the drift of the electron gas cause the induced relative increases in accumulation rate to occur at positions such as 2 that are shifted toward the anode from the density minimums. The net effect is that a striation in ion density induces a striation in ion accumulation rate with maximums that are shifted toward the anode from the minimums of the ion-density striation.

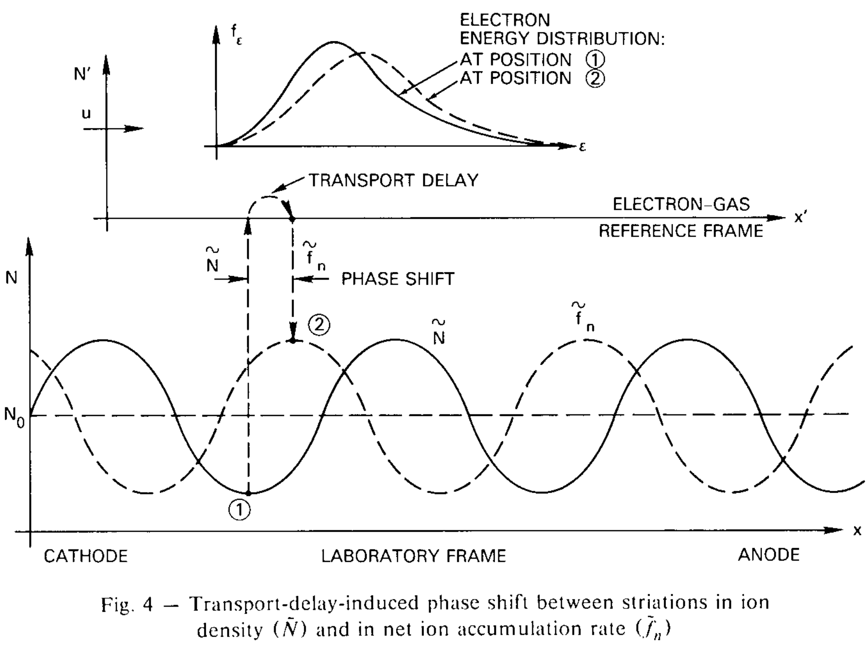

Fig. 4 — Transport-delay-induced phase shift between striations in ion density ($\tilde{N}$) and in net ion accumulation rate ($\tilde{f}_n$)

Figure 5 shows how this phase shift can result in the open-loop self-excitation of resonant wavelength striations in ion density. If the phase delay in the electron-gas reference frame between the ion-density minimums and the ion-accumulation-rate maximums is $\pi/2$, the rate maximums occur at positions such as 1. This causes the ion density at these positions to increase above the equilibrium value, and the net effect is a gradual translation of the ion-density waveform to the left. A phase delay of $3\pi/2$ produces accumulation-rate maximums at positions such as 2. This causes the ion density at these positions to increase above the equilibrium value, and the net effect is a gradual translation of the ion-density waveform to the right.

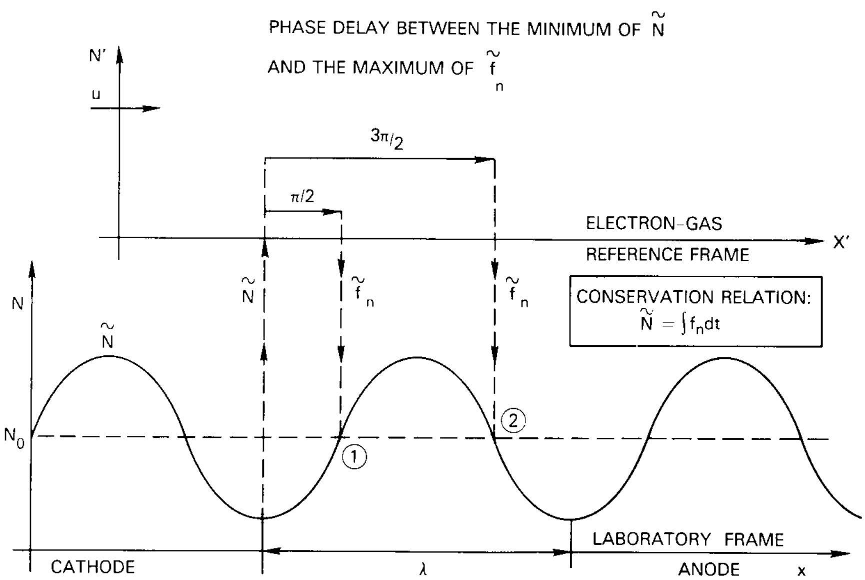

Fig. 5 — Open-loop mechanism by which resonant-wavelength striations are self-sustained as cathode-directed or anode-directed moving striations

Such an argument illustrates the open-loop mechanism by which resonant-wavelength ion-density striations can be self-sustained as cathode-directed or anode-directed moving striations. The following more formal argument substantiates this conclusion.

Due to the integral in the conservation relation (at the right in Fig. 5) an accumulation-rate striation generates a density striation that lags the rate striation by $\pi/2$. Therefore, if the wavelength of a density striation is such that the induced striation in accumulation rate leads the density striation by $\pi/2$, the induced rate striation will in turn generate a new density striation that lags the rate striation by $\pi/2$, so that it is exactly in phase with the initial density striation, thereby sustaining it. A phase delay of $\pi/2$ in the electron-gas reference frame between the minimum of $\tilde{N}$ and the maximum of $\tilde{f}_n$ makes the rate striation lead the density striation by $\pi/2$ for cathode-directed striations, thereby sustaining them, and a phase delay of $3\pi/2$ makes the rate striation lead the density striation by $\pi/2$ for anode-directed striations, thereby sustaining them.

Predicting the properties of striations in positive columns requires a detailed understanding of the interrelated glow plasma processes by which a density striation ultimately induces a certain phase striation in accumulation rate. Before this aspect of the theory is addressed, it should be pointed out that not only are self-excited striations not a succession of backcoupled ionization waves but self-excited striations are not even a feature just of positive columns, since a number of longitudinally distributed systems exhibit these types of striations due to open-loop transport delays. To illustrate that striations can occur in systems other than positive columns and to emphasize the basic nature of the open-loop instability leading to striations as well as clarifying the difference between self-excited striations and artificially excited ionization waves, an imagined electromechanical analog of the positive column is briefly discussed.

Figure 6 is a front plan view of the analog, which consists of a trough oriented along the $+x$ axis and an overhead conveyor belt moving in the $+x$ direction with velocity u_b that is partitioned so as to form many individual hoppers that dispense sand from adjustable pour valves. The vertical dashed lines conceptually partition the trough into many unit lengths, each of which contains an adjustable leak valve. The sand level and thus the number of sand particles N in a particular unit length along the trough is controlled by the hoppers according to the following scheme as they one after another pass over that unit length. Each hopper contains an identical servo system that senses the sand level and thus senses N in the unit length of the trough that is below the hopper at the time. The primed notation indicates parameters as perceived in the moving reference frame of the conveyor belt, and unprimed quantities are as observed in the reference frame of the trough. As depicted in Fig. 6, N is perceived as N', which generates a control signal C' that in turn modulates the pour rate P' from the hopper valve and, via the transmitted signal L', the leak rate L from the underlying leak valve. The hoppers also transmit the control signal C' which is perceived by the underlying unit lengths as C, and C in turn causes by some mechanism not shown a sand-particle drift velocity in the $-x$ direction. Thus, in addition to sand particles entering a unit length of the trough from the overhead pour valves and leaving via the leak valves, they also ingress and egress via the end sections of a unit length, so that P_n, the net sand-particle accumulation or leak rate in a particular unit length of the trough, is modulated by the hoppers as they pass over that unit length.

The following correspondences exist between the analog and the glow-discharge positive column. The trough corresponds to the positive column, the sand particles to the ion-electron pairs, the control signal to the longitudinal electric field, the conveyor belt and hopper servo systems to the electron gas and electron energy ($\mathscr{E}$) distribution function $f_{\mathscr{E}}$, the pour rate to the ionization rate, and the leak rate to the ambipolar recombination rate. In the positive column the drift of the electron gas relative to the striations in electric field induces modulations in the shape of $f_{\mathscr{E}}$ with time constants that depend on the particular energy interval. For example, the relaxation time constants for variations in the high-energy tail of $f_{\mathscr{E}}$ determines the phase of the striation in ionization rate, whereas a different time constant for variations in the body of $f_{\mathscr{E}}$ determines the phase of the striation in ambipolar recombination rate. The variations in the shape of $f_{\mathscr{E}}$ are modeled by the hopper servo system transfer functions, H_{nc}, H_{cp}, and H_{cl} in Fig. 6. The control law of the hopper servo system adjusts the net accumulation rate P_n of sand particles in each unit length along the trough so as to maintain overall along the trough a constant quiescent sand level N_0.

Figure 7 illustrates the open-loop mechanism by which initial resonant-wavelength striations in sand level are self-sustained as moving striations in the $+x$ or $-x$ direction. As the hoppers move past positions such as 1, where a relative deficiency in sand level exists, an increase in the net sand accumulation rate P_n is commanded in order to restore the sand level at these positions to its equilibrium value. However, delays associated with the hopper servo

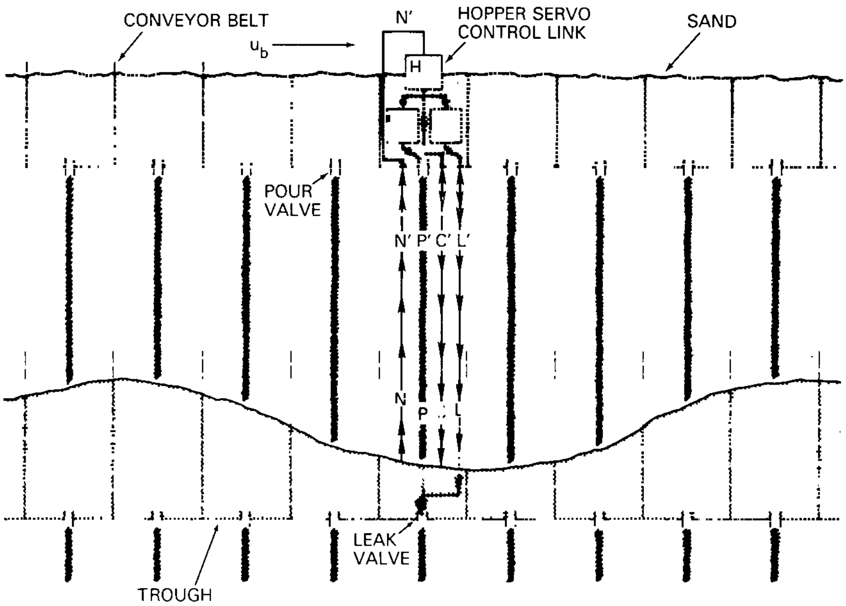

Fig. 6 — Control system by which a conveyor belt with hoppers could try to maintain a constant sand level along a trough

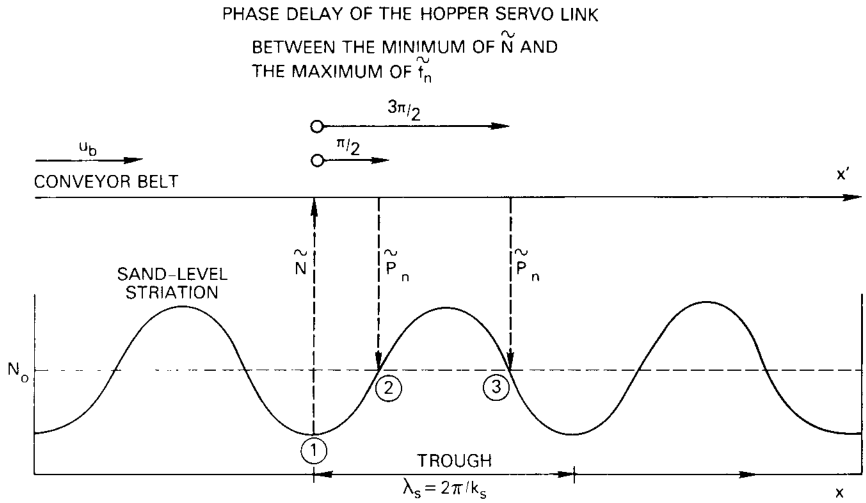

Fig. 7 — Open-loop mechanism by which resonant-wavelength striations in the sand level in Fig. 6 are self-sustained as moving striations in the $+x$ or $-x$ direction

system cause the commanded relative increases in sand accumulation rate to be shifted in the $+x$ direction from the relative minimums in sand level. Thus a sand-level striation induces a striation in sand accumulation rate with maximums that are shifted in the $+x$ direction from the minimums of the sand-level striation. If the phase delay between the sand-level minimums and the sand-accumulation-rate maximums is $\pi/2$, the rate maximums occur at positions such as 2. This causes the sand level at these positions to increase above the equilibrium value, and the net effect is a gradual translation of the sand-level waveform to the left. A phase delay of $3\pi/2$ produces accumulation-rate maximums at positions such as 3. This causes the sand level at these positions to increase above the equilibrium value, and the net effect is a gradual translation of the sand-level waveform to the right. The phase delay between the $\tilde{N}$ and $\tilde{P}_n$ striations results from an open-loop mechanism consisting of the motion of the conveyor belt coupled with the time delays of the hopper servo systems. A resonant-wavelength striation $\tilde{N}$ results in the unique phase delay of $\pi/2$ or $3\pi/2$ for which $\tilde{P}_n$ leads $\tilde{N}$ by exactly $\pi/2$, thereby sustaining $\pm x$-directed sand-level striations.

If the gain of the hopper control links is such that the operation is conditionally stable, an initial constant sand level along the trough will be maintained regardless of the phase delay of the hopper servo system. If the operation is perturbed, say by depositing a pile of sand at some point along the trough, a transient ringing response is illicited in the form of a packet of localized sand-level striations. The direction of the localized moving striations that delineate the packet envelope depends on whether the phase delay of the hopper servo system is in the vicinity of $\pi/2$ or $3\pi/2$, and the direction of the wave packet depends on whether the conveyor-belt-and-hopper mechanism carries the disturbance in the $+x$ direction faster or slower than the drift of the sand particles in the $-x$ direction. The disturbance does however move off in one direction or the other, and ultimately the sand level in the vicinity of the point of perturbation regains the initial constant level. This longitudinally propagating transient response is analagous to the ionization wave in a positive column. Since the conveyor-belt-and-trough mechanism is not bounded in length, self-excited striations are sustained by an open-loop transport-delay-induced phase lead of a rate striation relative to a density striation and not by a succession of transient responses caused by a backcoupling of transient disturbances.

INTERPRETING STRIATIONS VIA A STEADY-STATE MATHEMATICAL MODEL FOR THE POSITIVE COLUMN

Figure 8 is a block diagram of an electrical circuit equivalent to a steady-state mathematical model for the positive column. This model was derived by using a phasor representation for striations and a phasor calculus (Appendix A); these were used in the set of integral-differential equations that describe the pertinent glow-discharge processes in a striated positive column. Each block in this diagram characterizes the steady-state nature of one or a combination of these processes via a phasor magnitude-phase transformation.

The upper portion of the diagram (large rectangular dashed block) is like a radio-frequency (RF) link in that it accounts for the high-frequency variations in the distribution of electron energies that are caused by the drift of the electron gas relative to the striations in ion density. The lower block H_{nn} is like an intermediate-frequency (IF) link in that it accounts for the low-frequency variations in ion density in the laboratory frame that result from the integration of the net ion accumulation rate; that is, H_{nn} models the conservation relation for ions. The local oscillator and mixers account for the frequency translation between the laboratory frame and the primed frame that moves with the electron gas.

In the RF link the H_{ne} block models the longitudinal ambipolar and conduction electric fields, the H_{ea} block models radial ambipolar diffusion, and the H_{er}, $H_{en,p}$, and H_{es} blocks model respectively the electron-ground state, metastable-metastable, and electron-metastable ionization mechanisms, all producing singly ionized atomic ions. The $H_{en,x}$ block models the

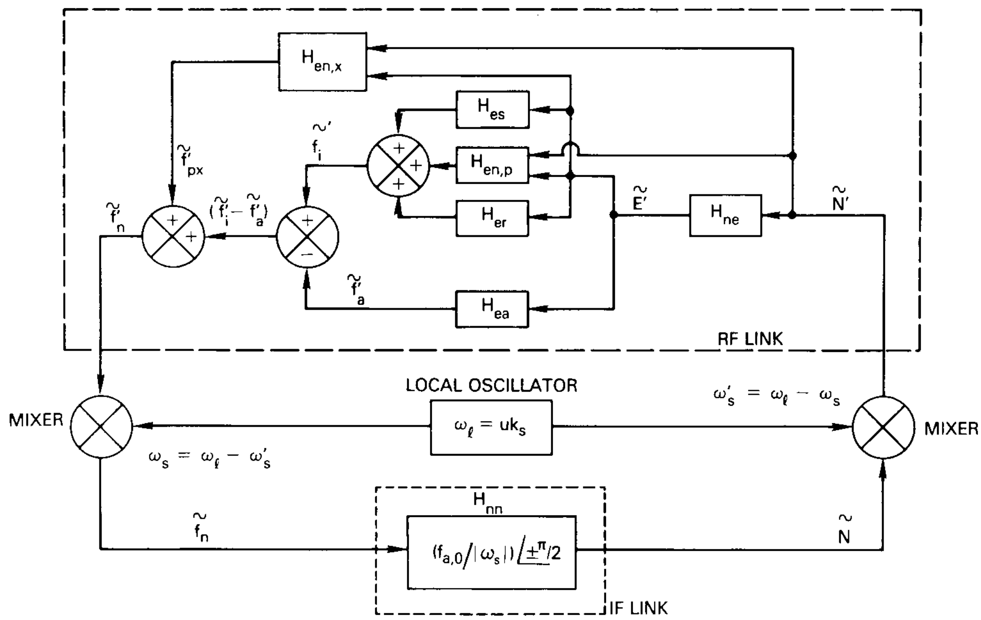

Fig. 8 — Electrical circuit that is equivalent to a steady-state mathematical model of the glow-discharge positive column

divergence of the longitudinal ion drift current. The subtractor gives the phasor difference between ionization f_i and recombination f_a rates, and the adder at the left gives the net ion accumulation rate f_n.

That the steady-state model of the striated positive column diagrams as a closed loop does not imply that the column functions as a feed-forward or a feedback link in a physical closed loop as in the backcoupled ionization wave theory. The significance of this diagram is that a striation in ion density along an unbounded length of column will modulate the distribution of electron energies of the drifting electron gas, thereby ultimately producing a certain phase striation in net ion accumulation rate that is integrated by the column to obtain a new striation in ion density along the column, thereby completing the chain of events that maintain the ion density along the column.

A resonant-wavelength ion-density striation corresponds to a net phase shift around the frequency translated RF-IF loop in figure 8 of 2π, so that the new striation in ion density is exactly in phase with the initial ion-density striation, thereby sustaining resonant-wavelength ion-density striations along the unbounded length of positive column. Standing striations correspond to self-sustained oscillations of this frequency-translated RF-IF loop with the IF at zero beat, and anode-directed and cathode-directed moving striations correspond to oscillations on either side of zero beat.

Since the electron-gas drift velocity u is much greater than striation velocities, an observer moving with the drifting electron gas perceives all types of striations (cathode-directed and anode-directed moving striations and standing striations) as cathode-directed moving striations with approximate striation velocity u. Therefore in the primed frame that moves with the electron gas the frequency of the striation-induced variations in the plasma parameters is given approximately by u/λ_s for both standing striations and anode-directed and cathode-directed moving striations, where λ_s is the striation wavelength. The phase lag through the RF link determines the phase of $\tilde{f}_n'$ relative to $\tilde{N}'$. The RF-link phase lag in turn depends on the striation frequency u/λ_s perceived by the drifting electron gas and on the sense of an inequality between relaxation time constants for changes in the shape of the electron-gas energy-distribution function in the energy intervals pertinent to ionization and ambipolar recombination. For one sense of this inequality $\tilde{f}_a'$ lags $\tilde{f}_i'$, which results in a resonant value of λ_s such that $\tilde{f}_n'$ lags $\tilde{N}'$ by $3\pi/2$, thereby causing $\tilde{f}_n$ to lead $\tilde{N}'$ by $\pi/2$ for cathode-directed striations (Fig. 9). For the opposite sense of the inequality $\tilde{f}_i'$ lags $\tilde{f}_a'$, which results in a resonant value of λ_s such that $\tilde{f}_n'$ lags $\tilde{N}'$ by $\pi/2$, thereby causing $\tilde{f}_n$ to lead $\tilde{N}'$ by $\pi/2$ for anode-directed striations (Fig. 9). The sense of the inequality depends on the nature of the fill gas and on the exact discharge conditions. For atomic gases $\tilde{f}_a'$ lags $\tilde{f}_i'$, resulting in an RF-link phase lag of $3\pi/2$ for resonant-wavelength cathode-directed striations. The low energy level inelastic losses in molecular gases tend to reverse the inequality, resulting in an RF-link phase lag of $\pi/2$ for resonant-wavelength anode-directed striations.

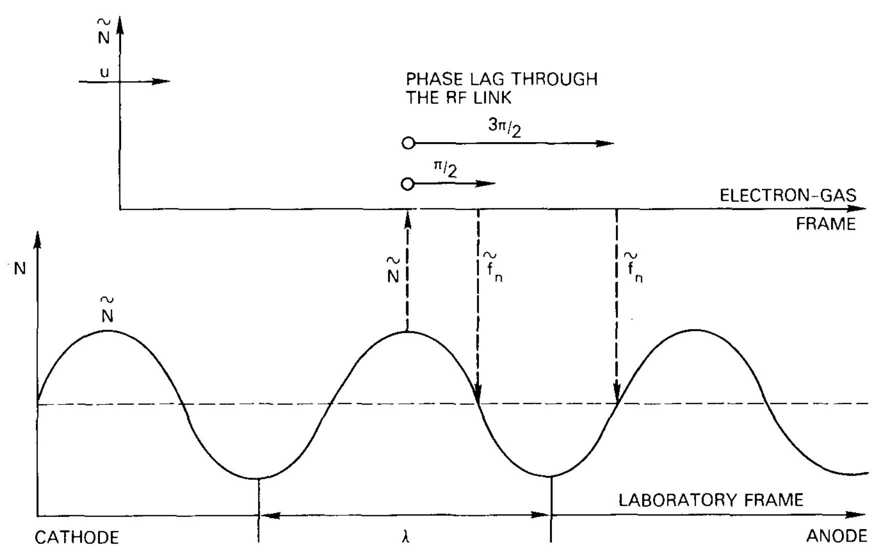

Fig. 9 — Phase lag through the RF link for cathode-directed and anode-directed striations

For some ranges of discharge conditions the $\tilde{f}_i' - \tilde{f}_a'$ and $\tilde{f}_{px}'$ contributions to $\tilde{f}_n'$ tend to be of equal amplitude and opposite phase. When cancellation is exact, striations are sustained that are stationary in the laboratory frame. However, in the frame of the drifting electron gas the mechanism that sustains standing striations is a dynamic balanced null in which the contribution of $\tilde{f}_i' - \tilde{f}_a'$ to $\tilde{f}_n'$ exactly cancels the contribution of $\tilde{f}_{px}'$. If the null unbalances, an $\tilde{f}_n$ is produced with the correct phase to cause the striation to move in the anode or cathode direction. This explains the frequently observed slight erratic drift of standing striations toward the cathode or anode. Also, the dependence on discharge conditions of the time-constant inequality that determines the phase of $\tilde{f}_i'$ relative to $\tilde{f}_a'$ explains how, for some gases, striations undergo a transition between cathode-directed, standing, and anode-directed striations as the discharge current or the pressure is changed.

The phase lags associated with the individual RF-link blocks H_{ne}, H_{ea}, H_{er}, etc. ultimately determine the RF-link phase lag. Relaxation time constants τ are associated with each of these blocks, and the phase lags θ of the blocks are of the form $\theta = \tan^{-1} \omega_s' \tau$, where $\omega_s' = 2\pi u/\lambda_s$ is the angular striation frequency in the reference frame of drifting electron gas. Analyses in the next section show that τ is inversely proportional to $N(E_0 u)$, the average number of electron-volts per second gained by the electron gas as it drifts in the quiescent longitudinal electric field E_0. Therefore $\omega_s' \tau \propto (u/\lambda_s)(1/E_0u)$, so that θ depends on the parameter $E_0\lambda_s$. The RF-link phase lag therefore depends on $E_0\lambda_s$, and the significance of Novak's law is that as discharge conditions change, the constant RF-link phase lag of $\pi/2$ or $3\pi/2$ required to sustain anode-directed or cathode-directed striations in turn requires a constant value of $E_0\lambda_s$.

The *r*, *s*, and *p* striation varieties in neon are a consequence of the fact that the net phase lag through the RF link depends on which of the three ionization-rate variations dominates the phase of $\tilde{f}_i'$, the net variation in ionization rate. For lower reduced pressure *pR*, electron-ground state ionization dominates the phase of $\tilde{f}_i'$, and the RF-link phase lag is via the H_{er} block, resulting in the distinct value of $E_0\lambda_s$ associated with the *r*-variety striation. For intermediate values of *pR*, metastable-metastable ionization dominates, resulting in the *p*-variety striation. For higher *pR* values, electron-metastable ionization dominates, resulting in the *s*-variety striation.

When the discharge is operated in the quiet region, all three ionization mechanisms contribute approximately equally, so that none dominates the net ionization rate. Self-excited striations are not possible under these conditions. However, if such a column is perturbed, variations are imparted to all three ionization rates, leading to a transient ringing response of the column that is currently interpreted as the simultaneous generation of ionization waves of the *r*, *s*, and *p* varieties.

THE DERIVATION OF THE STEADY-STATE MATHEMATICAL MODEL FOR THE POSITIVE COLUMN

The integral-differential expressions for the various pertinent glow-discharge processes in a striated positive column were formulated by using a hybrid hydrodynamic-kinetic approach based on the hydrodynamic equations of motion of the interpenetrating gaseous mixture of ions, electrons, and neutral atoms or molecules and on the relaxation characteristics for changes in the shape of the electron energy distribution function f_g as the electron gas drifts along the column. The neutral gas interacts with the ion and electron gases only through collisions. The ion and electron gases, however, interact with each other even in the absence of collisions because of the space-charge electric fields they can generate.

Normally one would solve for the space-charge electric field E_s generated as a consequence of slight unbalances in ion and electron densities by using Poisson's equation. However, for low-frequency motions of the electron and ion gases, such that density unbalances tend to develop at a rate much less than the electron and ion plasma frequencies, the inertia of the electron and ion gases is not a factor; that is the plasma has an overriding tendency to remain neutral, so that if the ion density N_p changes, the electron density N_e adjusts, essentially without delay, to make $N_p - N_e \approx 0$. Consequently, for the low-frequency motions of the ion and electron gases encountered in moving striations, it is permissible to assume that $N_p = N_e$ and that $\nabla \cdot E_s \neq 0$ at the same time. This is known as the plasma approximation and is essentially a statement that the space-charge density is of secondary importance, it will keep adjusting itself so that Poisson's equation remains satisfied, and that the space-charge electric field is determined from the hydrodynamic equations of motion via the required balance of forces on the drifting electron and ion gases.

Since the plasma approximation allows the assumption $N_p = N_e$, the subscript from the ion and electron densities is deleted, and N is used to represent the volume density of ion-electron pairs. Also, to simplify the notation, the plasma parameters of the ion gas are subscripted with a p, and the more frequently referred to plasma parameters of the electron gas are not subscripted.

The ion and electron gases tend to be accelerated along the longitudinal axis of the positive column (taken as the $+x$ axis in the cathode-to-anode direction) under the combined forces due to space-charge electric fields, pressure gradients, and friction due to collisions with the neutral gas molecules. However, since the inertia of the ion and electron gases is zero, the net resultant force on the ion and electron gases due to the above-mentioned effects must also be zero. Thus the space-charge electric field is constrained to a value that produces electrostatic forces on the electron and ion gases that exactly cancels the forces on these gases due to pressure gradients and collisional friction with the neutral gas molecules.

It is convenient to conceptually decompose the net longitudinal space-charge electric field E into two components: an ambipolar electric field E_a that cancels the force due to pressure gradients in the electron gas and a conduction electric field E_c that just balances the viscous retarding force due to electron-neutral collisions as the electron gas drifts along the positive column. E_c and E_a are given by

$$E_c = -\frac{m_e}{e} f_c u \tag{1}$$

and

$$E_a = -\frac{\nabla_x p_n}{eN}, \tag{2}$$

where m_e is the electron mass, e is the electron charge, f_c is the electron-neutral collision frequency, u is the electron drift velocity, and p_n is the partial pressure of the electron gas.

Comparing Eq. (1) with the form $u = \mu E_c$ defines the electron mobility as

$$\mu = (e/m_e) f_c^{-1}. \tag{3}$$

The conduction current I in the positive column is essentially due to the drift of the electron gas and can be written as

$$J_c = -eNu = \frac{I}{\pi R^2}, \tag{4}$$

where I is determined by the current source energizing the discharge and R is the radius of the positive column.

The conservation of the net space charge requires that

$$\nabla_x \cdot J_c = -\,\partial \rho_s / \partial t, \tag{5}$$

where $\rho_s = e(N_p - N_e)$ is the net free-space charge. Since $N_p = N_e$ for low-frequency variations of N_p and N_e when the plasma approximation is valid, $\nabla_x \cdot J_c = 0$.

That this is true may also be seen by noting that the relaxation time constant for the decay of free charge τ_r in a medium with conductivity σ is given by $\tau_r = \epsilon_0/\sigma$. For glow plasmas τ_r is of the order of 0.1 ns, so that for frequencies as high as approximately 10 GHz $\nabla_x \cdot J_c$ is essentially zero. The constraint $\nabla_x \cdot J_c = 0$ implies that there is no spatial variation in J_c, or that $\tilde{J}_c = 0$.

Using $u = \mu E_c$ in Eq. 4, writing the result in phasor notation (Appendix A), and using $\tilde{J}_c = 0$ gives the following phasor transfer-function relation:

$$\tilde{E}_c = [1 \angle \pi]\,(\tilde{N} + \tilde{\mu}). \tag{6}$$

The interpretation of Eq. 6 is that when striations are present, the plasma conductivity is spatially and temporally modulated. The fast relaxation time constant for the decay of free-space charge in the conducting plasma results in a homogeneous conduction current along the length of the positive column. The uniform conduction current causes a spatial and temporal modulation of the conduction electric field that is exactly out of phase with the modulations in the conductivity.

The variations in the electron-gas partial pressure p_n along the column cause the charged particles to diffuse longitudinally from regions of high p_n toward regions of low p_n. Diffusion in a glow plasma is ambipolar, since, to preserve charge neutrality, the charged particles must always move as ion-electron pairs. Since the free-diffusion coefficient for electrons D is much larger than that for ions, a steady state develops in which a slight residual positive space charge exists in the regions where p_n is large. In resulting longitudinal ambipolar electric field E_a impedes the diffusion of the electrons and assists the motion of the ions. In fact E_a is of such a magnitude that it essentially determines the motion of the ions, their self-diffusion being negligible.

The customary plasma-physics interpretation of electron temperature is

$$\frac{kT_e}{e} = K_f \mathscr{E}_m \tag{7}$$

where T_e is the electron temperature in kelvins, $\mathscr{E}_m$ is the mean electron energy in electronvolts, and K_f is a constant of the order of unity whose exact value depends on the particular form of the electron energy distribution function $f_{\mathscr{E}}$.

Using Eq. 7 in Eq. 2 gives

$$E_a = K_f \frac{\nabla_x(\mathscr{E}_m N)}{N}. \tag{8}$$

The significance of Eq. 8 is that as the electron gas drifts along a striated positive column, a longitudinal ambiplar electric field develops that produces a net electrostatic force on the electron gas that exactly neutralizes the diffusive forces due to gradients in electron temperature and density.

Using phasor notation in Eq. 8 and equating like terms gives $E_{a,0} = 0$ and the following phasor transfer-function relation:

$$E_{a,0}\,\tilde{E}_a = [K_f \mathscr{E}_{m,0}\, k_s \;\underline{|\pi/2}]\;(\tilde{N} + \tilde{\mathscr{E}}_m). \tag{9}$$

Using phasor notation in the relation $E = E_c + E_a$ gives

$$\tilde{E} = \tilde{E}_c + \frac{E_{a,0}}{E_0}\tilde{E}_a \tag{10}$$

and using Eq. 6 and 9 and the relation $k_s = 2\pi/\lambda_s$ in this equation yields

$$\tilde{E} = [1\underline{|\pi}]\;(\tilde{N} + \tilde{\mu}) + \left[\frac{2\pi K_f \mathscr{E}_{m,0}}{E_0\,\lambda_s}\underline{|\pi/2}\right]\;(\tilde{N} + \tilde{\mathscr{E}}_m). \tag{11}$$

The relative phase relationship between the phasors $\tilde{E}$, $\tilde{N}$, $\tilde{\mu}$, and $\tilde{\mathscr{E}}_m$ depends on the Novak potential $E_0\,\lambda_s$.

The charged particles in the positive column are lost due to recombination of the ions and electrons. In a glow-discharge plasma the rate of volume recombination is negligible compared with the rate at which the charged particles diffuse to the tube walls, where recombination more readily occurs. This radial diffusion is also ambipolar; that is, the charged particles move to the wall in ion-electron pairs. The average recombination frequency per charged particle due to ion-electron recombinations via radial ambipolar diffusion to the column wall is

$$f_a = (2.4/R)^2\,\mu_p\,(D/\mu), \tag{12}$$

and f_i is the net average ionization frequency per electron, which is the superposition of the ionization frequencies due to several distinct ionization mechanisms

The volume production and loss rates of ion-electron pairs due to ionization and ambipolar recombinations are

$$P = f_i N \tag{13}$$

and

$$L = f_a N. \tag{14}$$

The net charged-particle balance in a unit length of the column also depends on any net unbalance in the charged-particle currents into and out of the ends of a unit length of the column.

The positive ions move in accordance with the electric field, and the electrons follow so as to preserve charge neutrality, so that the longitudinal charged-particle current referred to is not a conduction or net current but rather a flow of ion-electron pairs and is given by

$$J_p = \mu_p\,N\,E. \tag{15}$$

The conservation of charged particles in a unit length of the column requires that

$$dN/dt = (P - L) - \nabla_x \cdot J_p. \tag{16}$$

Using Eqs. 13 through 15 in Eq. 16 and writing the result in phasor notation gives the relation

$$\tilde{N} = H_{nn}\, \tilde{f}_n, \tag{16$'$}$$

where

$$H_{nn} = f_{a,0} \Big/ |\omega_s| \underline{\big|\pm \pi/2} \tag{17}$$

and

$$\tilde{f}_n = (\tilde{f}_i - \tilde{f}_a) + \tilde{f}_{px}, \tag{18}$$

in which

$$\tilde{f}_{px} = [H_{en,x}]\, (\tilde{E} + \tilde{N}), \tag{19}$$

where

$$H_{en,x} = \left[\frac{(E_0\, R)}{(\lambda_s/R)\, \mathscr{E}_{m,0}} \underline{\big|\pi/2} \right] \tag{20}$$

In the substitutions leading to Eq. 20 the approximation $2\pi \approx 5.76$ and $D_0/\mu_0 \approx \mathscr{E}_{m,0}$ were used.

The phasor transfer function $|H_{nn}|$, models the conservation relation for charged particles and expresses that with regard to the accumulation of ion-electron pairs the positive-column envelope is an ideal integrator. The quiescent ambipolar recombination rate $f_{a,0}$, is the relaxation frequency for changes in ion density, and the integration gain, $|H_{nn}|$, depends on the ratio of $f_{a,0}$ to the angular striation frequency ω_s.

The term $\tilde{f}_i - \tilde{f}_a$ represents the modulation of the net accumulation rate of ion-electron pairs via ionization, and the term $\tilde{f}_{px}$ accounts for the modulation imparted to the net influx of ion-electron pairs into a unit length of the positive column due to the divergence of the ion current.

Since $f_a \propto D/\mu$, $\tilde{f}_a$ is given by $\tilde{D} - \tilde{\mu}$. As the following formulations will establish, the plasma-parameter phasors $\tilde{\mathscr{E}}_m$, $\tilde{D}$, $\tilde{\mu}$, and $\tilde{f}_i$ are fundamental quantities that are uniquely determined by the modulations in the shape of $f_{\mathscr{E}}$ induced by the drift of the electron gas in the striated longitudinal electric field $\tilde{E}$. Thus the relationships will be shown that $\tilde{f}_i$ and $\tilde{f}_a$ are determined by $\tilde{E}$ and that $\tilde{E}$ is in turn uniquely determined by $\tilde{N}$ via the iterative process represented by Eq. 11. Showing these relationships validates the basic form of the steady-state mathematical model presented in Fig. 8.

Since a hydrodynamic treatment of the glow-discharge plasma essentially attributes to each electron comprising the electron gas an energy equal to the mean energy of the entire electron gas, it cannot account for particular electrons in the electron gas which have energies that can cause specific quantum-mechanical excitations to or transitions between particular quantum states or energy levels of the neutral gas atoms or molecules. Consequently, the hydrodynamic approach is not suitable for determining the modulation of the various ionization mechanisms relative to $\tilde{E}$ or the modulations of other plasma parameters that depend on the instantaneous energy state of the electron gas such as $\tilde{D}$ and $\tilde{\mu}$.

The spatial-temporal dynamic state of the electron gas in the positive column of a glow discharge tube is rigorously defined by an electron distribution function in a six-dimensional phase space, such that $f_e(\vec{r}, \vec{v}, t)$ represents the electron distribution function, with the three components defining the space vector $\vec{r}$, the three components defining the velocity vector $\vec{v}$, and the time dimension t comprising the variables. In the case at hand (a quasi one-dimensional analysis of a glow discharge plasma along the longitudinal axes of the positive column) the electron energy distribution function adequately describes the spatial-temporal dynamic state of the electron gas.

In the normalized electron energy distribution function denoted by $f_{\mathscr{E}}$ $(\mathscr{E}, x, t)$ the three spatial dimensions are accounted for in the vairable x, the three velocity dimensions are accounted for in the energy variable $\mathscr{E}$, and, as before, the time variable is t. The function $f_{\mathscr{E}}$ is uniquely determined by the nature of the fill gas and by the reduced electric field E/p, and $f_{\mathscr{E}}$ in turn determines all of the plasma parameters of the electron gas such as N, D, and μ, so that the modulations of the plasma parameters relative to $\tilde{E}$ depend on the nature of their dependence on $f_{\mathscr{E}}$ and the modulation imparted to $f_{\mathscr{E}}$ by $\tilde{E}$.

The following additional plasma parameters are required to define the state of the glow-discharge positive column: f_x, the average electronic excitation frequency; f_{ir}, the direct electron neutral ionization frequency; f_{is}, the stepwise electron-metastable ionization frequency; f_{ip}, the stepwise metastable-metastable ionization frequency; n_x and n_r, the relative number of electrons with energies in excess of $\mathscr{E}_x$ and $\mathscr{E}_r$, the excitation and direct-ionization potentials; and n_l, the relative number of electrons in the low-energy tail of $f_{\mathscr{E}}$.

Figure 10 shows which energy intervals of $f_{\mathscr{E}}$ are important in determining these various plasma parameters. This figure also emphasizes that the form of $f_{\mathscr{E}}$ results from a dynamically balanced quiescent state in which the average number of electrons per second entering each energy interval just equals the number leaving. Each of the various pertinent energy intervals or regions of energy space such as η_x and η_r are analogous to parallel RC circuits driven by current sources in that, for example, the parameters f_x and f_{ir} represent discharge currents (the relative number of electrons per second leaving η_x and η_r) and i_x and i_r represent charging currents (the relative average number of electrons per second entering η_x and η_r via energy gain from the field E). As the figure shows, the net discharge current from the high-energy tail of $f_{\mathscr{E}}$, $f_x + 2f_{ir}$, is the charging current for n_l the low-energy tail of $f_{\mathscr{E}}$. The f_{ir} term has the factor 2 because each ionization of a ground-state neutral produces two low-energy electrons, whereas each excitation produces one low-energy electron. In the regime of relatively low discharge currents where striations occur, electron-electron interaction is neglible, so that electrons with mass m in the body of $f_{\mathscr{E}}$ lose energy only by elastic or vibrational collisions with the neutral atoms or molecules with mass M. In an elastic collision they lose on the average the fraction $2m/M$ of their initial energy, and in the case of molecular gases, when they excite vibrational energy levels they lose but a few tenths of an electron volt. The energy loss due to the excitation and ionization of metastables by electron impact is negligible compared with losses due to elastic or vibrational collisions. Thus there is essentially no discharge current from the body of $f_{\mathscr{E}}$, and $f_x + 2f_{ir}$ is like a circulating current between the low-energy and high-energy tails of $f_{\mathscr{E}}$.

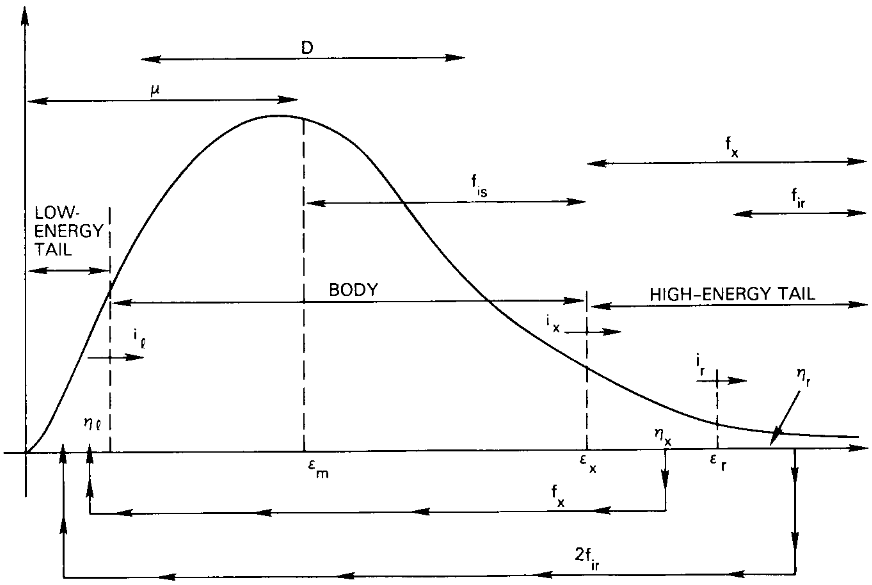

Fig. 10 — Circulating current in energy space between η_l and η_x, and the regions of $f_{\mathscr{E}}$ that determine μ, D, f_{is}, f_x, and f_{ir}

Figure 11 depicts an energy-vs-time history of an electron as it drifts along the positive column. This diagram is typically for lower discharge pressures and emphasizes the stochastic nature of the cyclic energy gain or recirculation current process by showing an electron with an initial low energy at $t = 0$ gaining energy $\mathscr{E}_x$ and then making excitations in various time intervals $f_{x,1}^{-1}$, $f_{x,2}^{-1}$, $f_{x,3}^{-1}$, $f_{x,4}^{-1}$, etc., with these intervals only on the average equaling f_x^{-1}. The electron drift along the positive column is essentially a random walk that is slightly biased in the $+x$ direction by E; an electron gains energy from E when its trajectory between collisions has a component along E, and it loses energy to E when its trajectory between collisions opposes E. An electron might typically gain or lose as much as 1 eV between collisions; however, if the net energy gain during an average excitation interval f_x^{-1} is averaged over the number of collisions that the electron makes before gaining $\mathscr{E}_x$, the average energy gained per collision is typically 0.1 eV or less.

As an electron drifts along the positive column, it gains on the average $E_0 u_0$ eV/s from the field. The fraction of energy gain C_x is due to the cyclic gain of $\mathscr{E}_x$ in the average time of f_x^{-1}, and the fraction C_{ir} is due to the cyclic gain of $\mathscr{E}_r$ in the average time f_{ir}^{-1}, so that

$$C_x(E_0 u_0) = \mathscr{E}_x f_x \tag{21}$$

and

$$C_{ir}(E_0 u_0) = \mathscr{E}_r f_{ir}. \tag{22}$$

In the same vein the average energy loss that is due to elastic and vibrational collisions is (2m/M) $f_c \mathscr{E}_m$ and $\mathscr{E}_v f_v$, so that

$$C_e(E_0 u_0) = \left(\frac{2m}{M}\right) f_c \mathscr{E}_m \tag{23}$$

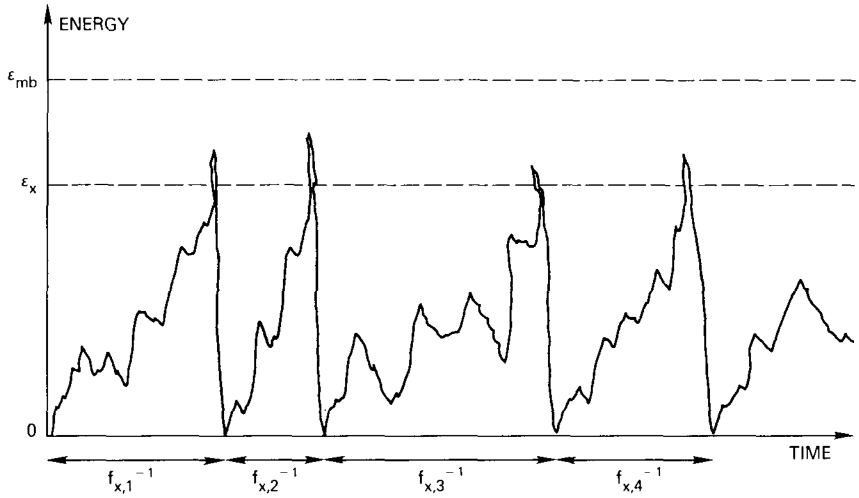

Fig. 11 — Typical electron energy-vs-time history for low pressure such that energy is lost predominantly by electronic excitation

and

$$C_v\ (E_0 u_0) = \mathscr{E}_v f_v, \tag{24}$$

where f_c is the average electron-neutral collision frequency, f_v is the average vibrational excitation frequency based on the average vibrational energy $\mathscr{E}_v$, and M is the mass of the fill-gas atom or molecule.

For atomic gases one can define a mean energy for elastic balance $\mathscr{E}_{mb}$ based on the assumption that elastic losses account for the entire energy input to the electron gas, so that on the average an electron with energy $\mathscr{E}_{mb}$ losses at each collision exactly the energy it gains from the field between collisions and thus is in a state of energy balance.

The expression for $\mathscr{E}_{mb}$ follows from Eq. 23 with $C_e = 1$ and is

$$\mathscr{E}_{mb} = 20\lambda_{e,1}\ (A W_g)^{1/2}\ (E_0/p), \tag{25}$$

where $\lambda_{e,1}$ is the electron-neutral mean free path at 1 torr and $A W_g$ is the atomic weight of the fill gas.

For higher pressures $\mathscr{E}_{mb} < \mathscr{E}_x$, and electrons drift along appreciable lengths of the positive column before the random fluctuations inherent in the dynamic elastic energy-balance process result in a large enough energy excursion above $\mathscr{E}_{mb}$ to cause an electronic excitation. A typical electron-energy history at higher pressures is depicted in Fig. 12. As p decreases, $\mathscr{E}_{mb}$ increases, decreasing the magnitude of the random energy excursion above $\mathscr{E}_{mb}$ necessary for excitation, which results in a corresponding increase in f_x. Finally, at lower pressures Fig. 11 applies, with $\mathscr{E}_{mb} > \mathscr{E}_x$, f_x correspondingly large, and electronic excitation accounting for essentially the entire energy input to the electron gas. In all pressure ranges, however, an electron makes many excitations before making an ionization, and on the average it makes exactly one ionization before it migrates to the tube wall via ambipolar diffusion and recombines with a positive ion.

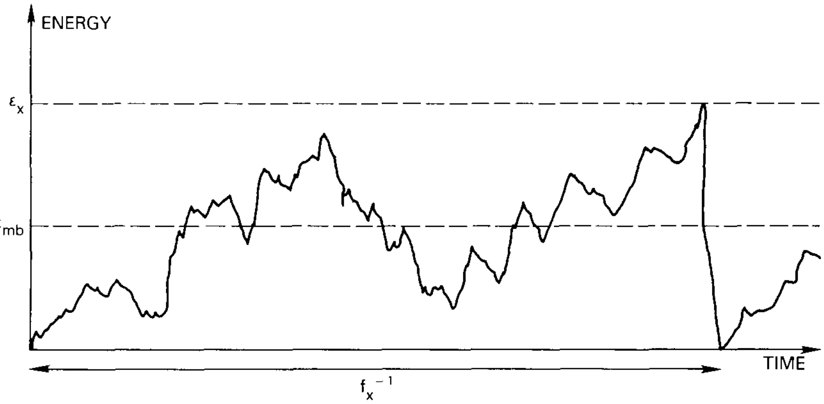

Fig. 12 — Typical electron energy-vs-time history for high pressure such that energy is lost predominantly by elastic collisions

In Ref. 20 C_x, C_e, C_v, and C_{ir} as a function of E_0/p were determined experimentally for a number of gases by passing a small electron current between parallel plates so that E_0/p could be varied over a wide range of values. The results for neon, argon, nitrogen, and hydrogen are given in Fig. 13. In the positive column E_0/p is determined by the balance between the production and loss of charged particles; however, for the low discharge currents of interest for a striated column, the functional dependencies of C_x, C_e, C_v, and C_{ir} on E_0/p in the positive column are essentially the same as the ones in these figures. These data show that in the lower pressure regime (high E_0/p) electronic excitation is the dominant loss mechanism for both atomic and molecular gases and that in the higher pressure regime elastic losses predominate for atomic gases and vibrational excitation losses dominate for molecular gases.

In the case of a striated positive column the shape of f_g continuously varies in a complicated but periodic manner, so that Fig. 10 represents in some sense the temporally averaged or quiescent shape of f_g. Likewise, the circulating current depicted in the figure between the high and low energy tails of f_g, which is essentially equal to f_x, is the quiescent value $f_{x,0}$.

As mentioned previously, the four pertinent regions of f_g (η_l, the body of f_g, η_x, and η_r) are analogous to parallel RC circuits with the input-output current pairs shown in Fig. 10 and with the respective analogous RC time constants τ_l, τ_b, τ_x, and τ_{ir}. Consequently, in the striated column the modulations imparted to the output current from each of the various energy regions of f_g lag those imparted to the input current by an angle for each region $\phi_r(\omega_s')$ given by

$$\phi_r(\omega_s') = \tan^{-1}(\omega_s' \tau_r), \tag{26}$$

where τ_r is the region's relaxation time constant and $\omega_s' = u_0 k_s$ is the angular frequency of $\tilde{E}$ in the reference frame of the drifting electron gas. The inverse RC time constant of a parallel RC circuit is equal to the quiescent discharge current per unit charge: $(\mathrm{RC})^{-1} = \tau_r^{-1} = I_0/Q_0$. The charge on the capacitor Q_0 corresponds to the relative number of electrons in a particular energy interval, so that the corresponding inverse RC time constant for η_x, for example, is

$$\tau_x^{-1} = f_{x,0}/n_{x,0}, \tag{27}$$

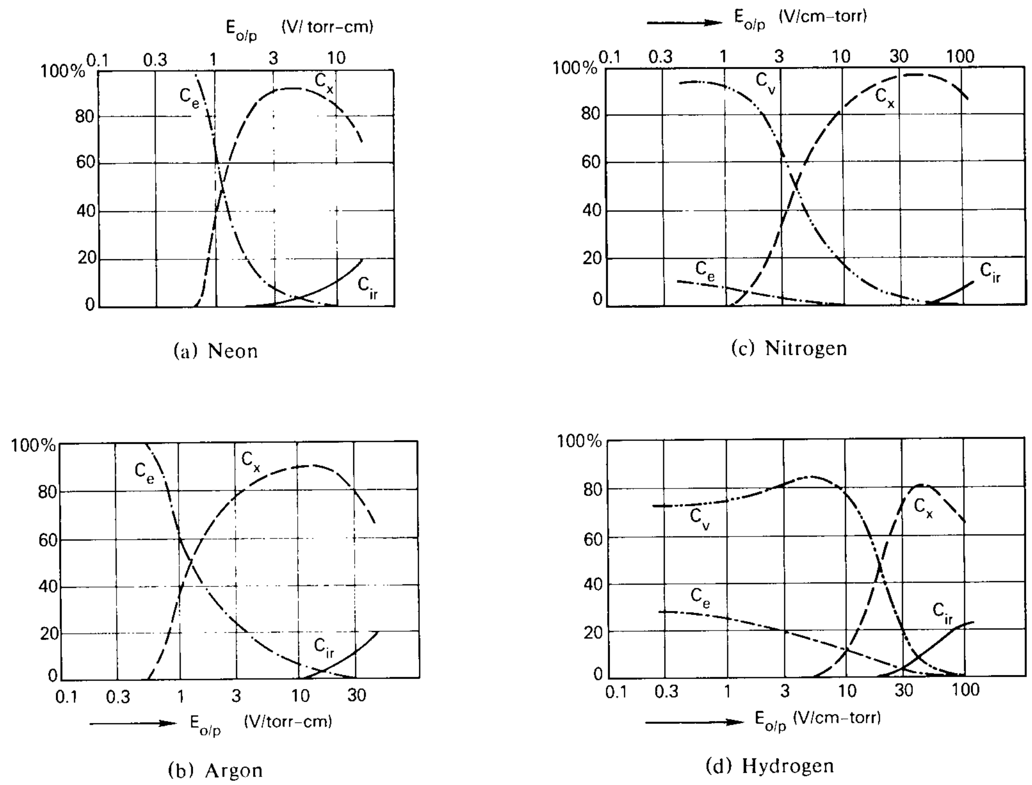

Fig. 13 — Dependence of C_e, C_x, and C_{ir} on E_0/p in a gas discharge

since $n_{x,0}$ and $f_{x,0}$ correspond respectively to the quiescent values of the capacitor charge and discharge current per unit charge.

Thus in the striated discharge $\tilde{f}_x$ lags $\tilde{i}_x$, by the angle $\phi_{ex}(\omega_s')$, given by Eq. 26 as

$$\phi_{ex}(\omega_s') = \tan^{-1}(\omega_s' \tau_x). \tag{28}$$

The striated field $\tilde{E}$ modulates i_x by modulating the component of λ_e in the direction of E_0, that is, by modulating the extent to which an electron's random walk is biased in the $+x$ direction. The time constant for this process is of the order of f_c^{-1}, and, since $f_c >> \omega_s'$, i_x follows changes in E essentially without delay, so that i_x is in phase with $\tilde{E}$. Thus, if the phasor transfer-function format is used, the dependence of f_x on $\tilde{E}$ can be written as

$$\tilde{f}_x = [H_{ex}(\omega_s', m_e)]\tilde{E}, \tag{29}$$

with

$$H_{ex}(\omega_s', m_e) = G_{ex}(\omega_s', m_e) \angle \phi_{ex}(\omega_s'), \tag{30}$$

where

$$G_{ex}(\omega_s', m_e) = G_{ex,0}(m_e)\cos[\phi_{ex}(\omega_x')] \tag{31}$$

and $\phi_{ex}(\omega_s')$ is given by Eq. 28. $G_{ex,0}(m_e)$ characterizes the nonlinearities associated with the modulation of the shape of $f_{\mathscr{E}}$ in the energy interval $\mathscr{E} \geqslant \mathscr{E}_x$ and the dependence of the nature of the nonlinearity on m_e, the modulation index of $\tilde{E}$, as discussed in detail in Appendix A.

Equations 28 through 31 constitute a general prototype phasor transfer-function format that characterizes the modulation of a plasma parameter that depends on $f_{\mathscr{E}}$. In subsequent formulations, this format should be assumed to hold unless otherwise stated, and only the analytical expressions for ϕ_{ej} and τ_{ej} will be given, where the subscript *ej* denotes that the modulation of the *j*th plasma parameter depends on the modulation of the longitudinal electric field E via its modulation of the shape of $f_{\mathscr{E}}$ in the particular energy range $\Delta\mathscr{E}$ on which the *j*th plasma parameter depends and where τ_{ej} is the effective RC or relaxation time constant for modulations in the shape of $f_{\mathscr{E}}$ in that particular energy interval $\Delta\mathscr{E}$.

An expression for $\phi_{ex}(\omega_s')$ that is based on the experimentally determined parameter C_x whose E_0/p dependence for various fill gases is given in Fig. 13 can be formulated as follows. Solving Eq. 21 for $f_{x,0}$ gives

$$f_{x,0} = \frac{C_{x,0}}{\mathscr{E}_x} E_0 u_0, \tag{32}$$

where $C_{x,0}$ denotes the quiescent fraction of the total input power to the electron gas $E_0 u_0$ that is dissipated via electronic excitation. Using Eq. 32 and 27 and the relation $\omega_s' = 2\pi u_0/\lambda_s$ in Eq. 28 yields

$$\phi_{ex}(\omega_s') = \tan^{-1}\left[\frac{2\pi\mathscr{E}_x}{E_0\lambda_s}\left(\frac{\eta_{x,0}}{C_{x,0}}\right)\right], \tag{33}$$

where $\eta_{x,0}$, the quiescent fraction of electrons with energies in excess of $\mathscr{E}_x$, can be determined by Langmuir probe measurements.

The ratio $n_{x,0}/C_{x,0}$ in Eq. 33 is approximately constant as E_0/p changes, since for a given fill gas the quiescent fractional dissipated power due to electronic excitational losses is approximately proportional to the quiescent relative number of electrons with energies in excess of $\mathscr{E}_x$. Novak's law, $E_0\lambda_s$ = constant, stems from the constraint that the RF-link phase lag remain constant, where $\phi_{ex}(E_0\lambda_s)$ given by Eq. 33 contributes to the net phase shift through the RF link.

Similar to Eq. 27 the equation for the effective inverse RC time constant for the modulation of n_r is

$$\tau_{ir} = \frac{f_{ir,0} + f_{xi,0}}{\eta_r}. \tag{34}$$

Electrons in η_r lose energy by excitation and by ionization, but since their energy is considerably greater than $\mathscr{E}_x$ and only slightly above $\mathscr{E}_r$, their probability of excitation exceeds considerably their probability of ionization, and the primary energy loss mechanism for these electrons therefore is excitation. Consequently $f_{xi,0}$, the average quiescent excitation frequency for the electrons in η_r, is considerably larger than $f_{ir,0}$, their average quiescent ionization frequency. Further, τ_{ir} is slightly less than τ_x, since electrons in η_r have a slightly larger average energy loss per collision than do electrons in η_x. Thus $\tilde{\eta}_r$ lags $\tilde{i}_r$ by an angle $\phi_{er}(\omega_s')$ that is slightly smaller than $\phi_{ex}(\omega_s')$. However, $\tilde{i}_r$ depends on both $\tilde{E}$ and $\tilde{\eta}_x$, so that $\tilde{i}_r$ lags $\tilde{E}$ by a small angle. This effect approximately offsets the smaller lag angle $\phi_{er}(\omega_s')$, so that $\tilde{\eta}_r$ is approximately in phase with $\tilde{\eta}_x$ and $\tilde{f}_{ir} \underset{\sim}{\propto} \tilde{f}_x$.

Since $i_{l,0}$, the quiescent discharge current from η_l, is equal to $f_{x,0}$, the quiescent charging current, then τ_l, the corresponding inverse RC time constant for η_l, is given by $\tau_l^{-1} = f_{x,0}/\eta_{l,0}$. Electrons in n_l have low enough energies that their trajectories between collisions are bent in the direction of E_0; hence the previous argument that $\tilde{E}$ modulates the mean free path in the direction of E_0 that led to $\tilde{i}_x \propto \tilde{E}$ does not apply for $\tilde{i}_l$. In fact, since electrons in n_l gain enough energy to leave n_l within a few collision periods, the concept of a mean free path is not applicable, and $\tilde{i}_l \propto \tilde{\eta}_l$ in much the same manner as for a vacuum diode operating in the space-charge-limited regime. Thus, $\tilde{\eta}_l$ lags $\tilde{f}_x$ by the angle

$$\phi_{xl}(\omega_s') = \tan^{-1}\left[\frac{2\pi\,\mathscr{E}_x}{E_0\lambda_s}\left(\frac{n_{l,0}}{C_{x,0}}\right)\right], \tag{35}$$

where as before $\eta_{l,0}$, the quiescent fraction of electrons with energies less than a few eV, can be determined by Langmuir probe measurements and $C_{x,0}$ is given by Fig. 13.

As discussed previously, $\phi_{ex}(\omega_s')$ given by Eq. 33 is approximately independent of the quiescent operating point of the discharge, since, as E_0/p changes, $n_{x,0}$ and $C_{x,0}$ change by approximately equal amounts. The quantity $n_{l,0}$ in Eq. 35, however, is itself approximately independent of E_0/p, although $n_{l,0}$ increases slightly as E_0/p decreases. For all gases, $C_{x,0}$ tends toward zero as E_0/p decreases, so that the ratio $\eta_{l,0}/C_{x,0}$ increases as p increases. Consequently, since $E_0\lambda_s \approx$ constant at higher discharge pressures, $\phi_{xl}(\omega_s')$ tends toward $\pi/2$ and $G_{xl}(\omega_s')$ tends toward zero, so that the modulation of η_l at higher pressures is negligible.

The modulation of $f_{\mathscr{E},b}$, the body of $f_{\mathscr{E}}$, that is, the shape of $f_{\mathscr{E}}$ in the intermediate energy ranges in the vicinity of $\mathscr{E}_m$ can be determined as follows. $N_0\mathscr{E}_{m,0}$ is the average quiescent number of electron-volts stored in the electron gas, and $N_0 u_0 E_0$ is the average quiescent number of electron-volts leaving the electron gas per second, so that $(\mathrm{RC})^{-1} = I_0/Q_0$ gives $\tau_b^{-1} = u_0 E_0/\mathscr{E}_{m,0}$. The angle $\phi_{eb}(\omega_s')$ by which the modulation imparted to the body of $f_{\mathscr{E}}$, denoted $f_{\mathscr{E},b}$, lags $\tilde{E}$ therefore is

$$\phi_{eb}(\omega_s') = \tan^{-1}\left[\frac{2\pi}{E_0\lambda_s}\,\mathscr{E}_{m,0}\right], \tag{36}$$

where $\mathscr{E}_{m,0}$ can be measured via probe techniques. $\mathscr{E}_{m,0}$ in Eq. 36 increases as E_0/p increases, so that $E_0\lambda_s \approx$ constant implies that as the discharge pressure decreases, $\phi_{eb}(\omega_s')$ tends toward $\pi/2$ and $G_{eb}(\omega_s')$ tends toward zero. Consequently for lower pressure the modulation of the body of $f_{\mathscr{E}}$ is negligible. Since $\mathscr{E}_m$ and D depend primarily on $f_{\mathscr{E},b}$, the phase lags of $\tilde{\mathscr{E}}_m$ and $\tilde{D}$ relative to $\tilde{E}$ are given by $\phi_{eb}(\omega_s')$.

As shown in Fig. 10, μ depends on both the body and the low-energy tail of $f_{\mathscr{E}}$, and due to the f_c^{-1} dependence (Eq. 3) $\tilde{\mu}$ is especially sensitive to the modulation imparted to n_l. Thus, $\tilde{\mu}$ can be written as $\tilde{\mu} = \tilde{\mu}_b + \tilde{\mu}_l$, where $\tilde{\mu}_b \propto \tilde{f}_{\mathscr{E},b}$ and $\tilde{\mu}_l \propto \tilde{n}_l$, with $\tilde{n}_l$ in turn depending on $\tilde{f}_x$ via $\phi_{xl}(\omega_s')$ given by Eq. 35. Figure 14 is a block diagram of the composite phasor transfer function $H_{e\mu}\,(\omega_s', m_e)$ that relates $\tilde{\mu} = \tilde{\mu}_b + \tilde{\mu}_l$ to $\tilde{E}$. The interpretation of the phasor transfer functions is according to the format Eqs. 28 through 31, where in the case of H_{ex}, ϕ_{ex} is given by Eq. 33, in the case of H_{xl}, ϕ_{xl} is given by Eq. 35, and in the case of H_{eb}, ϕ_{eb} is given by Eq. 36. In the (1/2)H_{eb} block, the 1/2 factor results because $\mu_b \propto \mathscr{E}_m^{-1/2}$ so that, as discussed in Appendix A, $\tilde{\mu}_b \propto (1/2)\tilde{\mathscr{E}}_m \propto (1/2)\tilde{f}_{\mathscr{E},b}$.

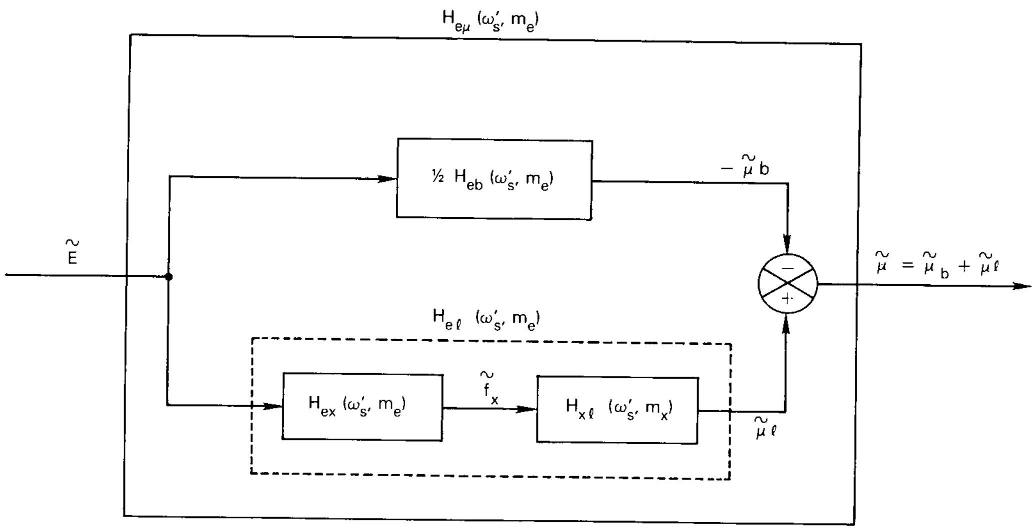

Fig. 14 — Diagram defining the composite phasor transfer function $H_{e\mu}(\omega_s', m_e)$ that relates $\tilde{\mu} = \tilde{\mu}_b + \tilde{\mu}_l$ to $\tilde{E}$

The phasor diagrams in Fig. 15 illustrate how the output $\tilde{\mu}$ varies relative to the input $\tilde{E}$ as the pressure decreases from high to intermediate to low values. The constructions show the phasor relationships as viewed in the reference frame of the drifting electron gas, so that, as shown, the phasors rotate counterclockwise at the angular rate $\omega_s' = u_0 k_s$ and a phase lag is reckoned clockwise. The primed notation is retained to distinguish between $\omega_s' = u_0 k_s$ and $\omega_s = v_s k_s$, but as a matter of convenience it is not used to denote the phasors themselves, since the spatial geometry in the various phasor constructions is independent of the reference frame, even though in the laboratory frame their sense of rotation does depend on the striation direction. As shown by the diagrams, as p decreases, $\phi_{e\mu}$, the phase lag of $\tilde{\mu}$ relative to $\tilde{E}$, decreases. According to the previously discussed dependence of ϕ_{eb} and ϕ_{xl} on the discharge operating point, at higher pressures $|\tilde{n}_l|$ and thus $|\tilde{\mu}_l|$ is small and $\tilde{\mu} \approx \tilde{\mu}_b$, whereas for lower pressures G_{eb} and thus $|\tilde{\mathscr{E}}_m|$ is small and $\tilde{\mu} \approx \tilde{\mu}_l$. At intermediate pressures the composite dependence of $\tilde{\mu}$ on the modulations to both the body and the low-energy tail of $f_{\mathscr{E}}$ must be taken into account.

Figure 16 is a block diagram of the composite phasor transfer function H_{ea} that determines the dependence of $\tilde{f}_a = \tilde{D} - \tilde{\mu}$ on $\tilde{E}$, where $H_{e\mu}$ is defined by Fig. 14. The phasor diagrams in Fig. 17 show how the output $\tilde{f}_a$ varies relative to the input $\tilde{E}$ as the pressure changes. As the diagrams show, for high and intermediate pressures $\tilde{f}_a$ lags $\tilde{E}$ by a small angle ϕ_{ea}. For low pressure $\tilde{f}_a$ is advanced approximately $\pi/2$ relative to its position at intermediate and high pressures.

For low pressure the direct ionization mechanism dominates, so that the phase of $\tilde{f}_i$ is determined by the phase of $\tilde{f}_{ir}$. As previously discussed, $\tilde{f}_{ir} \propto \tilde{f}_x$, so that $\tilde{f}_i$ (dashed arrow in Fig. 17c) lags $\tilde{E}$ by ϕ_{ex}. Thus (Fig. 17c) $\tilde{f}_i$ lags $\tilde{E}$ and $\tilde{f}_a$ leads $\tilde{E}$, so that $\tilde{f}_a$ and $\tilde{f}_i$ are approximately out of phase for low pressure. At high pressure, $\tilde{f}_a$ lags $\tilde{E}$ by approximately $\pi/4$, and

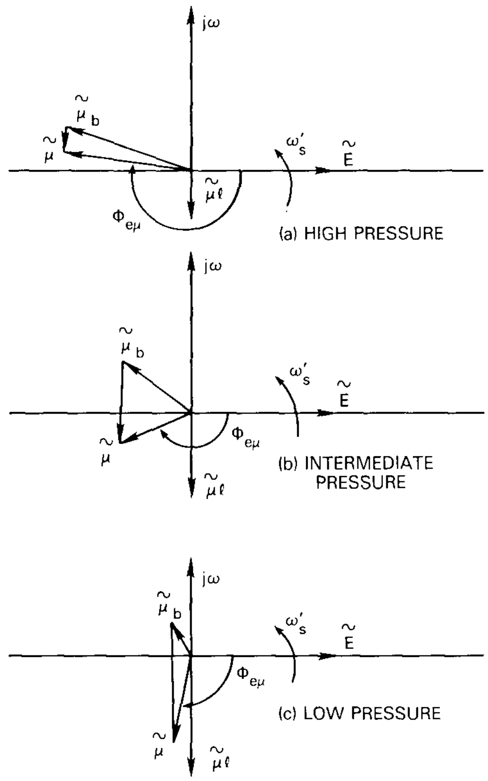

Fig. 15 — Dependence of $\tilde{\mu} = \tilde{\mu}_b + \tilde{\mu}_l$ on $\tilde{E}$ for high, intermediate, and low pressure

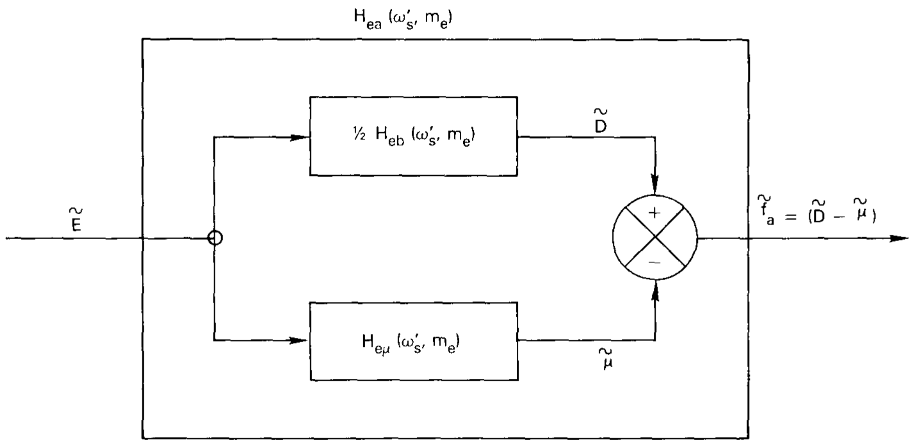

Fig. 16 — Diagram defining the composite phasor transfer function $H_{ea}(\omega_s', m_e)$ that relates $\tilde{f}_a = \tilde{D} - \tilde{\mu}$ to $\tilde{E}$

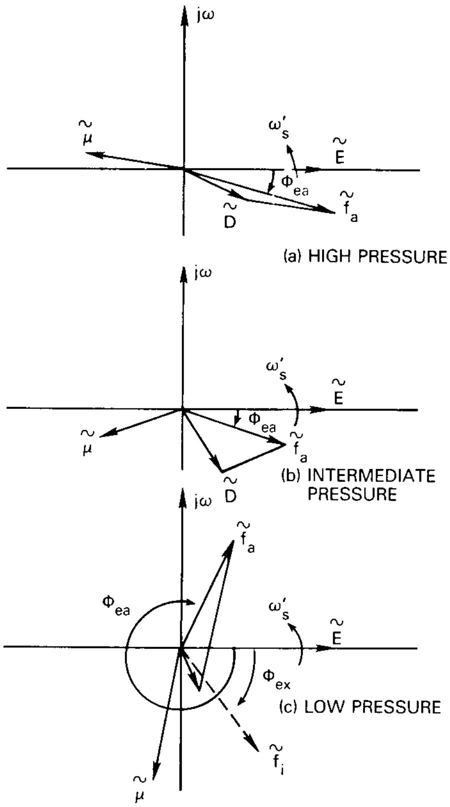

Fig. 17 — Dependence of $\tilde{f}_a = \tilde{D} - \tilde{\mu}$ on $\tilde{E}$ for high, intermediate, and low pressure

the phase of $\tilde{f}_i$ is determined by the stepwise electron-metastable ionization mechanism, which like the direct mechanism has a simple RC response, so that $\tilde{f}_i$ also lags $\tilde{E}$ by approximately $\pi/4$. Hence $\tilde{f}_a$ and $\tilde{f}_i$ are approximately in phase for high pressure.

Thus the formulation used in this theory predicts an out-of-phase relationship between $\tilde{f}_a$ and $\tilde{f}_i$ at low pressure and an in-phase relationship at higher pressures. Other formulations, such as Pekarek's, are essentially based on a hydrodynamic approach in that it is assumed that the ionization rate f_i is proportional to the "electron temperature" or to $\mathscr{E}_m$, the mean electron energy. The Einstein relation $D/\mu = kT_e/e$ is also assumed to be valid in that $f_a \propto \mathscr{E}_m$ is assumed, where $\mathscr{E}_m$ is the mean value of $f_{\mathscr{E}}$. Such an approach tacitly assumes that the shape of $f_{\mathscr{E}}$ is invariant, so that the variations in the plasma parameters f_i, D, and μ and thus in $f_a \propto D/\mu$ that depend on $f_{\mathscr{E}}$ is via the single parameter $\mathscr{E}_m$. It is further assumed that $\mathscr{E}_m \propto E_0/p$, so that the variations of all the plasma parameters are tied to the variations in $\tilde{E}$ via the variations $\tilde{E}$ imparts to $\mathscr{E}_m$. Consequently the hydrodynamic approach predicts that $\tilde{f}_a$ and $\tilde{f}_i$ are always approximately in phase.

The formulation used in this theory, on the other hand, is tantamount to solving the Boltzmann equation in that taken into account are the modulations imparted to the various distinct energy ranges of $f_{\mathscr{E}}$, with each energy range having a characteristic time constant that depends on the types of collisions the electrons in that energy range can encounter. The significance of this approach as opposed to the hydrodynamic approach heretofore used is that it correctly predicts the relationship between $\tilde{f}_a$ and $\tilde{f}_i$ measured in Ref. 20 for the low-pressure r-variety striation in neon, which relationship is that "the maximum of the ionization rate variation is approximately in opposite phase with the electron mean energy variations." This measured result was considered so puzzling, since, as noted [20], it is exactly opposite to the predictions of Pekarek's theory, that the experiment was subsequently repeated by several other researchers [21]. The out-of-phase relationship between $\tilde{f}_a$ and $\tilde{f}_i$ was observed in each of these experiments, and one of the experimenters [20] remarked that "it appears from this result that the tail of the distribution function, in this case, is uncoupled from the body of the distribution." The formulation used in this theory explains this uncoupling as the tail and body of $f_{\mathscr{E}}$ reacting to changes in E with different characteristic relaxation time constants, which in turn leads to changes in the shape or form of $f_{\mathscr{E}}$.

Figure 18 is a block diagram of Eq. 11, which defines the dependence of $\tilde{E}$ on $\tilde{N}$, $\tilde{\mu}$, and $\tilde{\mathscr{E}}_m$. The figure defines the composite phasor transfer function H_{ne}, which denotes the iterative processes by which $\tilde{N}$ uniquely determines $\tilde{E}$. The phasor diagrams in Fig. 19 show how $\tilde{E}$ depends on $\tilde{N}$ for high, intermediate, and low discharge pressure. The phase of $\tilde{E}_c$ relative to $\tilde{N}$ depends on $\tilde{\mu}$, which in turn is determined by the $H_{e\mu}$ branch in Fig. 18.

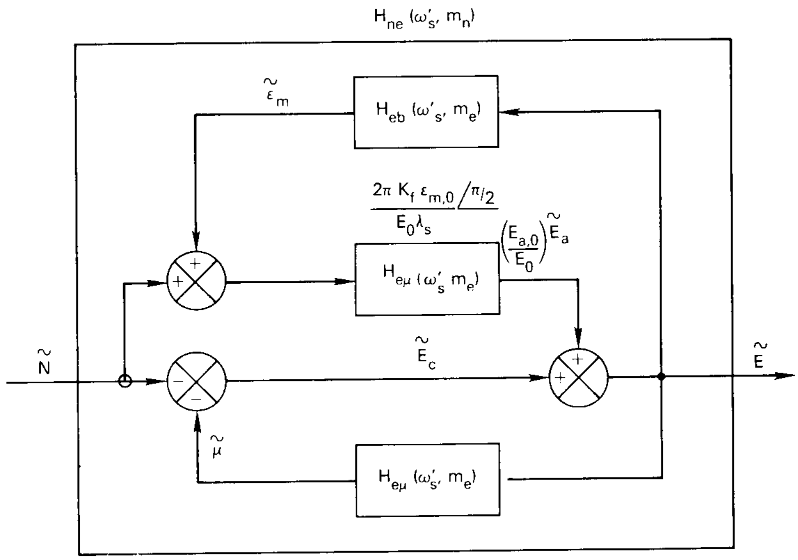

Fig. 18 — Diagram defining the composite phasor transfer function $H_{ne}(\omega_s', m_n)$ that relates $\tilde{E}$ to $\tilde{N}$

The dependence of $\tilde{f}_{is}$ on $\tilde{E}$ is via the modulation imparted to the upper energy range of the body of $f_{\mathscr{E}}$ in the approximate energy interval $\mathscr{E}_m \lesssim \mathscr{E} \lesssim 2\mathscr{E}_m$. The average energy loss for electrons in this energy interval of $f_{\mathscr{E},b}$ is slightly larger than that for the entire $f_{\mathscr{E},b}$, so that τ_{is}, the time constant for the modulation of f_{is}, is slightly shorter than τ_b, the time constant for the modulation of $f_{\mathscr{E},b}$. Consequently $\phi_{es}(\omega_s')$, the phase lag of f_{is} relative to $\tilde{E}$, is somewhat smaller than $\phi_{eb}(\omega_s')$ given by Eq. 36.

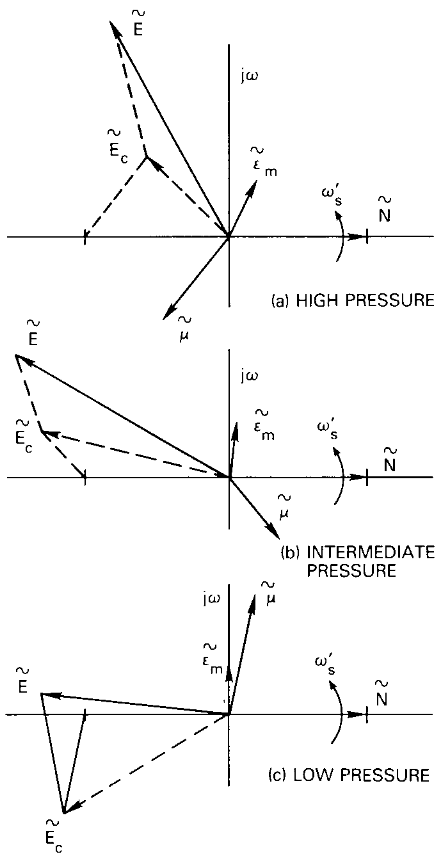

Fig. 19 — Dependence of $\tilde{E}$ on $\tilde{N}$ for high, intermediate, and low pressure

The modulation of the electron-metastable ionization rate also depends on any modulation imparted to N_m, the metastable density. It will be shown, however, that $|\tilde{N}_m|$ is significant only in the narrow range of pressure where the p-variety striation (resulting from metastable-metastable ionization) is generated and is negligible in the region where the s-variety striation (resulting from electron-metastable ionization) is self-excited. The modulation of the metastable-metastable ionization mechanism does not depend directly on the modulation of f_g and is given by $\tilde{f}_{ip} = 2\tilde{N}_m - \tilde{N}$. The formulation relating $\tilde{N}_m$ to the other plasma parameters will be presented shortly.

Since the net ionization frequency f_i is given by $f_i = f_{ir} + f_{is} + f_{ip}$ and since $f_{i,0} = f_{a,0}$ for quiescent charged-particle balance, $\tilde{f}_i$ is given by

$$\tilde{f}_i = \frac{f_{ir,0}}{f_{a,0}} \tilde{f}_{ir} + \frac{f_{is,0}}{f_{a,0}} \tilde{f}_{is} + \frac{f_{ip,0}}{f_{a,0}} \tilde{f}_{ip}. \tag{37}$$

Equation 37 shows that the relative quiescent contribution of a particular ionization mechanism to the total quiescent ionization rate acts as a phasor gain in determining the effect of modulations of the particular mechanism on the net ionization rate.

Just as is the case for the charged particles, there exists characteristic production and loss mechanisms for the metastables, so that N_m is also constrained by a conservation relation $dN_m/dt = P_m - L_m$, where P_m and L_m denote the volume production and loss rates for the metastables. The production of metastables is given by $P_m = K_m f_x N$, where K_m is that fraction of the total electronic excitations that decay to metastable states. In phasor notation $\tilde{P}_m = \tilde{f}_x + \tilde{N}$. The loss of metastables is given by $L_m = f_m\, N_m$, where f_m is the net metastable decay frequency, so that $\tilde{L}_m = \tilde{f}_m + \tilde{N}_m$. Using these relations in the continuity expression gives the result

$$\tilde{N}_m = H_m\ (\tilde{f}_x + \tilde{N} - \tilde{f}_m), \tag{38}$$

where $H_m = G_m \phi_m$, with $G_m = \cos \phi_m$ and $\phi_m = \tan^{-1} \dfrac{|\omega_s|}{f_{m,0}}$.

There are four pertinent metastable destruction mechanisms, so that $f_m = f_{mm} + f_{mg}$ $f_{em} + f_{md}$. The term f_{mm} is due to metastable-metastable collisions in which one of the metastables is ionized and the other returned to the ground state. The term f_{mg} is due to metastable-ground state neutral collisions in which the thermal energy of the neutral is sufficient to induce a transition from the metastable state to a nearby radiating state which spontaneously decays to the ground state. The term f_{em} is due to electron-metastable collisions that destroy metastables by ionizing them and by inducing transitions from the metastable states to a multiplicity of radiating states which in turn spontaneously decay to the ground state. The term f_{md} results from metastable diffusion to the column wall, where wall collisions deexcite the metastables.

Even for the maximum value of N_m in the positive column of a glow discharge the term f_{mm} is negligible. The terms f_{mg} and f_{em} are both proportional to the discharge pressure p, and f_{md} goes as p^{-1}. Consequently f_m achieves a minimum, thereby resulting in a maximum of N_m, when $f_{mg} + f_{em} = f_{md}$. This condition defines a unique value of reduced pressure $(pR)^*$ for which N_m is a maximum:

$$(pR)^* = \left[\frac{5.76\ D_{m,1}}{\left\{ \dfrac{4.2 \times 10^{15}\ K_{em}\ Q_{em}\ \mathscr{E}_{m,0}}{\lambda_{e,1}\ E_0 R} \right\} \dfrac{I}{R} + K_{mg}} \right]^{1/2}, \tag{39}$$

where $D_{m,1}$ is the metastable diffusion coefficient at 1 torr, K_{em} and K_{mg} characterize the destruction of metastables by electron neutral gas collisions, Q_{em} is the electron-metastable collision cross section, and $\lambda_{e,1}$ is the electron-neutral mean free path at 1 torr. For $pR < (pR)^*$ metastable diffusion losses dominate, and for $pR > (pR)^*$ metastable collisional losses dominate. For $pR = (pR)^*$ the two loss rates are equal, with the consequence that $f_{m,0}$ is a minimum and $N_{m,0}$ is a maximum.

Since $f_{is} \propto N_m$ and $f_{ip} \propto N_m^2$, the relative contribution of the f_{is} mechanism to f_i increases as PR increases above $(pR)^*$. The f_{ip} mechanism makes a relative maximum contribution to f_i when $pR = (pR)^*$, and the relative contribution of both the f_{is} and f_{ip} mechanisms are less when $pR < (pR)^*$, when the direct f_{ir} mechanism makes the major relative contribution to f_i. This argument in conjunction with experimental results presented later explains the previous assignments of the direct, the stepwise electron-metastable, and the stepwise metastable-metastable ionization mechanisms to respectively the r, s, and p striation varieties.

Since the electron-metastable destruction mechanism is the only one modulated by the striations, $\tilde{f}_m$ is given by

$$\tilde{f}_m = \frac{f_{em,0}}{f_{m,0}} \left(\tilde{N} + \frac{1}{2} \tilde{\mathscr{E}}_m \right) \tag{40}$$

Using Eq. 40 in Eq. 38 gives

$$\tilde{N}_m = H_m \left[\tilde{f}_x + \left(1 - \frac{f_{em,0}}{f_{m,0}} \right) \tilde{N} - \frac{1}{2} \tilde{\mathscr{E}}_m \right] \tag{41}$$

Figure 20 is a block diagram of Eq. 41 substituted into the relation $\tilde{f}_{ip} = 2\tilde{N}_m - \tilde{N}$, and it defines the composite phasor transfer function $H_{en,p}$ that relates $\tilde{f}_{ip}$ to $\tilde{E}$ and $\tilde{N}$.

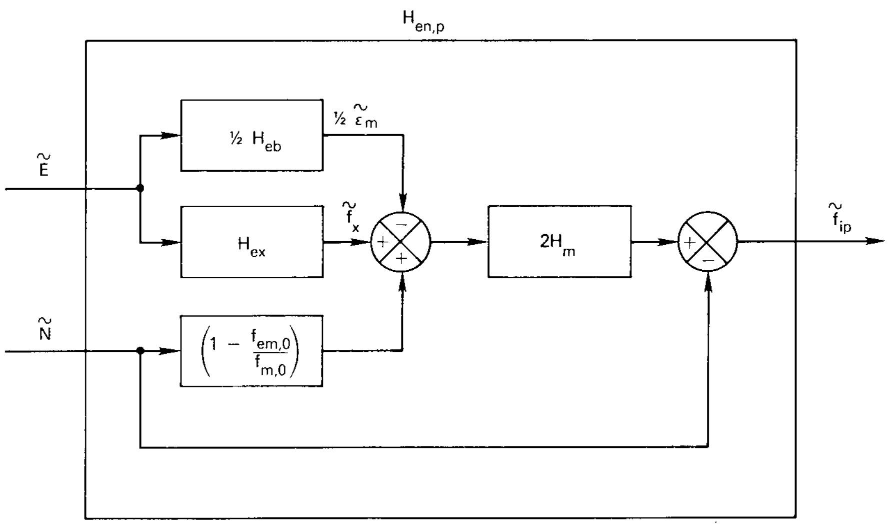

Fig. 20 — Diagram defining the composite phasor transfer function $H_{en,p}$ that relates $\tilde{f}_{ip}$ to $\tilde{E}$ and $\tilde{N}$

The derivation of the phasor transfer functions represented by each block in the diagram in Fig. 8 has been presented. In summary, with reference to Fig. 8, H_{nn} models the conservation relation for ion-electron pairs and is given by Eq. 17. H_{ne} is defined by Fig. 18 and models the conduction and ambipolar contributions to the longitudinal electric field. H_{ea} is defined by Fig. 16 and models the dependence of ambipolar recombination on $\tilde{E}$ via its dependence on $\tilde{D}$ and $\tilde{\mu}$. H_{er} is proportional to H_{ex} given by Eq. 30 and models the dependence of the direct electron-ground state ionization rate on $\tilde{E}$. $H_{en,p}$ is defined by Fig. 20 and models the dependence of the stepwise metastable-metastable ionization rate on $\tilde{E}$ and $\tilde{N}$. H_{es} is approximately equal to H_{eb} defined by Eq. 36 and models the dependence of the stepwise electron-metastable ionization rate on $\tilde{E}$. $H_{en,x}$ is given by Eq. 20 and models the net influx of ions into a unit length of positive column due to divergence of the ion current through its end sections.

USING THE MATHEMATICAL MODEL TO PREDICT STRIATION PROPERTIES

Figure 21 is a block diagram of an electrical equivalent circuit of the simplified steady-state mathematical model for the striated positive column in which H_{ei} denotes the transfer function for the dominant ionization mechanism: H_{er} for direct ionization, $H_{en,p}$ for metastable-metastable ionization, and H_{es} for electron-metastable ionization. When the phasor variables $\tilde{N}$, $\tilde{E}$, $\tilde{f}_n$, etc. are regarded as ac voltages, the stability properties of this electrical equivalent circuit predict the stability properties of the positive column with regard to striations.

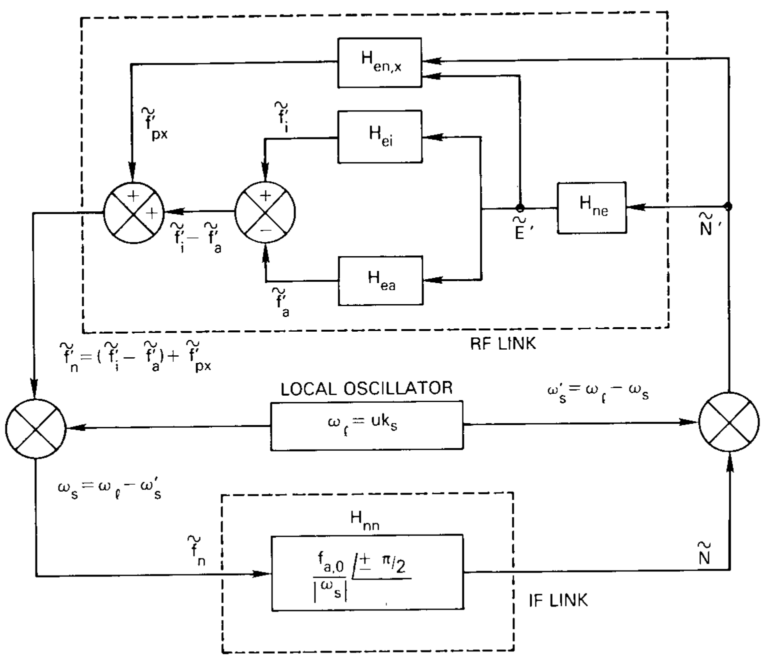

Fig. 21 — Simplified steady-state model of a positive column

A resonant-wavelength striation corresponds to a net phase shift around the frequency-translated RF-IF loop (denoted by ϕ_l) of 2π. The $\phi_l = 2\pi$ condition causes positive regeneration that leads to self-excited loop oscillations if the net loop gain (denoted by G_l) is sufficiently large. Self-sustained striations correspond to steady-state oscillations of the electrical loop, and, as will be shown, the parameters of such striations can be predicted from the $\phi_l = 2\pi$, $G_l = 1$ constraint for steady-state oscillations of the electrical loop.

Phase shifts in the RF and IF links are coherent in the sense that a phase shift $\phi_{\mathrm{IF}}(\omega_s)$ at ω_s in the IF link is equivalent to an equal phase shift of $\phi_{\mathrm{RF}}(\omega'_s)$ at ω'_s in the RF link. The net loop phase shift ϕ_l therefore is

$$\phi_l = \phi_{\mathrm{IF}}(\omega_s) + \phi_{\mathrm{RF}}(\omega'_s). \tag{42}$$

In the laboratory frame positive ω_s corresponds to anode-directed striations, negative ω_s to cathode-directed striations, and $\omega_s = 0$ to standing striations. Electrical loop oscillations with the IF on either side of zero beat (with ω_s positive or negative) correspond to anode-directed and cathode-directed moving striations, and loop oscillations with the IF at zero beat (with $\omega_s = 0$) correspond to standing striations. In the laboratory frame represented by the IF link the sign of the $\pi/2$ phase lag resulting from the integration of $\tilde{f}_n$ is determined by the sign of ω_s, because the sense of reckoning a phase lag depends on the striation direction. Since the electron drift velocity is greater than striation velocities, striations always appear to move in the cathode direction when viewed from the electron-gas frame represented by the RF link. Consequently, the $-\pi/2$ IF-link phase shift for ω_s negative is equivalent to a $\pi/2$ RF-link phase lag, whereas the $\pi/2$ IF-link phase shift for ω_s positive is equivalent to a $\pi/2$ RF-link phase lead, which in turn is equivalent to a $3\pi/2$ RF-link phase lag.

The net result is that the $\phi_l = 2\pi$ constraint which defines resonant-wavelength striations can be achieved in two distinct ways: by $\phi_{\mathrm{RF}} = \pi/2$ or $3\pi/2$. As depicted in Fig. 9, $\phi_{\mathrm{RF}} = \pi/2$ sustains anode-directed striations, and $\phi_{\mathrm{RF}} = 3\pi/2$ sustains cathode-directed striations. Since $\omega_s' = uk_s - \omega_s$ and $uk_s >> \omega_s$, $\omega_s' \approx uk_s$. Since a given discharge current and pressure determines u, $\phi_{\mathrm{RF}}(\omega_s')$ essentially depends only on $\lambda_s = 2\pi/k_s$. The resonant value of λ_s therefore is selected by the constraint $\phi_{\mathrm{RF}}(\omega_s') = \pi/2$ or $3\pi/2$.

The net loop gain G_l can be written as

$$G_l = G_{\mathrm{RF}}\, G_{\mathrm{IF}}, \tag{43}$$

where G_{RF} is the gain of the RF link and G_{IF} is the gain of the IF link. Since $\omega_s' \approx uk_s$, G_{RF} essentially depends only on λ_s, whereas G_{IF} depends on ω_s. Consequently, for fixed λ_s, G_l depends only on ω_s, and the $G_l(\omega_s) = 1$ constraint determines the value of ω_s that corresponds to a given resonant value of λ_s for steady-state striations. The following presentation shows how a phasor construction can be used to predict the values of λ_s and ω_s for steady-state striations.

Figure 22 is a phasor diagram that illustrates the phasor relationships between the RF-link phasors $\tilde{N}'$, $\tilde{E}'$, $\tilde{f}_i'$, $\tilde{f}_a'$, $\tilde{f}_{px}'$, and $\tilde{f}_n'$ that result in $\phi_{\mathrm{RF}} = 3\pi/2$ and thus in self-sustained $-x$-directed moving striations. In this diagram the phasors rotate counterclockwise at the angular rate ω_s' and represent the temporal variations of the various plasma parameters as seen by an observer moving with the electron gas. Phase lags in this diagram are reckoned clockwise. Since $\tilde{N}'$ is the input to the RF link, it is along the positive real axis, and the magnitudes and phases of the other phasors are referenced to it. The composite transfer function H_{ne} is defined by Fig. 18. However, the pertinent points in the following discussion are not affected by using the simplifying approximation $H_{ne} = 1\underline{|260°}$, so that, as shown in Fig. 22, $\tilde{E}'$ lags $\tilde{N}'$ by 260° and $|\tilde{E}'| = |\tilde{N}'|$.

The transfer functions H_{ei} and H_{ea} have low-pass frequency responses with corner frequencies at τ_{ei}^{-1} and τ_{ea}^{-1}, where τ_{ei} and τ_{ea} are the relaxation time constants of f_g in the energy intervals appropriate for ionization and ambipolar diffusion. Consequently H_{ei} and H_{ea} are of the form (with j indicating either i or a)

$$H_{ej}(\omega_s', m_e) = G_{ej}(\omega_s', m_e)\underline{|\phi_{ej}(\omega_s')}, \tag{44}$$

where

$$\phi_{ej}(\omega_s') = \tan^{-1}(\omega_s' \tau_{ej}) \tag{45}$$

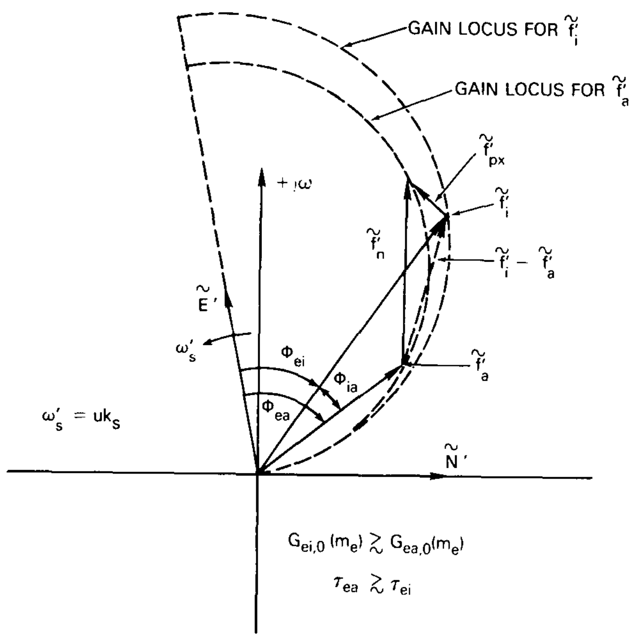

Fig. 22 — Phasor construction for a $-x$-directed (cathode-directed) moving striation

and

$$G_{ej}(\omega_s', m_e) = G_{ej,0}(m_e) \cos [\phi_{e_j}(\omega_s')], \tag{46}$$

in which m_e is the modulation index of $\tilde{E}$ and $G_{ej,0}(m_e)$ is a decreasing function of m_e that characterizes the nature of the nonlinearity associated with the modulation of the shape of $f_{\mathscr{E}}$ in the energy interval $\Delta \mathscr{E}_j$. As ω_s' increases from zero (λ_s decreases from infinity), the tips of $\tilde{f}_i'$ and $\tilde{f}_a'$ move along the indicated gain loci according to the cos $[\phi(\omega_s')]$ rolloff dictated by Eq. 46.

Figure 22 represents a discharge operating condition for which $G_{ei,0}(m_e) \gtrsim G_{ea,0}(m_e)$ and $\tau_{ea} \gtrsim \tau_{ei}$. For any particular value of ω_s', therefore, $|\tilde{f}_{ei}'| \geq |\tilde{f}_{ea}'|$ and $\tilde{f}_{ea}'$ lags $\tilde{f}_{ei}'$ by the angle

$$\phi_{ia}(\omega_s') = |\phi_{ei}(\omega_s') - \phi_{ea}(\omega_s')|, \tag{47}$$

where $\phi_{ei}(\omega_s')$ and $\phi_{ea}(\omega_s')$ are given by Eq. 45. Over approximately a two-decade variation in ω_s' the angle $\phi_{ia}(\omega_s')$ gradually increases as ω_s' increases achieves a maximum for $\omega_s' = (\tau_{ea}\,\tau_{ei})^{-1/2}$, and gradually approaches zero for $\omega_s' >> 10\,\tau_{ei}^{-1}$. Therefore, as ω_s' increases from zero, the phase of $(\tilde{f}_i' - \tilde{f}_a')$ becomes more lagging relative to $\tilde{E}'$ and thus relative to $\tilde{N}'$ and $|\tilde{f}_i' - \tilde{f}_a'|$ gradually decreases.

The phasor $\tilde{f}_{px}'$ is given by Eqs. 19 and 20 as

$$\tilde{f}_{px}' = \left[\frac{E_0 R}{(\lambda_s/R)\,\mathscr{E}_{m,0}} \;\underline{\left|\pi/2\right.} \right] (\tilde{E}' + \tilde{N}'). \tag{48}$$

Since $\tilde{E}'$ is fixed relative to $\tilde{N}'$, Eq. 48 shows that the phase of $\tilde{f}_{px}'$ is also fixed relative to $\tilde{N}'$ and that $|\tilde{f}_{px}'| \propto \lambda_s^{-1}$.

Figure 22 shows the unique resonant value of λ_s such that $(\tilde{f}_i' - \tilde{f}_a') + \tilde{f}_{px}' = \tilde{f}_n'$ lags $\tilde{N}'$ by exactly $3\pi/2$, corresponding to $\phi_{\mathrm{RF}}(\lambda_s) = 3\pi/2$. Since the phase and magnitude of $\tilde{f}_i' - \tilde{f}_a'$ change gradually over a two-decade variation in λ_s, $\phi_{\mathrm{RF}}(\lambda_s)$ is most sensitive to changes in λ_s via the effect of $|\tilde{f}_{px}'| \propto \lambda_s^{-1}$ on the phase of $\tilde{f}_n'$. Consequently, the modulation of the ionization and ambipolar diffusion rates have only a coarse effect on the selection of the resonant striation wavelength, whereas the modulation of the net divergence of the ion-electron pair drift current through the end sections of a unit length of the positive column exhibits a high-Q fine-tuning effect, thereby determining the precise resonant value of λ_s.

Since $G_{\mathrm{IF}} = |H_{nn}|$, Eq. 17 gives G_{IF} as

$$G_{\mathrm{IF}} = f_{a,0}/|\omega_s|. \tag{49}$$

Because $G_{\mathrm{IF}} \propto |\omega_s|^{-1}$, there always exists a sufficiently small magnitude of steady-state striation velocity $|v_s| = |\omega_s|/k_s$ for the resonant value of k_s given by $\phi_{\mathrm{RF}}(k_s) = 3\pi/2$ to ensure that $G_l > 1$ also holds.

Since all of the phasors in Fig. 22 are referenced to $\tilde{N}'$, and since $\tilde{E}' \propto \tilde{N}'$, the net effect of changing $m_n = |\tilde{N}'|$ is to change $|\tilde{f}_i'|$ and $|\tilde{f}_a'|$ relative to $|\tilde{N}'|$ via the dependencies $G_{ei,0}(m_e)$ and $G_{ea,0}(m_e)$. The value of m_n increases via regeneration until m_n is large enough to influence $|\tilde{f}_i'|$ and $|\tilde{f}_a'|$ to the extent that the $3\pi/2$ phase lag of $\tilde{f}_n'$ relative to $\tilde{N}'$ is disturbed, thereby spoiling the $\phi_{\mathrm{RF}} = 3\pi/2$ condition for self-sustained cathode-directed striations.

G_{RF} can be determined from the phasor diagram as $G_{\mathrm{RF}} = |\tilde{f}_n'|/|\tilde{N}'|$, and using Eq. 49 for G_{IF} and the constraint $G_{\mathrm{RF}}\, G_{\mathrm{IF}} = 1$ gives the steady-state value of $|\omega_s|$ as

$$|\omega_s| = f_{a,0}\,\frac{|\tilde{f}_n'|}{|\tilde{N}'|}. \tag{50}$$

Using $f_{a,0} = (2.4/R)^2 \mu_p D_0/\mu_0$ and the approximations $D_0/\mu_0 \approx \mathscr{E}_{m,0}$ and $2\pi \approx (2.4)^2$ in Eq. 50 gives for $f_s = 2\pi/|\omega_s|$

$$Rf_s = \mu_{p,1}\frac{\mathscr{E}_{m,0}}{(pR)}\,\frac{|\tilde{f}_n'|}{|\tilde{N}'|}, \tag{51}$$

where $\mu_{p,1}$ is the ion mobility at 1 torr, that is, $\mu_p \approx \mu_{p,1}/p$, and the terms are arranged to form reduced parameters.

Multiplying both sides of Eq. 48 by E_0 and solving for $E_0\lambda_s$ gives

$$E_0\lambda_s = \frac{(E_0R)^2}{\mathscr{E}_{m,0}}\,\frac{|\tilde{N}' + \tilde{E}'|}{|\tilde{f}_{px}'|}. \tag{52}$$

As will be shown in the next section, the phasor diagram in Fig. 22 corresponds closely to the actual-plasma-parameter phasor relationships in the neon column in the $pR \approx 3$ torr-cm regime where the s-variety moving striation is spontaneously generated. In a neon discharge $E_0R \approx 4$ volts [22], $\mathscr{E}_{m,0} \approx 4$ eV for $(pR) \approx 3$ torr-cm [23], and $\mu_{p,1} \approx 3000$ cm^2/V-s for the neon atomic ion [24]. Using these values and the values $|\tilde{f}_n'|/|\tilde{N}'| \approx 1|$ and $|\tilde{N}' + \tilde{E}'|/|\tilde{f}_{px}'| \approx 5$ as obtained from the phasor diagram in Fig. 22 in Eqs. 51 and 52 gives $E_0\lambda_s \approx 20$ volts and $Rf_s \approx 4$ kHz-cm, in good agreement with measured values for the s-variety striation in neon in the upper pR region where it is spontaneously generated.

For some molecular gases such as hydrogen the relaxation characteristics of f_g are such that the sense of the gain and time-constant inequalities that lead to the phasor diagram in Fig. 22 are reversed. Figure 23 shows the resonant condition that occurs in this case, in which $G_{ei,0}(m_e) \lesssim G_{ea,0}(m_e)$ and $\tau_{ea} \lesssim \tau_{ei}$. Since $\tau_{ei} \gtrsim \tau_{ea}$, $\tilde{f}_i'$ now lags $\tilde{f}_a'$ for any particular value of λ_s. In this case a resonant value of λ_s occurs when $\tilde{f}_n'$ lags $\tilde{N}'$ by exactly $\pi/2$. This corresponds to $\phi_{RF}(\lambda_s) = \pi/2$, as required for self-sustained anode-directed striations.

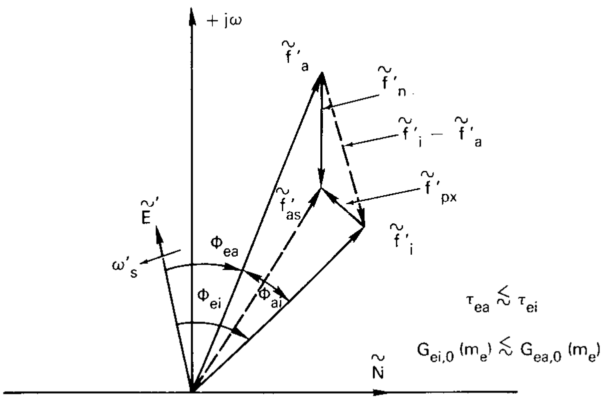

Fig. 23 — Phasor construction for anode-directed striations $\tilde{f}_a'$ and for standing striations $\tilde{f}_{as}'$ (dashed phasor)

Large-amplitude unattenuated standing striations in molecular gases can also be clearly understood via Fig. 23. If the values of $G_{ei,0}(m_e)$ and τ_{ei} remain the same and τ_{ea} is increased slightly while still satisfying the inequality $\tau_{ea} \lesssim \tau_{ei}$, and if $G_{ea,0}(m_e)$ is decreased so that now $G_{ea,0} \lesssim G_{ei,0}$, then $\tilde{f}_i'$ and $\tilde{f}_{px}'$ stay the same and $\tilde{f}_a'$ transitions to $\tilde{f}_{as}'$ (dashed phasor in Fig. 23). Now, $\tilde{f}_i' - \tilde{f}_a'$ is exactly out of phase with $\tilde{f}_{px}'$, and $|\tilde{f}_i' - \tilde{f}_{as}'| = |\tilde{f}_{px}'|$. Consequently $\tilde{f}_n' = (\tilde{f}_i' - \tilde{f}_{as}') - \tilde{f}_{px}' = 0$, so that from Eq. 50 $|\omega_s| = 0$. This situation also corresponds to the limiting case in which ϕ_{RF} is on the verge of flipping 180° from $\pi/2$ to $3\pi/2$ or vice versa. Thus standing striations are self-sustained via the same mechanism that sustains anode-directed and cathode-directed moving striations.

The steady-state value of $|\omega_s| = 0$ for standing striations implies that $G_{IF} = \infty$ and $G_{RF} = 0$. As can be seen from Fig. 23, however, standing striations are actually a balanced null condition in which slight unbalances cause a net $\tilde{f}_n'$ in the proper direction ($\phi_{RF} = \pi/2$ or $\phi_{RF} = 3\pi/2$) to correct the original unbalance, so that on the average $\phi_l = 2\pi$, $G_l = 1$, and $|\omega_s| = 0$. This picture is supported by experiment in that observations of standing striations in the positive column show them to be in a tenuous state in which they drift slightly toward the anode or cathode.

Although anode-directed and cathode-directed moving striations and standing striations appear to be markedly different in the laboratory reference frame, analyses in the reference frame of the drifting electron gas, as in Figs. 22 and 23, make clear that they are essentially the same phenomenon. Slight relative changes in the gains and time constants that characterize the modulations imparted to the shape of f_g result in the generation of the entire class of striation phenomena.

PREDICTING AND COMPARING WITH EXPERIMENT THE THRESHOLD PRESSURES AND CURRENTS AND THE PROPERTIES OF THE *p, r,* AND *s* STRIATION VARIETIES IN NEON

In this section the model for the striated positive column is applied to the neon discharge. It will be shown that the model accurately predicts every feature of the multifaceted striation phenomenon in the neon positive column, such as the values of the striation parameters for the *p, r,* and *s* varieties, their location in the reduced-current-pressure plane, and the upper threshold pressures and currents above which the striations are quenched. In addition to the measurements in a pure neon discharge an experiment was performed in which trace amounts of argon were added to the discharge. The results of this experiment, discussed in the next section, show that the values of the Novak potentials are in no way associated with quantum-level differences of the fill gas. The experimental results in the neon-argon admixture discharge are also accurately predicted by the model.

Figure 24 depicts a somewhat simplified quantum-energy-level diagram for the neon atom. The electronic configuration of a neon atom in its ground state consists of two electrons in the 1s shell or orbit, two electrons in the $2s$ shell, and six electrons in the $2p$ shell and is denoted as the ($1s^2$, $2s^2$, $2p^6$) ground state. The fine structure of the ($1s^2$, $2s^2$, $2p^5$, $3s$) excited level, which is produced by an electron transition from the $2p$ level to the $3s$ level and therefore is the first excited level of the neon atom, consists of four discrete quantum states that are spread over a narrow (approximately 0.2 eV) range of energies and located approximately 16.2 eV above the ground state. Two of these states ($^1P_1$ and $^3P_1$) are connected to the ground state by allowed radiative transitions in the ultraviolet portion of the spectrum, at 73.6 nm and 74.3 nm respectively. The other two states ($^3P_0$ and $^3P_2$) are called metastable states as a consequence of their not being connected to the ground state by an allowed radiative transition. The second excited level of the neon atom has the electronic configuration ($1s^2$, $2s^2$, $2p^5$, $3p$) and consists of ten discrete states spread over a narrow range of energies and located approximately 18.5 eV above the ground state and thus approximately 2.3 eV above the $3s$ level. The $3p$ states are not connected directly to the ground state by an allowed radiative transition; hence neon atoms excited to these states by electron impact must decay to the ground state via intermediary allowed radiative transitions in the red portion of the spectrum with wavelengths of the order of 600 nm to the $3s$ levels and then via the allowed radiative transitions at 74.3 and 73.6 nm to the ground state.

The ionization level of the neon atom is at 21.5 eV above the ground state, and, although radiative recombination of electrons and neon ions can occur by neon ions capturing electrons, thereby forming excited neon atoms, the predominant recombination process is via radial ambipolar diffusion to the walls of the positive column. Neon ground-state atoms are being continuously excited to metastable levels by electron-neutral collisions involving electrons with energies exceeding approximately 16.2 eV. Since these metastable atoms cannot decay spontaneously to the ground state, their concentration increases until the destruction of metastables, by mechanisms such as the diffusion of metastables to the positive column wall, where they are deenergized by nonradiative processes, brings the production-loss rate for the metastable species into balance, thereby achieving a steady-state metastable density. The metastable number density N_m is a function of the discharge-tube parameters current and pressure, and for $pR = (pR)^*$, given by Eq. 39, N_m is a maximum. Measurements in a neon positive column show that the maximum value of N_m is about 0.01% to 0.1% of the ground-state number density N_g. The three primary ionization mechanisms for the production of atomic neon ions are

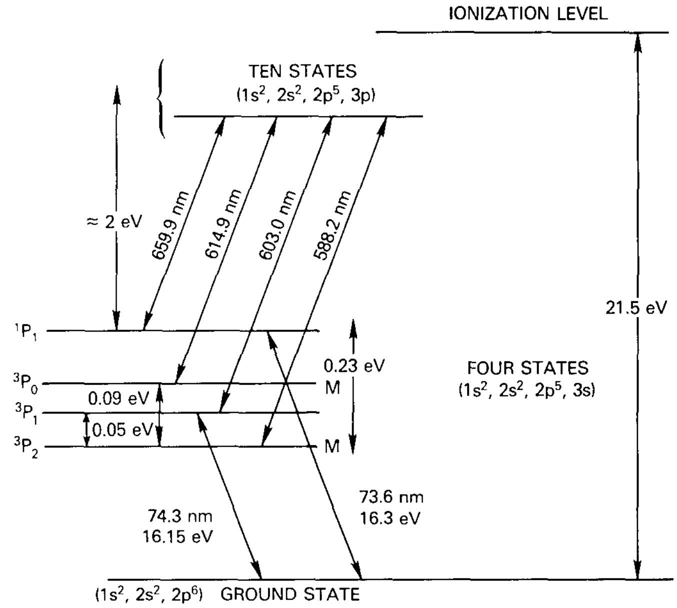

Fig. 24 — Simplified energy-level diagram for neon

the direct ionization of a ground-state neon atom by an electron whose energy exceeds approximately 21.5 eV, the ionization of a metastable neon atom by an electron whose energy exceeds approximately 5 eV, and the ionization of a metastable neon atom by collision with another metastable neon atom, which results in the ionization of one and the deexcitation of the other. The dependences on the electric field of the ionization rates associated with these three ionization mechanisms are respectively modeled by the transfer functions H_{er}, H_{es}, and $H_{en,p}$ in the equivalent electrical circuit in Fig. 8.

Figure 25 shows a comprehensive overview of the striation phenomena in neon which was constructed from the data available in the current and pressure maps in Appendix D. As can be seen in the overview, for lower values of reduced current I/R, in the range 0 to 5 mA/cm, the quiet region extends over a several-torr-cm range of reduced pressure pR centered on a value between 1 and 2 torr-cm. As the value of I/R increases, the quiet region is compressed into an ever narrowing strip in the pR dimension, and for values of I/R in excess of approximately 20 mA/cm the quiet region ceases to exist. For values of pR less than approximately 0.5 torr-cm, no spatially and temporally coherent striation phenomena exist, and, as can be seen in the many data pages in Appendix D, the various plasma parameters exhibit broadband noise-like fluctuations. In Fig. 25 the lower boundary of the r domain marks the lower pR range for the existence of the normal glow-discharge positive column in neon. For pR values lower than this, ambipolar diffusion of the charged particles transitions into free diffusion.

When the discharge tube is operating in the quiet region, a wave-of-stratification or ionization wave can be generated by applying a pulse perturbation to the normally homogeneous positive column, and the resulting ionization-wave parameters can be measured by the space-time-display technique as explained in Appendix C.

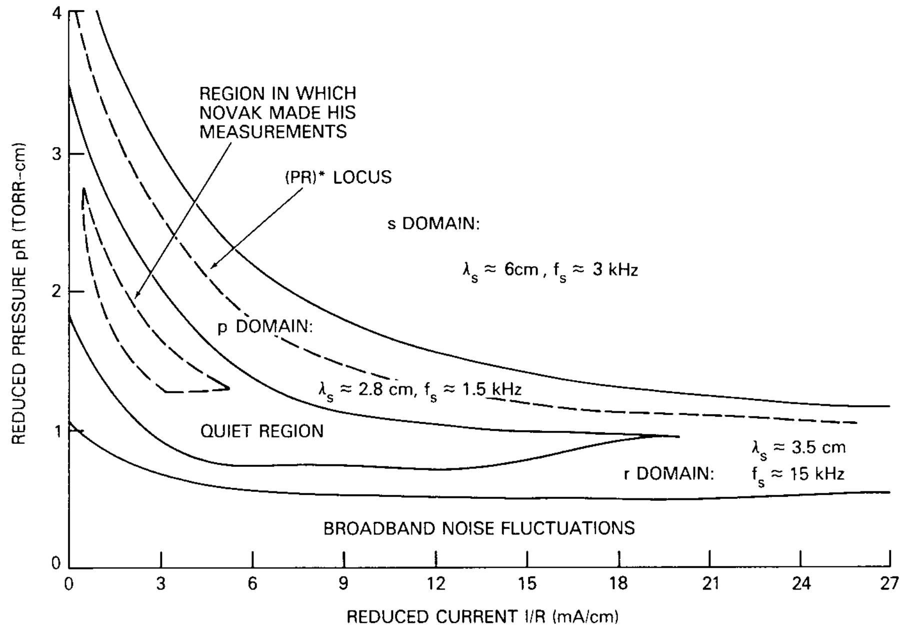

Fig. 25 — Overview of striation in a neon positive column with $R \simeq 1$ cm

In the experiments described in Appendix C, the quiet region in a neon positive column was carefully mapped with regard to delineating the various subdomains within the quiet region for the existence of the *p, r,* and *s* ionization-wave varieties and measuring the parameters of the *p, r,* and *s* ionization-wave varieties within these subdomains. To this end, the discharge tube was biased at various $(I/R,\ pR)$ operating points which formed a gridded pattern throughout the quiet region, and space-time displays of the ionization wave were recorded at each operating point. The results of this mapping are presented in Appendix D (Figs. D1 through D7). As can be seen from these displays, over some subdomains of the quiet region two wave varieties exist simultaneously, and over a small subdomain in the quiet region all three varieties exist simultaneously. The qualitative features of the striation overview diagram for neon (Fig. 25) are predicted by the model as follows. The regions in the reduced-current-pressure plane in which the three varieties of moving striations are self-excited coincide with the regions in which the associated ionization mechanisms are relatively dominant, thereby controlling the phase of the variations in the net ionization rate.

As will be shown, the different values of the striation parameters frequency and wavelength for the *r, p,* and *s* striation varieties can be predicted by using a graphic phasor construction technique. In this technique those values of λ_s and f_s are solved for that result in the $\phi_l = 2\pi$, $G_l = 1$, constraint for self-excited oscillations of the electrical equivalent circuit via the H_{er}, $H_{en,p}$, and H_{es} branches respectively. When the operating point of the discharge tube is biased into the quiet region, each of the three ionization mechanisms contribute approximately equally to the total ionization rate f_i, and since none dominates the phase of $\tilde{f}_i$, striations are not self-excited, and the positive column is longitudinally homogeneous. If this quiescent state of the positive column is disturbed due to a spatially localized pulse-type perturbation, ringinglike variations are induced in the three ionization rates, thereby exciting the three distinct transient responses currently known as the *p, r,* and *s* ionization-wave varieties.

As was pointed out following Eq. 39, the electron-metastable ionization mechanism dominates at higher pressures where $pR > (pR)^*$, and this ionization mechanism is responsible for the *s*-variety striation in neon. The metastable-metastable ionization mechanism dominates at intermediate pressures in the vicinity of $(pR)^*$ and is responsible for the *p*-variety striation. The direct ionization mechanism dominates at lower pressures where $pR < (pR)^*$ and is responsible for the *r*-variety striation. To compare the predictions of the model with the striation overview diagram for neon, the fundamental constants in Eq. 39 for $(pR)^*$ must be evaluated for neon. In Eq. 39 $D_{m,1}$ is the metastable diffusion coefficient at 1 torr and according to measurements on decaying neon plasmas is approximately 150 cm^2/s [25]. The value of the electron-metastable collision cross section Q_{em} can be estimated by a hard-sphere scattering approximation in which the collision cross section for collisional encounters between a fast particle with radius r_1, and a stationary particle with radius r_2 is

$$Q_{12} = \pi\ (r_1 + r_2)^2. \tag{53}$$

The outer electrons of the ground-state neon atom are in the 2*s* and 2*p* states with principal quantum number $n = 2$, whereas the outer electron of the metastable neon atom is in the 3*s* state with principal quantum number $n = 3$. Consequently the effective collisional radii of the metastable and ground-state neon atoms are related by

$$\frac{r_m}{r_g} = \left(\frac{n_m}{n_g}\right)^2 = \left(\frac{3}{2}\right)^2 = 2.25 \tag{54}$$

and their effective collision cross sections are related by

$$\frac{Q_{mm}}{Q_{gg}} = \left(\frac{r_m}{r_g}\right)^2 \approx 5. \tag{55}$$

For electron-atom encounters the hard-sphere theory predicts an electron-metastable collision cross section

$$Q_{em} = \frac{1}{4\sqrt{2}}\ Q_{mm}, \tag{56}$$

so that Q_{em} and Q_{eg} are related by

$$\frac{Q_{em}}{Q_{eg}} = \frac{Q_{mm}}{Q_{gg}}. \tag{57}$$

Use of Eq. 55 in Eq. 57 gives

$$Q_{em} = 5Q_{eg}. \tag{58}$$

The value of Q_{eg} obtained from measurements of the scattering of monoenergetic electron beams in neon gives $Q_{eg} = 3 \times 10^{-16}$ cm^2, so that Q_{em} is approximately 1.5×10^{-15} cm^2.

Spectral transmission measurements in a decaying afterglow have shown that of the two metastable levels in neon one state is preferentially excited to the extent that the metastable number density of the $^3P_2$ state exceeds that of the $^3P_0$ state by several orders of magnitude. Consequently, essentially the entire metastable number density in an active neon positive column is in the $^3P_2$ state, and, as Fig. 24 shows, the electron energies associated with the possible electron-metastable encounters that can excite the $^3P_2$ states to a radiating state include the nearby $^3P_1$ and $^1P_1$ levels, requiring electron energies of 0.05 eV and 0.2 eV respectively, the ten $3p$ states, requiring electron energies of approximately 2 eV, and many other higher states, with excitation energies up to and including the approximate 5-eV ionization potential of the $^3P_2$ states. Since the mean energy of the electron gas in a neon positive column is of the order of 5 eV, essentially all of the electrons involved in the electron-metastable encounters have energies in excess of 0.05 eV and thus can excite metastables to radiating states.

A rigorous calculation of the coefficient K_{em} in Eq. 39 would involve the averaging over all possible transitions to radiating states from the $^3P_2$ state of individual terms of the form

$$K_{em,j} = \int_{\mathscr{E}_j}^{\infty} K_{em,j} (\mathscr{E}) f_{\mathscr{E}} (\mathscr{E}) \, d\mathscr{E}, \tag{59}$$

where $\mathscr{E}_j$ is the minimum electron energy required to induce the jth transition, $K_{em,j}(\mathscr{E})$ is the probability per collision of inducing the jth transition for an electron with energy $\mathscr{E}$, and $f_{\mathscr{E}}(\mathscr{E})$ is the normalized electron-energy distribution function. Theoretical and/or experimental data on the average value of K_{em} are lacking for an active discharge. However the following argument provides a good enough estimate of K_{em} so that the volume loss rate of metastables due to their deexcitation by electrons can be calculated in order to ascertain the importance of this loss mechanism relative to the other three loss mechanisms.

Figure 26 depicts the qualitative features of $K_{em,j}(\mathscr{E})$ curves for the $\mathscr{E}_j = 0.05$ eV, $\mathscr{E}_j = 2$ eV, and $\mathscr{E}_j = 5$ eV transitions. Also, an electron-energy distribution function has been superimposed on these curves. A typical transition probability is zero for $\mathscr{E} \leqslant \mathscr{E}_j$, increases to a broad maximum of about 0.05 to 0.5, depending on the particular transition, for $\mathscr{E} \approx 10\mathscr{E}_j$, and gradually decreases for $\mathscr{E} > 10\mathscr{E}_j$. Due to the multiplicity of transitions to radiating states above 2 eV, electrons with energies exceeding 2 eV have a high average probability of inducing a transition, probably of the order of 0.7. Of these transitions roughly 25% return to the $^3P_2$ metastable state, so that the net or effective transition probability is approximately $0.75 \times 0.7 = 0.53$. Electrons with energies less than 2 eV can induce transitions to only the $^3P_1$ or $^1P_1$ states. Assuming the $K_{em,j}(\mathscr{E})$ curves for these states increase from zero at 0.05 eV toward a broad maximum of about 0.1 at 0.5 eV implies that since the two events are mutually exclusive, electrons whose energies are in the range 0 to 2 eV have a total probability of about 0.2 of inducing a transition to a radiating state. For the values of reduced electric field of interest, namely, $1 \leqslant E_0/p \leqslant 5$ V/ torr-cm, approximately 70% of the electrons have energies in excess of 2 eV, so that the approximate average value of K_{em} is

$$K_{em} = (0.2)\ (0.3) + (0.53)\ (0.7) = 0.06 + 0.37 \approx 0.4. \tag{60}$$

Values are known for $\lambda_{e,1}$ and K_{mg} in Eq. 39. The value of $\lambda_{e,1}$, the electron-neutral mean free path at 1 torr, is approximately 0.1 cm in a neon discharge, and Ref. 26 gives the value of the proportionality constant K_{mg} for the conversion of metastables to radiating states via collisions with thermal neutrals as 50 s^{-1}—$torr^{-1}$.

There are two distinct pressure regimes in a neon discharge. Figure 27 shows the dependence of E_0/p on pR for $I/R = 1$ mA/cm and was obtained from experimental measurements on a neon discharge reported in Ref. 22 . For $pR \lesssim 10$ torr-cm, $E_0R \approx$ constant independent of p, and $N/p \approx$ constant independent of R. For low reduced currents, namely, $I/R \approx 1$ to 10 mA/cm, $E_0R \approx 4$ volts, so that

$$E_0/p \approx 4\ (pR)^{-1}. \tag{61}$$

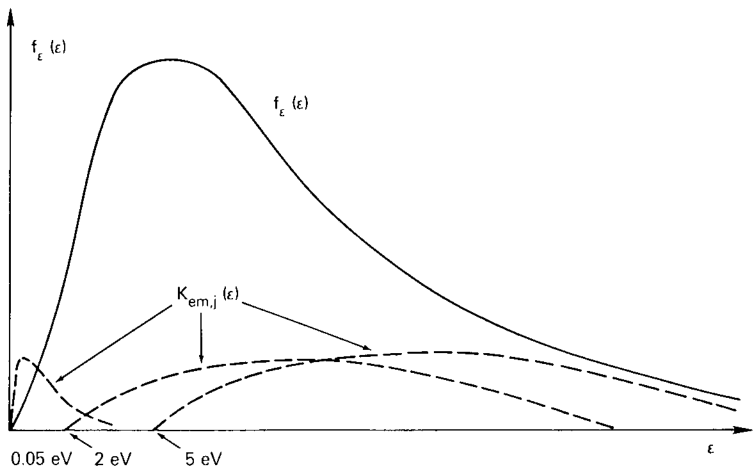

Fig. 26 — Transition probabilities $K_{em,j}(\mathscr{E})$ for transitions from the $^3P_2$ metastable state

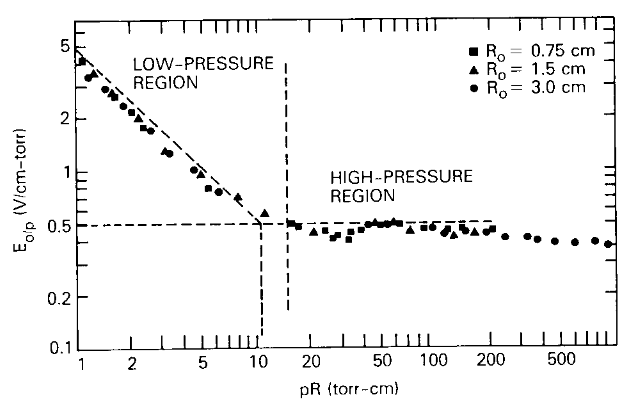

Fig. 27 — Dependence of E_0/p on pR for I/R = 1 mA/cm in a neon discharge as reported in Ref. 22

For $pR \gtrsim 10$ torr-cm, $E_0/p \approx$ constant independent of R, and $NR \approx$ constant independent of p. As shown in the figure, for $pR \gtrsim 10$ torr-cm, $E_0/p \approx 0.5$ V/cm-torr. As shown in the striation overview diagram in Fig. 25, the striation phenomena in neon occur in the lower pressure regime for $pR \lesssim 10$ torr-cm. Thus, the value of E_0R in Eq. 39 is approximately constant and equal to 4 volts.

In the lower pR range that constitutes the $(I/R,\ pR)$ domain within which the p-variety moving striation is self-excited, namely, pR equal to several torr-cm, depending on I/R (Fig. 25), almost all of the energy absorbed from the field by the electron gas is dissipated via electronic excitation. According to Ref. 27 the mean electron energy $\mathscr{E}_m$ for this situation is approximately $\mathscr{E}_x/2$, where $\mathscr{E}_x$ is the first excitation potential of the neutral gas atom. Using the preceding numerical values for $D_{m,1}$, Q_{em}, K_{em}, $\lambda_{e,1}$, K_{mg}, and E_0R in Eq. 39 gives

$$(pR)^* = \frac{4.2}{[(I/R) + 1]^{1/2}} \text{ torr-cm}, \tag{62}$$

where I/R is in mA/cm.

According to the model a coherent oscillation via the metastable-metastable ionization mechanism generates the p-variety moving striation. Since $f_{ip,0}/f_{i,0}$ is a maximum for $N_{m,0}$ a maximum and thus for $pR = (pR)^*$, Eq. 62 gives the locus in the $(I/R,\ pR)$ plane where $f_{ip,0}/f_{i,0}$ is a maximum. This locus is the dashed line labeled $(pR)^*$ in the striation overview diagram (Fig. 25) and coincides exactly with the striplike domain within which the p-variety moving striation is self-excited. Only within this limited domain where pR is in the vicinity of $(pR)^*$ is $f_{ip,0}/f_{i,0}$ sufficiently large for $\tilde{f}_{ip}$ to essentially determine the phase of $\tilde{f}_i$, which is necessary for the p-type striation to be self-excited. Thus the model correctly predicts the region in the $(I/R, pR)$ plane where the p-variety moving striation is self-excited.

As was discussed prior to Eq. 39, Eq. 62 for $(pR)^*$ as a function of I/R was based on the assumption that f_{mm}, the rate of destruction of metastables due to metastable-metastable collisions in which one of the metastables is ionized and the other deexcited, is negligible compared with the other metastable destruction mechanisms that contribute to f_m, the net metastable destruction rate. This assumption will now be justified for neon. The expression for f_{mm} is

$$f_{mm} = 2H_{imm}\, Q_{mm}\, \mathrm{v}_m\, N_m. \tag{63}$$

According to Ref. 28 approximately every fifth metastable-metastable collision results in the ionization of a metastable, so that $H_{imm} \approx 1/5$. From Eq. 56, $Q_{mm} = 4\sqrt{2}\, Q_{em}$ or $Q_{mm} = 8.5 \times 10^{-15}$ cm^2. A known relation is $\mathrm{v}_m = 1.8 \times 10^5/(AW_m)^{1/2}$ cm/s, so that for neon with an atomic weight $AW = 20$, $\mathrm{v}_m = 4 \times 10^4$ cm/s. Using these values in Eq. 63 gives

$$f_{mm} = 10^{-10}\, N_m. \tag{64}$$

The maximum value of N_m and thus of f_{mm} occurs for $pR = (pR)^*$, which in turn occurs when f_m is a minimum. For a 1-cm-radius positive column Eq. 62 gives $p^* \approx 1$ torr approximately independent of I for $10\text{mA} \leqslant I \leqslant 20$ mA. The corresponding minimum value of f_m is approximately 1.5 kHz. The corresponding maximum value of N_m is

$$N_m = \frac{2 \times 10^{15}\, K_m C_x E_0}{\mathscr{E}_x\, R^2 f_m}\, I. \tag{65}$$

From Fig. 13a $C_x = 0.8$ for $E_0/p \approx 2$ V/cm-torr, and according to Ref. 29 approximately 1/2 of all electronic excitations in neon decay to metastable states, so that $K_m \approx 1/2$. Using the preceding numerical values in Eq. 65 gives

$$N_m \approx 10^{11} I \text{ cm}^{-3}, \tag{66}$$

where I is in mA. Using this equation in Eq. 64 gives

$$f_{mm} = 10I \text{ Hz}, \tag{67}$$

so that for $I = 20$ mA $f_{mm} \approx 200$ Hz and the maximum contribution of f_{mm} to f_m is only about 10%.

Within the quiet region which separates the p and r domains (for $I/R \lesssim 20$ mA/cm) all three ionization mechanisms contribute approximately equally to f_i and self-sustained coherent oscillations in f_{is}, f_{ip}, f_{ir} are not possible, since none of the ionization mechanisms can define the phase of $\tilde{f}_i$. In the region of the $(I/R,\ pR)$ plane below the quiet region, $f_{ir,0}/f_{i,0}$ is large enough for $\tilde{f}_{ir}$ to determine the phase of $\tilde{f}_i$, and the r-variety striation is self-excited. As will be shown with a phasor construction resulting in the $\phi_l = 2\pi$, $G_l = 1$ condition via the H_{er} branch, when the direct-ionization mechanism is dominant, the gain of the H_{er} branch increases approximately as $1/p^2$, so that only within the limited pR region constituting the narrow strip-like r domain in the $(I/R,\ pR)$ plane can the $\phi_l = 2\pi$ condition be satisfied.

Above the p domain is the large s domain that encompasses almost a decade in the pR dimension. In this domain $\tilde{f}_{is}$ determines the phase of $\tilde{f}_i$, and the corresponding phasor construction will show how the $\phi_l = 2\pi$, $G_l = 1$ condition via the H_{es} ionization branch can be maintained over the large range of values of pR that constitute the s domain.

As reported in Ref. 22 and illustrated in the experimental results of Appendix D (Figs. D37 and D54), for $pR \gtrsim 10$ torr-cm the striations are quenched. This upper pressure threshold observed is predicted by the model in the following way. In the upper pressure ranges the striations are of the s variety, and the $\phi_l = 2\pi$ condition via the H_{es} ionization branch is necessary for these striations to be self-excited. In this case the net phase shift ϕ_l of the electrical loop in Fig. 8 depends on ϕ_{es}, the phase lag of $\tilde{f}_i$ relative to $\tilde{E}$ via the H_{es} branch. As discussed between Eqs. 36 and 37, ϕ_{es} in turn is approximately given by ϕ_{eb}, which is given by Eq. 36. As pR increases, E_0/p decreases, and $\mathscr{E}_{m,0}$ decreases accordingly. Thus, in accordance with Eq. 36, for a large enough value of pR, $\phi_{eb} \lesssim 45°$ and the phase lag through the H_{es} branch is no longer large enough for the $\phi_l = 2\pi$ condition for self-excited oscillations to be satisfied. The $\phi_{es} \gtrsim 45°$ criterion for self-excited s-variety striations is obtained from the phasor construction for s-variety striations shown in Fig. 28a and discussed later.

Thus, in accordance with Eq. 36, the upper pressure threshold for self-excited striations is determined from the condition that

$$\frac{2\pi}{E_0\lambda_s}\mathscr{E}_{m,0} \lesssim 1. \tag{68}$$

As Fig. 13a shows, for $E_0/p \lesssim 0.8$ V/cm-torr, $C_e \approx 1$ in a neon discharge. Therefore, for $pR \gtrsim 10$ torr-cm essentially all of the energy absorbed from the field by the drifting electron gas is dissipated via elastic collisional losses with the neutrals. Consequently, the electron gas is in a state of elastic energy balance, and its mean energy $\mathscr{E}_m$ therefore is approximately $\mathscr{E}_{mb}$ given by Eq. 25. Using the numerical values for neon in Eq. 25 gives

$$\mathscr{E}_m \approx \mathscr{E}_{mb} = 9(E_0/p). \tag{69}$$

Using this equation in Eq. 68 and solving for $(pR)_t$, the upper pressure theshold for self-excited striations, yields

$$(pR)_t = \frac{18\pi}{\lambda_s/R}. \tag{70}$$

For the s-variety striation $\lambda_s/R \approx 6$, so that Eq. 70 predicts a threshold pR of approximately 10 torr-cm, in close agreement with the experimental data.

Reference 30 reports on measurements of critical currents above which striations in neon are quenched. These critical currents are quite large, of the order of 1 A for a 1-cm-radius tube, and they were not verified in the present experiments. However, these upper threshold currents are predicted by the model in the following way. The relaxation time constants for $f_{\mathscr{E}}$ used in the model apply only if the discharge current and thus the electron density is low enough that electron-electron collisions are negligible. Reference 31 gives τ_{ee}, a relaxation time constant for $f_{\mathscr{E}}$ due to energy exchange via elastic electron-electron collision, as

$$\tau_{ee} = \frac{4 \times 10^4 \, T_e^{3/2}}{N_e} \text{ seconds,} \tag{71}$$

where T_e is the electron temperature in kelvins and N_e is the electron density in m^{-3}. Using Eq. 4 for N_e and the relation $\mathscr{E}_m = kT_e/e$ in Eq. 71 gives

$$\tau_{ee} = \frac{7.4 \times 10^{-4} \, \mathscr{E}_m \, E_0 R^2 \lambda_{e,1}}{Ip} \text{ seconds,} \tag{72}$$

where I is in mA. For I large enough that $\omega_s' \tau_{ee} \lesssim 1$, where $\omega_s' = 2\pi u_0/\lambda_s$, the relaxation characteristics of $f_{\mathscr{E}}$ are essentially determined by elastic electron-electron energy exchange. Consequently the phase lags for variations in the shape of $f_{\mathscr{E}}$ are now small enough that the $\phi_l = 2\pi$ condition for self-excited oscillations is no longer possible. Thus for $\lambda_{e,1} = 10^{-1}$ cm Eq. 72 predicts an upper reduced threshold current $(I/R)_t$ of

$$(I/R)_t \gtrsim \frac{3 \times 10^3 \, \mathscr{E}_m^{1/2} (E_0/p)^2}{\lambda_s/R}. \tag{73}$$

At these higher discharge currents, the electron-metastable ionization mechanism dominates due to the large metastable density, and only the *s*-variety striation is generated. That only a single striation variety exists at high currents whereas three varieties exist at lower currents was reported in Ref. 14. From the data in Appendix D, $\lambda_s/R \approx 6$ for the *s*-variety striation, and at higher currents $\mathscr{E}_m \approx 3$ eV and $E_0/p \approx 1.5$ V/cm-torr, so that Eq. 73 gives a threshold I/R of approximately 1 A/cm, in good agreement with the measurements reported in Ref. 19.

The particular values of f_s and λ_s for the *s*, *r*, and *p* varieties of striations in neon are predicted by the corresponding phasor constructions in Figs. 28a, 28b, 29, and 30. The dependencies of f_s and λ_s on the quiescent operating point of the discharge as well as the dispersion relation $\omega_s(k_s)$ for each of the three striation varieties is also determined from the phasor diagrams.

The phasors in these diagrams rotate counterclockwise at the angular rate $\omega_s' = 2\pi u_0/\lambda_s$ and represent the temporal variations of the various plasma parameters as perceived in the moving reference frame of the drifting electron gas. In the case of the neon discharge, and all other rare gas discharges for that matter, the moving striations are cathode directed, so that $\omega_s = 2\pi f_s$ is negative. Since $|\omega_s'| >> |\omega_s|$, ω_s' is always negative, with the consequence that cathode-directed or anode-directed moving striations and standing striations are essentially indistinguishable in the electron-gas frame of reference. All three types of striations result in the same high-frequency temporal variations $\tilde{E}'$, and the resulting periodic modulations in the shape of $f_{\mathscr{E}}$ in turn impart periodic modulations with various lagging phases to all of the plasma parameters that depend on $f_{\mathscr{E}}$. The phasor diagrams in Figs 28, 29, and 30 represent the unique relationships between the plasma phasors that result in the $G_l = 1$, $\phi_l = 2\pi$ condition being achieved via the H_{es}, H_{er}, and $H_{en,p}$ ionization branches respectively.

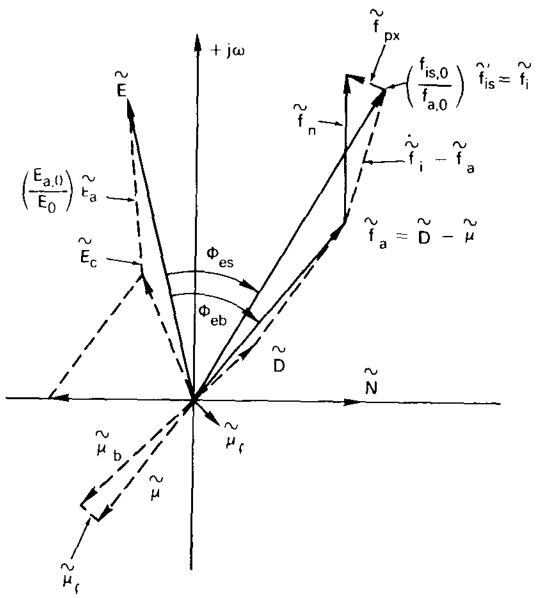

Fig. 28a — Phasor construction for the *s*-variety striation in the upper *pR* region of the *s* domain ($pR \approx 4$ torr-cm)

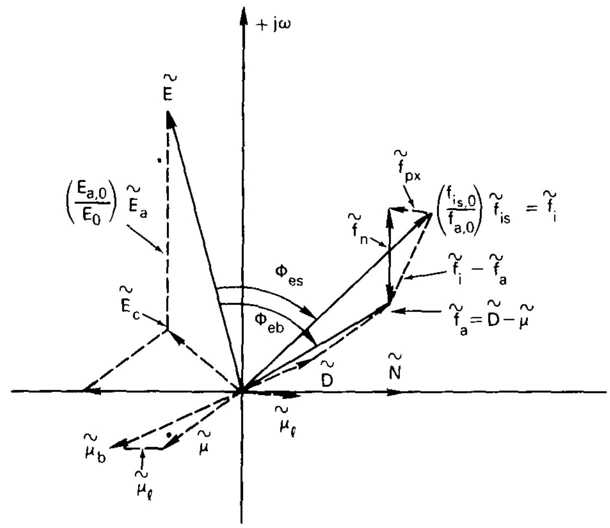

Fig. 28b — Phasor construction for the *s*-variety striation in the lower *pR* region of the *s* domain ($pR \approx 2.5$ torr-cm)

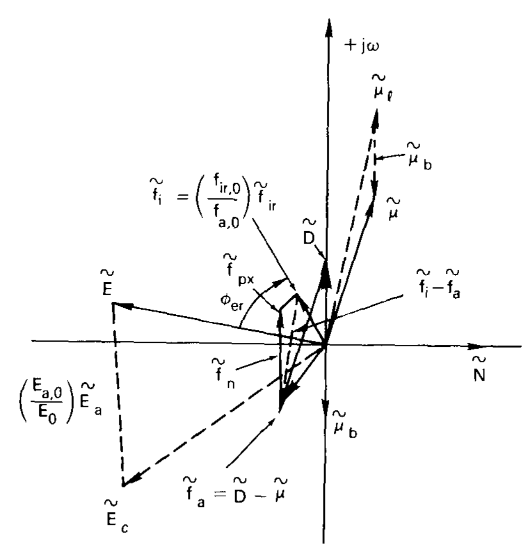

Fig. 29 — Phasor construction for the *r*-variety striation ($pR \approx 0.7$ torr-cm)

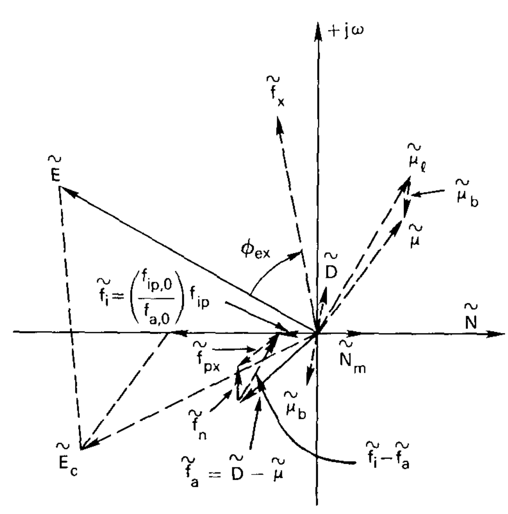

Fig. 30 — Phasor construction for the *p*-variety striation ($pR \approx 1.5$ torr-cm)

The mechanics of the phasor constructions follow directly from the equivalent electrical circuit in Fig. 8. The input $\tilde{N}$ to the RF link is along the positive real axes, and the magnitudes and phases of the other plasma phasors are specified relative to $\tilde{N}$. The pertinent analytical expressions and fundamental phasor relationships that characterize the block diagram of the mathematical model that was derived are given below:

$$G_{nn} = \frac{f_{a,0}}{|\omega_s|} = \frac{5.76\, \mu_{p,1}\, \mathscr{E}_{m,0}}{|\omega_s| R\,(pR)}, \tag{74}$$

$$\phi_{ex} = \tan^{-1}\left[\frac{2\pi\, \mathscr{E}_x}{E_0 \lambda_s}\left(\frac{n_{x,0}}{C_{x,0}}\right)\right], \tag{75}$$

$$\phi_{xl} = \tan^{-1}\left[\frac{2\pi\, \mathscr{E}_x}{E_0 \lambda_s}\left(\frac{n_{l,0}}{C_{x,0}}\right)\right], \tag{76}$$

$$\phi_{eb} = \tan^{-1}\left(\frac{2\pi}{E_0 \lambda_s}\, \mathscr{E}_{m,0}\right), \tag{77}$$

$$\tilde{D} \propto \tilde{\mathscr{E}}_m, \tag{78}$$

$$\tilde{\mu}_b \propto \tilde{\mathscr{E}}_m \; \underline{|\pi}, \tag{79}$$

$$\tilde{\mu}_l \propto \tilde{f}_x, \tag{80}$$

$$\tilde{\mu} = \tilde{\mu}_b + \tilde{\mu}_l, \tag{81}$$

$$\tilde{f}_a = \tilde{D} - \tilde{\mu}, \tag{82}$$

$$f_{a,0} = \left[\left(\frac{2.4}{R}\right)^2 \frac{\mu_{p,1}}{p}\, \mathscr{E}_{m,0}\right], \tag{83}$$

$$\tilde{E}_c = (1\underline{|\pi})\; (\tilde{N} + \tilde{\mu}), \tag{84}$$

$$\frac{E_{a,0}}{E_0}\, \tilde{E}_a = \left(\frac{2\pi K_f \mathscr{E}_{m,0}}{E_0 \lambda_s}\; \underline{|\pi/2}\right) (\tilde{N} + \tilde{\mathscr{E}}_m), \tag{85}$$

$$\tilde{E} = \tilde{E}_c + \frac{E_{a,0}}{E_0}\, \tilde{E}_a, \tag{86}$$

$$\phi_m = \tan^{-1} \frac{|\omega_s|}{f_{m,0}}, \tag{87}$$

$$f_{m,0} = K_{mg}\, p + \frac{4.2 \times 10^{15} K_{em} Q_{em} \mathscr{E}_{m,0}}{E_0 R^2 \lambda_{e,1}}\, Ip + \frac{5.76}{R^2}\, \frac{D_{m,1}}{p} \tag{88}$$

$$\tilde{N}_m = [(\cos\phi_m \underline{|\phi_m})]\, (\tilde{f}_x + \tilde{N} - \tilde{f}_m), \tag{89}$$

$$\tilde{f}_m = \frac{f_{em,0}}{f_{m,0}} \left(\tilde{N} + \frac{1}{2}\, \tilde{\mathscr{E}}_m\right), \tag{90}$$

$$f_{em,0} = \left[\frac{4.2 \times 10^{15}\, K_{em}\, Q_{em}\, \mathscr{E}_{m,0}}{E_0 R^2\, \lambda_{e,1}}\right] Ip \tag{91}$$

and

$$\tilde{f}_{px} = \left[\frac{(E_0 R)}{(\lambda_s/R)\mathscr{E}_{m,0}} \underline{\lfloor \pi/2} \right] (\tilde{E} + \tilde{N}). \tag{92}$$

Figures 28a and 28b are phasor constructions that represent the generation of the s wave in respectively the upper and lower pR regions of the s-wave domain. The phasors $\tilde{N}$, $\tilde{E}$, $\tilde{f}_a$, $\tilde{f}_{is}$, and $\tilde{f}_n$ are shown in solid lines, and the individual phasor constructions comprising them are indicated by dashed lines. Since the s-wave domain encompasses relatively large values of pR, the modulation of $f_{\mathscr{E},b}$ (the body of $f_{\mathscr{E}}$) primarily determines the characteristics of the s-variety moving striation.

Figures 28a and 28b illustrate the following salient features. Equation 77 shows that since $\mathscr{E}_{m,0}$ increases as pR decreases, ϕ_{eb} becomes more lagging as pR decreases. The phases of $\tilde{D}$ and $\tilde{\mu}_b$ are determined by ϕ_{eb}, and the phase of $\tilde{f}_{is}$ is determined by $\phi_{es} \lesssim \phi_{eb}$, since f_{is} depends on the upper energy range of $f_{\mathscr{E},b}$. The phase of $\tilde{\mu}_l$ is given by $\phi_{el} = \phi_{ex} + \phi_{xl}$ (Eqs. 75 and 76), but, as calculations will show, $|\tilde{\mu}_l|$ is small for higher pressures, so that $\tilde{\mu}_l$ has a negligible effect on the construction. The phasor $\tilde{f}_a$ is given by $\tilde{f}_a = \tilde{D} - \tilde{\mu}$ and slightly lags $\tilde{f}_{is}$. The phasor unbalance $|\tilde{f}_{is} - \tilde{f}_a|$ in the ionization and ambipolar recombination rates plus the phasor unbalance $\tilde{f}_{px}$ in the particle drift current equals the net phasor unbalance $\tilde{f}_n$ in the charged-particle production rate. The phasor $\tilde{f}_n$ leads $\tilde{N}$ by exactly $\pi/2$, as required for a self-sustained cathode-directed moving striation. As seen in the constructions, the precise phase of $\tilde{f}_n$ is particularly sensitive to $|\tilde{f}_{px}|$, which is given by

$$|\tilde{f}_{px}| = \frac{E_0 R}{(\lambda_s/R)\,\mathscr{E}_{m,0}} \; |\tilde{E} + \tilde{N}|. \tag{93}$$

Solving this equation for λ_s/R gives

$$\lambda_s/R = \frac{E_0 R}{\mathscr{E}_{m,0}} \; \frac{|\tilde{E} + \tilde{N}|}{|\tilde{f}_{px}|}. \tag{94}$$

Figure 31 shows a data display for a 0.95-cm-radius tube, with p shown at the right as a continuous parameter. The construction in Fig. 28a applies to the $p = 4$ torr upper region of the s-wave domain, and the construction in Fig. 28b applies to the $p = 2.5$ torr lower region. As can be seen from Figs. 28a and 28b, $|\tilde{E} + \tilde{N}|/|\tilde{f}_{px}| \approx 6$ for both the $p = 4$ torr and $p = 2.5$ torr constructions. The trace of E_0 vs p in Fig. 31 shows that $E_0 \approx 3.7$ V/cm for $p = 4$ torr and $E_0 \approx 3.5$ V/cm for $p = 2.5$ torr. Probe measurements in a neon discharge show that $\mathscr{E}_{m,0} \approx 4$ eV at $E_0/p \approx 1$ V/cm-torr, which is the case for $pR \approx 4$ torr-cm, and that $\mathscr{E}_{m,0}$ increases approximately as $(E_0/p)^{1/4}$ as E_0/p decreases. Thus, $\mathscr{E}_{m,0}$ increases to approximately 4.3 eV for $pR \approx 2.5$ torr-cm, where $E_0/p \approx 1.4$ V/cm-torr. With use of these values E_0 and $\mathscr{E}_{m,0}$ for the $p = 4$ torr and $p = 2.5$ torr regions gives

$$\lambda_s/R = \frac{3.7}{4}\, 6 = 5.6 \tag{95}$$

for $p = 4$ torr and

$$\lambda_s/R = \frac{3.5}{4.3} 6 = 4.9 \tag{96}$$

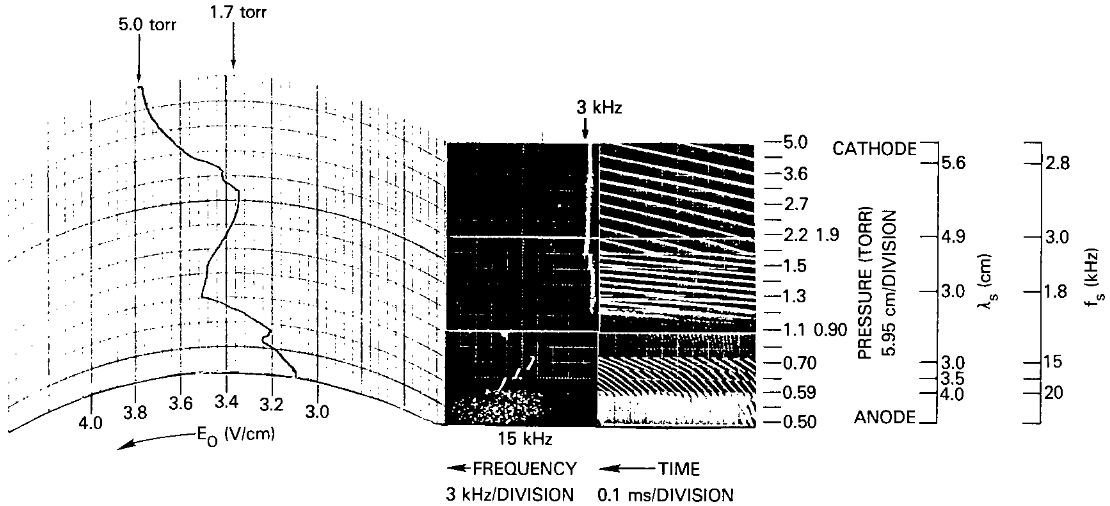

Fig. 31 — Typical data display for striations of the s, p, and r, varieties in neon

for $p = 2.5$ torr. These results are in perfect agreement with the measured values of λ_s at 4 torr as and 2.5 torr as shown at the right in Fig. 31.

In Fig. 31 the quiet region extends from about 0.75 torr to almost 1.2 torr. Measurements shown in Fig. D3 in Appendix D at $p = 0.9$ torr on the s-variety wave of stratification excited in this quiet region (for $I = 10$ mA) give $\lambda_s \approx 3.7$ cm. Figure 31 shows that $E_0 \approx 3.5$ V/cm at $p = 1$ torr, so that $E_0/p = 3.5$ V/cm-torr. Thus, $\mathscr{E}_{m,0}$ is increased by $(3.5)^{1/4} \approx 1.4$ and is $4(1.4) = 5.6$ eV in this region. Using these values in Eq. 94 gives

$$\lambda_s/R = \frac{3.5}{5.6}\, 6 = 3.7. \tag{97}$$

Thus, the model correctly predicts the value of λ_s for the s-variety striation in neon and its decrease with pressure, thereby supporting the assertion that the s-variety wave of stratification is the transient ringing response of the electrical loop (Fig. 8) via the H_{es} ionization branch.

Since the net phasor gain of the RF link G_{RF} is $|\tilde{f}_n|/|\tilde{N}|$ and the IF link gain G_{IF} is $f_{a,0}/|\omega_s|$, the $G_l = 1$ condition requires that

$$|\omega_s| = f_{a,0}\frac{|\tilde{f}_n|}{|\tilde{N}|}. \tag{98}$$

Substituting $\mu_{p,1} = 3000$ cm^2/s for the neon atomic ion mobility into Eq. 83 for $f_{a,0}$ and using the result in Eq. 98 gives

$$|f_s| = \frac{2.8 \times 10^3\, \mathscr{E}_{m,0}}{R\,(pR)}\, \frac{|\tilde{f}_n|}{|\tilde{N}|}\ \mathrm{Hz}. \tag{99}$$

From Fig. 28a $|\tilde{f}_n|/|\tilde{N}| \approx 1$ for $p = 4$ torr, and using $\mathscr{E}_{m,0} = 4$ eV in Eq. 99 gives

$$|f_s| = \frac{2.8 \times 10^3(4)}{4}\, 1 = 2.8\ \mathrm{kHz} \tag{100}$$

for $p = 4$ torr, in exact agreement with the measured value 2.8 kHz indicated at the right in Fig. 31 for $p = 4$ torr.

For $p = 2.5$ torr Fig. 28b shows that $|\tilde{f}_n|/|\tilde{N}| \approx 0.6$, and using $\mathscr{E}_{m,0} = 4.3$ eV and $p = 2.5$ torr in Eq. 99 gives

$$|f_s| = \frac{2.8 \times 10^3(4.3)}{2.5}(0.6) = 2.9 \text{ kHz} \tag{101}$$

as compared with 3.0 kHz measured for $p = 2.5$ torr.

In addition to predicting accurate values of f_s, the phasor construction technique clearly illustrates the mechanism by which f_s remains approximately constant throughout the entire $(I/R,\ pR)$ s-wave domain for a given-radius tube and, as shown in Eq. 99, scaling as R^{-1} for tubes with different radii. Figure 31 shows that as p decreases from 5 torr to 1.7 torr, f_s for the s wave increases but slightly: from roughly 2.8 kHz to 3.0 kHz. Such a dependence of f_s on p is clear from the phasor constructions, since even though $f_a \propto 1/p$, $|\tilde{f}_n|/|\tilde{N}| \underset{\sim}{\propto} p$, so that their product and therefore f_s is approximately constant.

Due to the asympotical nature of the $\cos[\tan^{-1}(\omega_s' \tau_r)]$ function that determines the phase lags of $\tilde{f}_{is}$ and $\tilde{f}_a$ relative to $\tilde{E}$, the phasor geometry shown in Fig. 28b for $p = 2.5$ torr approximately holds for $p = 1$ torr as well. Using $p = 1$ torr and $\mathscr{E}_{m,0} = 5.6$ eV in Eq. 99 gives

$$|f_s| = \frac{2.8 \times 10^3(5.6)}{1}\, 0.6 = 9.5 \text{ kHz}. \tag{102}$$

The measured value of f_s from the data for the s wave of stratification in Fig. D3 gives $f_s = 11$ kHz. Thus the values of both f_s and λ_s for the s wave of stratification are correctly predicted by the oscillation characteristics of the equivalent electrical circuit via the H_{es} electron-metastable ionization branch.

The dispersion relation $\omega_s(k_s)$ for the s-variety striation can be ascertained from the phasor constructions in the following way. As λ_s decreases (k_s increases) at a fixed quiescent operating point (for constant pressure), the lag $\phi_{eb}(\omega_s')$ increases and $|\tilde{f}_n|/|\tilde{N}|$ decreases in somewhat the same manner as if the pressure had actually decreased. Therefore $|\omega_s|$ decreases as k_s increases, and, since $\omega_s < 0$, this means that $\partial\omega_s/\partial k_s > 0$, indicating an anode-directed group velocity.

That the phasor constructions in Figs. 28a and 28b for $p = 4$ torr and $p = 2.5$ torr are accurate constructions based on the mathematical model is shown in the following discussion. Using $\mathscr{E}_x \approx 17$ eV and $E_0\lambda_s \approx 20$ V for the s wave in Eqs. 75 through 77 gives

$$\phi_{ex} = \tan^{-1}\left[5.4\left(\frac{n_{x,0}}{C_{x,0}}\right)\right], \tag{103}$$

$$\phi_{xl} = \tan^{-1}\left[5.4\left(\frac{n_{l,0}}{C_{x,0}}\right)\right], \tag{104}$$

and

$$\phi_{eb} = \tan^{-1}(0.3\mathscr{E}_{m,0}). \tag{105}$$

Since $\mathscr{E}_{m,0} = 4$ eV for $p = 4$ torr, Eq. 105 gives $\phi_{eb} \approx 50°$, which is the value of ϕ_{eb} in Fig. 28a.

Probe measurements show that $n_{x,0} \underset{\sim}{\propto} 1/p$, and from Fig. 13a $C_{x,0} \underset{\sim}{\propto} p$ in the $1 \le E_0/p \le 3$ V/torr-cm range of interest. In this range of E_0/p, $n_{x,0}$ increases from approximately 5% to 15% and $C_{x,0}$ increases from 0.4 to approximately 0.9, so that $n_{x,0}/C_{x,0} \approx 0.17$ throughout the 1 to 3 V/cm-torr range of E_0/p. Using this value in Eq. 103 gives $\phi_{ex} \approx 45°$ independent of pressure.

However, $n_{l,0}$ in Eq. 104 is approximately constant as E_0/p changes. Since $f_{\mathscr{E}}$ transitions toward a Maxwellian form as E_0/p increases, $n_{l,0}$ increases slightly as E_0/p increases. However, the approximation $n_{l,0} \approx 20\%$ independent of pressure is fairly good, and using this in Eq. 104 shows that ϕ_{xl} decreases from 70° for $p = 4$ torr to 50° for $p = 2.5$ torr. Thus $\tilde{\mu}_l$ lags $\tilde{E}$ by $\phi_{ex} + \phi_{xl} = 115°$ for $p = 4$ torr and by 95° for $p = 2.5$ torr. Also, for $p = 2.5$ torr $|\tilde{\mu}_l|$ is increased by the factor cos 50°/cos 70° ≈ 2.

Finally, using $K_f = 2/3$ (as for a Maxwellian distribution) in Eq. 85 gives

$$\frac{E_{a,0}}{E_0}\,\tilde{E}_a = [(0.75\,\underline{\left|\pi/2\right)}]\;(\tilde{N} + \tilde{\mathscr{E}}_m), \tag{106}$$

as shown in the constructions.

Figure 29 is the phasor construction for the r wave, which, as shown in Fig. 31, is self-excited in the interval 0.6 to 0.7 torr. In this interval $E_0/p \approx 3.5/0.7 = 5$ V/cm-torr, so that $\mathscr{E}_{m,0} = 5^{1/4}(4) = 6$ eV. For the r wave $E_0\lambda_s \approx 12$ V, so that Eqs. 75 through 77 give $\phi_{ex} \approx 55°$, $\phi_{xl} \approx 55°$, and $\phi_{eb} \approx 70°$. Since $\phi_{eb} \approx 70°$, the modulation of the body of $f_{\mathscr{E}}$ is attenuated by approximately a factor of cos 45°/cos 70° ≈ 2 from its value in the higher pressure s-wave domain. Thus, as shown in Fig. 29, $\tilde{\mu}$ is primarily determined by $\tilde{\mu}_l$, the modulation of the low-energy tail of $f_{\mathscr{E}}$. Consequently $\tilde{f}_a = \tilde{D} - \tilde{\mu}$ and $\tilde{f}_{ir}$ tend to be out of phase. Figure 29 shows that $|\tilde{E} + \tilde{N}|/|\tilde{f}_{px}| \approx 5$ for the r wave, and using this value and $E_0R \approx 3.5$ V and $\mathscr{E}_{m,0} \approx 6$ eV in Eq. 94 gives

$$\lambda_s/R = \frac{3.5}{6}\,5 = 3.0, \tag{107}$$

in exact agreement with the measured value of $\lambda_s = 3.0$ cm indicated in Fig. 31 for the r wave.

Figure 29 also shows that $|\tilde{f}_n|/|\tilde{N}| \approx 0.6$, and using this value and $\mathscr{E}_{m,0} = 6$ eV and $p = 0.7$ torr in Eq. 99 gives

$$|f_s| = \frac{2.8 \times 10^3(6)}{0.7}\,0.6 = 14.5 \text{ kHz}, \tag{108}$$

again in exact agreement with the value of f_s for the r wave at $p = 0.7$ torr shown in Fig. 31.

Figure 31 also shows that the frequency of the r wave increases from 14.5 kHz at $p = 0.7$ torr to 20 kHz at $p = 0.6$ torr. Thus f_s for the r wave increases by a factor of 1.4 while p decreases by a factor of $(1.4)^{1/2} = 1.17$, indicating that $f_s \propto 1/p^2$ in the self-sustained r-wave domain. That the model predicts exactly such a pressure dependence for the frequency of the r wave is shown in Fig. 32, where the pertinent geometry affecting $\tilde{f}_n$ is expanded. The three separate constructions in Fig. 32 correspond to the three continuous segments of the f_s-vs-p curve in Fig. 31.

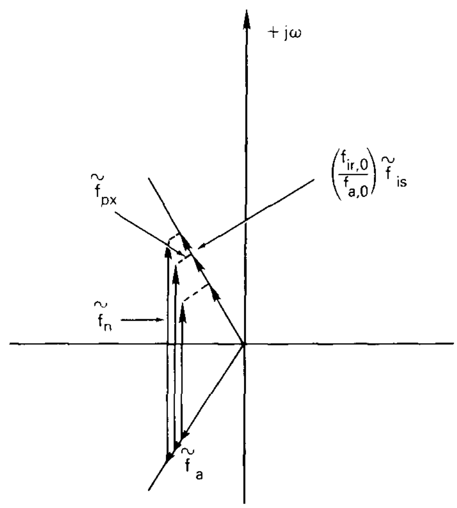

Fig. 32 — Phasor construction showing how the r-wave striation geometry changes with pressure

The quiescent value of the direct ionization rate is proportional to $(E_0/p)^2$. Thus, since $f_{ir,0} \propto 1/p^2$ and $f_{a,0} \propto 1/p$, $f_{ir,0}/f_{a,0} \propto 1/p$, so that the magnitude of the $(f_{ir,0}/f_{a,0})\ \tilde{f}_{ir}$ phasor increases as $1/p$. Since $|\tilde{f}_a|$ is approximately constant, $|\tilde{f}_n|$ increases approximately as $1/p$, and since $f_s \propto f_{a,0}$ from Eq. 98, this leads to a $f_s \propto 1/p^2$ dependence for the r wave.

Thus, for the three constructions in Fig. 32, $|\tilde{f}_{px}|$ decreases as $|\tilde{f}_n|$ increases, and via Eq. 94 this predicts the result in Fig. 31 that λ_s for the r wave increases from approximately 3.0 cm to 3.5 cm and then to 4.0 cm for the three segments of the f_s-vs-p curve.

That the group velocity of the r wave is anode directed is also clear from Fig. 29, since a decrease in λ_s results in a decrease in both $|\tilde{f}_a|$ and $|\tilde{f}_{ir}|$, which in turn leads to a decrease in $|\tilde{f}_n|$. Thus, since $\omega_s < 0$ and $|\omega_s|$ decreases as k_s increases, $\partial\omega_s/\partial k_s$ is positive, indicating an anode-directed group velocity.

Figure 30 is the phasor construction for the p wave, which is spontaneously generated in the $p = 1.2$ to 1.7 torr range (Fig. 31). In this region $pR \approx (pR)^*$, so that $(f_{em,0}/f_{m,0}) \approx 1/2$, which when substituted into Eq. 90 gives $\tilde{f}_m = \tilde{N}/2 - \tilde{\mathscr{E}}_m/4$. Since $\phi_m \approx 80°$, Eq. 89 gives the location of $\tilde{N}_m$ as lagging $\tilde{f}_x + (\tilde{N}/2)$ by 80°. Since cos 80° = 0.17,

$$|\tilde{N}_m| \approx 0.17|\tilde{f}_x + \frac{1}{2}\tilde{N}|. \tag{109}$$

Thus $\tilde{N}_m$ is approximately in phase with $\tilde{N}$ and $|\tilde{N}_m| \approx 0.25\ |\tilde{N}|$, so that $\tilde{f}_{ip} = 2\tilde{N}_m - \tilde{N}$ is out of phase with $\tilde{N}$ and $|\tilde{f}_{ip}| \approx 0.5|\tilde{N}|$.

For $p = 1.5$ torr $E_0/p \approx 2.3$ V/cm-torr, so that $\mathscr{E}_{m,0} \approx 2.3^{1/4}(4) = 5$ eV. From Fig. 30 $|\tilde{E} + \tilde{N}|/|\tilde{f}_{px}| \approx 4$, so that Eq. 94 gives

$$(\lambda_s/R) = \frac{3.5}{5}\ 4 = 2.8 \tag{110}$$

as compared with the measured value $\lambda_s \approx 3.0$ cm at 1.5 torr in Fig. 31. From the construction $|\tilde{f}_n|/|\tilde{N}| \approx 0.2$, so that Eq. 99 gives

$$|f_s| = \frac{2.8 \times 10^3(5)}{1.5} 0.2 = 1.8 \text{ kHz}, \tag{111}$$

in exact agreement with the measured value in Fig. 31.

The model therefore yields precise predictions of the striation parameters for the s, r, and p varieties in neon and their detailed dependencies on the quiescent glow-discharge operating point.

PREDICTING AND COMPARING WITH EXPERIMENT THE PROPERTIES OF STRIATIONS IN A NEON PENNING DISCHARGE WITH AN ARGON ADMIXTURE AND THE NOVAK POTENTIAL FOR STRIATIONS IN ARGON AND HELIUM

Some of the early theories put forth in attempts to explain striations contained variations on the theme of electrons cyclicly acquiring energy from the longitudinal electric field at one position and losing it via ionization and or excitation at another as they drifted along the positive column. For example, Penning [3] found that $E_0\lambda_s$, the potential across a striation wavelength for the few standing striations that occur at the cathode end of positive columns containing rare gases, approximately equals certain excitation potentials of the fill-gas ground-state atoms, such as the 18.5-volt excitation potential to the $2p$ state in neon. Such theories imply a correlation between the Novak potentials and certain quantum energy levels or level differences of the fill gas. In this section an experiment is discussed in which trace amounts of argon were added to a neon discharge. The results of this experiment are interpreted according to the model derived in an earlier section, and they conclusively show that the Novak potentials are not associated with quantum level differences of the fill gas per se.

The theory presented herein explains the physical significance of the Novak potentials as being those distinct values of $E_0\lambda_s$ that result in the $\phi_l = 2\pi$ condition for oscillations of the electrical-equivalent-circuit model of the column (Fig. 8), via the H_{er}, $H_{en,p}$, and H_{es} ionization branches. Further evidence of the correctness of this explanation is provided by the measurements presented in Appendix D, Figs. D55 through D62.

This experiment investigated the effect of adding small admixtures of argon to the neon discharge. The Penning effect is described by the equation

$$\text{Ne}^* + \text{Ar} \rightarrow \text{Ar}^+ + \text{Ne} + \text{e}; \tag{112}$$

that is, a neon metastable atom ionizes an argon impurity atom, producing an argon atomic ion-electron pair and a ground-state neon atom. Argon concentrations as low as 0.1% cause a drastic change in the relative balance between the three ionization mechanisms that maintain a neon discharge.

The series of space-time, spectral raster, and E_0 displays in Figs. D55 through D62 are the results of measurements in a 0.95-cm-radius tube at a pressure of 1.5 torr with the current a continuous variable (0 to 30 mA) in which the concentration of the argon admixture was increased for each successive current scan. It is readily evident from the displays that as the argon concentration increases, E_0 decreases and both f_s and λ_s increase. Also, as the argon concentration increases, the current interval within which the p wave is self-excited is shifted toward lower values and the corresponding interval for the s wave is shifted toward higher values. When the argon concentration was increased to approximately 0.1%, the p-variety striation was quenched, and as the argon concentration was increased to approximately 0.2%, the s-variety striation was quenched.

These observations can be explained by the model in the following way. The displays show that as the argon concentration increases from zero to approximately 0.2%, E_0 decreases by approximately a factor of 1.25 and λ_s for the s wave increases by a factor of approximately 2.5, so that $E_0\lambda_s$ increases by approximately a factor of 2: from approximately 20 V to 40 V. Such a continuous dependence of $E_0\lambda_s$ on the argon concentration cannot possibly be explained by attributing Novak's potentials to various quantum-level differences of the fill gas or gases. Just such a dependence of $E_0\lambda_s$ on the argon concentration, however, is predicted by the model. As the argon concentration increases, $f_{is,0}/f_{a,0}$ decreases as the result of two separate effects. As a consequence of the Penning ionization mechanism the discharge in the neon-argon admixture is maintained by an additional ionization mechanism, so that as the argon concentration increases, the relative quiescent contribution of the electron-metastable ionization mechanism decreases. Also, the positive ions in the discharge now consist of a mix of Ne^+ atomic neon ions and Ar^+ atomic argon ions. The mobility of the Ar^+ ion is approximately twice that of the Ne^+ ion. This is because argon ions do not undergo charge-exchange collisions with the neon neutrals.

In Ref. 32 the relative fraction of the Ar^+ ion as a function of the percentage of admixed argon was measured by cataphoretic segregation in an active neon-argon discharge. According to these measurements, at 0.2% argon the discharge contains approximately 50% Ar^+ ions and 50% Ne^+ ions. Thus, for the 0.2% Ar discharge the average ion mobility is approximately

$$\bar{\mu}_p = \frac{1}{2}\,\mu_{\mathrm{Ne}^+} + \frac{1}{2}\,\mu_{\mathrm{Ar}^+} \tag{113a}$$

or

$$\bar{\mu}_p = 4500\ \mathrm{cm^2/V\text{-}s}. \tag{113b}$$

The quiescent value of f_a therefore is increased by approximately a factor of $4500/3000 = 1.5$.

Figure 33 shows on an expanded scale the s-wave phasor construction geometry that determines $|\tilde{f}_{px}|$ and thus λ_s (Eq. 94) and $|\tilde{f}_n|$ and thereby f_s (Eq. 99). As the argon concentration increases, $f_{is,0}/f_{a,0}$ decreases. Figure 33 depicts the situation for 0% Ar and for 0.2% Ar. These constructions show that as the argon concentation increases from zero toward 0.2%, $|\tilde{f}_{px}|$ decreases by a factor of 2.5 and $|\tilde{f}_n|$ decreases by a factor of 1.3. Both E_0 and $\mathscr{E}_{m,0}$ in Eq. 94 decrease by approximately the same amount as the argon concentration increases, so that the factor of 2.5 decrease in $|\tilde{f}_{px}|$ results in a factor of 2.5 increase in λ_s.

As seen from Eq. 99, a factor of 1.3 decrease in $|\tilde{f}_n|$ decreases f_s by a factor of 1.3. However, as the argon concentration increases from 0% to 0.2%, μ_p increases by a factor of 1.5, so that Eq. 99 predicts a net increase in f_s by a factor of $1.5/1.3 = 1.2$, in exact agreement with the measured increase in f_s.

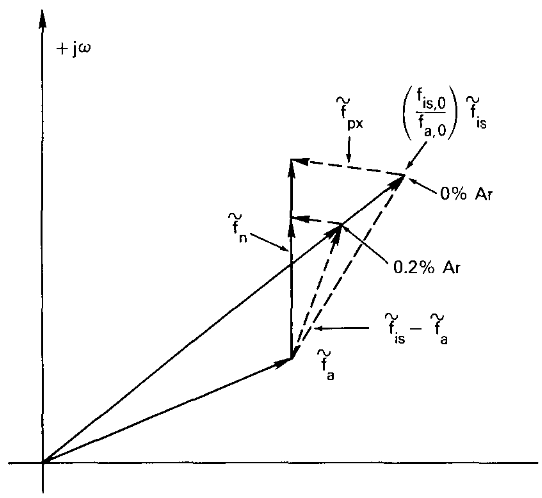

Fig. 33 — Phasor construction showing how the *s*-wave geometry changes with argon concentration

The displays show that as the argon concentration increases, the *s* wave is gradually quenched, first at lower discharge currents and then, as the argon concentration increases, at successfully higher discharge currents until finally for approximately 0.2% Ar the *s* wave is quenched at the highest currents for which measurements were made (30 mA). Such a dependence can be explained as follows: $f_{is} \propto N_0$ and in turn $N_0 \propto I$, so that the relative contribution of the f_{is} electron-metastable ionization mechanism increases with I. Thus the decrease in $f_{is,0}/f_{a,0}$ due to the increase in the argon concentration is partially overcome at larger values of I. For a large enough increase in the argon concentration, however, the Penning ionization mechanism dominates and the relative phase of $\tilde{f}_i$ is no longer determined by $\tilde{f}_{is}$, so that the *s* wave is quenched.

The *p* domain shifts to lower currents as the argon concentration increases because the additional metastable destruction rate due to the Penning effect lowers the value of $(pR)^*$. A lower value of I is required to balance the increase in $f_{m,0}$ due to the Penning effect, so that the *p* terms and $1/p$ terms in the $f_{m,0}$ expression (Eq. 88) are again equal.

The model also correctly predicts the values of the Novak potentials for the *p, r,* and *s* waves in argon and helium. Table 1 shows the measured values of $E_0\lambda_s$ for Ne, Ar, and He as reported in Ref. 14 . Also shown are the ratios of $E_0\lambda_s$ for the *p, r,* and *s* waves in argon and helium to the corresponding value of $E_0\lambda_s$ in neon.

Figures 13a and 13b show that in the E_0/p range of interest for striations electronic excitation is the dominant energy-loss mechanism in rare-gas discharges. Thus it is plausible to assume that the relative phase between $\tilde{f}_x$ and $\tilde{E}$ is an invariant characteristic of a particular striation variety in the rare gases. As previously pointed out, the constraint $E_0\lambda_s \approx$ constant for a particular wave variety leads via Eq. 33 to the condition that $\phi_{ex}(E_0\lambda_s) \approx$ constant independent of the exact discharge operating point for a given fill gas. It is possible then that the value of $\phi_{ex}(E_0\lambda_s)$ has an even more universal significance than the Novak potentials in that the value

Table 1 — Measured Values of Novak's Potentials and the Electronic Excitation Potential for Neon, Argon, and Helium [14]

Fill Gas	$E_0\lambda_s$ (volts)			$E_0\lambda_s$ Relative to Neon			$\mathscr{E}_x$	$\mathscr{E}_x$ Relative to Neon
	p	r	s	p	r	s		
Neon	9.4	12.7	19.5	1	1	1	16.1	1
Argon	6.7	9.5	12.0	0.71	0.74	0.62	11.6	0.7
Helium	14.2	—	30	1.5	—	1.5	21.2	1.3

of $\phi_{ex}(E_0\lambda_s)$ for a particular striation variety is not only approximately independent of the exact discharge operating point for a given fill gas but is also approximately independent of the particular atomic fill gas.

If this hypothesis is true, the argument in Eq. 33 should be approximately constant for a particular striation variety for all atomic fill gases:

$$\frac{2\pi\,\mathscr{E}_x}{E_0\lambda_s}\left(\frac{n_{x,0}}{C_{x,0}}\right) \approx \text{constant}. \tag{114}$$

For the assumption that $n_{x,0}/C_{x,0} \approx$ constant for the various atomic fill gases (that the same relative number of electrons in the high-energy tail for f_g are required to result in the same relative energy loss due to electronic excitation), Eq. 114 predicts that the ratios of the Novak potentials for the various gases should be approximately equal to the corresponding ratios of their electronic excitation potentials. As shown in Table 1 the ratios of $E_0\lambda_s$ for the p, r, and s waves in neon, argon, and helium are within 10% of the corresponding ratios of $\mathscr{E}_x$, supporting the hypothesis that $\phi_{ex}(E_0\lambda_s) \approx$ constant for a given wave variety independent of the fill gas.

PREDICTING AND COMPARING WITH EXPERIMENT THE CHARACTERISTICS OF STRIATION FREQUENCY SPECTRA

The frequency spectra of the temporal variations of the plasma parameters caused by moving striations exhibit a peculiar harmonic content. Figure 34 is a typical composite display format as explained in Appendix C. The three displays at the right are from top to bottom the power spectra of the discharge luminosity for discharge currents of 5 mA, 15 mA, and 25 mA. The discharge operating point is in the s-wave region.

Previous investigators have briefly mentioned that striation spectra contain harmonic responses and have attributed them to conventional harmonic responses generated by large signal nonlinearities. The amplitude profiles of actual striation spectra, however, are not consistent with such a viewpoint. If the nth-order harmonic responses are due to a nonlinearity of the nth degree, their amplitudes would be reduced by the factor $(1/n)(m/2)^{n-1}$ relative to the amplitude of the fundamental with modulation index m. The spectral power of the nth-order harmonic responses therefore would be reduced by the factor $(1/n)^2(m/2)^{2(n-1)}$ relative to the spectral power of the fundamental response.

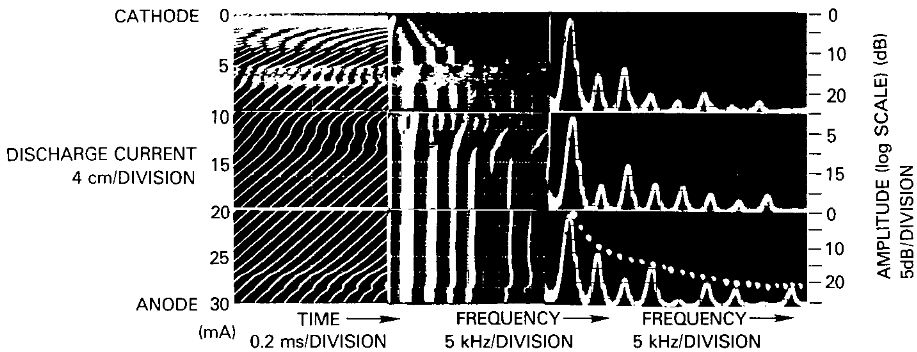

Fig. 34 — Data display illustrating the higher order modes of the s-variety striation

The amplitudes of the fundamental response in the three power spectra shown in Fig. 34 are approximately equal. The amplitudes of corresponding harmonic responses, however, change markedly from one display to the next. Detailed analyses of other such displays in Appendix D confirm that the relative amplitudes of the harmonic responses do not vary as m^2. In fact, as illustrated in Fig. 34, the relative amplitudes of the various harmonic responses are completely independent of m. Their values are, however, sensitive to the precise operating point of the discharge.

Also, the observed amplitudes of the higher order harmonics significantly exceed the predictions based on nonlinearities. The $(1/n)^2(m/2)^{2(n-1)}$ weighting factor predicts maximum amplitudes ($m = 1$), second harmonic amplitudes that are 12 dB below the fundamental for the second harmonic, third harmonic amplitudes that are 21.5 dB below the fundamental, etc. Thus, the maximum ninth-order harmonic amplitude would be 67 dB below the fundamental. The 25-mA spectral display in Fig. 34, however, shows a ninth-order harmonic response that is only approximately 20 dB below the fundamental. Superimposed on this 25-mA display is the envelope corresponding to a harmonic weighting profile of $1/n^2$, where n is the harmonic order. As seen from this display, the harmonics of order 2, 4, 6, 7, and 9 fit this profile exactly. A comprehensive examination of the measured data in Appendix D reveals that the $1/n^2$ weighting is an upper bound for observed power spectral harmonic amplitudes. As will be seen, the electrical equivalent circuit of the column (Fig. 8) is such that the $\phi_l = 2\pi$ condition for loop oscillations can be achieved for integral values of n that range from 1 to approximately 10 according to the scheme $\phi_l(\omega_s') = 2\pi$, $\phi_l(2\omega_s') = 2\pi$, $\phi_l(3\omega_s') = 2\pi$, ... , $\phi_l(n\omega_s') = 2\pi$. These loop oscillations correspond to the generation of spatial harmonics whose wavenumbers are related to $n\omega_s'$ via $nk_s = n\omega_s'/u$.

All of the higher order striations are synchronized and move at the same velocity given by $v_s = \omega_s/k_s$, so that they in turn cause higher order temporal variations in the laboratory reference frame at the harmonic frequencies $n\omega_s$. The $G_l = 1$ condition corresponding to the various higher order modes of loop oscillation is achieved for a value of $m_n = |\tilde{N}|$ such that $|\tilde{N}|$ for the nth-order mode has a maximum value of $(1/n)|\tilde{N}|$, in agreement with observed spectral responses. It is somewhat surprising that these higher order spatial modes can be predicted for an unbounded-length system with an open-loop instability. Normally one invokes longitudinal boundary conditions to account for higher order spatial modes, bounding the column length to

L, for example, and accounting for higher order spatial modes via $k_s = n(2\pi/L)$, as was done in Ref. 17. If such was the case, λ_s in a positive column for which $L = 10\lambda_s$ would vary by approximately 10% as the cathode-to-anode spacing was changed by λ_s. Experiments designed along these lines with a movable anode, however, have shown λ_s to be essentially independent of L.

The manner in which the $\phi_l(n\omega_s') = 2\pi$ constraint for the higher order modes is satisfied can be explained via the simplified electrical loop in Fig. 21. The phasor transfer function H_{ne} in Fig. 21 is defined by Fig. 18. The magnitude or gain of the $H_{en,a}$ branch in Fig. 18 that accounts for the ambipolar field is inversely proportional to λ_s and thus proportional to k_s. Consequently G_{ne}, the gain associated with H_{ne} in the RF link in Fig. 21, is approximately proportional to n. Hence an nth-order spatial harmonic with a wavenumber nk_s which appears as an nth-order temporal harmonic with a frequency $n\omega_s' = nk_s u$ in the RF link requires an input of only $(1/n)|\tilde{N}'|$ to produce the same $|\tilde{E}'|$ output from H_{ne} as the input of $|\tilde{N}'|$ with the fundamental frequency $\omega_s' = k_s u$.

The gain $G_{en,x}$ is given by Eq. 20, which defines $H_{en,x}$. Since $G_{en,x} \propto k_s$, $G_{en,x} \propto n$ for the higher order modes. As can be seen from the following argument, however, $G_{en,x} \propto n$ holds only for n less than a certain value. Equation 20 results from the divergence operation: $\nabla_x \cdot I_p$. Consequently, the relation $G_{en,x} \propto k_s$ given in Eq. 20 holds exactly only if a unit length of the positive column is of zero extent in the x direction. In order for the charged-particle production and loss rates to be modulated within a unit length of the column as the electron gas drifts through, the unit length must have a width Δx such that $\Delta x \gtrsim 10\lambda_e$, where λ_e is the electron mean free path. The spatial averaging of $\nabla_x \cdot I_p$ within Δx causes the effective value of $G_{en,x}$ to be lower than that predicted by Eq. 20. The magnitude of the reduction in $G_{en,x}$ increases with n, and for values of n larger than $n = n^*$, where n^* is given by the condition $\lambda_{s,n^*}/2 \leq \Delta x$, a unit length averages an even or odd number of half cycles of $\nabla_x \cdot I_p$. This picture predicts a tendency to select either even or odd higher order modes for $n \gtrsim n^*$, depending on the value of λ_{s,n^*} relative to the value of Δx. Since $\Delta x \propto \lambda_e$, Δx scales as $\Delta x \propto R$ for tubes of different radii at similar operating points and scales as $\Delta x \propto 1/p$ for different operating conditions in a tube with a fixed radius. Consequently this picture also predicts that the highest allowed mode number or the maximum number of modes goes as p.

The data in Appendix D support this picture in that they show a pronounced tendency toward even or odd mode numbers, depending on discharge operating point, and show that as p increases, the maximum allowed mode number increases. Typically, $n \approx 3$ to 4 for $pr \approx 0.5$ to 1.0 torr-cm, $n \approx 6$ to 9 as pr increases to $pr \approx 2$ to 4 torr-cm, and finally $n \approx 10$ to 12 for $pr \approx 4$ to 6 torr-cm.

Figure 35 is a composite phasor construction that shows the relationships between $\tilde{N}'$, $\tilde{E}'$, $\tilde{f}_i'$, $\tilde{f}_a'$ $\tilde{f}_{px}'$, and $\tilde{f}_n'$ for modes $n = 1$, 2, 4, and 10. For each of the mode constructions the $\phi_l(n\omega_s') = 2\pi$ constraints correspond to $\tilde{f}_n'$ lying in the $+j\omega$-axis direction, or to $\phi_{\mathrm{RF}}(n\omega_s') = 3\pi/2$, thereby satisfying the $\phi_l(n\omega_s') = 2\pi$ constraint for self-excited x-axis or cathode-directed moving striations.

In the s-wave region of the current-pressure plane $\tau_i \approx \tau_a \approx \tau$, so that the phase lags $\phi_{ei}(n\omega_s')$ and $\phi_{ea}(n\omega_s')$ are approximately equal and are denoted by $\phi(n\omega_s')$ in Table 2, which gives the values of $\phi_n(n\omega_s')$ and the gain reduction factor $\cos\phi_n(n\omega_s')$ for $n = 1$ through 12.

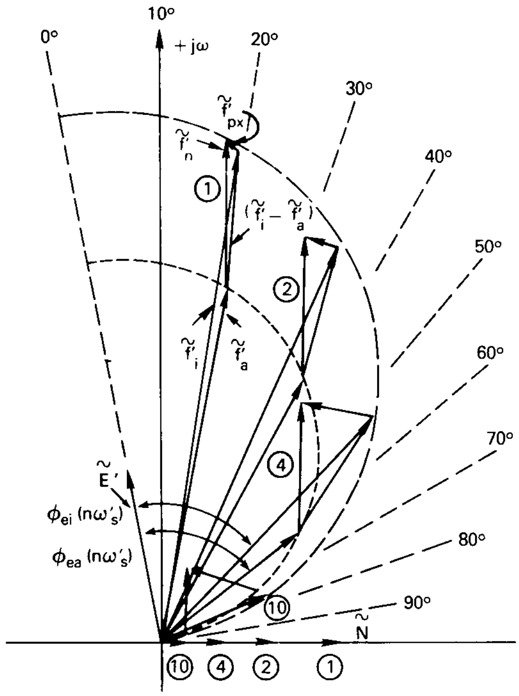

Fig. 35 — Composite phasor construc-
tion for n = 1, 2, 4, and 10

Table 2 — Gain and Phase Lags for the Higher Order Modes

n	$(n\omega_s'\tau)$	$\phi_{ie}(n\omega_s') = \tan^{-1}(n\omega_s'\tau)$	$\cos\phi_n(n\omega_s')$
1	0.4	20°	0.9
2	0.7	36°	0.8
3	1.1	47°	0.7
4	1.4	55°	0.6
5	1.8	61°	0.5
6	2.2	65°	0.4
7	2.5	68°	0.4
8	2.9	71°	0.3
9	3.2	73°	0.3
10	3.6	74°	0.3
11	4.0	75°	0.2
12	4.3	76°	0.2
13	4.7	77°	0.2
14	5.0	78°	0.2

As shown in Fig. 35, $\phi_{RF}(\omega_s') = 3\pi/2$ for the fundamental occurs for $\phi_1(\omega_s') = 20°$. This determines the fundamental wavenumber $k_s = \omega_s/u$ via the relation $\phi_1(\omega_s') = \tan^{-1}(\omega_s'\tau) = 20°$, so that $\omega_s'\tau = 0.4$, and $k_s = 0.4/\tau u$. According to Fig. 35, $n = 2$ corresponds to $\phi_2(2\omega_s') = 36°$, $n = 4$ corresponds to $\phi_4(4\omega_s') = 55°$ and $n = 10$ corresponds to $\phi_{10}(10\omega_s') = 74°$. For $n = 1$ the relation $|\tilde{f}_{px}'| \propto \lambda_s^{-1}$ determines the fundamental value of λ_s as that value that results in $\tilde{f}_n = (\tilde{f}_i' - \tilde{f}_a') + \tilde{f}_{px}'$ being exactly in phase with the $+j\omega$ axis. As n increases, $(\tilde{f}_i - \tilde{f}_a)$ lags the $+j\omega$ axis by a progressively larger angle. Since λ_s decreases for the higher order modes, $|\tilde{f}_{px}'| \propto \lambda_s^{-1}$ increases and leads the $+j\omega$ axis by an increasing amount, so that $\tilde{f}_n' = (\tilde{f}_i' - \tilde{f}_a') + \tilde{f}_{px}'$ remains exactly in phase with the $+j\omega$ axis, thereby maintaining the $\phi_{RF}(n\omega_s') = 3\pi/2$ condition and thus the $\phi_l(n\omega_s') = 2\pi$ condition for $-x$-directed striations.

Heretofore it was simply asserted that the $\phi_l(n\omega_s') = 2\pi$ condition was achieved for integral values of n. It appears from the higher order mode geometry shown in Fig. 35, however, that the $\phi_{RF}(n\omega_s') = 3\pi/2$ condition might be achieved for nonintegral values of n as well. The following argument shows why the higher order spatial modes lock in at precisely integral multiples of n.

For $n = 1$ the $\phi_l(n\omega_s') = 2\pi$ condition is required to exist for arbitrarily small values of $m_n = |\tilde{N}|$, so that the fundamental spatial variation at k_s can build up from the noise. As was discussed between Eqs. 42 and 43 and between Eqs. 49 and 50, this uniquely determines the values of k_s, m_n, and the sign of ω_s. The magnitude $|\omega_s|$ is unrestrained, so that the $G_l(\omega_s', m_n, |\omega_s|) = 1$ condition can always be achieved. In the case of the higher order spatial modes, however, $|\omega_{s,n}|$ is constrained via $|\omega_{s,n}| = n|\omega_s|$. Consequently the $\phi_l(n\omega_s', m_n) = 2\pi$ condition for $n > 1$ must be achieved for those values of $n\omega_s'$ and m_n such that the $G_l(n\omega_s', m_n, |\omega_{s,n}|) = 1$ condition also holds. The net result is that in general there exists large-signal values of m_n that simultaneously satisfy the $\phi_l = 2\pi$, $G_l = 1$ condition, but these spatial variations cannot spontaneously build up from the noise. The following argument shows how pseudo harmonics at integral multiples of ω_s' occur as a consequence of periodic velocity modulation imparted to the drifting electron gas. These higher order harmonic variations in $\tilde{f}_n'$ are in turn integrated by the column to produce higher order spatial variations in $\tilde{N}$ whose magnitudes are large enough to satisfy the $\phi_l(n\omega_s', m_n) = 2\pi$ condition. The amplitudes of the pseudo harmonics are increased via regeneration, and the resulting large-amplitude harmonic structure is self-sustained via the $\phi_l(n\omega_s', m_n) = 2\pi$, $G_l(n\omega_s', m_n, |\omega_{s,n}|) = 1$ condition.

Since the instantaneous electron drift velocity u depends on E, and since E has a spatial periodic structure, there is a modulation of u about a quiescent value u_0 which corresponds to a frequency modulation of the local oscillator in the electrical equivalent circuit in Fig. 21 about a quiescent value $\omega_{l,0} = u_0 k_s$. The modulation frequency ω_m is the temporal frequency of E as perceived in the reference frame of the drifting electron gas. Hence $\omega_m = \omega_s'$ and the frequency modulation index $\Delta\omega/\omega_m$ is the perceived variation of E about its quiescent value E_0, or the modulation index of $\tilde{E}$, so that $\Delta\omega_s/\omega_m = m_e$. Since $G_{ne} \propto n$, $m_{e,n} \propto nm_{n,n}$, where as before n denotes the mode number and $m_{e,n}$, $m_{n,n}$, etc. denote the modulation indices of the various plasma parameters for the nth mode. The spectrum of a frequency modulated signal at ω_0 exhibits sidebands at frequencies $\omega_0 \pm p\omega_m$, where p is an integer and the sideband amplitudes are given by the Bessel function $J_p(\Delta\omega/\omega_m)$. In the case at hand, $\omega_0 = \omega_s'$, and $\omega_m = \omega_s'$, and $\Delta\omega/\omega_m = m_{n,1}$, so that the frequency spectrum in the RF link due to the fundamental spatial variation in ion density along the column at k_s consists of the fundamental responses ω_s'

and sideband response with amplitude $J_p(m_{n,1})$ at frequencies $\omega_s' \pm p\omega_s'$, where p is an integer and $m_{n,1}$ is the modulation index of the fundamental spatial variation at k_s. The effect of the velocity modulation of the drifting electron gas can be incorporated in the equivalent electrical circuit in Fig. 21 by providing a frequency-modulation input to the local oscillator that is controlled by u such that $\omega_l = k_s u_0(1 + \tilde{u})$.

Unlike conventional harmonic responses due to nonlinearities, these FM sidebands or pseudo-harmonic responses arise even if the RF signal-processing link is perfectly linear. For example, a fundamental spatial variation at k_s with amplitude $m_{n,1} = 0.2$ introduces a second-harmonic temporal response in the RF link at $2\omega_s'$ whose amplitude is given by $m_{n,2} = J_1(0.2)m_{n,1} = 0.1m_{n,1}$. This signal at $2\omega_s'$ is identical to the one that would be perceived by the electron gas drifting with a constant velocity if a second-order spatial harmonic variation in ion density at $2k_s$ with relative amplitude $m_{n,2} = 0.1\ m_{n,1}$ actually existed along the column. The important point is that even for a linear RF link the signal at $2\omega_s'$ due to the FM effect produces an output $f_{n,2}$ at $2\omega_s'$ which is in turn integrated by the column to produce a second-harmonic spatial variation in ion density at $2k_s$. If $\phi_{\mathrm{RF}}(2\omega_s') \approx 3\pi/2$, this second-order spatial mode can build up via regeneration. This larger second-order mode in turn generates FM sidebands at $2\omega_s' \pm p\omega_s'$, so that it can trigger the regenerative buildup of a third-order spatial mode at $3\omega_s'$, etc.

In the case of the fundamental mode, m_n builds up from an arbitrarily small value via regeneration until the large-signal decreases in $|\tilde{f}_i'|$ and $|\tilde{f}_a'|$ due to the decreasing functions $G_{ei,0}(m_e)$ and $G_{ea,0}(m_e)$ no longer track, thereby tending to spoil the $\phi_l(\omega_s') = 2\pi$ condition for regeneration. As mentioned earlier, for larger values of m_n there exist other values of ω_s' such that $\phi_l(\omega_s', m_n) = 2\pi$, but spatial variations cannot build up spontaneously from arbitrarily small levels at these values of ω_s'. Since $G_{ne} \propto n$, $|\tilde{E}'|$ is pushed into the large-signal regime for all of the higher order modes as well. Since the buildup of the higher order modes is seeded via the FM effect and by any nonlinearities that exist, $m_{n,n}$ for a higher order mode need not build up from arbitrarily small values, with the consequence that the value of $m_{n,n}$ can adjust so as to help achieve the $\phi_{\mathrm{RF}}(n\omega_s', m_{n,n})$ condition for the various higher order modes. The stable $G_l = 1$, $\phi_l = 2\pi$ large-signal operating points for the higher order modes therefore depend on both the value of $m_{n,n}$ and the parameters that characterize the RF link, which explains why observed harmonic spectra exhibit marked changes for slight changes in discharge operating point.

Two additional features of the striation spectrum can be explained by bounding the length of the positive column to L. Instead of a pure sinusoid, the drifting electron gas now sees a pulsed signal at ω_s' as it transverses the column of length L. The pulse duration is $\tau = L/u_0$, where u_0 is the quiescent or average electron-gas drift velocity. Independent of the value of u_0, however, the electron gas sees L/λ_s cycles as it transverses the column. Consequently the normalized line width $\Delta f_s/f_s$ of the striation spectrum observed near the anode end of the positive column should be given by $\Delta f_s/f_s = \lambda_s/L$. This agrees with observed values for tubes of different radii. Since $\lambda_s \propto R$, decreasing R for fixed L decreases $\Delta f_s/f_s$, which is in accordance with observed line-width ratios in tubes with smaller radii.

The striation line width Δf_s is given by $\Delta f_s = \lambda_s f_s/L = \mathrm{v}_s/L$. Since all of the higher order spatial modes have the same striation velocity as the fundamental, the preceding picture predicts that $\Delta f_{s,n} = \mathrm{v}_s/L$ is the same for each for the modes. It is clear from Fig. 34 and the other spectral data in Appendix D that $\Delta f_{s,n}$ is the same for each of the higher order modes. In addition, since $\lambda_s \propto R$ and $f_s \propto 1/R, v_s$ is independent of R and depends only on the variety of the striation. This is also supported by the data in Appendix D. The value of Δf_s for the *s*-variety striation, for example, is the same for both the $R = 1$ cm and $R = 1/2$ cm tubes, which were of the same length.

One final peculiarity of striation spectra has been observed in discharge tubes whose radii are several millimeters or less. Figure 36 depicts the striation spectra reported in Ref. 33 for a He-Ne laser. For discharge currents of 20 mA and 40 mA the striation spectrum is as previously discussed: singular spectral responses at f_s and several higher order harmonics with equal line widths Δf_s. For other discharge currents, however, each of these singular responses exhibit closely spaced sidebands, as if the basic striation waveform was being frequency modulated at a frequency f_m that is a small fraction of f_s, the fundamental striation frequency. This anomalous FM effect is observed only in tubes with small radii. In the case at hand, $R = 2$ mm, $L = 50$ cm, $f_s = 400$ kHz, and $f_m = 40$ kHz. As shown in the 30-mA and 60-mA displays, when this FM effect is present, the magnitude depends on the exact discharge operating point.

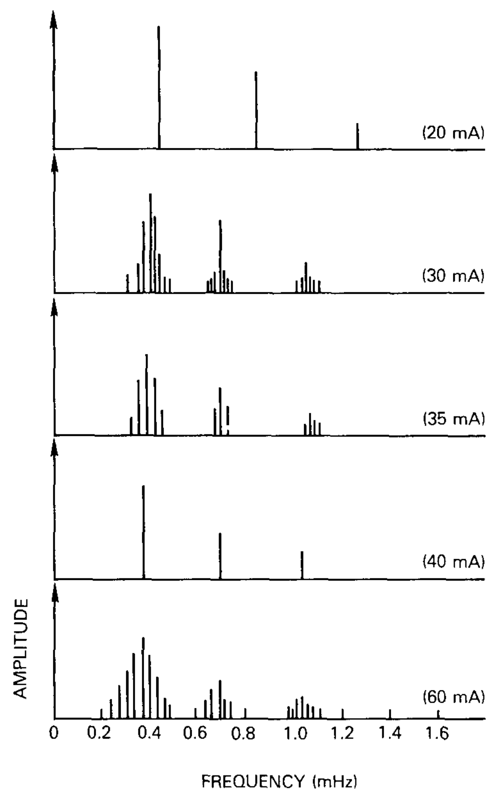

Fig. 36 — Oscillation spectrum of the discharge current in a He-Ne laser as reported in Ref. 33

Although the corresponding physical implications in the discharge are not entirely clear, the existence of such a low-frequency FM effect whose presence or absence depends on the precise discharge operating point can be explained in the following way. As previously discussed, the electron gas perceives L/λ_s cycles as it traverses the column in $\tau = L/u_0$ seconds. This waveform serves as a sample function for the local oscillator in the equivalent-electrical-circuit model of the positive column. From this viewpoint the local-oscillator output consists of a continuous succession of these basic sample waveforms of duration τ. The corresponding physical picture in the discharge is that as the electron gas reaches the anode end of the column, the phase of the modulations imparted to its electron energy distribution is transferred to the energy distribution of the electron gas at the cathode end of the column. Such a phase coherency from one traversal of the column to the next results because the spatial variation in ion density along the column is quasi-stationary relative to a traversal of the column by the electron gas.

If the condition $L/\lambda_s = q$, where q is an integer, is not satisfied, the local-oscillator output waveform contains phase discontinuities that occur every τ seconds. This phase modulation of the local oscillator causes FM sidebands about f_s and each of the higher order harmonics nf_s whose spacing is equal to $f_m = 1/\tau$ and whose amplitudes depend on the magnitude of the phase discontinuity. This basic picture is in accordance with the observed FM effect previously discussed in that although λ_s is essentially independent of L, its value does exhibit dependence on the discharge operating point, and only a several-percent change in λ_s suffices to cause L/λ_s to change from one integral value to another, thereby causing the presence or absence of phase discontinuities. This picture predicts an FM sideband spacing of $f_m = \tau^{-1} = u_0/L$. In the case at hand $L = 50$ cm and, from Ref. 34, $u_0 = 2 \times 10^6$ cm/s (the electron drift velocity for electrons in helium). Thus, this picture predicts $f_m = 2 \times 10^6/50 = 40$ kHz, in exact agreement with observation.

The reason this FM effect exists only for small-radius tubes can also be explained by the equivalent-electrical-circuit model of the column. The frequency response of the IF link is that of a simple low-pass filter with a cutoff frequency of $f_c = f_{a,0}/2\pi$, where $f_{a,0}$ is the quiescent value of the ambipolar decay frequency per charged particle. Only those disturbances in ion density with temporal variations less than approximately f_c can occur, since higher frequency variations are attenuated by the low-pass nature of the IF link. Since $f_{a,0} \propto 1/R$, $f_c \propto 1/R$ and, as R decreases, progressively higher frequency variations in ion density can exist in the column. In the case at hand $f_m = u_0/L = 40$ kHz and, for the He-Ne discharge at 1.5 torr, $Rf_{a,0} \approx 600$ kHz-cm, so that $Rf_c \approx 100$ kHz-cm. Thus, for $R \approx 0.2$ cm, $f_c \approx 400$ kHz, so that $f_m \lesssim f_c$ and the anomalous FM sidebands are observed.

In a pure neon discharge $Rf_{a,0} \approx 70$ kHz-cm for $pR \approx 1$ torr-cm, so that $Rf_c \approx 10$ kHz-cm. Since $u_0 \approx 4 \times 10^6$ cm/s at $pR = 1$ torr-cm, then for the $L = 60$ cm tubes used in the experiments described in Appendix C $f_m = u_0/L = 50$ kHz. Since $f_c = 10$ kHz and 20 kHz respectively for the 1-cm-radius and 1/2-cm-radius tubes, $f_m > f_c$, and the anomalous FM effect is not predicted for these tubes.

The implication of the preceding viewpoint with regard to the positive column is that a transient is generated in the reference frame of an observer who is moving with the electron gas as it drifts along the positive column, because his frame is virtually instantaneously cycled from the anode end to the cathode end of the positive column via the external circuit. As the electron gas drifts along the column, the particular electrons in the gas do not retain their individual identities, since electrons are diffusing to the tube wall, being created by ionization, etc. A particular distribution of electron energies on the other hand does retain an identity as the gas drifts along the column. Although the FM sideband spacing is given by the reciprocal cathode-to-anode transient time of the electron gas in support of the above argument, it might be that the higher value of f_c in small-radius tubes allows other anomalous high-frequency oscillatory discharge disturbances such as relaxation oscillations or anode spot oscillations to occur, thereby accounting for the observed spectra.

Appendix A

PHASOR NOTATION AND PHASOR ARITHMETIC, CALCULUS, AND TRANSFER FUNCTIONS

A one-dimensional sinusoidal traveling-wave variation of a quantity $A(x, t)$ about a quiescent value A_0 can be represented by

$$A(x, t) = A_0 \left[1 + \frac{\delta A}{A_0} \cos(kx - \omega t + \phi_a)\right], \tag{A1}$$

where $\delta A/A_0$ is the percentage modulation of $A(x, t)$ about the quiescent value A_0, $k = 2\pi/\lambda$ is the wavenumber, $\omega = 2\pi f$ is the angular frequency, and ϕ_a is the phase. Constraining the wavenumber to positive values ($k \geqslant 0$) results in $\omega > 0$ representing a $+x$-directed traveling wave for which $v = \omega/k > 0$ and positive ϕ_a is a phase lag and in $\omega < 0$ representing a $-x$-directed traveling wave for which $v = \omega/k < 0$ and positive ϕ_a is a phase lead.

With use of a phasor notation, Eq. A1 can be written as

$$A(x, t) = A_0(1 + \tilde{A}), \tag{A2}$$

where a comparison of Eqs. A1 and A2 defines the phasor $\tilde{A}$.

Figure A1 depicts the phasor representation of $A(x, t)$ as the projection of the rotating phasor $\tilde{A}$ on the positive real axis with the origin located at the quiescent value A_o. As indicated in the figure, an increase in x corresponds to a clockwise rotation of the coordinate system with the phasor stationary, and an increase in t corresponds to phasor rotation in a fixed coordinate system. For a $+x$-directed traveling wave $\tilde{A}$ rotates clockwise at the angular rate ω corresponding to $\omega > 0$ and thus to $v_s > 0$, and for a $-x$-directed traveling wave $\tilde{A}$ rotates counterclockwise at the angular rate ω corresponding to $\omega < 0$ and thus $v_s < 0$.

The phase angle ϕ_a is reckoned relative to the positive real axis as shown in the figure and represents a phase lag for $\omega > 0$ (clockwise phasor rotation) and a phase lead for $\omega < 0$ (counterclockwise phasor rotation). The phasor magnitude is given by $|\tilde{A}| = \delta A/A_0 = m_a$, where m_a is the modulation index or percentage modulation of $A(x, t)$ about its quiescent value.

The basic arithmetic operations for phasors (addition, subtraction, multiplication, and division) and the differentiation of phasors are summarized in Table A1. Addition and subtraction of phasors is straightforward; the resultant quiescent value is just the sum or difference of the individual quiescent values, and the net sinusoidal variation about the resultant quiescent value is given by a rotating phasor that is the vector sum or difference of the individual rotating phasors.

The expressions for phasor multiplication and division result from neglecting the second-order crossproduct terms like $\tilde{A} \cdot \tilde{B}$ and using the approximation $(1 + \tilde{B})^{-1} \approx (1 - \tilde{B})$, which holds for $m_b = |\tilde{B}| << 1$.

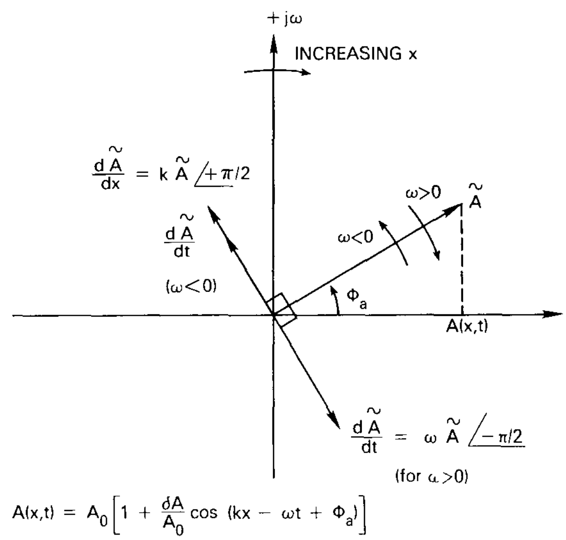

Fig. A1 — Phasor representation of $A(x, t)$ as the projection of the rotating phasor $\tilde{A}$ on the positive real axis

The modulation indices of the phasors associated with the plasma variables encountered in moving striations are typically 0.1 to 0.3. In any event, since the angular frequencies of the crossproduct terms are 2ω, they do not contribute to the fundamental frequency variation of the resultant even for modulation indices approaching unity.

One result of phasor differentiation is $d\tilde{A}/dx = k\tilde{A}\ \underline{|\pi/2}$, which leads $\tilde{A}$ by $\pi/2$ if $\omega < 0$ but lags $\tilde{A}$ by $\pi/2$ if $\omega > 0$. On the other hand $d\tilde{A}/dt = |\omega|\tilde{A}\ \underline{|\mp\pi/2}$ leads $\tilde{A}$ for ω both positive and negative, and this is reflected in the convention that the upper sign holds when $\omega > 0$ and the lower sign holds when $\omega > 0$. Thus, as shown in Fig. A1, the position of the phasor $d\tilde{A}/dx$ relative to $\tilde{A}$ is the same for ω positive or negative, whereas the position of the phasor $d\tilde{A}/dt$ shifts by π as ω changes sign from positive to negative.

An all-pass linear gain (a constant) relating two quantities does not affect their corresponding phasor magnitudes (their modulation indices), since both the quiescent or dc term and the temporal or ac term are changed by equal amounts. Thus the phasor transfer function corresponding to an all-pass linear network is unity. Nonlinear networks and band-limited linear networks, however, change the dc and ac terms disproportionately, resulting in a change in the modulation index or phasor magnitude. A simple low-pass network with a corner frequency $\omega_c = \tau_r^{-1}$, where τ_r is the effective RC time constant (relaxation time constant) of the low-pass network, passes the dc term unattenuated while attenuating the ac term by the factor $\cos\phi(\omega)$, where $\phi(\omega) = \tan^{-1}(\omega\tau_r)$. Thus a prototype phasor transfer function corresponding to a linear low-pass network $H_{llp}(\omega)$ is

$$H_{llp}(\omega) = G_{llp}(\omega)\underline{/\phi_{llp}(\omega)}, \tag{A3}$$

where

$$G_{llp}(\omega) = \cos\phi_{llp}(\omega) \tag{A4}$$

and

$$\phi_{llp}(\omega) = \tan^{-1}(\omega \tau_r). \tag{A5}$$

If a quantity $A(x, t)$ is determined by a quantity $B(x, t)$ via a nonlinear process, say a square-law device, so that $A(x, t) = [B(x, t)]^2$, the relation between the corresponding phasors is

$$A(x, t) = A_0(1 + \tilde{A}) = [B_0(1 + \tilde{B})]^2$$

or

$$A_0(1 + \tilde{A}) = B_0^2(1 + 2\tilde{B} + \tilde{B} \cdot \tilde{B}). \tag{A6}$$

Since $\tilde{B}$ is of the form $\tilde{B} = m_b \cos \omega t$, $\tilde{B} \cdot \tilde{B}$ is given by

$$\tilde{B} \cdot \tilde{B} = \frac{1}{2} m_b^2(1 + \cos 2\omega t). \tag{A7}$$

Since the $\tilde{B} \cdot \tilde{B}$ term in Eq. A6 is at 2ω, it does not contribute to the fundamental frequency variation of $A(x, t)$. However, it does produce a dc level shift of $(1/2)m_b^2$. When this shift in quiescent level is taken into account, Eq. A6 becomes

$$A_0(1 + \tilde{A}) = B_0^2 \left[\left(1 + \frac{1}{2} m_b^2\right) + 2\tilde{B}\right]$$

or

$$A_0(1 + \tilde{A}) = B_0^2 \left(1 + \frac{1}{2} m_b^2\right) \left[1 + \left(\frac{2}{1 + \frac{1}{2} m_b^2}\right)\tilde{B}\right]. \tag{A8}$$

Thus, according to Eq. A8, the phasor transfer function H_{sld} corresponding to an ideal square-law device (one that exhibits an all-pass frequency response and whose square law holds for arbitrarily large modulation indices) is

$$H_{sld} = \frac{2}{1 + \frac{1}{2} m^2}, \tag{A9}$$

where m is the modulation index of the input phasor. Equation A9 shows that the phasor gain of an ideal nonlinear device is a decreasing function of the input modulation index. In the case at hand, where the nonlinearities are a consequence of the modulation characteristics of the shape of the electron energy distribution function, a certain degree of nonlinearity holds only for modulation indices below a given value. For indices that exceed this value the degree of nonlinearity is reduced. Thus, as m increases, the phasor gain corresponding to the nonlinear modulation characteristics of f_g decreases, as the result of increases in the dc level and reductions in the degree of nonlinearity.

A general prototype phasor transfer function that characterizes the modulation of a plasma parameter that depends on f_g can be written as

$$H_{ej}(\omega_s', m_e) = G_{ej}(\omega_s', m_e)\underline{/\phi_{ej}(\omega_s')}, \tag{A10}$$

where

$$\phi_{ej}(\omega_s') = \tan^{-1}(\omega_s'\tau_{ej}) \tag{A11}$$

and

$$G_{ej}(\omega_s', m_e) = G_{ej,0}(m_e) \cos \phi_{ej}(\omega_s'). \tag{A12}$$

The subscript ej denotes that the modulation of the jth plasma parameter depends on the modulation of the longitudinal electric field E via its modulation of the shape of $f_{\mathscr{E}}$ in the particular energy range $\Delta\mathscr{E}_j$ on which the jth plasma parameter depends. The arguement ω_s' is the striation frequency in the reference frame of the drifting electron gas, and τ_{ej} is the effective RC or relaxation time constant for modulations in the shape of $f_{\mathscr{E}}$ in the energy interval $\Delta\mathscr{E}_j$. The argument m_e is the modulation index of E, and $G_{ej,0}(m_e)$ is a decreasing function of m_e similar to Eq. A9 that characterizes the nature of the nonlinearity associated with the modulation of the shape of $f_{\mathscr{E}}$ in the energy interval $\Delta\mathscr{E}_j$.

Table A1 — Arithmetic and Calculus of Phasors

- Addition/Subtraction

$$[A(x,t) \pm B(x,t)] = [(A_0 \pm B_0) + (A_0\tilde{A} \pm B_0\tilde{B})]$$

- Multiplication

$$[A(x,t) \cdot B(x,t)] \approx (A_0B_0)(1 + \tilde{A} + \tilde{B})$$

- Division

$$[A(x,t)/B(x,t)] \approx (A_0/B_0)(1 + \tilde{A} - \tilde{B})$$

- Differentiation

$$\begin{aligned} dA(x,t)/dx &= A_0 d\tilde{A}/dx = A_0 k\tilde{A}\,\underline{|\pi/2} \\ dA(x,t)/dt &= A_0 d\tilde{A}/dt = A_0|\omega|\tilde{A}\,\underline{|-\pi/2}, \quad \omega > 0 \\ &= A_0|\omega|\tilde{A}\,\underline{|\pi/2}, \quad \omega < 0 \end{aligned}$$

Appendix B
STRIATIONS IN RF EXCITED POSITIVE COLUMNS

Standing striations occur in the positive column of not only a discharge energized by a dc current source but also a discharge energized by an RF current source. To efficiently couple energy to the electron gas, the frequency of the RF source f_0 is significantly lower than f_c, the average electron-neutral collision frequency. An electron drift velocity is established within several times the electron-neutral collision period $f_c^{-1} \approx 1$ ns in a typical glow plasma. Since $f_0 << f_c$, an electron drift velocity is established during a half cycle of the RF current source, so that during each half cycle the energy transfer mechanisms between the instantaneous RF field and the electron gas are essentially the same as those that were previously discussed for the dc column: elastic and inelastic collisions. For an RF source, however, the distance $u_0/2f_c$ along the column that the electron gas drifts during a half cycle is only a fraction of a centimeter.

The electron-energy time histories in Figs. 11 and 12 represent also the situation in an RF discharge, but unlike the dc case, where a net increase in electron energy corresponds to the electron's net displacement along the column, electrons in the RF positive column cycle between the low-energy and high-energy tails of f_g while remaining in the same unit length of column. Since $u_0 = 0$ for an RF discharge, the electron gas does not see a time-varying field at $\omega_s' = u_0 k_s$ by virtue of its drift along a spatially varying field; rather it sees the appied RF field at frequency f_0. The various relaxation frequencies associated with the modulation of f_g are less than f_0. Consequently the magnitude of the temporal modulation of f_g due to the applied RF field is negligible; that is, f_g does not respond to the instantaneous RF field but rather to its rms value. In an RF discharge the shape or form of f_g depends on E_{rms}/p in essentially the same manner as the dependence of the form of f_g on E_0/p in a quiescent homogeneous dc discharge.

As previously mentioned, since $f_0 << f_c$, the drift velocity of the electron gas follows the instantaneous applied RF field, so that the instantaneous conduction current along the positive column J_c is proportional to the instantaneous RF field. Since $f_0 << f_p$, where f_p is the electron plasma frequency, $\nabla_x \cdot J_c = 0$, and the argument leading to Eq. 6 holds for the RF case as well. $\tilde{E}_c$ now refers to the spatial variation along the column of the rms value of the conduction electric field that occurs when standing striations are present. Figure B1 shows the required spatial relationships among the rms values of the various plasma parameters for the generation of self-sustained standing striations along the RF column.

Substituting $dN/dt = 0$ into the equation for the conservation of charged particles in a unit length of the column (Eq. 16) gives

$$P(x) - L(x) = \nabla_x \cdot J_p(x), \tag{B1}$$

where $P = f_i N$, $L = f_a N$, and J_p is the longitudinal ambipolar diffusion current of ion-electron pairs away from regions of a relative maximum in $p_n = eK_f \mathscr{E}_m N$, the partical pressure of the electron gas. J_p is given by $J_p = \mu_p NE_a$, and, using Eq. 8 for E_a, the longitudinal ambipolar electric field due to pressure gradients in the electron gas, in this expression for J_p yields

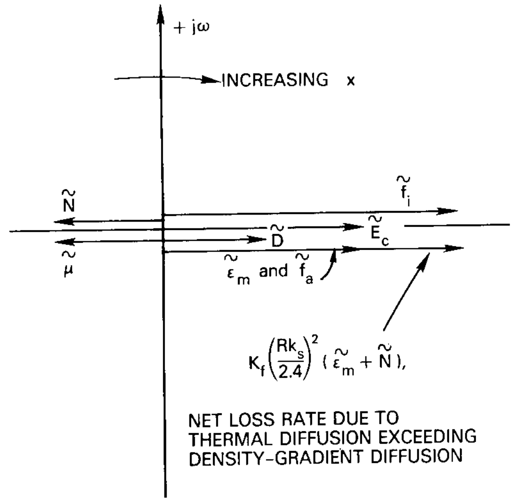

Fig. B1 — Phasor diagram illustrating the spatial variations of the plasma parameters in a striated RF positive column

$$J_p(x) = K_f\, \mu_p\, \nabla_x\, [\mathscr{E}_m(x)\; N(x)]. \tag{B2}$$

Finally, substituting Eq. B2 into Eq. B1, writing the result in phasor notation, and equating like terms yields $P_0 = L_0$, so that $f_{i,0}N_0 = f_{a,0}N_0$, and yields the phasor transfer-function relation

$$\tilde{f}_i - \tilde{f}_a = \left[K_f\left(\frac{Rk_s}{2.4}\right)^2 \lfloor\!\underline{\pi}\right] (\tilde{\mathscr{E}}_m + \tilde{N}). \tag{B3}$$

If a certain steady-state spatial variation $\tilde{N}$ in charged-particle density with wavelength $\lambda_s = 2\pi/k_s$ is to exist along the RF column, Eq. B3 must be satisfied. The left-hand side of Eq. B3 represents the net effect on the charged-particle balance along the column due to spatial variations in the ionization rate and the radial ambipolar recombination rate. The right-hand side represents the net effect on the charged-particle balance due to diffusion caused by temperature and density gradients along the column.

Since $f_{\mathscr{E}}$ responds only to the rms value of applied field, the electron gas in the unit length at position x along a striated RF column sees a constant value of E_c/p, where the rms value E_c is like an effective dc value. Thus, as shown in the phasor diagram in Fig. B1, the spatial modulations of the various plasma parameters that depend on $f_{\mathscr{E}}$ are either exactly in or out of phase with $\tilde{E}_c$, since their dc dependence on $f_{\mathscr{E}}$ is either one of proportionality or inverse proportionality.

In the steady-state situation depicted in Fig. B1 , $\tilde{N}$ and $\tilde{\mu}$ are out of phase with $\tilde{E}_c$, and $|\tilde{N}| \approx |\tilde{\mu}| \approx |\tilde{E}_c|/2$. This relationship is dictated by the requirement that $\tilde{E}_c = (1\, \lfloor\!\underline{\pi})(\tilde{N} + \tilde{\mu})$, $\tilde{D}$ is in phase with $\tilde{E}_c$, and $|\tilde{D}| = |\tilde{E}_c|/2$, so that $\tilde{f}_a = \tilde{D} - \tilde{\mu}$ is in phase with $\tilde{E}_c$ and $|\tilde{f}_a| \approx |\tilde{E}_c|$. Since $\mathscr{E}_m \propto E_c/p$, $\tilde{\mathscr{E}}_m$ is in phase with $\tilde{E}_c$ and $|\tilde{\mathscr{E}}_m| \approx |\tilde{E}_c|$. Also, $\tilde{f}_i$

is in phase with $\tilde{E}_c$ and $|\tilde{f}_i| \approx 3/2|\tilde{E}_c|$, reflecting the fact that $\tilde{f}_i$ is a more sensitive function of E_c/p than is $\mathscr{E}_m$. Thus $\tilde{f}_i - \tilde{f}_a$ is in phase with $\tilde{E}_c$ and $|\tilde{f}_i - \tilde{f}_a| \approx |\tilde{E}_c|/2$.

The left-hand side of the charged-particle balance equation, Eq. B3, therefore lies along the positive real axes and has a magnitude $|\tilde{E}_c|/2$. Since $\tilde{\mathscr{E}}_m$ and $\tilde{N}$ are out of phase and $|\tilde{\mathscr{E}}_m| \approx 2|\tilde{N}| = |\tilde{E}_c|$, the right-hand side of Eq. B3 also lies along the positive real axes and has a magnitude $K_f(Rk_s/2.4)^2\,|\tilde{E}_c|/2$. Equation B3 is satisfied therefore for a striation wavelength given by $\lambda_s/R = 2.6\,K_f^{1/2}$. Using $K_f \approx 2/3$, as for a Maxwellian distribution, gives $\lambda_s/R \approx 2$, which agrees with the measurements in an RF discharge reported in Ref. 35 .

Solving Eq. B3 for λ_s/R gives

$$\lambda_s/R = 2.6K_f^{1/2}\left(\frac{|\tilde{\mathscr{E}}_m - \tilde{N}|}{|\tilde{f}_i - \tilde{f}_a|}\right)^{1/2} \qquad \text{(B4)}$$

which shows how the exact value of λ_s/R depends on the precise magnitude relationships between the phasors $\tilde{\mathscr{E}}_m$, $\tilde{N}$, $\tilde{f}_i$, and $\tilde{f}_a$.

The ionization rate exceeds the recombination rate in regions of higher E_c, so that the denominator in Eq. B4 is equal to the net charged-particle production rate in regions of higher E_c. The numerator of Eq. B4 is due to the difference between the thermal diffusion of charged particles away from regions of higher electron temperature and their diffusion into regions of relatively lower density. As shown in Fig. B1, the thermal diffusion exceeds the density-gradient diffusion by an amount that depends on λ_s/R. The value of λ_s/R therefore is determined by the condition that the net loss rate due to diffusion is exactly compensated by the net production rate due to ionization.

That the RF positive column has inherent instabilities which lead to the spontaneous generation of the striated column represented by Fig. B1 can be seen from the following argument. An increase in E_c at some localized position along an initially homogeneous RF column leads to increases in $\mathscr{E}_m$, f_a, and f_i after a time delay of the order of τ_r, where τ_r is the relaxation time constant of $f_{\mathscr{E}}$. Changes in N follow the ambipolar decay time constant τ_a, and since $\tau_r << \tau_a$, the initial change in N is negligible. Since the percentage increases in $\mathscr{E}_m$ and f_a are approximately equal to that of E_c, whereas the percentage increase in f_i is only slightly larger than that of E_c, the net increase in charged-particle loss rate due to thermal diffusion plus the increased recombination rate exceeds the increase in production rate due to ionization, so that there is a net loss of charged particles from the position of increased E_c. After a time delay of the order of τ_a, N decreases at the position of maximum E_c and, due to the thermal diffusion, N increases in the regions adjacent to the position of increased E_c. Since E_c is inversely proportional to N, this causes a decrease in E_c in these adjacent regions, which in turn causes a decrease in $\mathscr{E}_m$ and a corresponding increase in μ. Since E_c is also inversely proportional to μ, a regeneration develops in that an initial increase in E_c leads to a decrease in E_c in adjacent regions, which in turn increases μ, leading to an additional decrease in E_c in the adjacent regions. Thus, $\mathscr{E}_m$ is further decreased in these regions, resulting in an inflow of charged particles due to thermal diffusion from the outer set of adjacent regions centered on the original disturbance. The thermal diffusion from these outer adjacent regions causes a reduction of N in these regions, thereby increasing E_c and $\mathscr{E}_m$, which in turn further intensifies the thermal diffusion from these regions, leading to further reduction in N in these regions. This process continues until the entire RF column is striated, and the percentage variation of the plasma parameters (the corresponding phasor magnitude) increases until the steady-state condition depicted in Fig. B1 is obtained.

In the dc column the drifting electron gas makes adjustments in f_i and f_a that tend to neutralize any intial spatial disturbances in N. Due to the relaxation time constants τ_r associated with the adjustments in $f_{\mathscr{E}}$, however, these corrections lag the initial disturbances by a delay that depends on the value of $\omega_s' = u_0 k_s$ relative to τ_r^{-1}. There exists a resonant spatial frequency k_s such that the corrections to an initial disturbance at k_s lag by exactly $\pi/2$ or by $3\pi/2$, thereby causing a regenerative buildup of the initial disturbance in the form of moving striations. Thermal diffusion plays a negligible role in the self-excitation process in the dc column, since modulations in $\mathscr{E}_m$ are significant only at high pressure, and even then $\mathscr{E}_m$ only slightly shifts the phase of $\tilde{E}$ relative to $\tilde{N}$. In the RF column, however, thermal diffusion is the destabilizing mechanism resulting in the spatial regenerative buildup of standing striations. In the absence of thermal diffusion an increase in E_c would result in a net increase in charged-particle production rate, resulting in an increase in N, which would cause a decrease in E_c, thereby correcting the initial deviation in E_c.

Appendix C

EXPERIMENTAL TECHNIQUE AND APPARATUS FOR THE MEASUREMENT OF STRIATION PARAMETERS

In the experiments described in this appendix the parameters of the striation phenomena in a neon positive column were measured and displayed in a systematic manner throughout the entire regime of reduced current and pressure in which they occur. The striation parameters f_s, λ_s, and v_s were measured in four neon positive-column glow-discharge tubes with different radii. The measurements were with current as a continuous parameter and pressure a discrete parameter and with pressure as a continuous parameter and current a discrete parameter. In this way, the entire regime of reduced current and pressure $(I/R,\ pR)$ in which striation phenomena occur was comprehensively investigated.

Several state-of-the-art measuring techniques in plasmas were modified for incorporation into an automated facility for measuring striation parameters. This facility could record and display in a compact format all of the pertinent striation parameters, and their variation with the discharge parameters reduced current and pressure, over the entire two-dimensional reduced-current-and pressure region $(I/R,\ pR)$ of interest. A block diagram of the measurements facility is shown in Fig. C1.

Two RCA 7102 photomultiplier tubes (photomultipliers 1 and 2 in Fig. C1) with neutral-density filters were used to detect the modulation in sidelight intensity produced by the moving striations. A 15-mm-diameter lens with a focal length of 15 mm was used in each of the photomultiplier optical imaging systems. The optical imaging geometry was chosen so that the image magnification was 10, and since the active-area diameter of the 7102 photomultiplier tube is 30 mm, a longitudinal spatial resolution along the x axis of the discharge tube's positive column of 3 mm was achieved. This provided a minimum resolution of $\lambda_s/10$ for the smallest diameter positive column investigated. Photomultiplier 1 was maintained in a fixed position near the anode end of the positive column. Photomultiplier 2 was mounted on a motor-driven carriage, and a dual ganged potentiometer supplied analog signals which were proportional to the position of the carriage along the length of the discharge tube's positive column.

The discharge tubes consisted of positive columns constructed from Pyrex medium-wall tubing 60 cm long, a 3-by-15-cm cylindrical titanium cathode, and a nickel pin anode. The same cathode was used for each of the four positive columns of different radii. In the largest diameter discharge tube (R = 0.95 cm) nickel pin plasma probes were inserted at the anode and cathode ends of the positive column to monitor the total potential across the positive column. This potential is a measure of the longitudinal space-charge electric field E_0 averaged over the entire length of the positive column, and its value was recorded as a function of the continuous variables current and pressure as the striation parameters were mapped over the reduced-current-and-pressure plane.

After the complete series of measurements on a positive column of a specific radius was completed, the discharge-tube cathode was abrasively cleaned, the newly constructed tube was

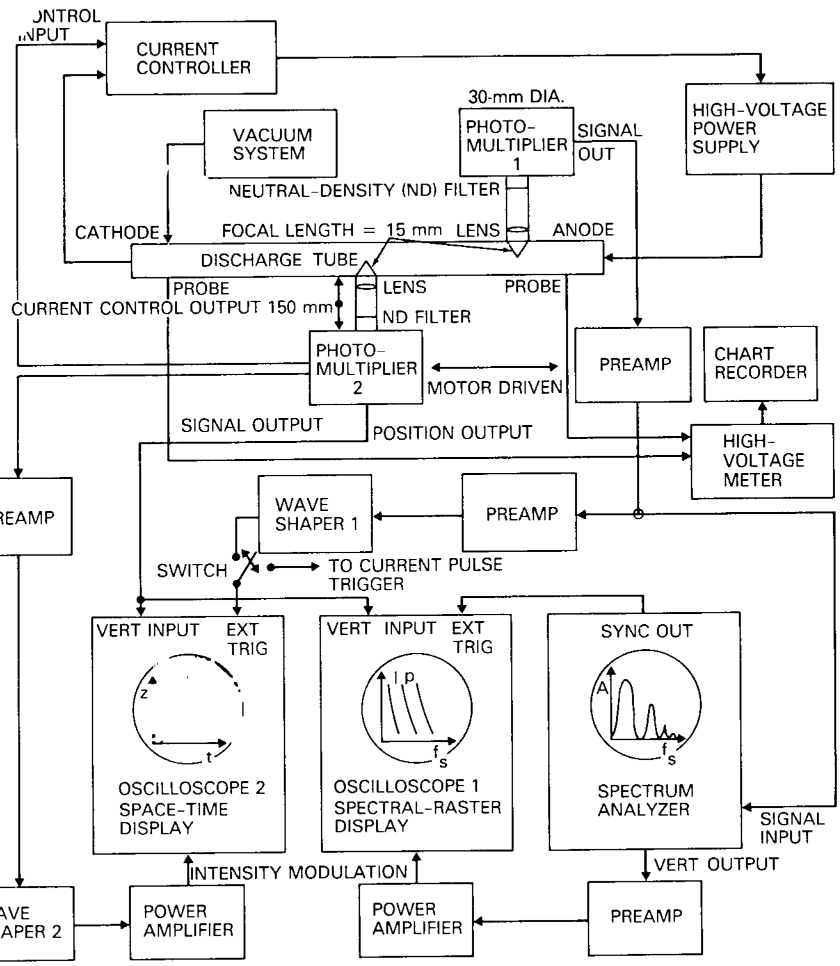

Fig. C1 — Experimental apparatus

operated with an oxygen discharge, and the tube was pumped for at least 24 hours. During each complete series of measurements the discharge tube was permanently connected to the vacuum system, which used a zeolite trap for water vapor. After each 1 to 2 hours of operating time during the measurements on a positive column of a given radius, the zeolite trap was outgassed, and the discharge tube was baked and pumped overnight. For each measurement the discharge-tube pressure before filling was of the order of 10^{-7} torr, so that the impurity concentration was less than several parts per million.

The current controller consisted of a pentode which used negative feedback from a cathode resistor to achieve and effective source impedance $(\mu + 1)R_k$ of several megohms. The magnitude of this current source was controlled by an analog signal applied to the bias circuit of the pentode control grid. The current controller effectively isolated the discharge tube from the external circuit parameters, so that to a high degree of accuracy the discharge current could be considered an independent variable.

Some earlier experiments used an external ballast resistor in series with a high-voltage power supply to excite the discharge tube. However, due to the interaction of the current and voltage of the discharge tube and their effects on the striation parameters being measured, an extremely-high-impedance current source must be used to excite the discharge tube if the true dependence on current and pressure of the striation parameters is to be measured.

Oscilloscope 1 produced a televisionlike display of the spectral content of the discharge tube's positive-column sidelight intensity modulation. This display technique is similar to that reported by H. Lashinsky [36]. In this experiment, however, the raster was generated by an analog vertical sweep voltage which was proportional to the position along the discharge tube of photomultiplier 2. As shown in Fig. C1, the time axis of oscilloscope 1 was synchronized to the sweep rate of the spectrum analyzer. The beam of CRT 1 contains the spectral information in the form of intensity modulation, and while the raster was being formed, it was photographed by an oscilloscope camera operated in the time-exposure mode.

The spontaneously generated moving-striation frequencies and their dependencies on current and pressure were not known a priori. In this instance the spectral-raster display was a good detection technique, since considerable signal-to-noise enhancement results from the optical averaging performed by the phosphorescent coating on the oscilloscope CRT and the photographic film. The scan speed of the motor-driven photomultiplier tube was such that the vertical sweep rate of the oscilloscope was 1 mm/s. The effective resolution of the CRT was 0.1 mm. The sweep rate of the spectrum analyzer was 10 ms/sweep. Thus the intensity information present in each horizontal resolution cell of the CRT was the result of an average over ten samples of the input signal. The time interval between samples was $f \approx 1$ ms, so that for noise whose power spectral densities extend over intervals larger than 1 kHz the samples are essentially independent. Since the striation frequencies being measured exceed 1 kHz, the bandpass noise in their vicinity was decorrelated from one scan of the spectrum analyzer to the next, so that an integration improvement factor of approximately 3 was obtained for the ten sweeps comprising one vertical resolution cell of the CRT. The final optical averaging depends on the ability of the eye to recognize the signal against the gray noise background.

Oscilloscope 2 displays a so-called space-time diagram of the striation phenomena. The space-time display technique used in this experiment is an extension of the one first reported by Stirand et al. [37] for measurements on the wave of stratification. As used in this experiment the technique essentially displays the propagation in the space-time plane of the striation phase fronts as they propagate along the x axis of the positive column. Wave shaper 2 produces a narrow pulse which is coincident with the zero-crossing time of the positive-going edge of the input signal to photomultiplier 2. The time sweep of oscilloscope 2 is triggered by the output signal from photomultiplier 1 when recording space-time histories of moving striations and from the current pulse trigger [38] when making space-time diagrams of a wave of stratification. For both types of measurements the vertical sweep is controlled by the analog position signal from the motor-driven carriage. Wave shaper 2 intensifies the beam trace on CRT 2 when motor-driven photomultiplier 2 detects the zero crossing of a positive-going signal.

Thus, for a periodic traveling-wave perturbation whose velocity is directed toward the cathode, the space-time display diagrammed in Fig. C2 results. For an artificially excited wave of stratification whose striation velocity u_s is directed toward the anode and whose striation packet velocity v_s is directed toward the cathode, the space-time display diagrammed in Fig. C3 results.

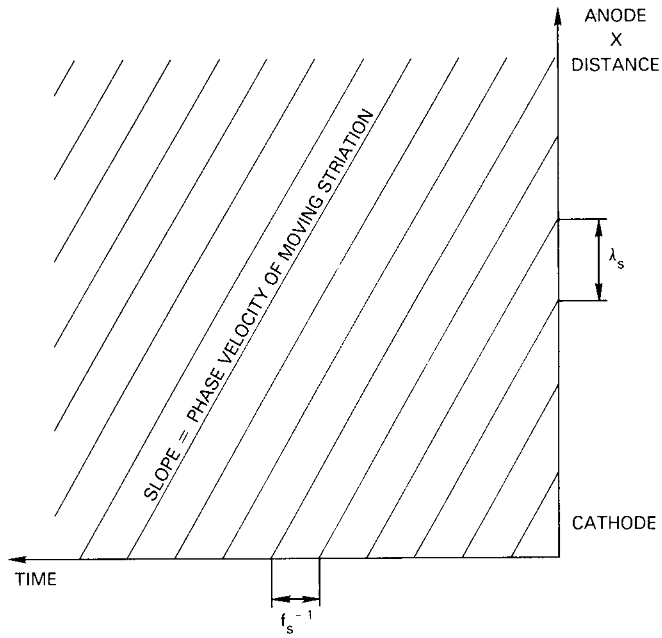

Fig. C2 — Space-time display of a periodic moving striation whose velocity is toward the cathode

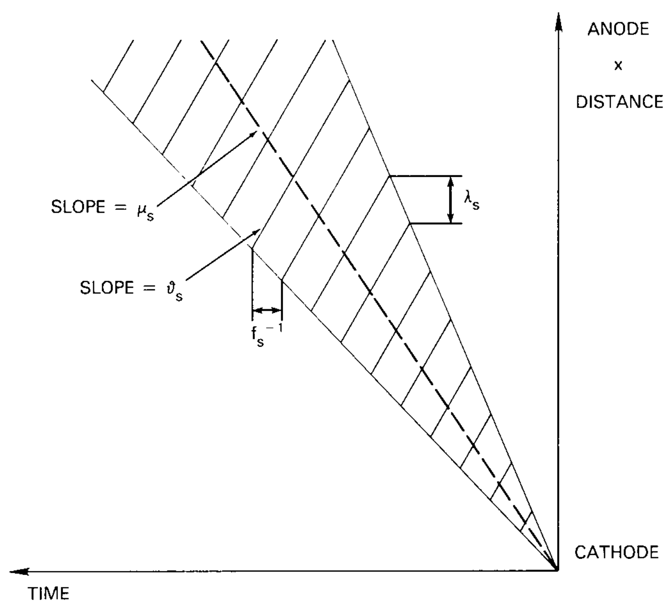

Fig. C3 — Space-time display of a wave stratification whose striation packet velocity (group velocity u_s) is toward the anode and whose striation velocity is toward the cathode

The space-time displays were also photographed as they were being formed by an oscilloscope camera operating in the time-exposure mode. Approximately 60 seconds were required to complete one vertical scan of the 6-cm CRT face.

Photomultiplier 2 scanned a 25-cm-long segment of the positive column near the anode end of the discharge tube which corresponded to a single scan of the 6-cm CRT face. As shown in Fig. C4, the striation amplitude along this segment of the positive column was essentially constant. As reported by Cooper et al [19], any changes in the striation wave parameters due to operating the discharge tube near critical values of reduced currents or pressures where striation parameters exhibit thresholds or change abruptly are initially observed near the cathode end of the positive column.

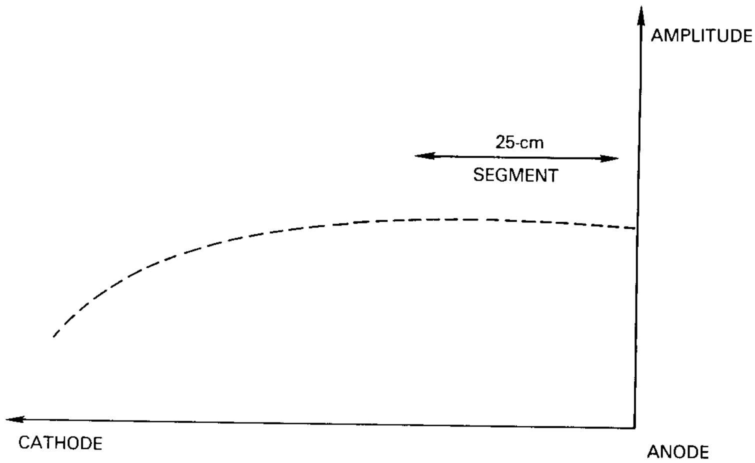

Fig. C4 — Moving striation amplitude as a function of distance from the anode

As photomultiplier 2 traversed the 25-cm segment along the positive column, the position-current control signal swept the discharge-tube current through a 10-mA interval, and for each successive 10-mA increment of discharge-tube current photomultiplier 2 was rescanned over the same 25-cm segment of the positive column. The 1/2-cm/s scan speed of photomultiplier 2 resulted in a 0.2-mA/s sweep rate for the discharge-tube current. Three scans of the 25-cm positive-column segment were required to measure the dependence of the striation parameters on the independent variable, current, throughout a 0-to-30-mA range, a separate time exposure being required for each 10-mA increment. Thus, current was a continuous parameter, and the procedure was repeated for each value of the discrete parameter, pressure.

The same sort of measurements were made with pressure as the continuous parameter and current the discrete parameter by sweeping the pressure over approximately a 3-torr interval for each 25-cm scan of the positive column. The resulting pressure sweep rate was about 0.05 torr/s.

The spectral-raster and space-time display techniques both considerably enhance the signal-to-noise ratio compared with that of direct observation of the temporal variations in a discharge tube energized by a voltage source and a ballast resistor, which was the observation method used by some earlier investigators. Figure C5 shows that the space-time display offers more signal-to-noise enhancement than does the spectral-raster display. Over the 15-to-30-mA current interval the signal is barely distinguishable from the broadband noise on the spectral-raster display, whereas on the space-time display not only is the presence of the signal readily apparent, but its parameters f_s, λ_s, and v_s are also easily measured. The space-time display exhibits superior performance because it more closely approximates quasi-matched-filter detection, which approaches the optimum detection scheme for a sinusoidal signal in broadband noise. As shown in Fig. C6, from the standpoint of the total display generated the spectral-raster technique is somewhat analogous to a low-pass filter with a cutoff frequency given by the full-scale frequency setting of the spectrum analyzer, whereas the space-time display is more like synchronous detection and thus analogous to a bandpass filter whose center frequency is determined by the time sweep rate of the oscilloscope. Of course one must have more accurate initial information of striation frequency in order to correctly adjust the sweep rate of oscilloscope 2 to make the passband of the space-time display coincident with the striation frequency being measured.

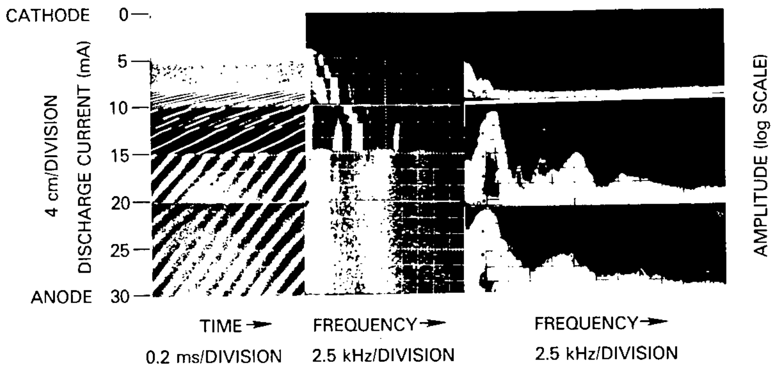

Fig. C5 — Comparison of the space-time (left) and spectral-raster (middle) display techniques

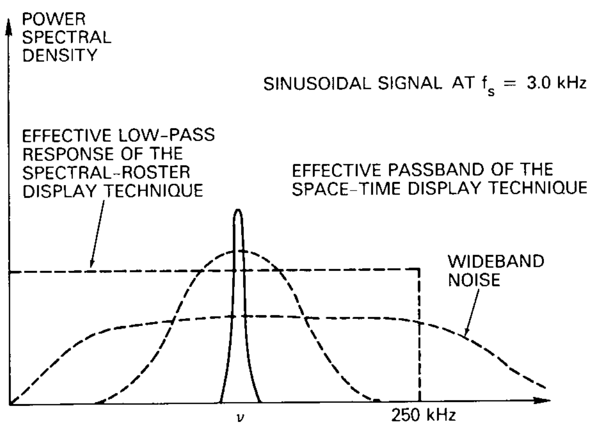

Fig. C6 — Effective passbands of the space-time and spectral-raster detections for the displays in Fig. C5

The facility described in this appendix was used not only for measuring and recording the striation parameters f_s, λ_s, etc. over the $(I/R,\ pR)$ domain in which striations exist in pure neon but also for several other experiments in which various trace impurities such as hydrogen and argon were added to the neon fill gas.

Appendix D
EXPERIMENTAL RESULTS

The data in this appendix (Figs. D1 through D62) are categorized by the radius of the discharge tube's positive column, and they consist of photographic and strip-chart recordings of displays that were generated with the aid of the automated facility described in Appendix C for measuring striation parameters. The striation parameters frequency f_s, wavelength λ_s, and velocity v_s for any value of discharge-tube current I and pressure p, can be read directly from the spectral-raster and space-time photographic records by following the formats shown in Figs. C2 and C3. Also, by referring to the appropriate data displays in this appendix, the variation of the striation parameters, f_s, λ_s, and v_s as a continuous function of the independent discharge-tube variables current and pressure can be ascertained over the entire regime of current and pressure mapped.

The displays in Figs. D8 through D62 are oriented so that one can follow across from a specific value of one of the continuous parameters, current or pressure, and observe the striation spectrum from the spectral-raster display and the striation parameters f_s, λ_s, and v_s from the space-time display. When current is the continuous parameter and pressure is the discrete parameter, a photograph of the spectrum analyzer CRT is displayed for currents of 5 mA, 15 mA, and 25 mA. By comparing these photographs with the adjacent spectral-raster displays, the relative magnitudes of the striation spectral components at other currents in the interval 0 to 30 mA can be estimated.

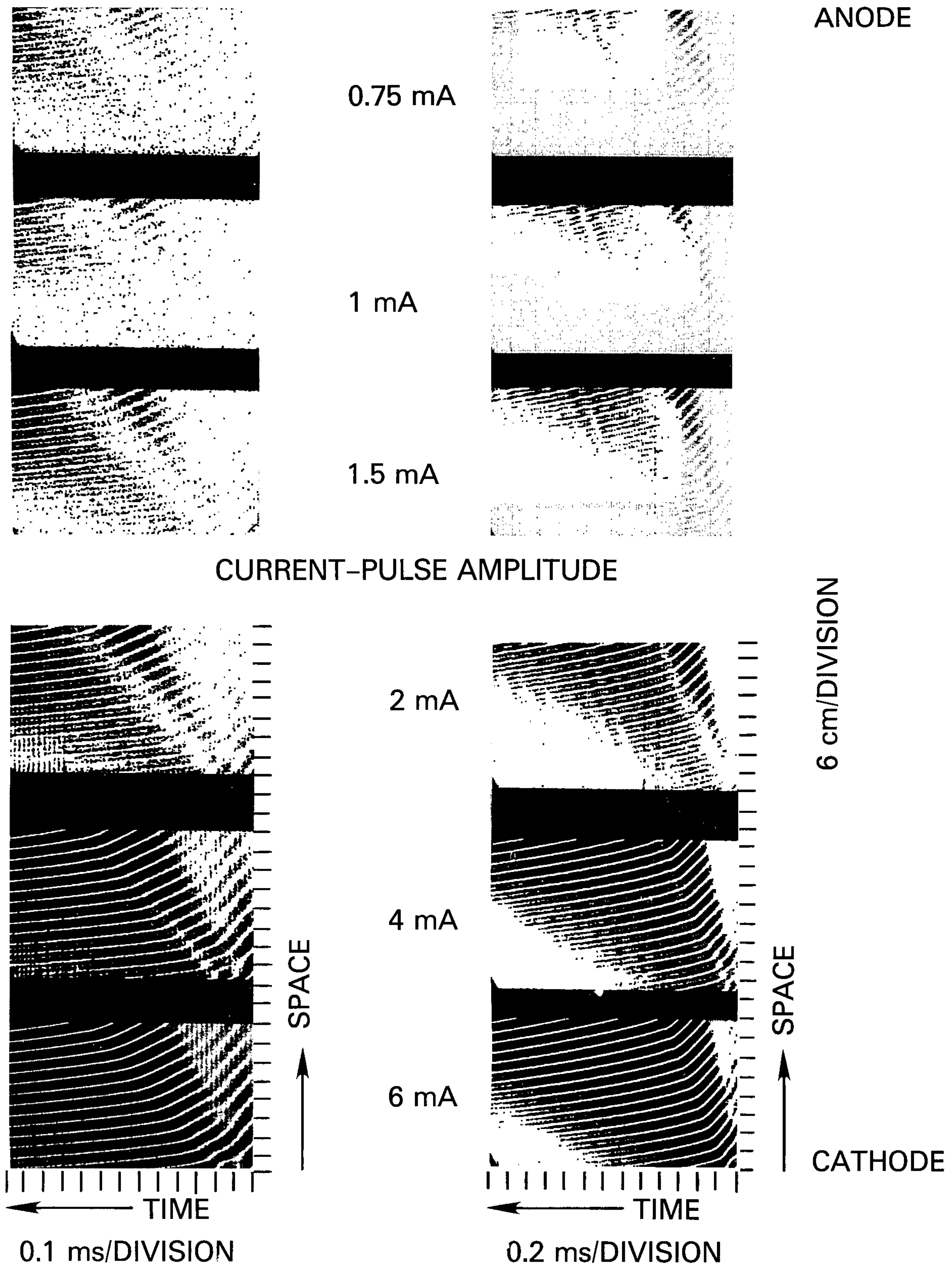

Fig. D1 — Display for current I = 15 mA, pressure p = 0.9 torr, and radius R = 0.95 cm

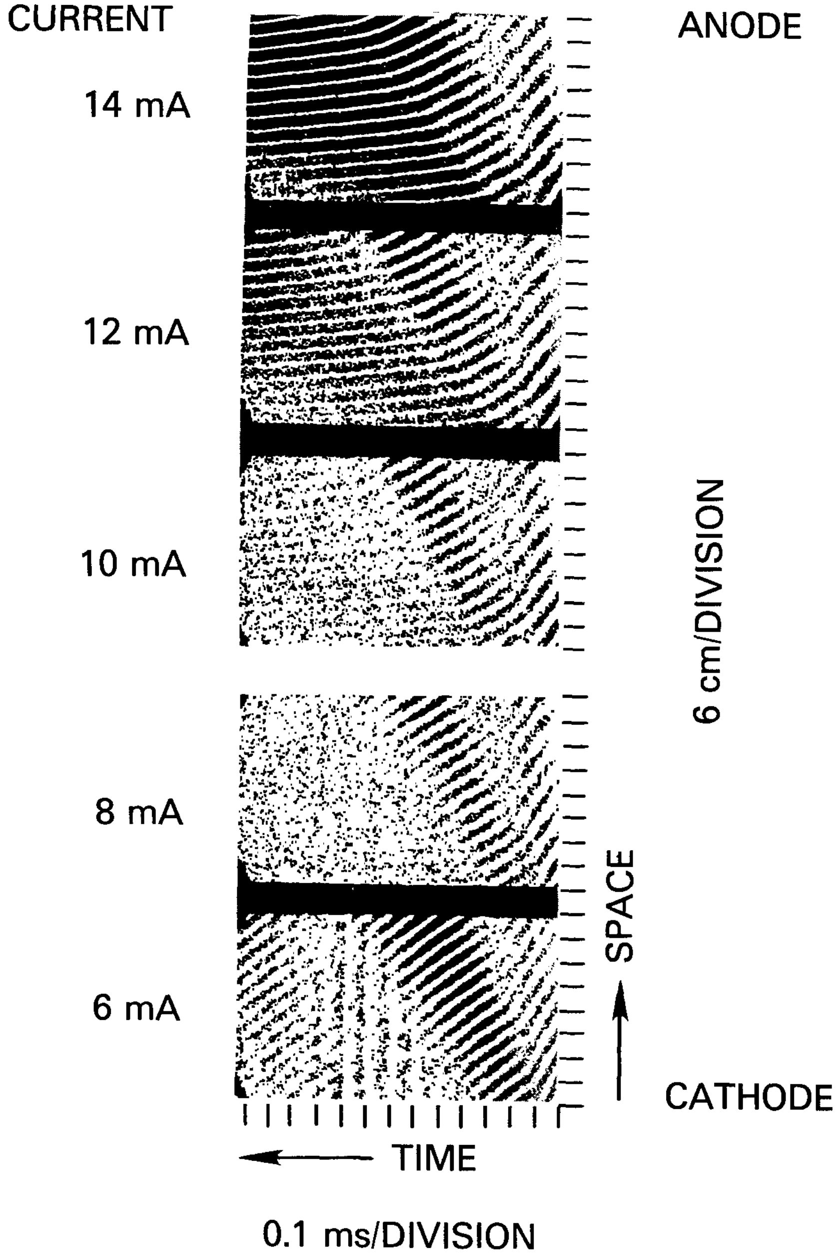

Fig. D2 — Pressure p = 0.9 torr and radius R = 0.95 cm

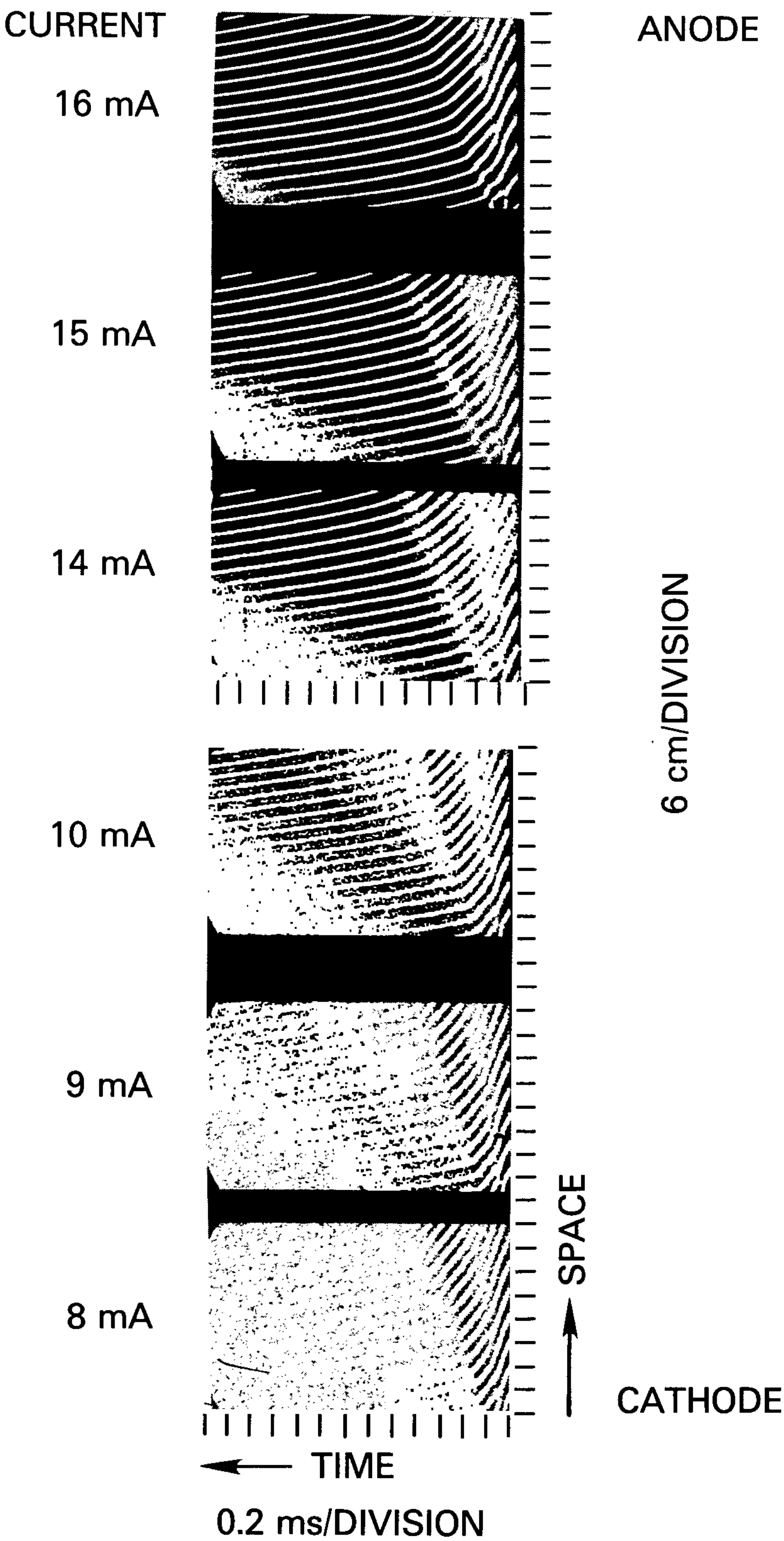

Fig. D3 — Pressure p = 0.9 torr and radius R = 0.95 cm

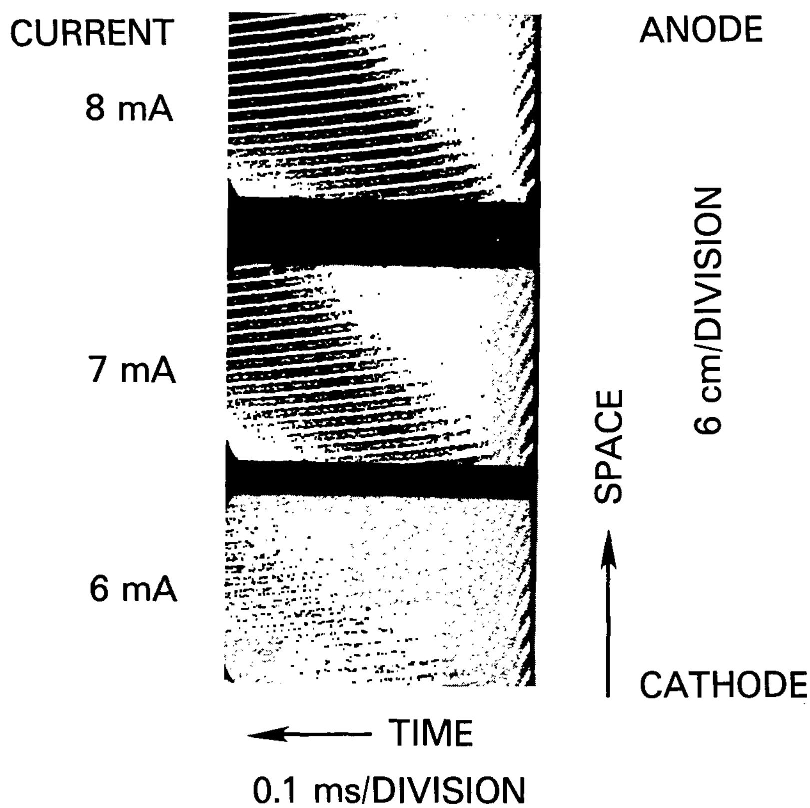

Fig. D4 — Pressure p = 1.0 torr and radius R = 0.95 cm

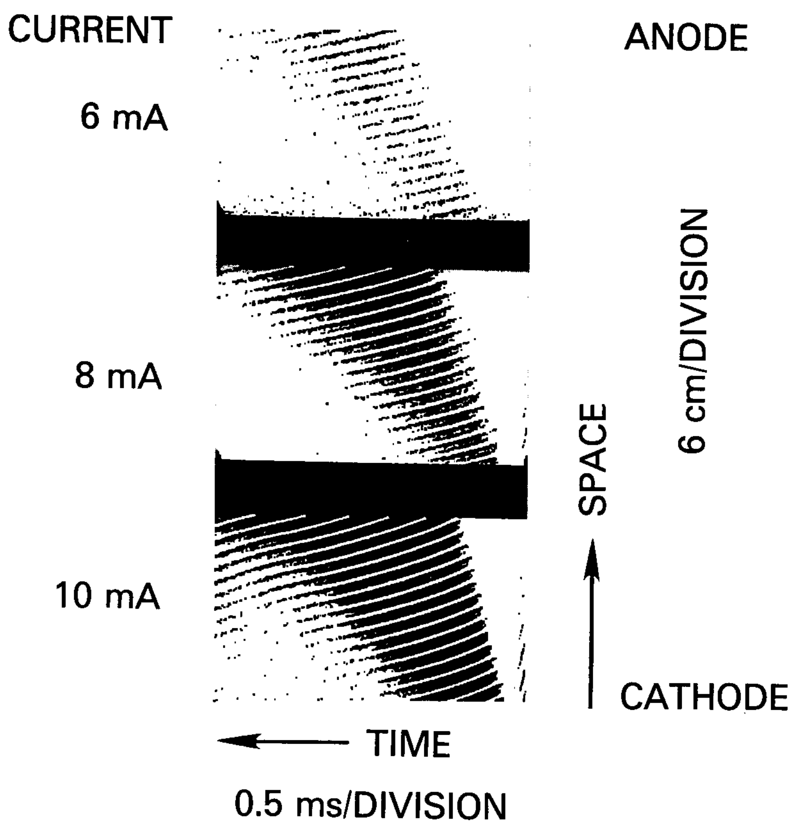

Fig. D5 — Pressure p = 1.0 torr and radius R = 0.95 cm

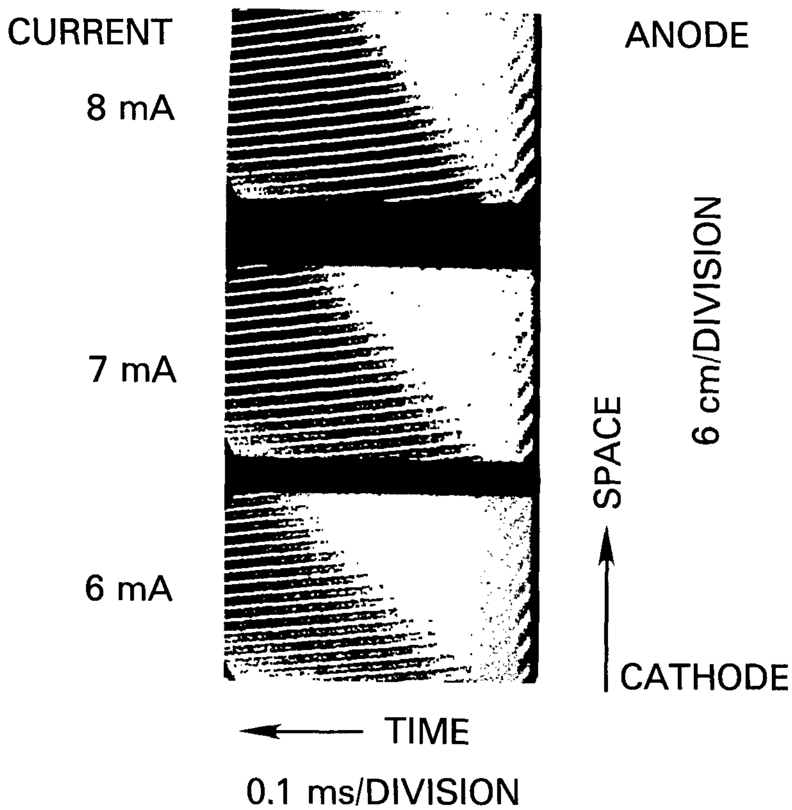

Fig. D6 — Pressure p = 1.1 torr and radius R = 0.95 cm

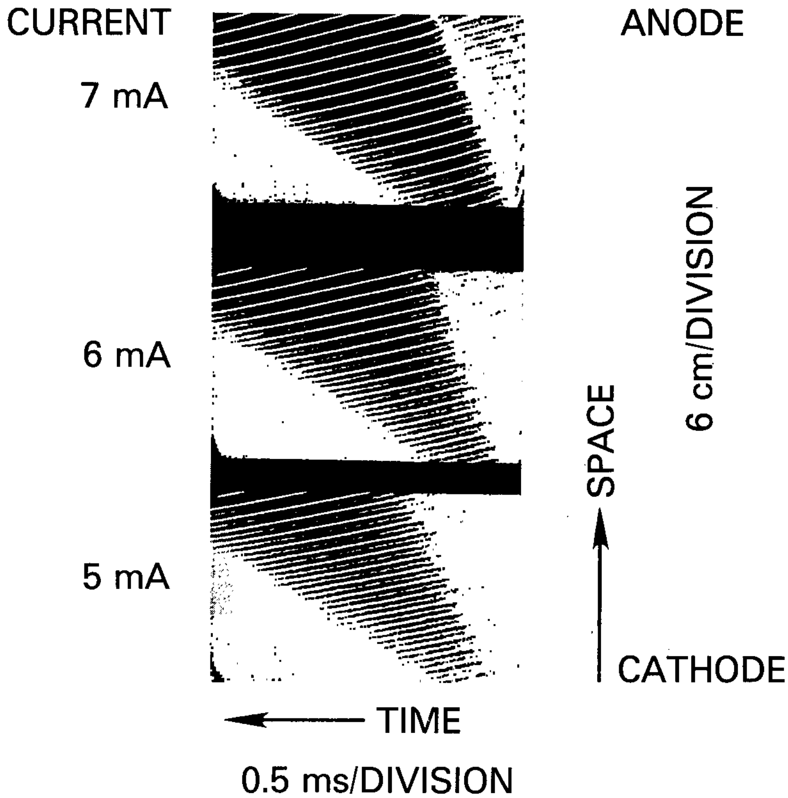

Fig. D7 — Pressure p = 1.2 torr and radius R = 0.95 cm

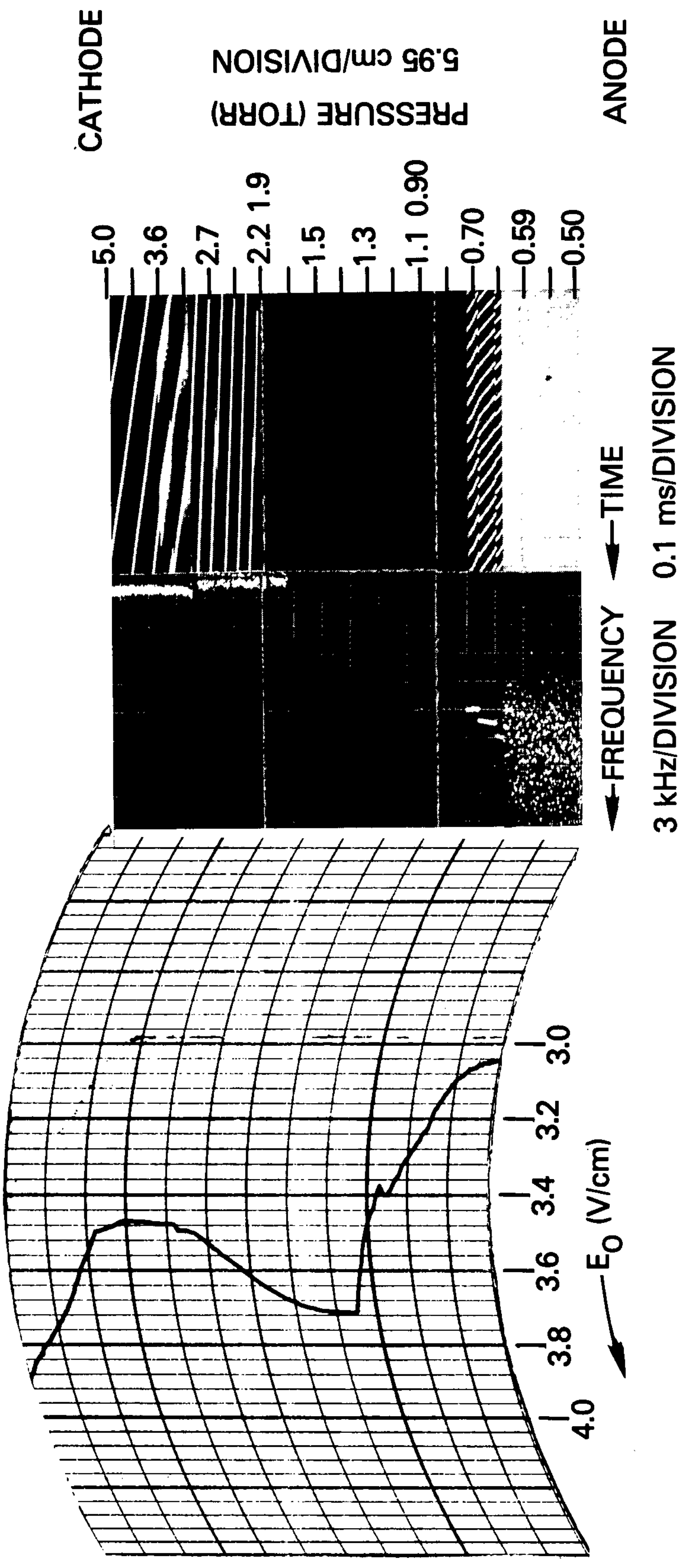

Fig. D8 — Current I = 4 mA, radius R = 0.95 cm, and I/R = 4.2 mA/cm

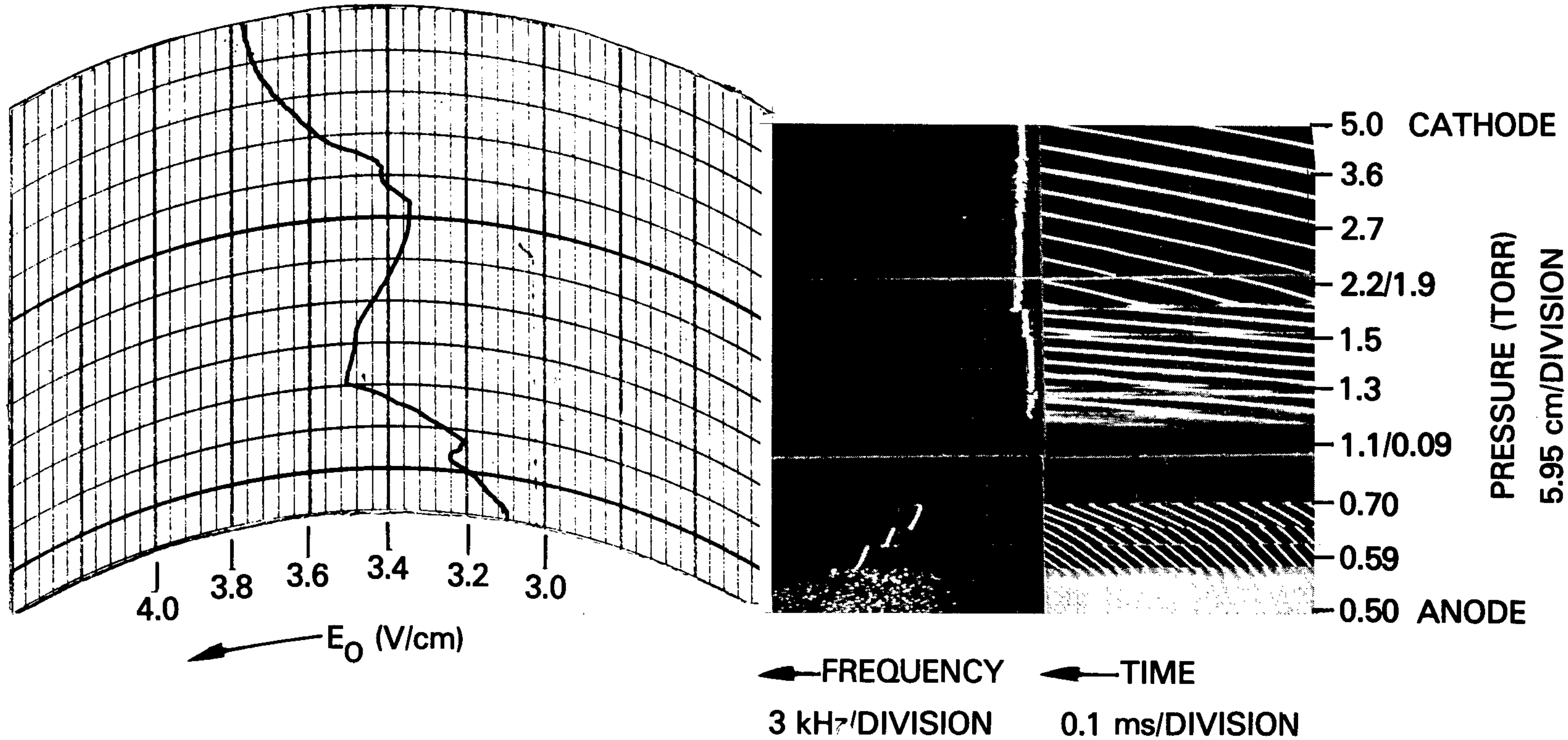

Fig. D9 — Current I = 10 mA, radius R = 0.95 cm, and I/R = 10.5 mA/cm

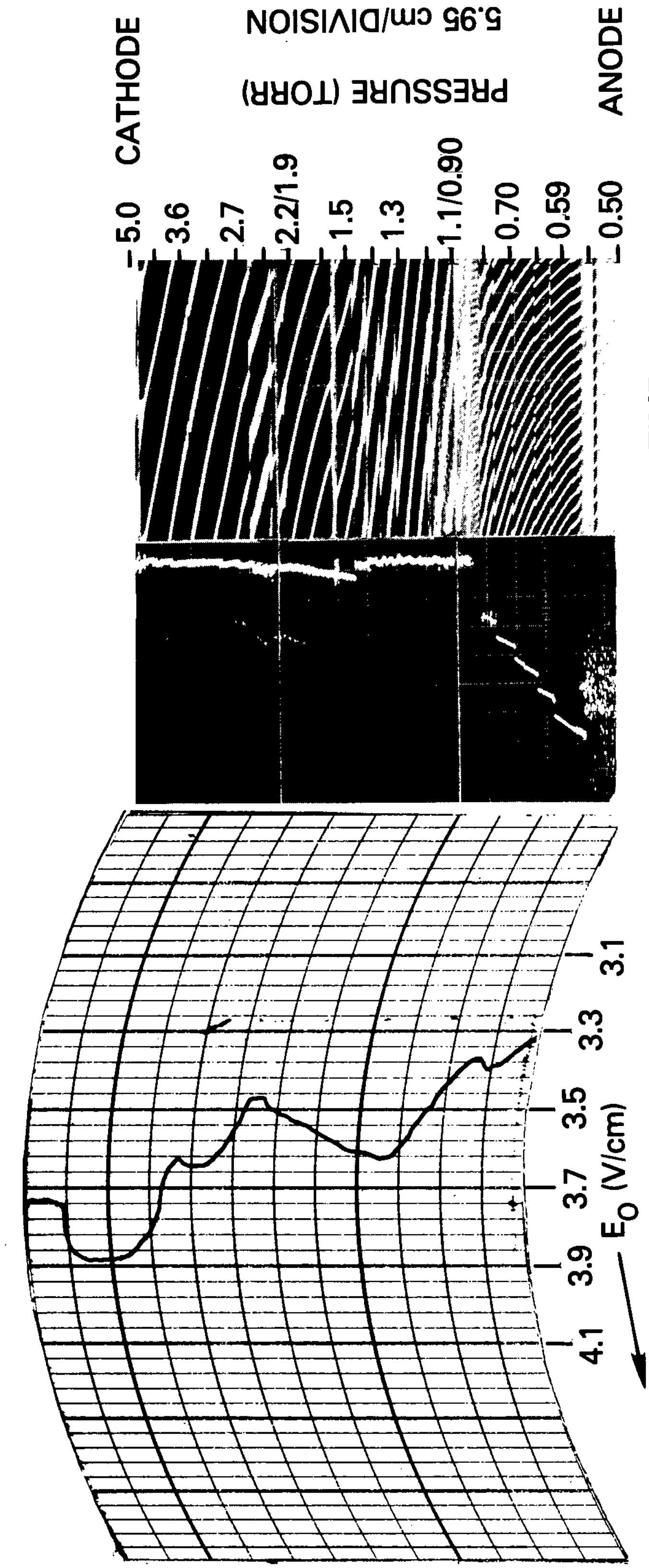

Fig. D10 — Current I = 15 mA, radius R = 0.95 cm, and I/R = 1.58 mA/cm

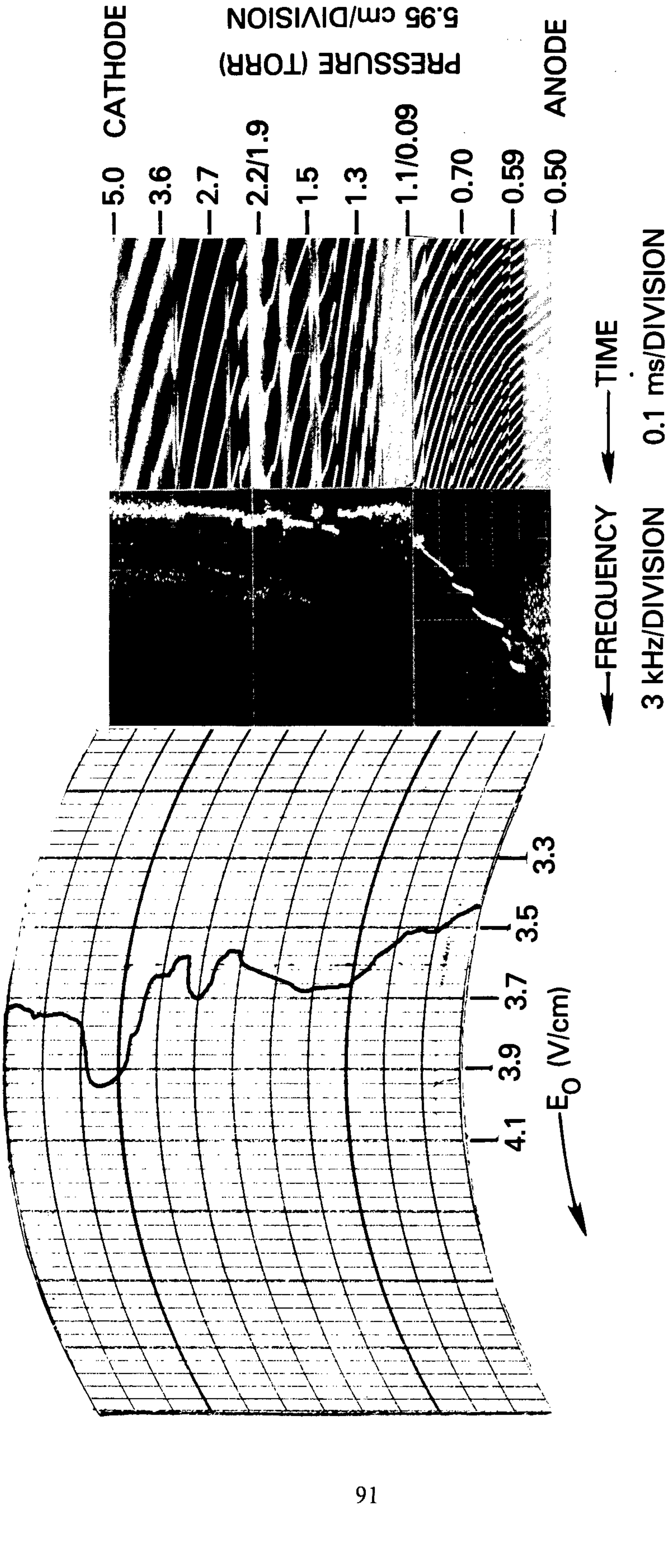

Fig. D11 — Current I = 20 mA, radius R = 0.95 cm, and I/R = 21.1 mA/cm

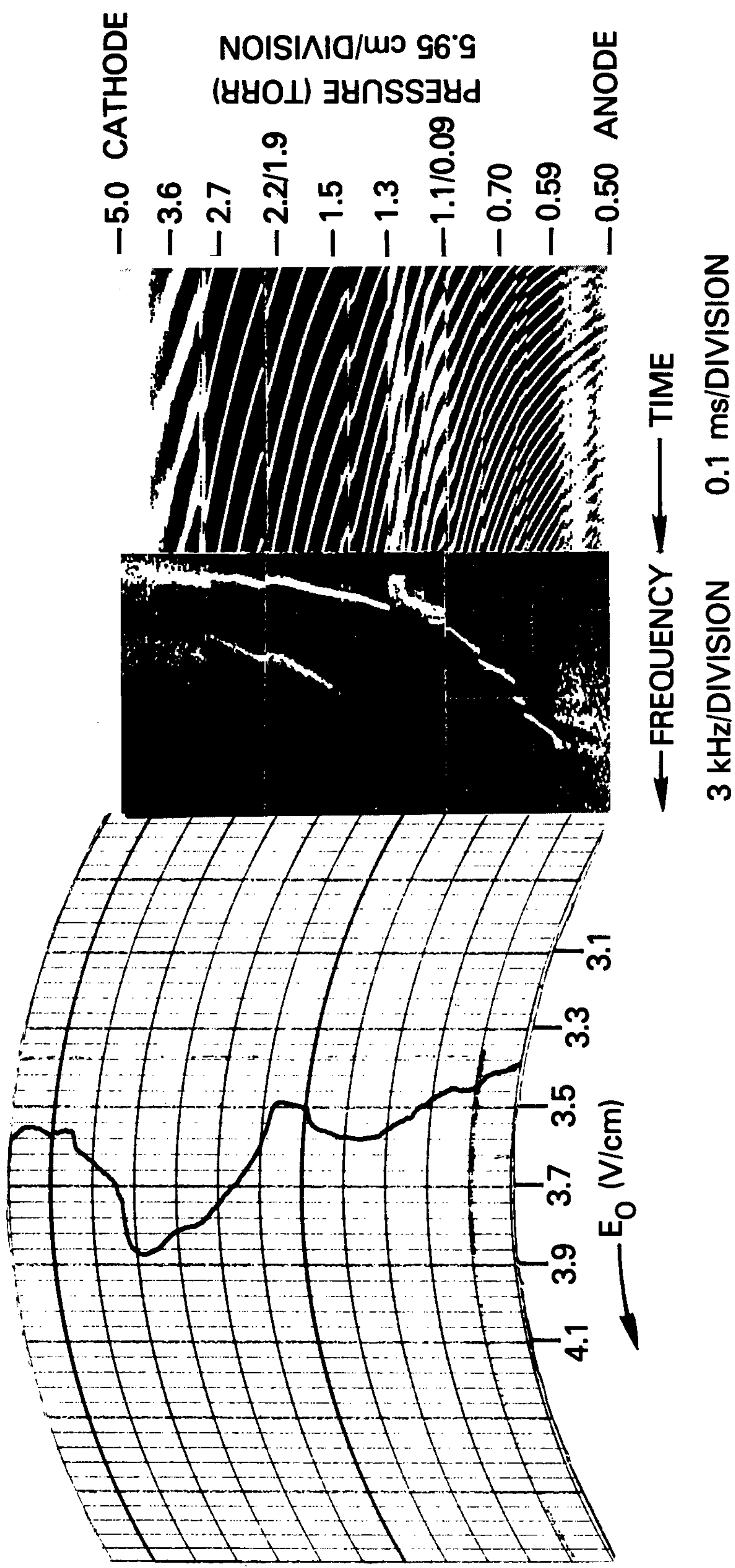

Fig. D12 — Current I = 25 mA, radius R = 0.95 cm, and I/R = 26.3 mA/cm

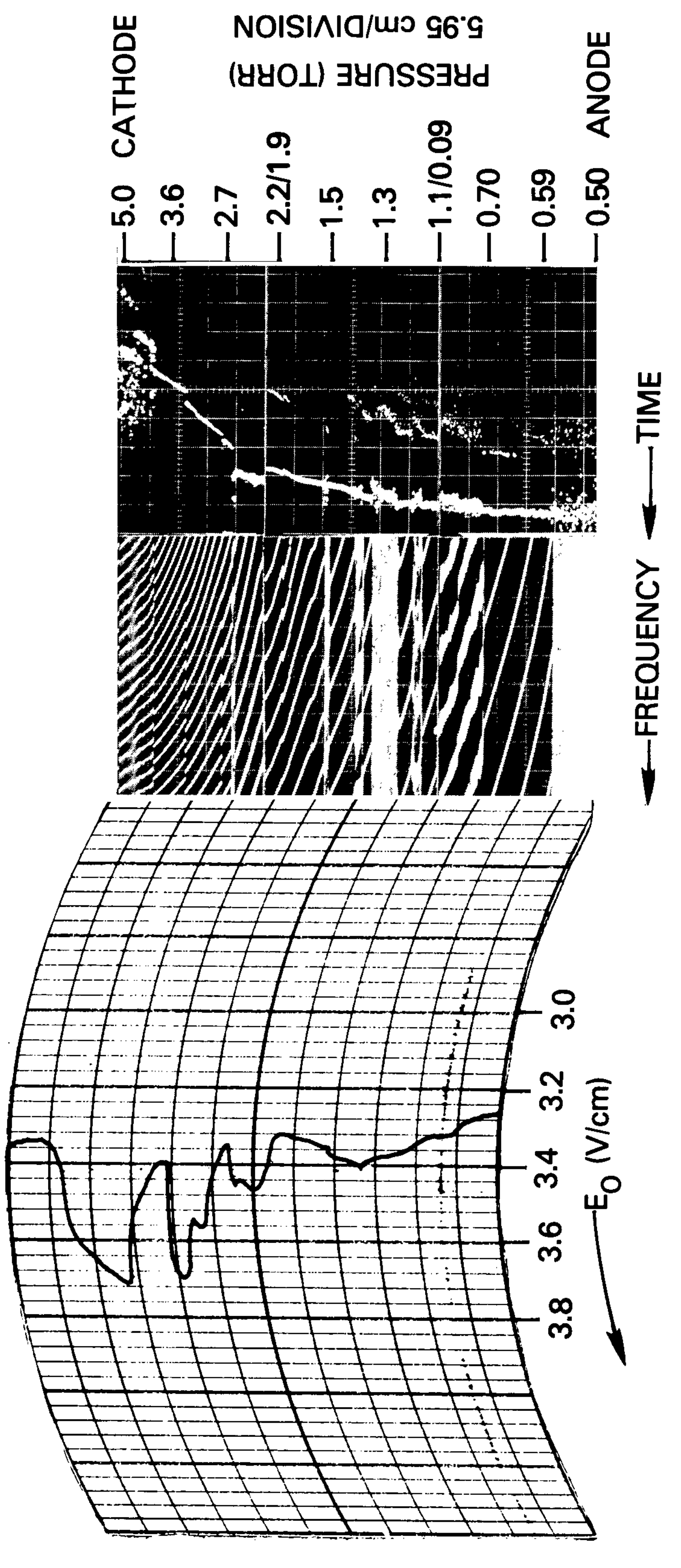

Fig. D13 — Current I = 30 mA, radius R = 0.95 cm, and I/R = 31.6 mA/cm

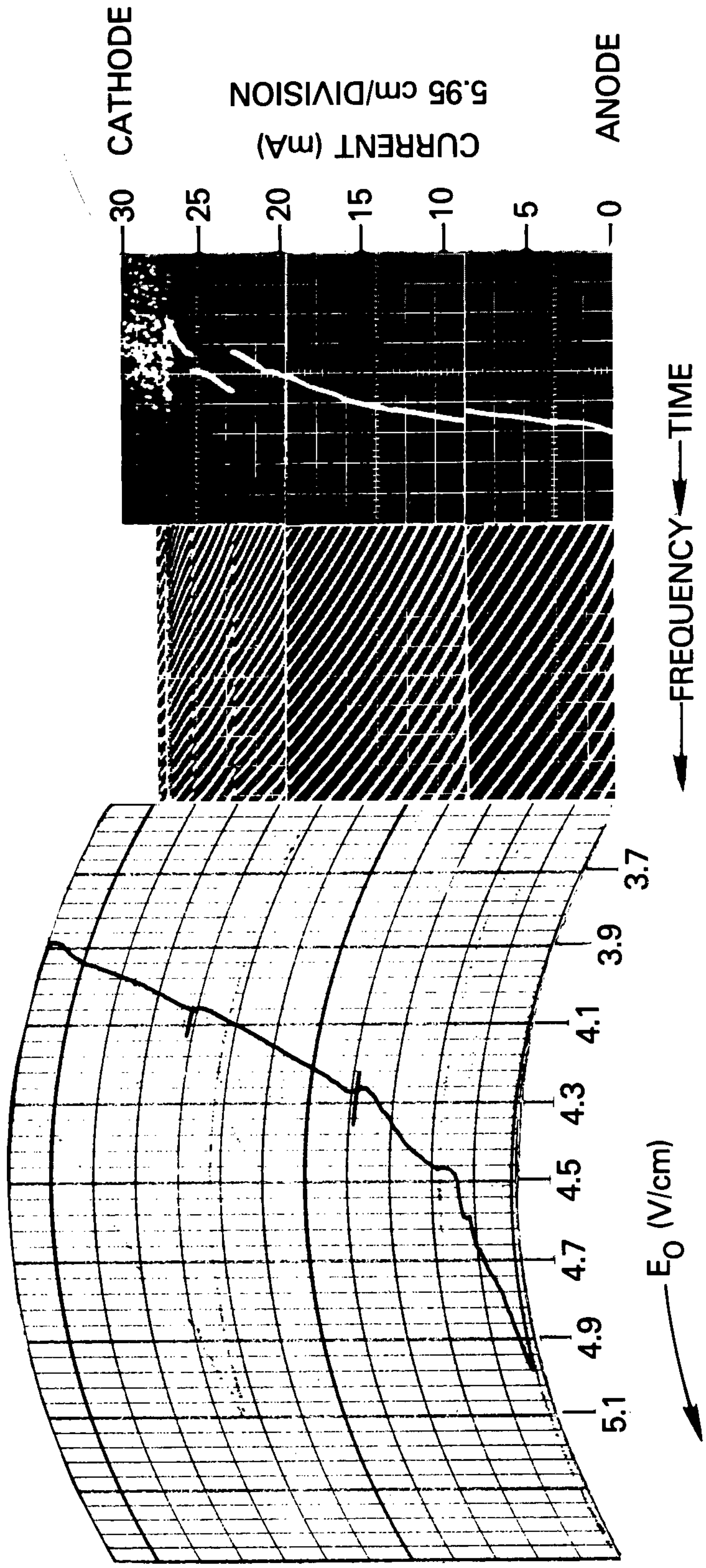

Fig. D14 — Pressure $p = 0.70$ torr, radius $R = 0.95$ cm, and $pR = 0.67$ torr-cm

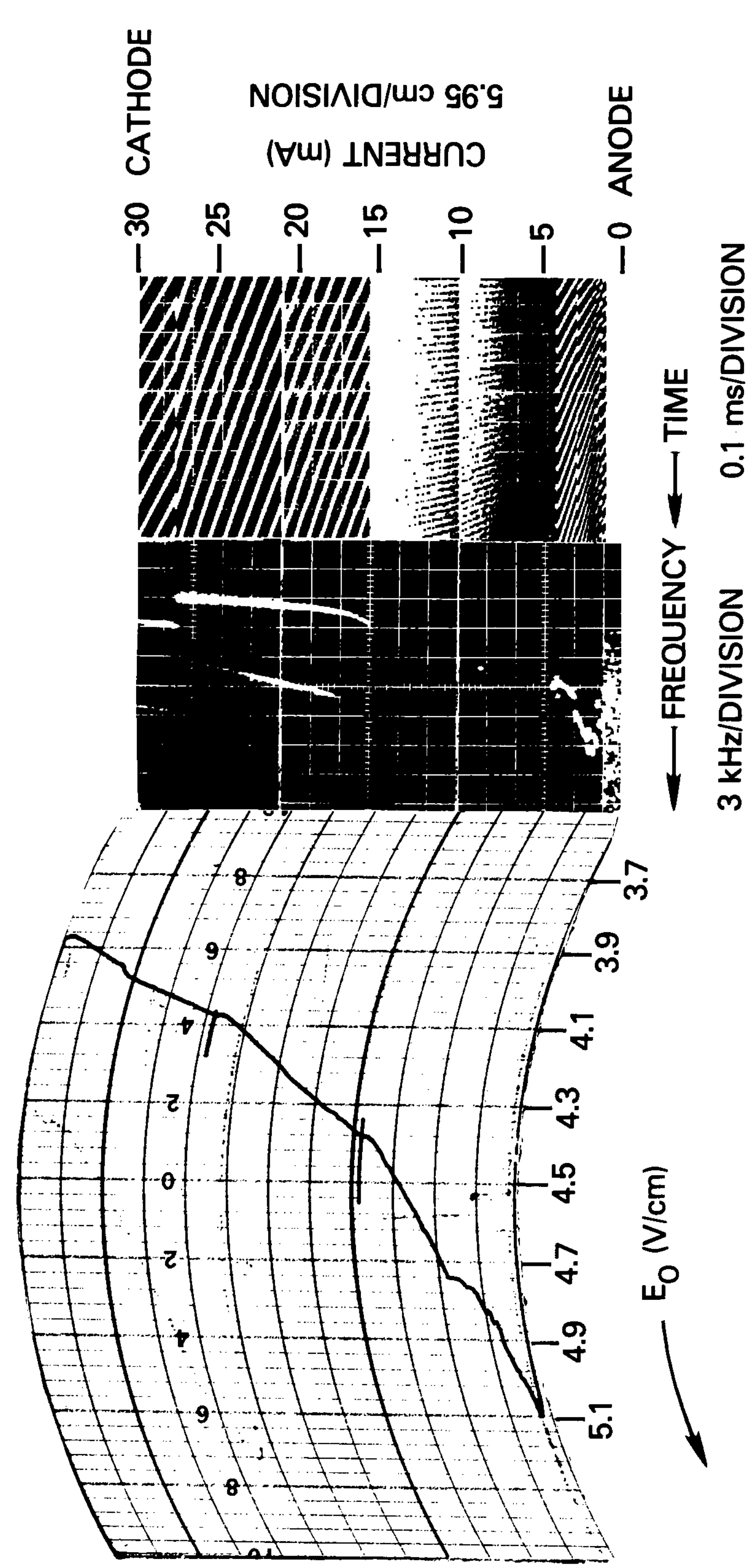

Fig. D15— Pressure p = 0.80 torr, radius R = 0.95 cm, and pR = 0.76 torr-cm

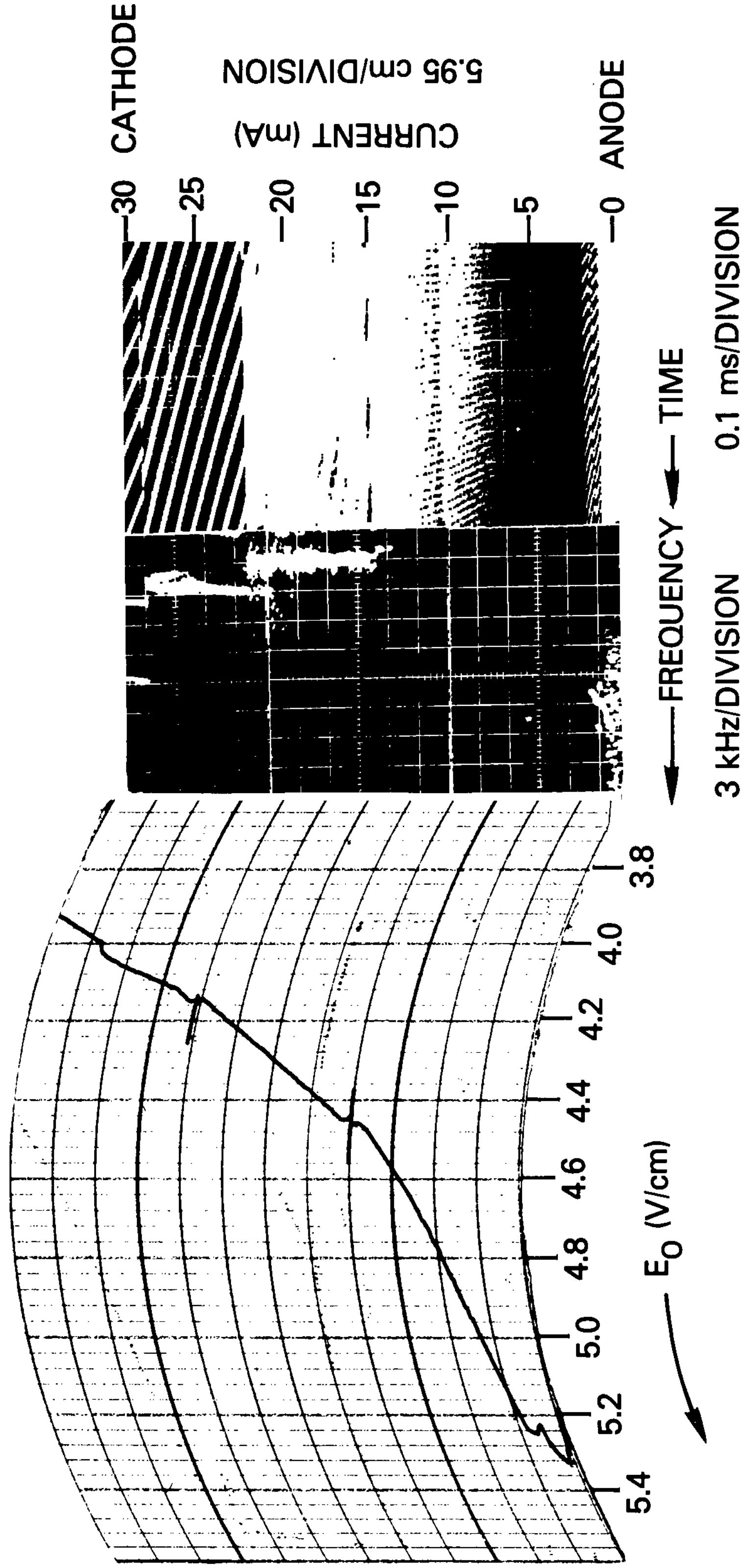

Fig. D16 — Pressure $p = 0.90$ torr, radius $R = 0.95$ cm, and $pR = 0.86$ torr-cm

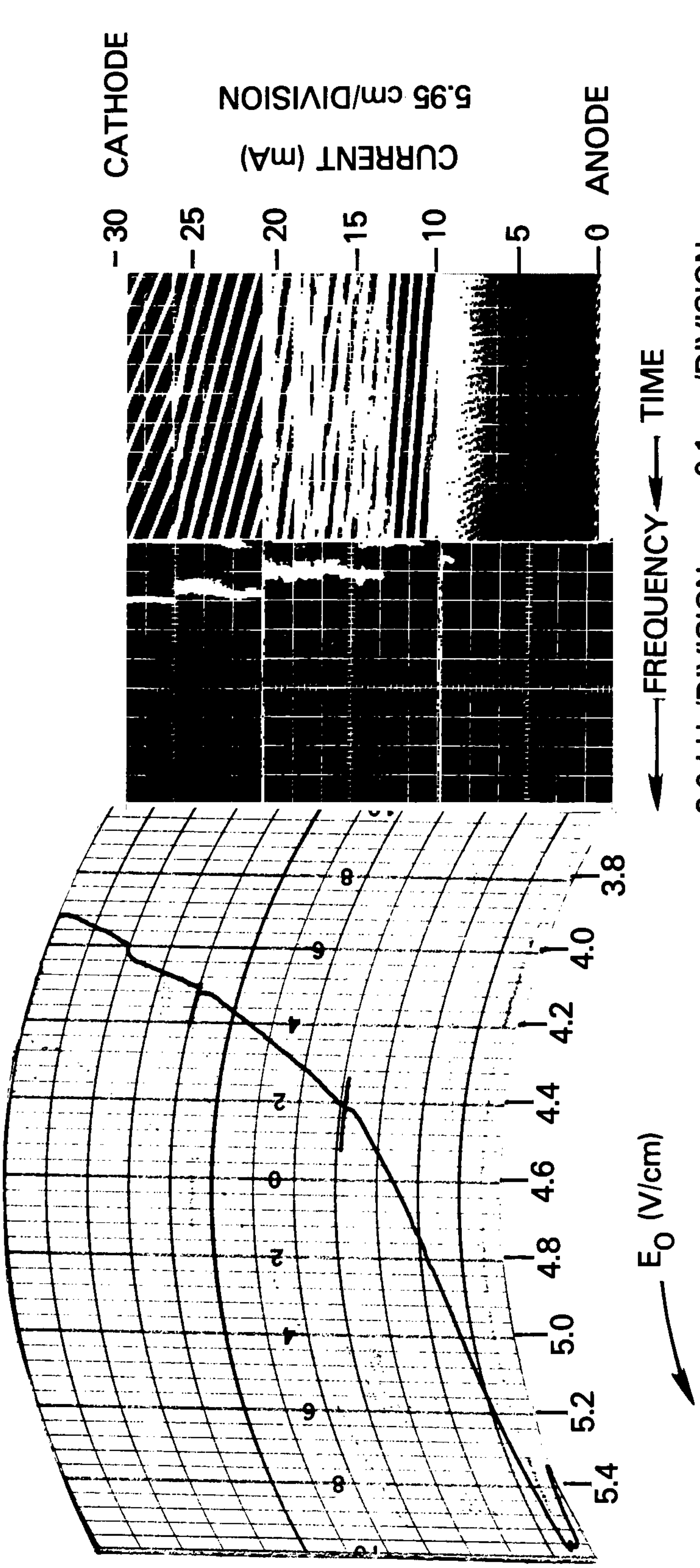

Fig. D17 — Pressure p = 1.0 torr, radius R = 0.95 cm, and pR = 0.95 torr-cm

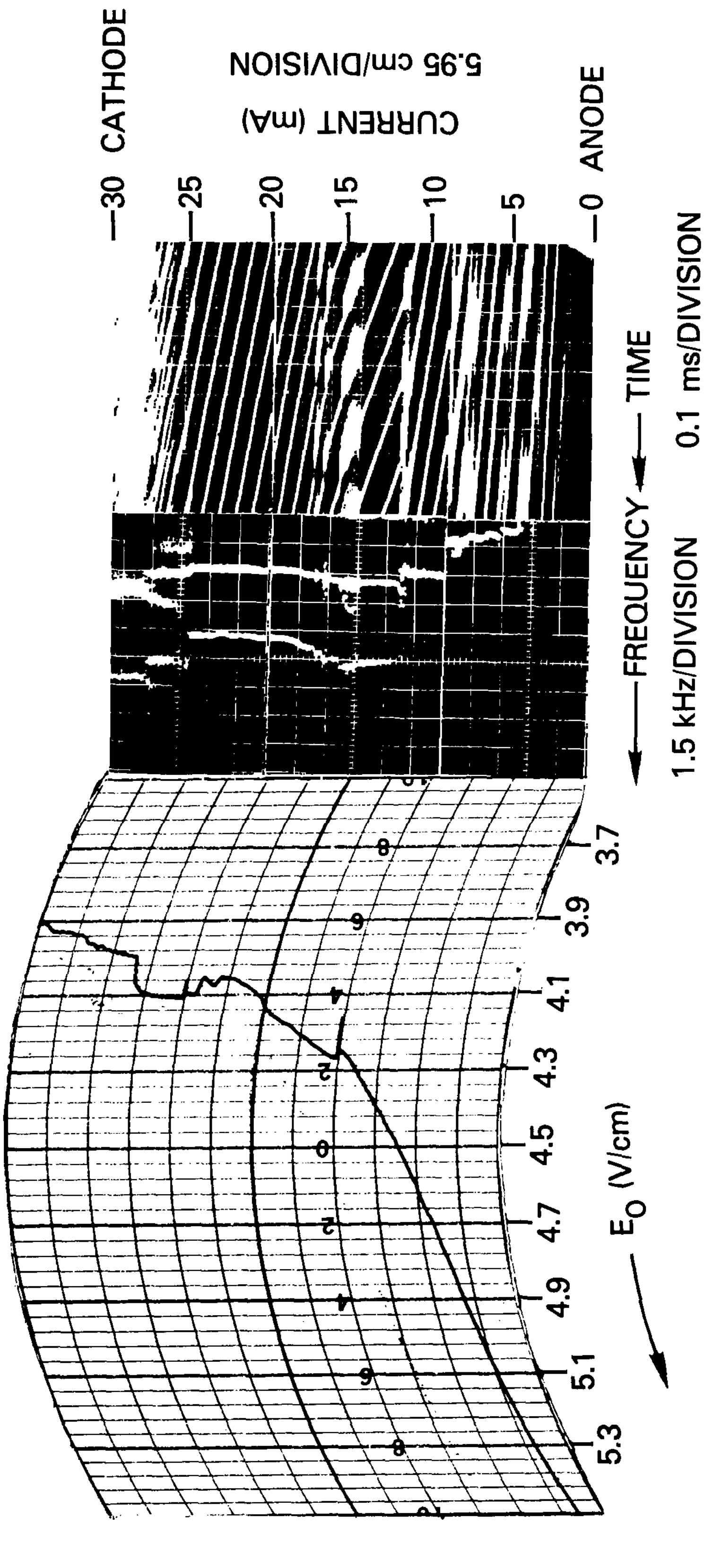

Fig. D18 — Pressure $p = 1.4$ torr, radius $R = 0.95$ cm, and $pR = 1.3$ torr-cm

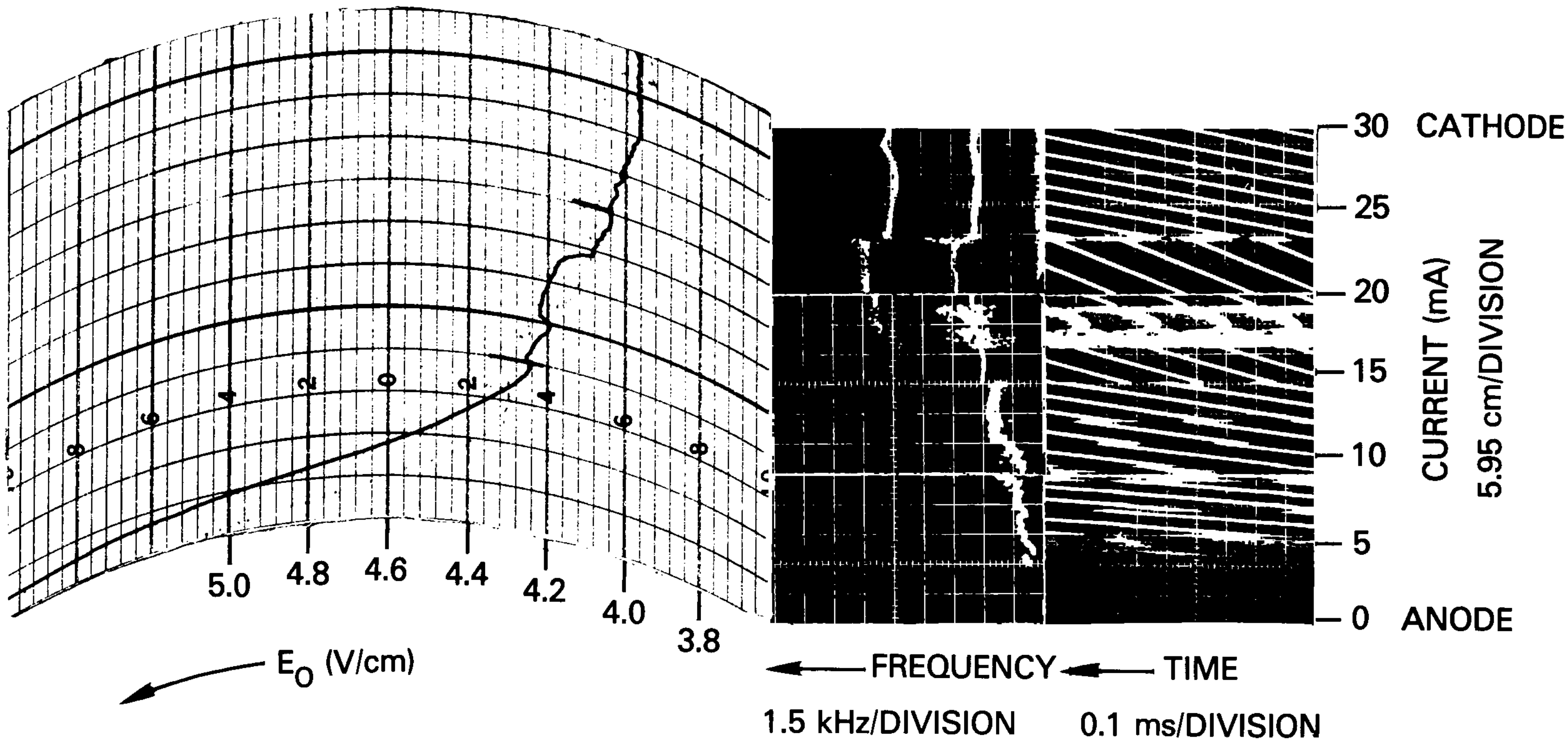

Fig. D19 — Pressure p = 1.6 torr, radius R = 0.95 cm, and pR = 1.5 torr-cm

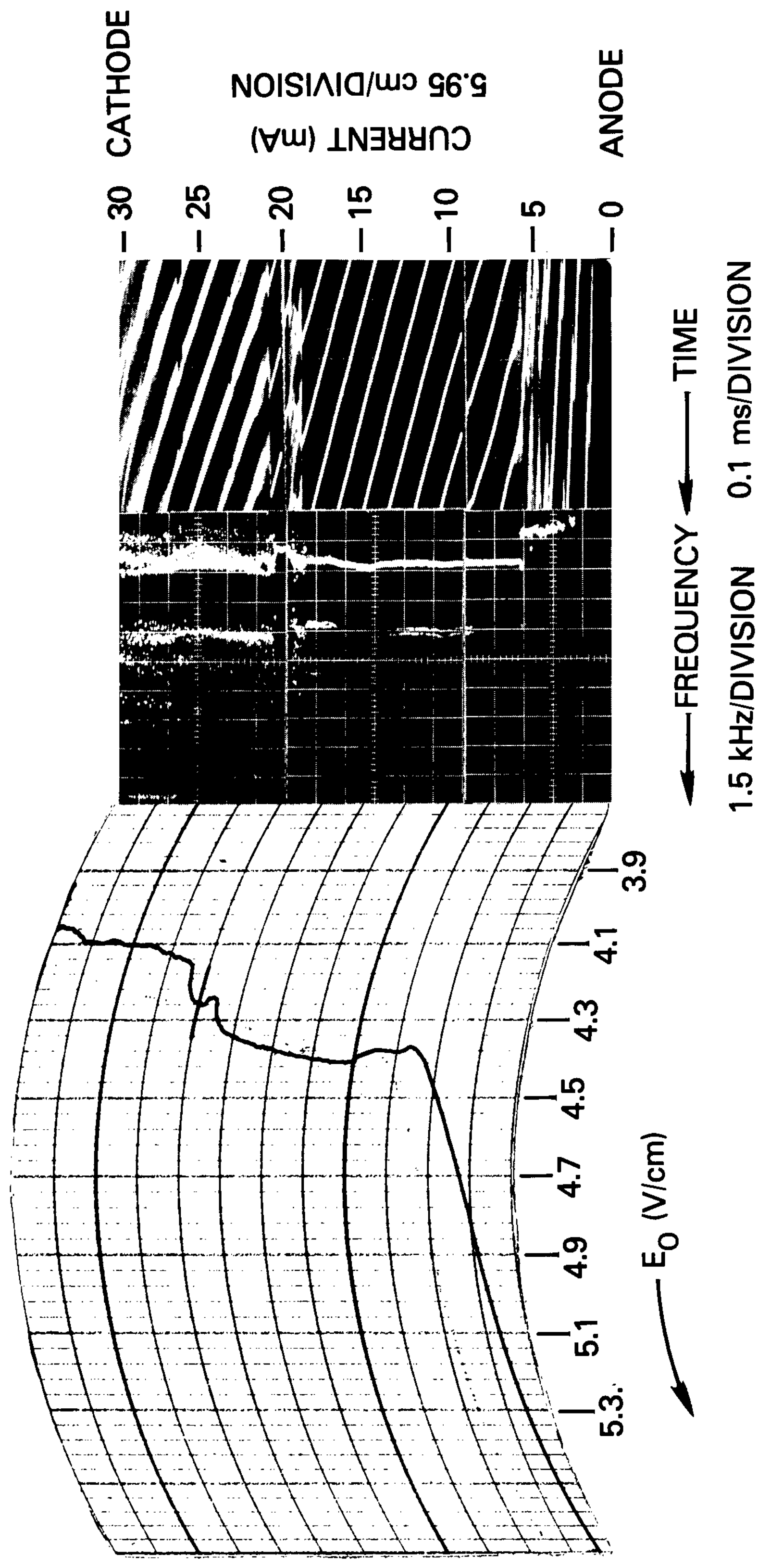

Fig. D20 — Pressure p = 2.0 torr, radius R = 0.95 cm, and pR = 1.9 torr-cm

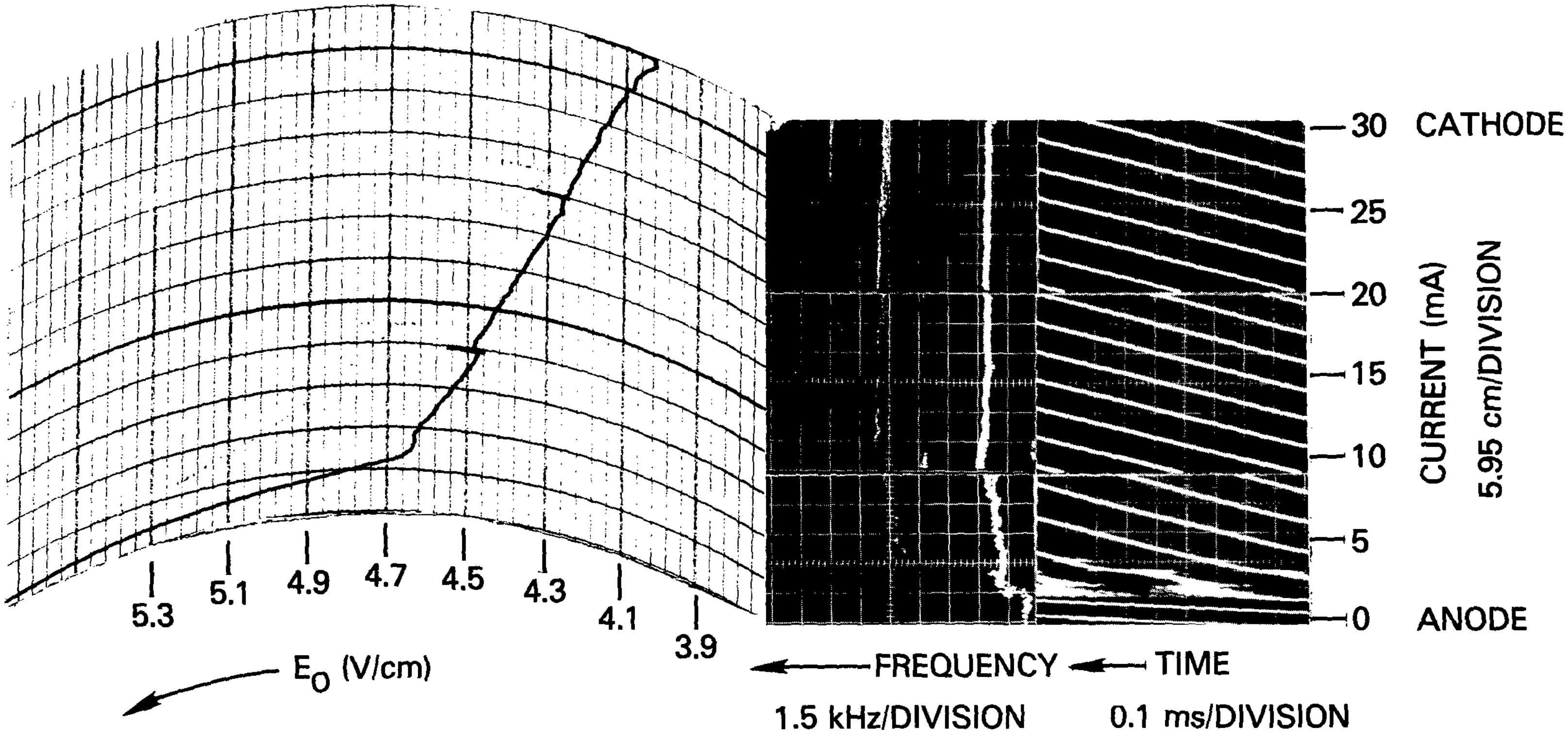

Fig. D21 — Pressure p = 3.0 torr, radius R = 0.95 cm, and pR = 2.85 torr-cm

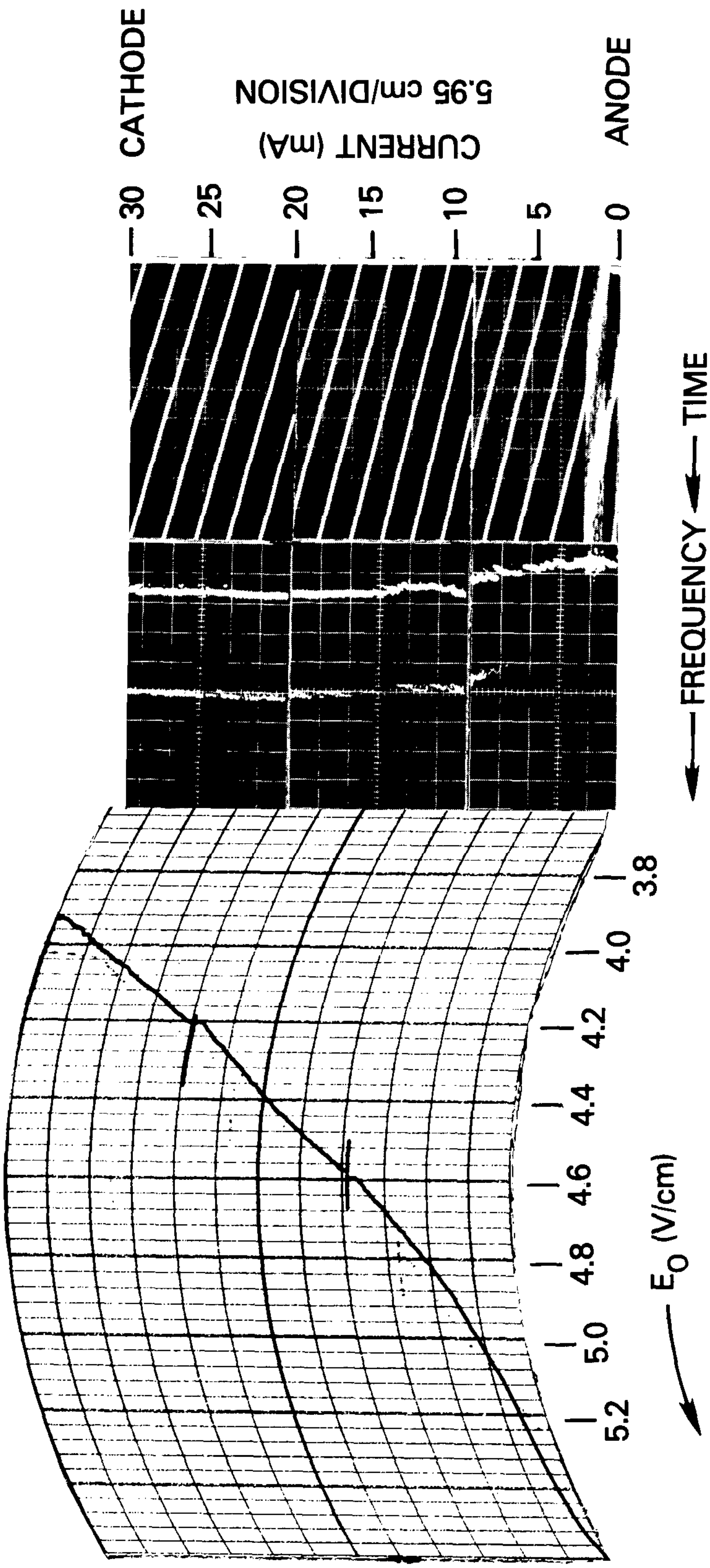

Fig. D22 — Pressure p = 4.0 torr, radius R = 0.95 cm, and pR = 3.8 torr-cm

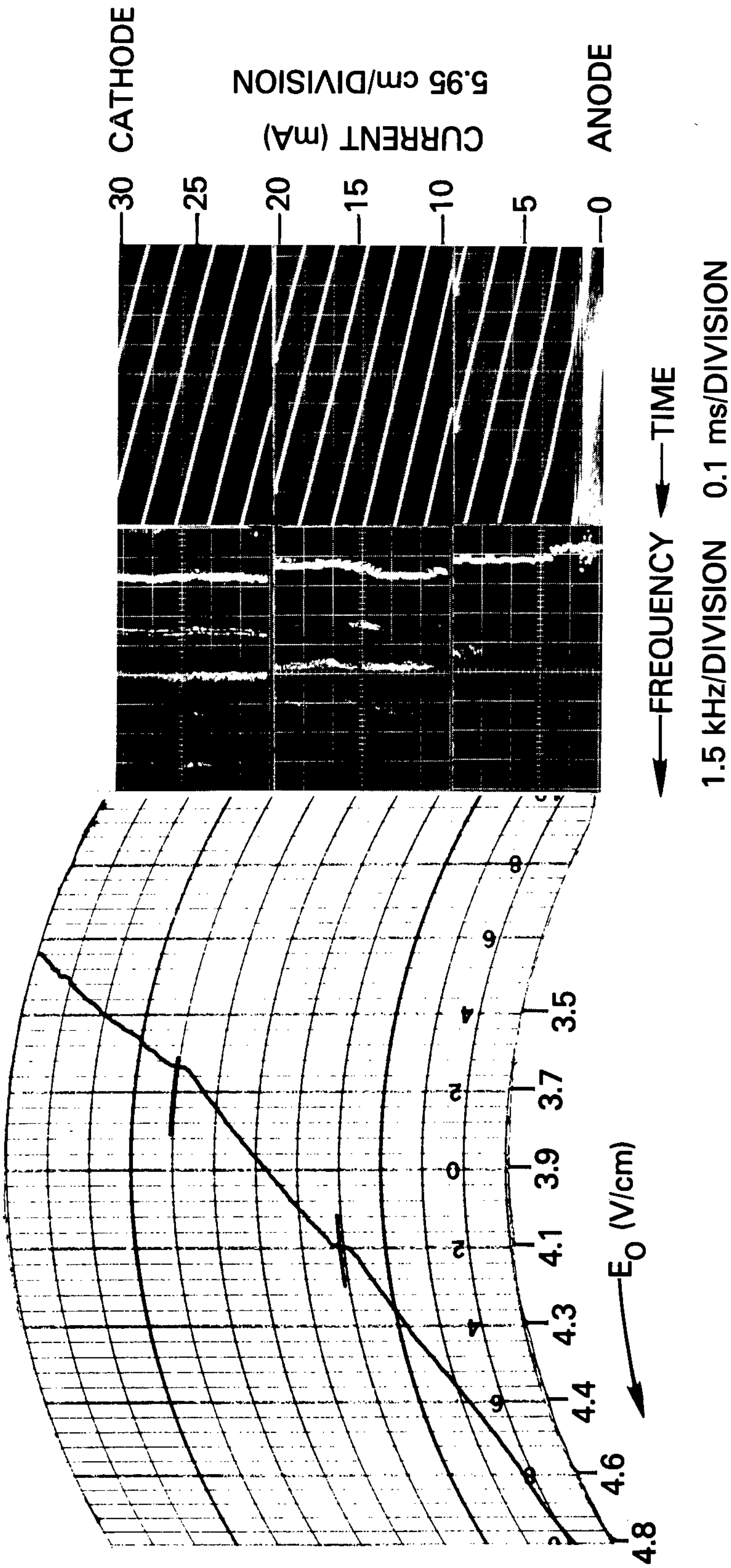

Fig. D23 — Pressure p = 5.0 torr, radius R = 0.95 cm, and pR = 4.75 torr-cm

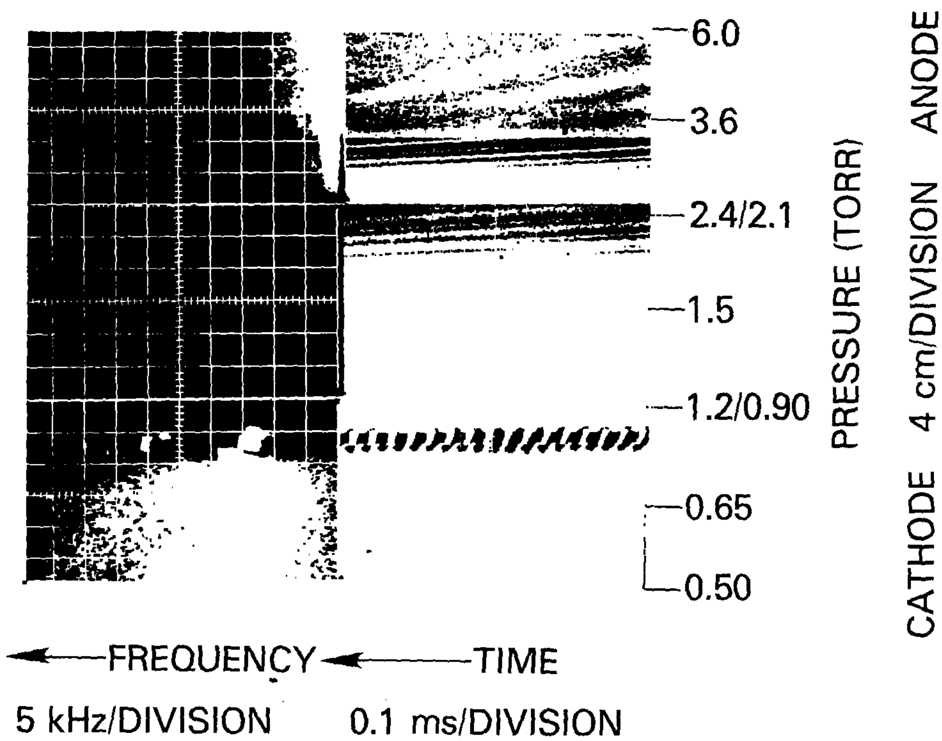

Fig. D24 — Current $I = 2.5$ mA, radius $R = 0.95$ cm, and $I/R = 2.6$ mA/cm

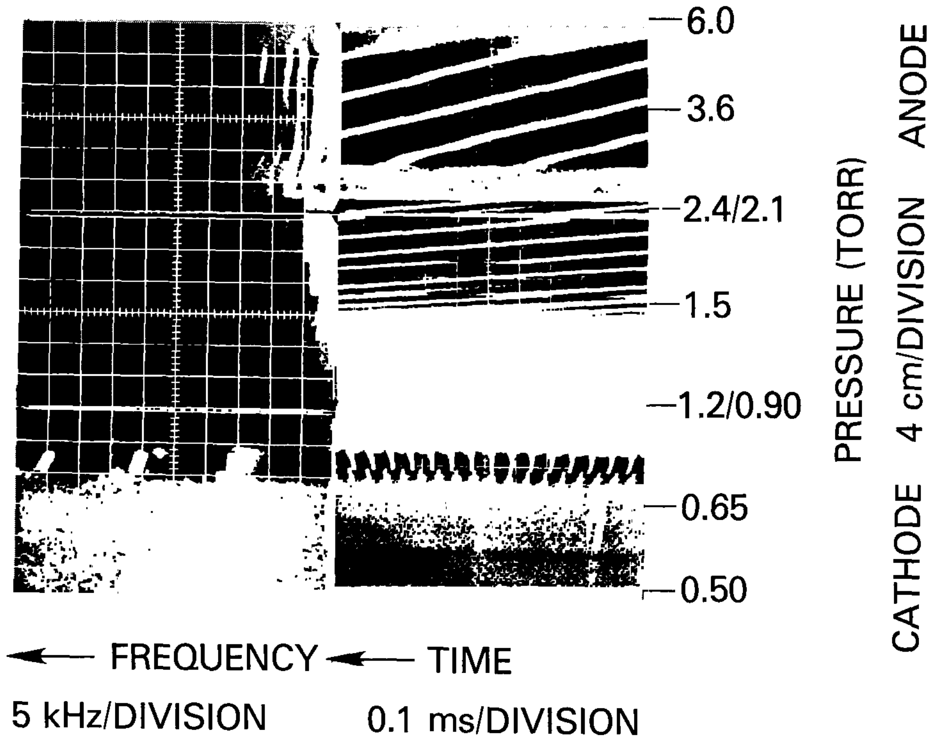

Fig. D25 — Current I = 5.0 mA, radius R = 0.95 cm, and I/R = 5.3 mA/cm

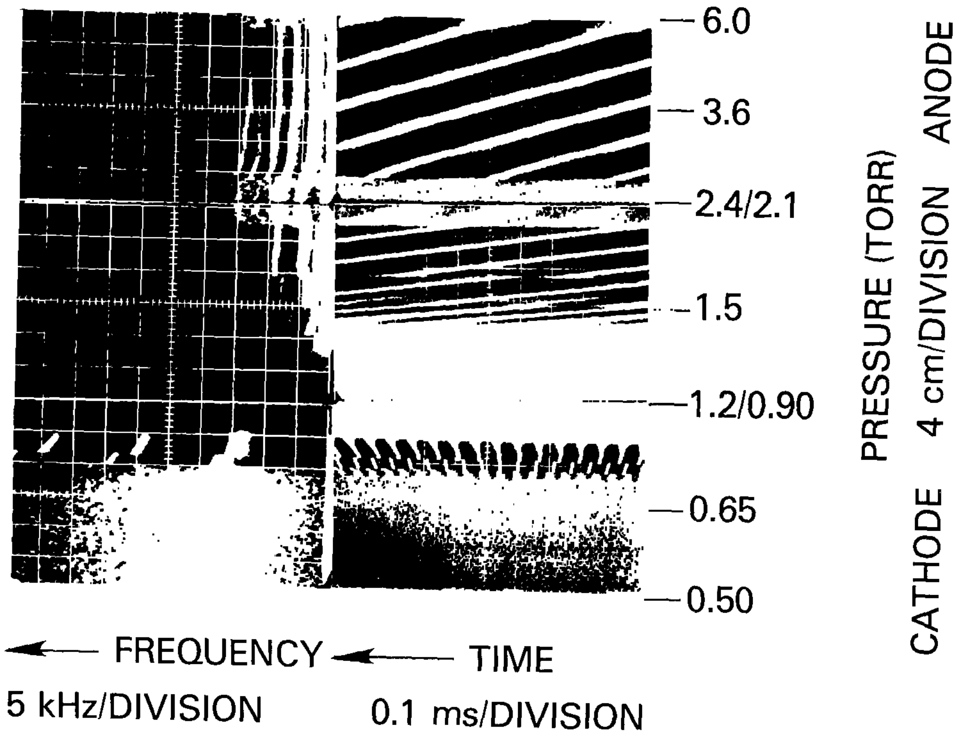

Fig. D26 — Current $I = 7.5$ mA, radius $R = 0.95$ cm, and $I/R = 7.8$ mA/cm

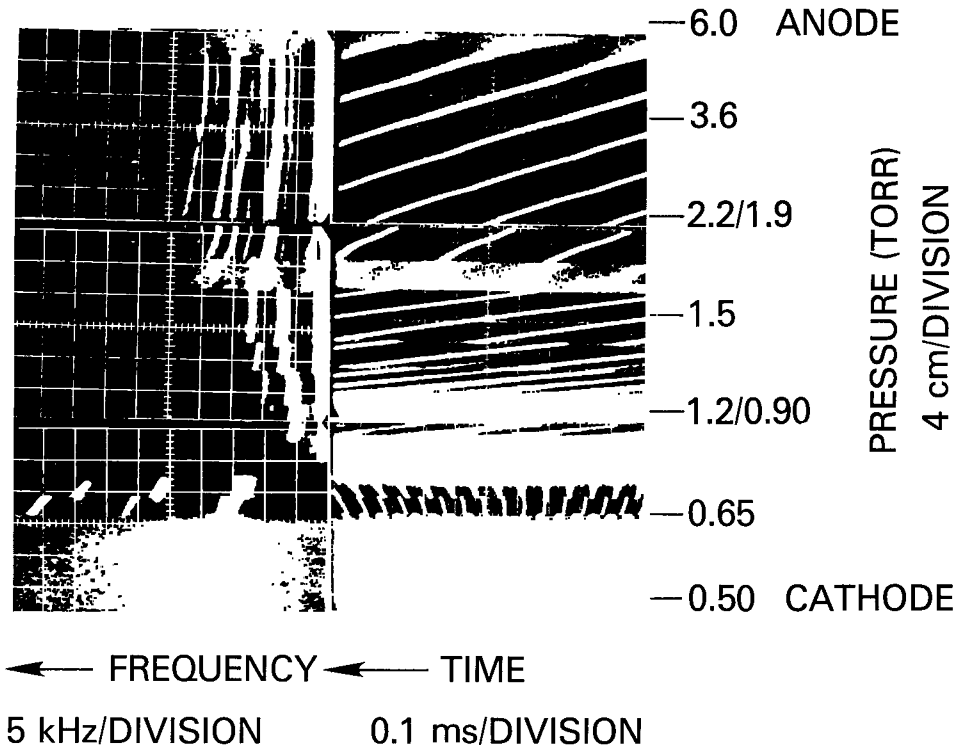

Fig. D27 — Current I = 10 mA, radius R = 0.95 cm, and I/R = 10.5 mA/cm

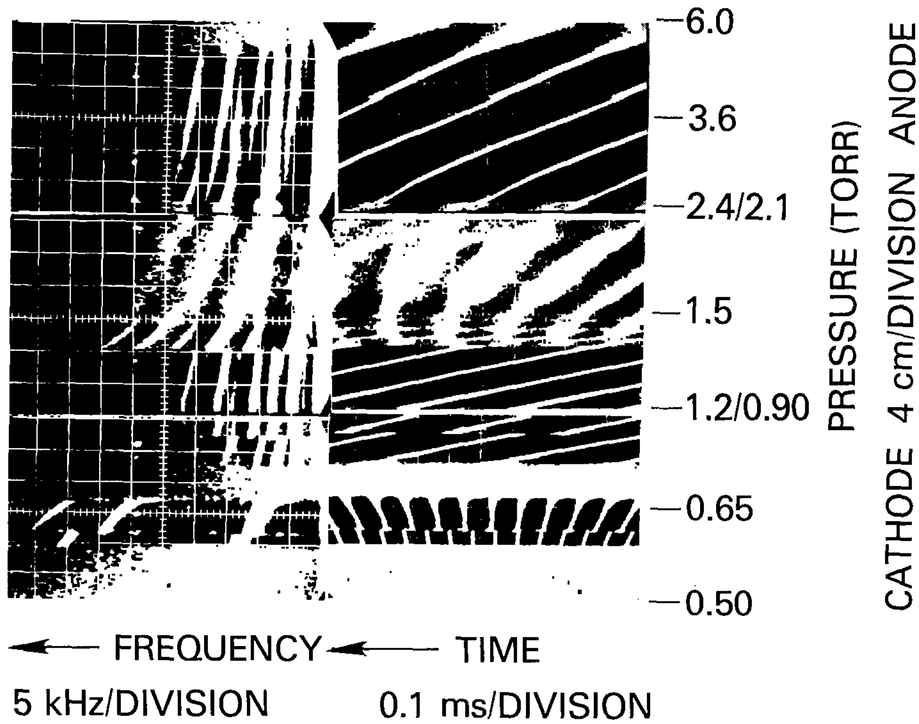

Fig. D28 — Current I = 20 mA, radius R = 0.95 cm, and I/R = 21 mA/cm

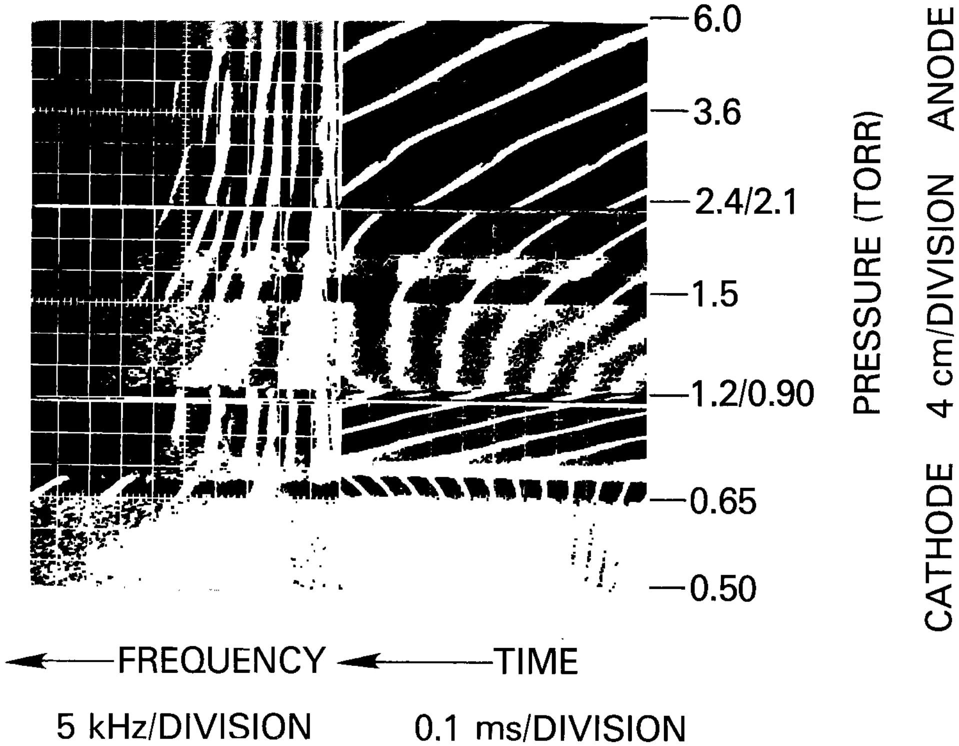

Fig. D29 — Current $I = 30$ mA, radius $R = 0.95$ cm, and $I/R = 31.6$ mA/cm

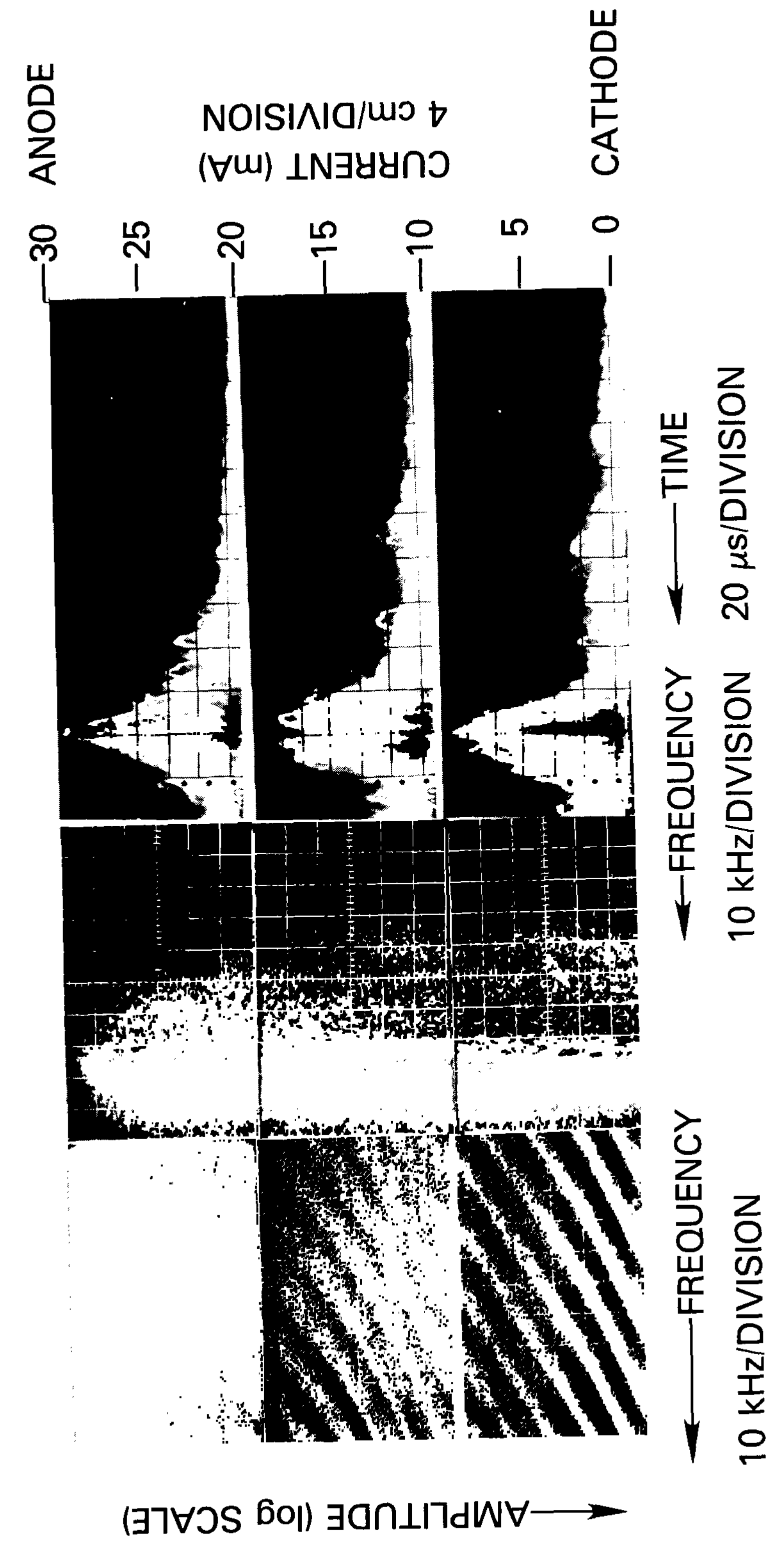

Fig. D30 — Pressure p = 0.4 torr, radius R = 0.95 cm, and pR = 0.38 torr-cm

Fig. D31 — Pressure p = 0.53 torr, radius R = 0.95 cm, and pR = 0.5 torr-cm

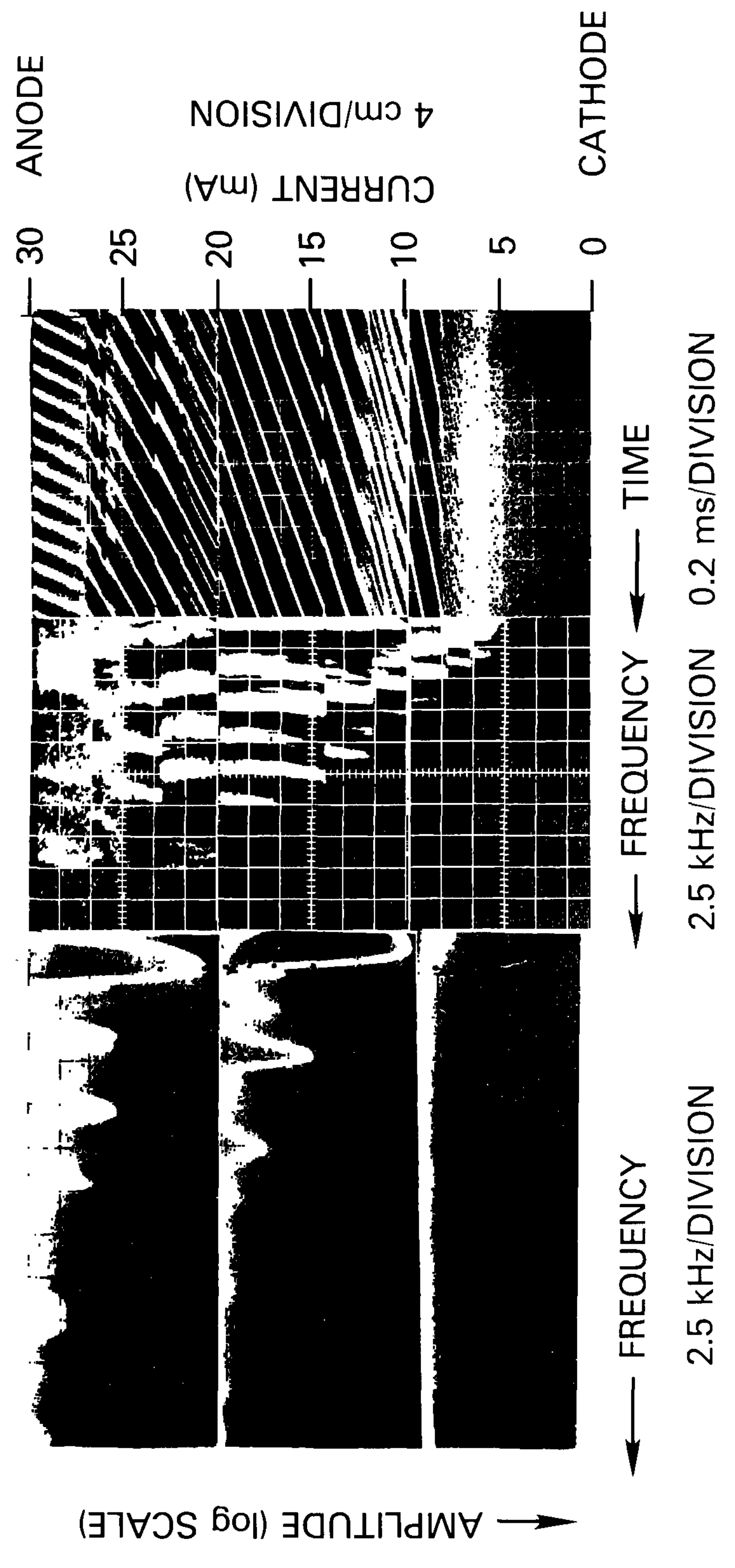

Fig. D32 — Pressure p = 1.05 torr, radius R = 0.95 cm, and pR = 1.0 torr-cm

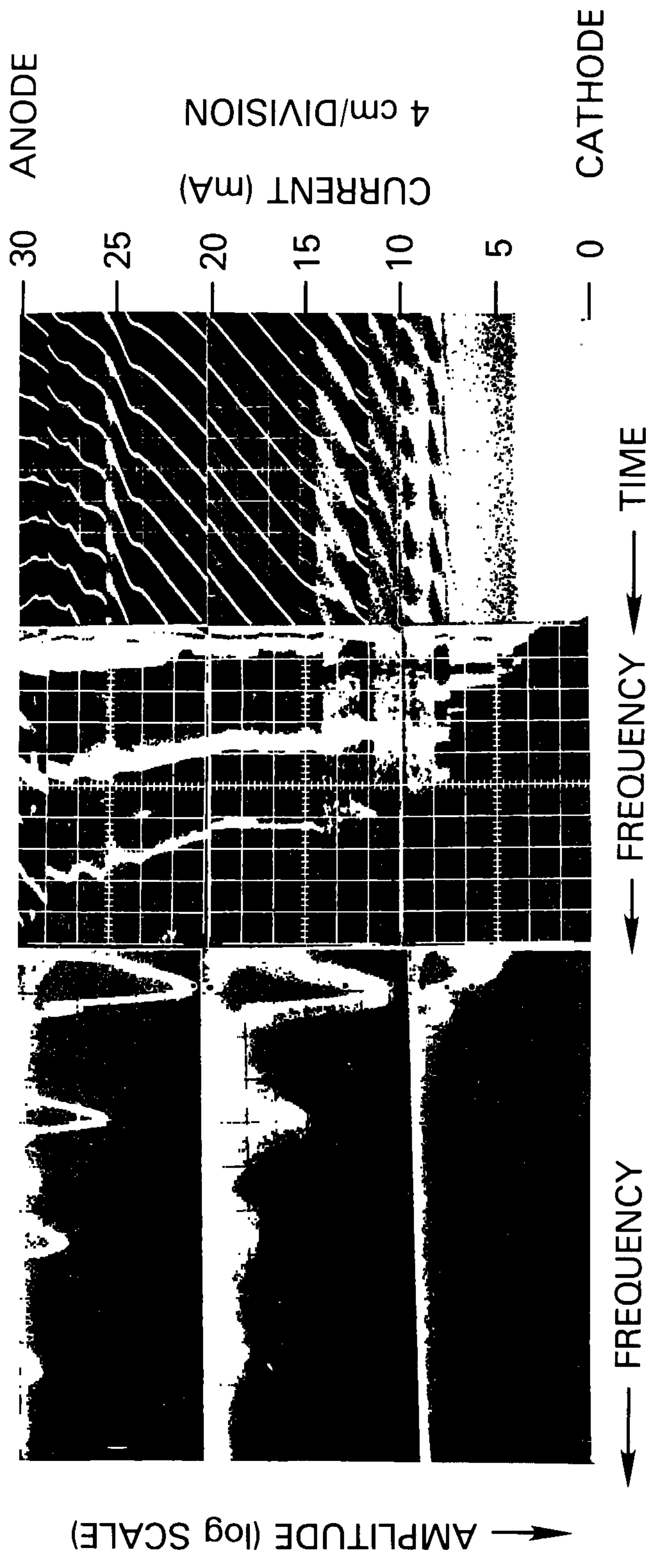

Fig. D33 — Pressure p = 2.1 torr, radius R = 0.95 cm, and pR = 2.0 torr-cm

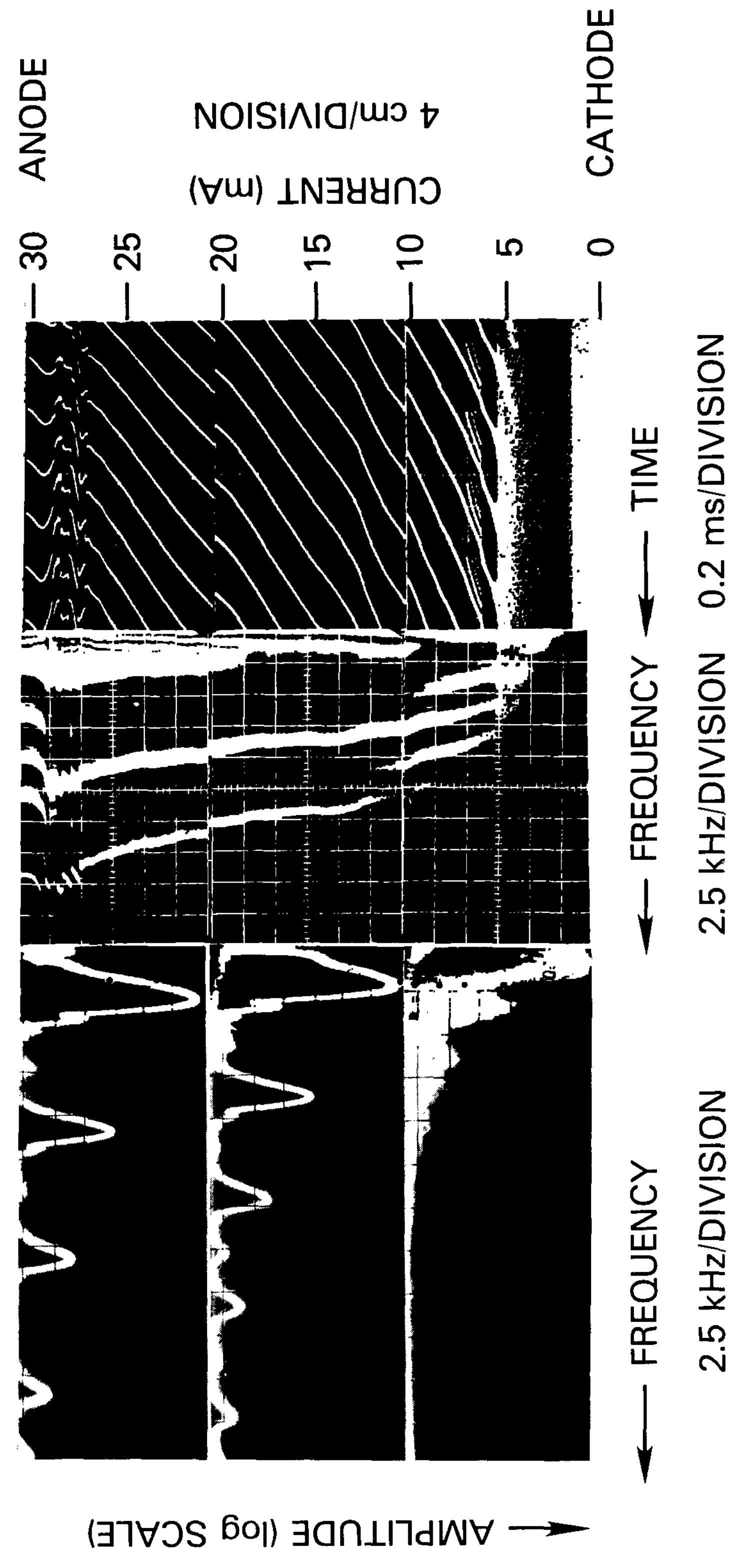

Fig. D34 — Pressure p = 3.2 torr, radius R = 0.95 cm, and pR = 3.0 torr-cm

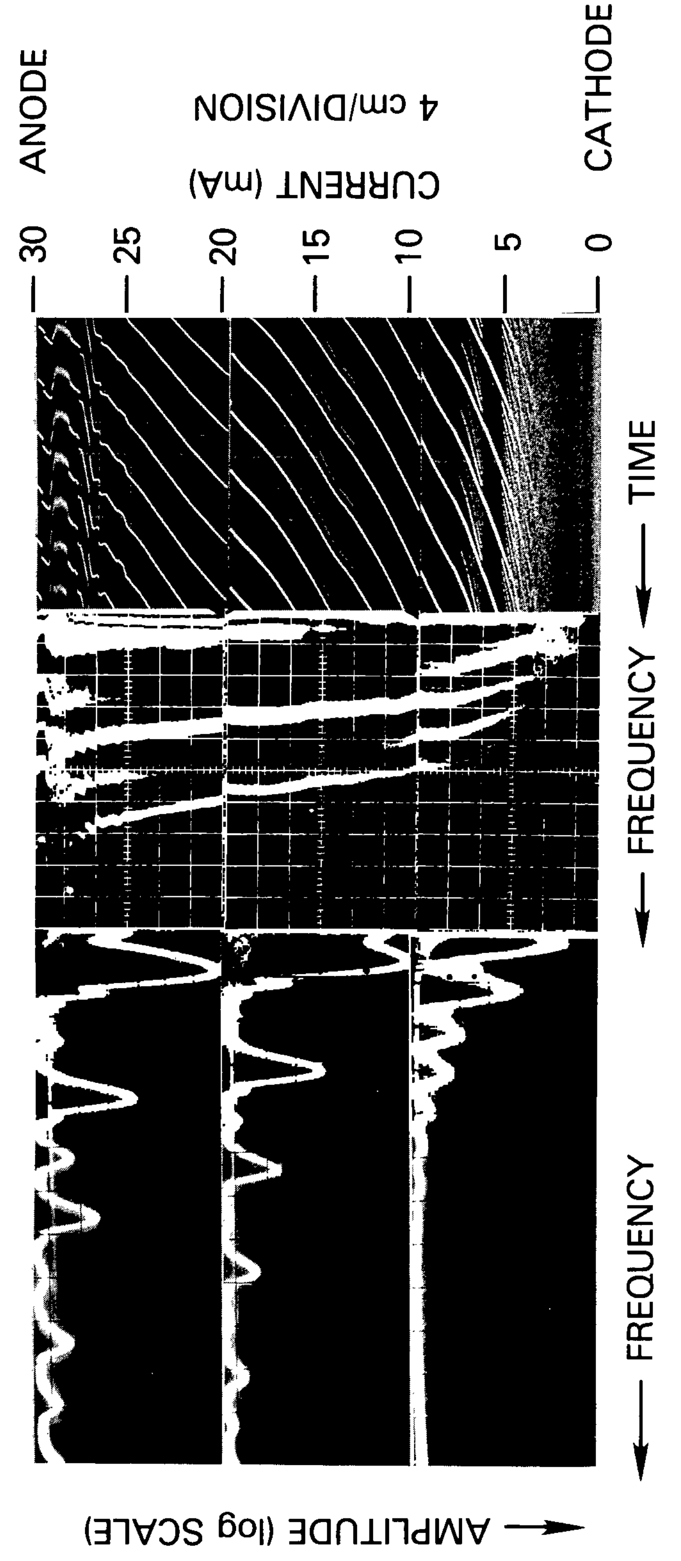

Fig. D35 — Pressure p = 4.2 torr, radius R = 0.95 cm, and pR = 4.0 torr-cm

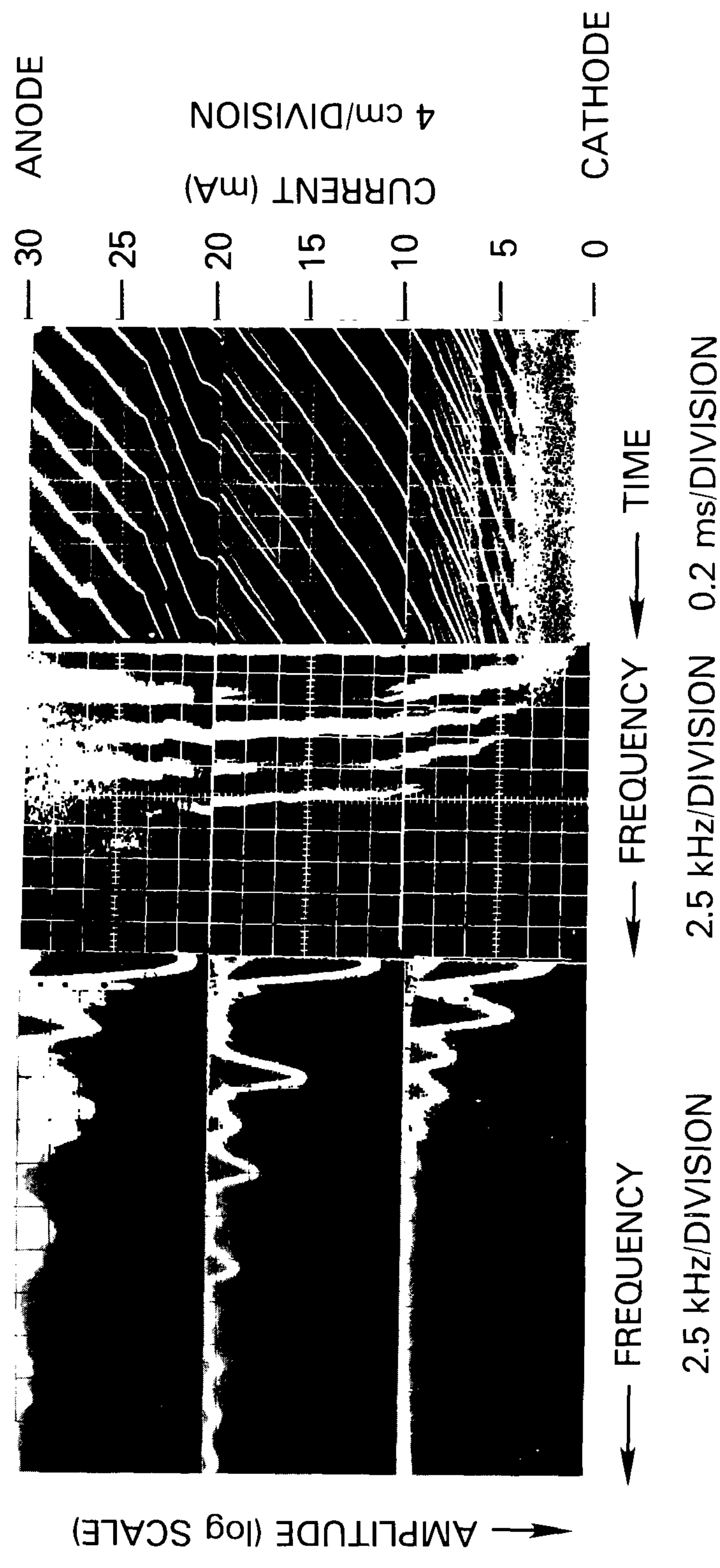

Fig. D36 — Pressure p = 5.3 torr, radius R = 0.95 cm, and pR = 5.0 torr-cm

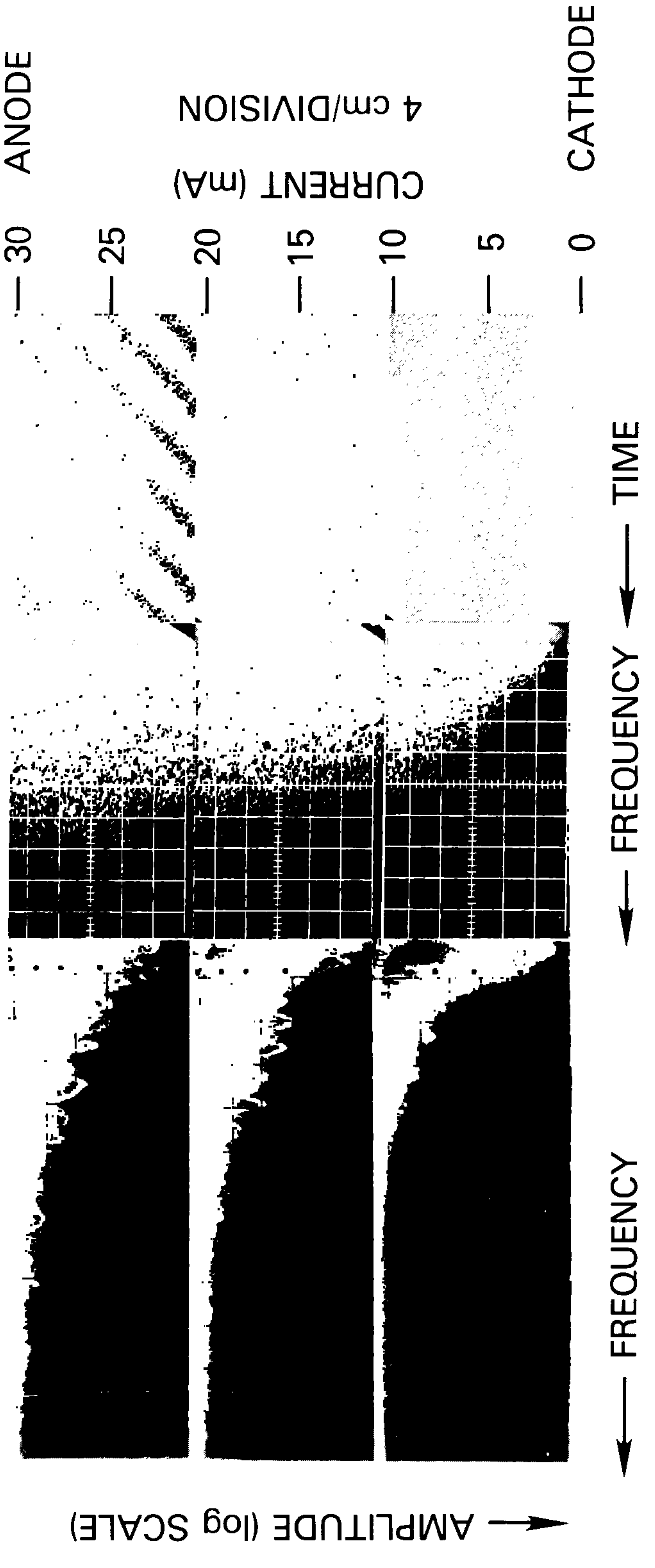

Fig. D37 — Pressure $p = 7.9$ torr, radius $R = 0.95$ cm, and $pR = 7.5$ torr-cm

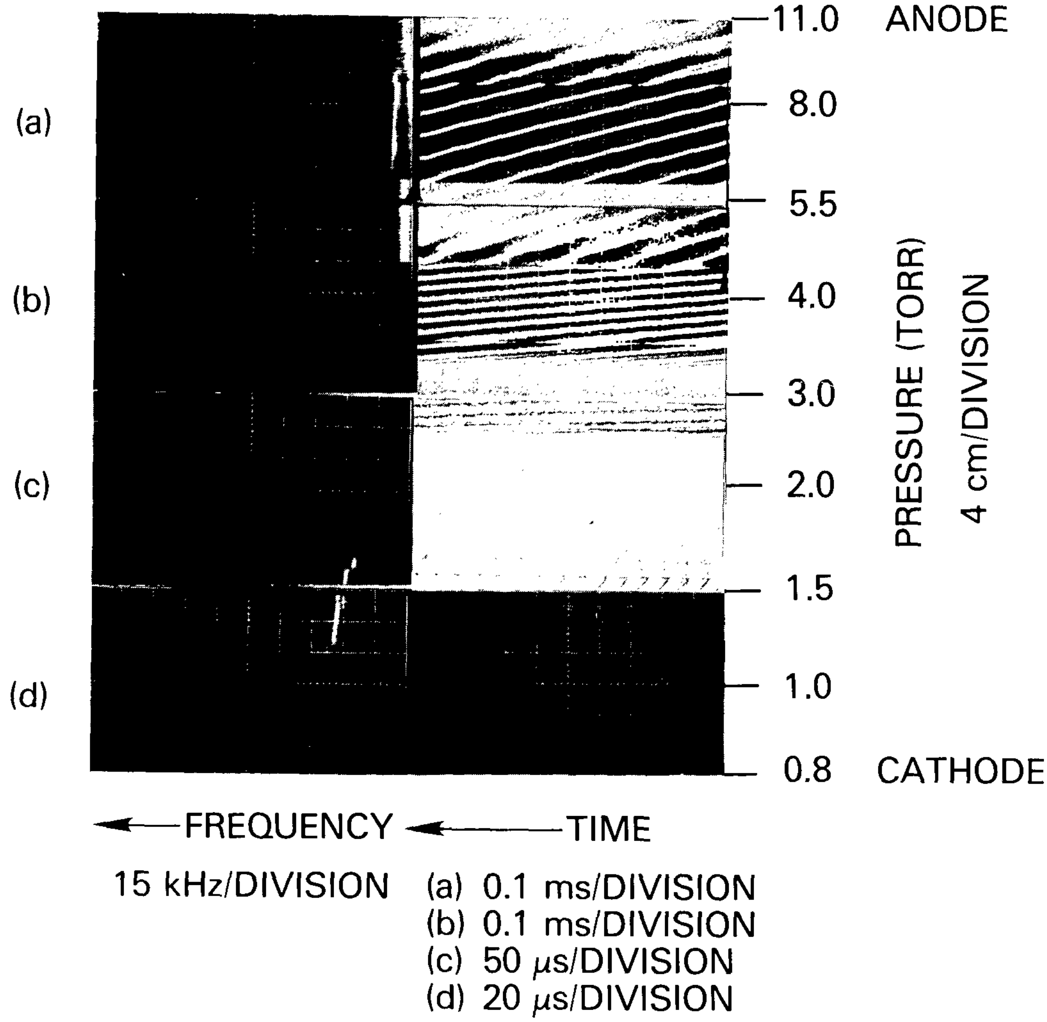

Fig. D38 — Current I = 2.5 mA, radius R = 0.5 cm, and I/R = 5 mA/cm

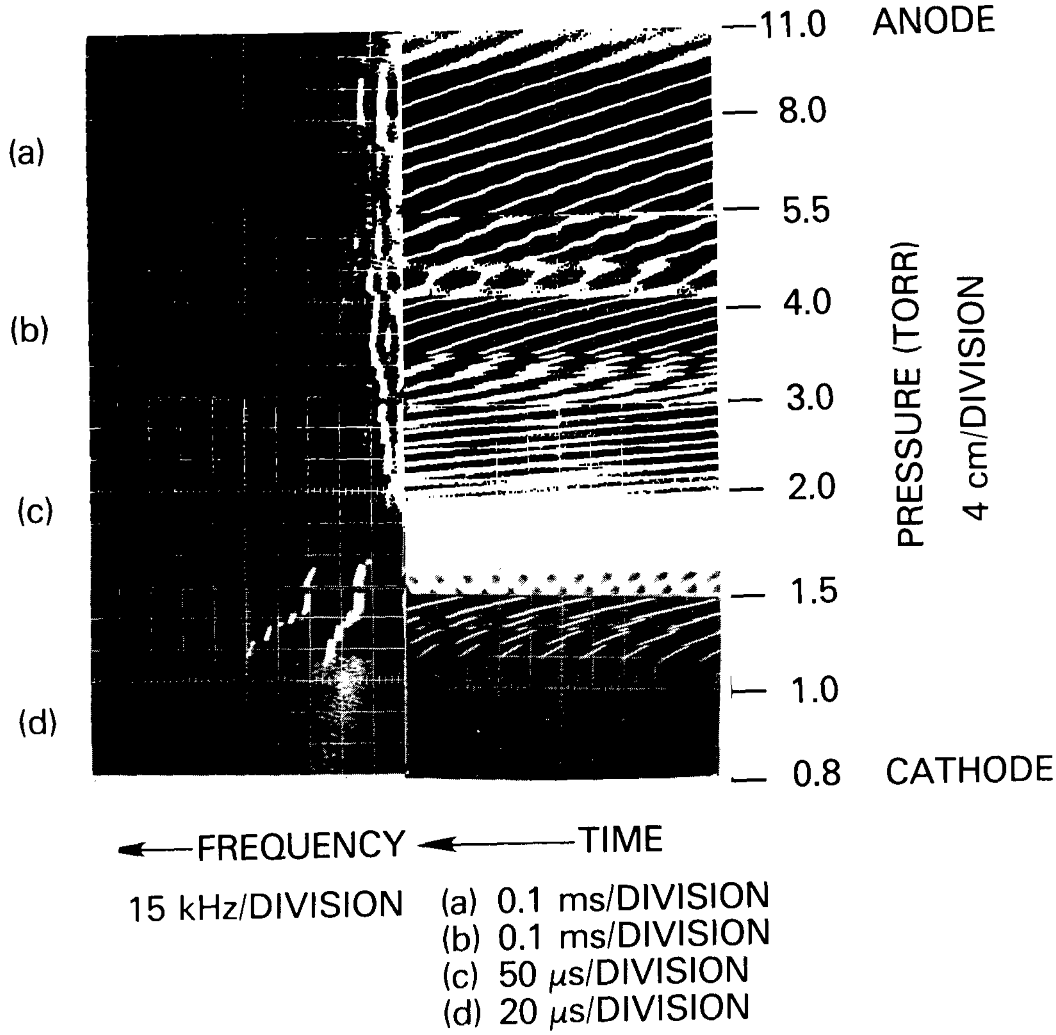

Fig. D39 — Current I = 5.0 mA, radius R = 0.5 cm, and I/R = 10 mA/cm

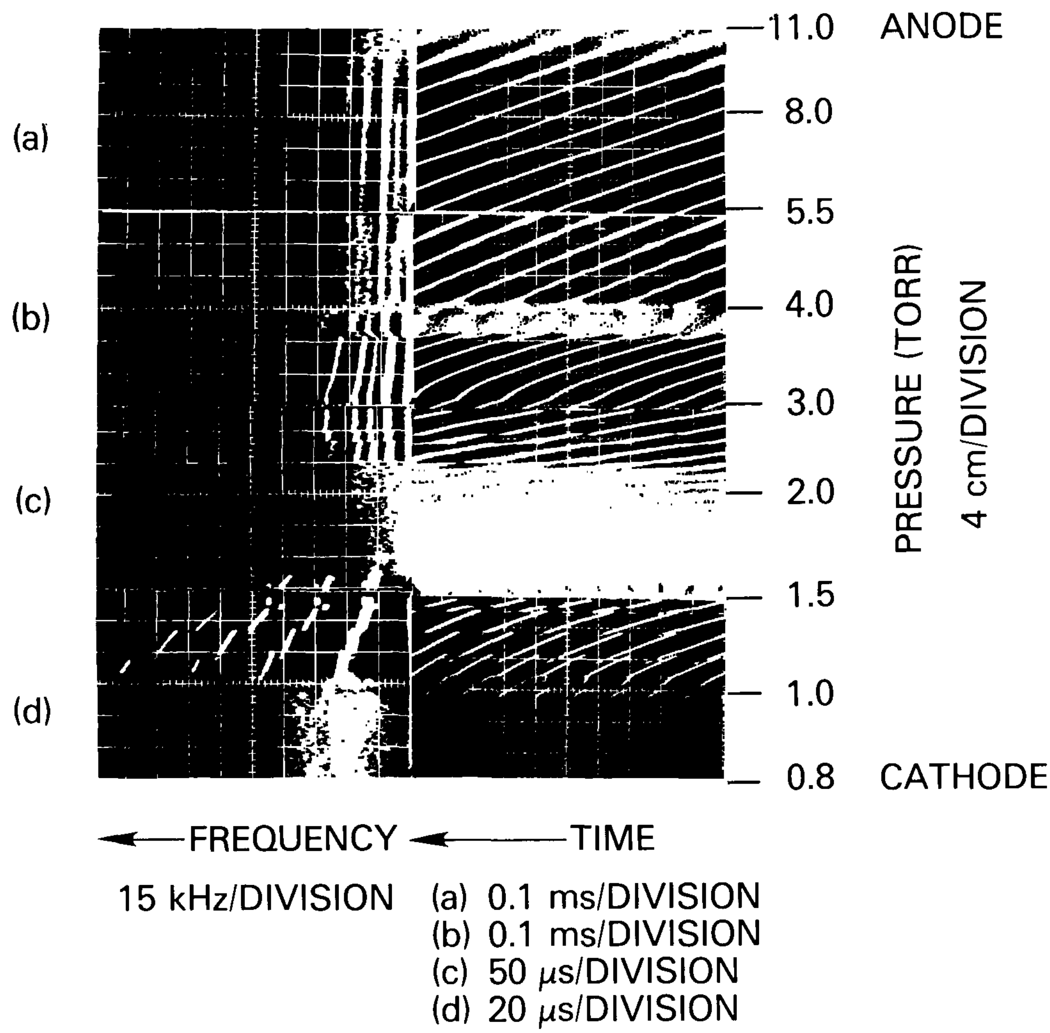

Fig. D40 – Current I = 7.5 mA, radius R = 0.5 cm, and I/R = 15 mA/cm

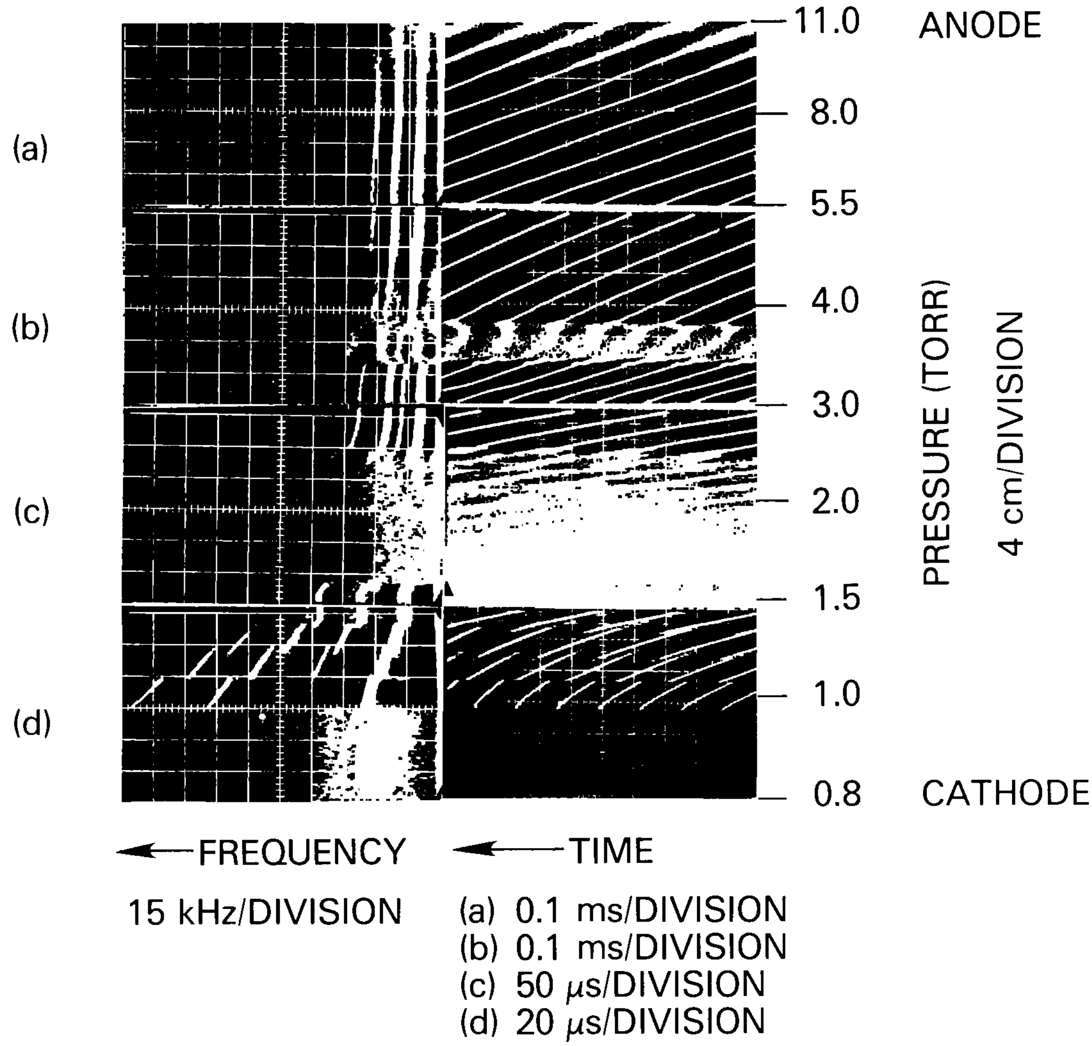

Fig. D41 — Current I = 10 mA, radius R = 0.5 cm, and I/R = 20 mA/cm

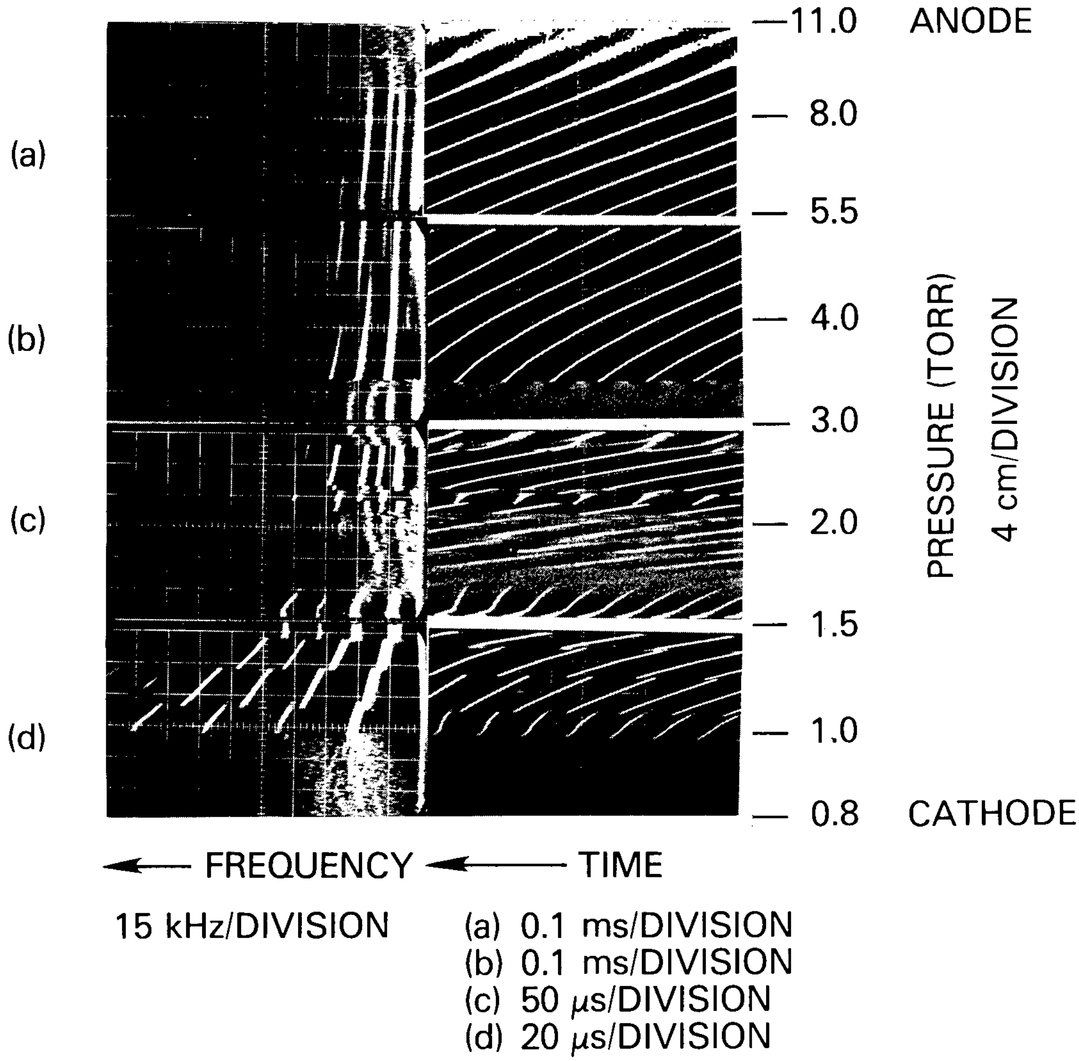

Fig. D42 — Current I = 15 mA, radius R = 0.5 cm, and I/R = 30 mA/cm

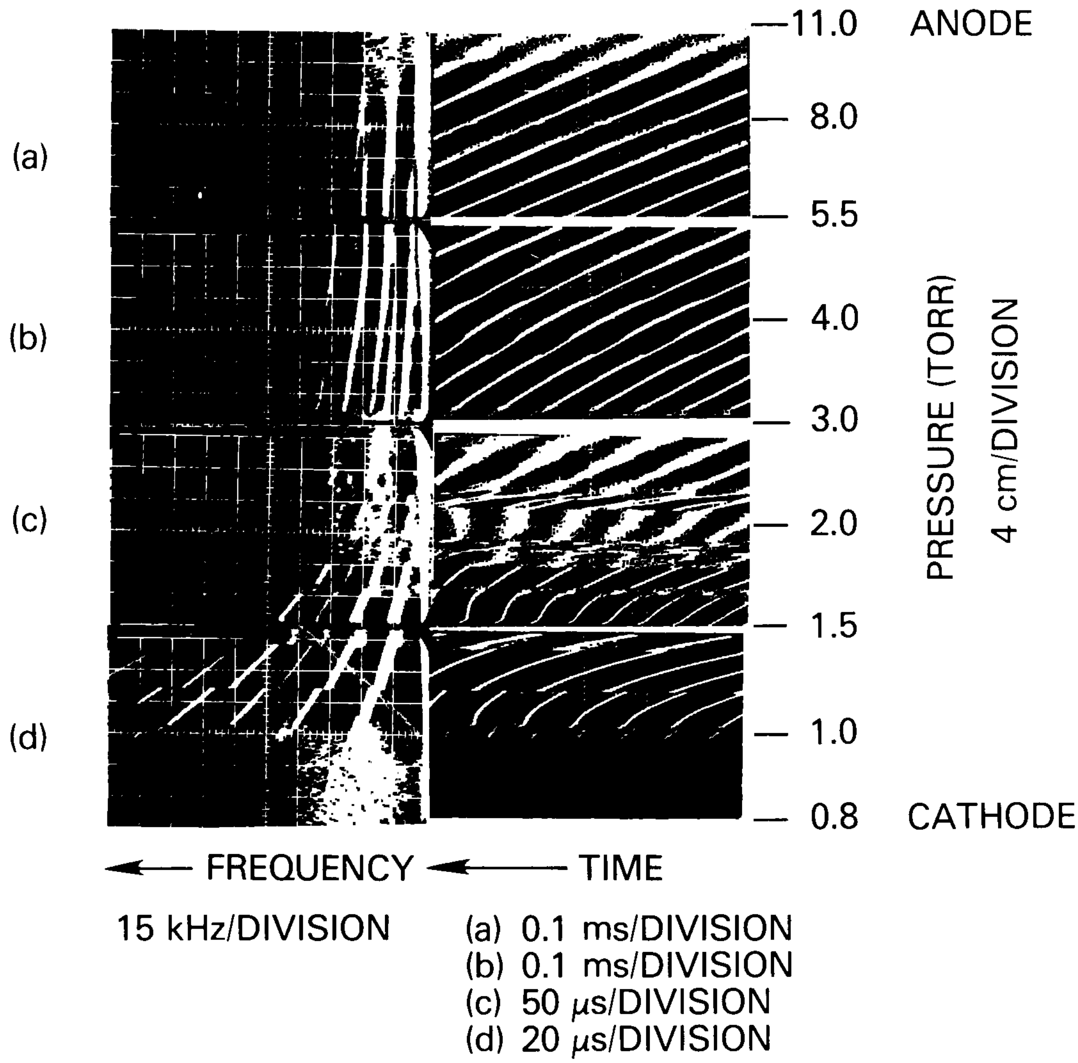

Fig. D43 — Current I = 20 mA, radius R = 0.5 cm, and I/R = 40 mA/cm

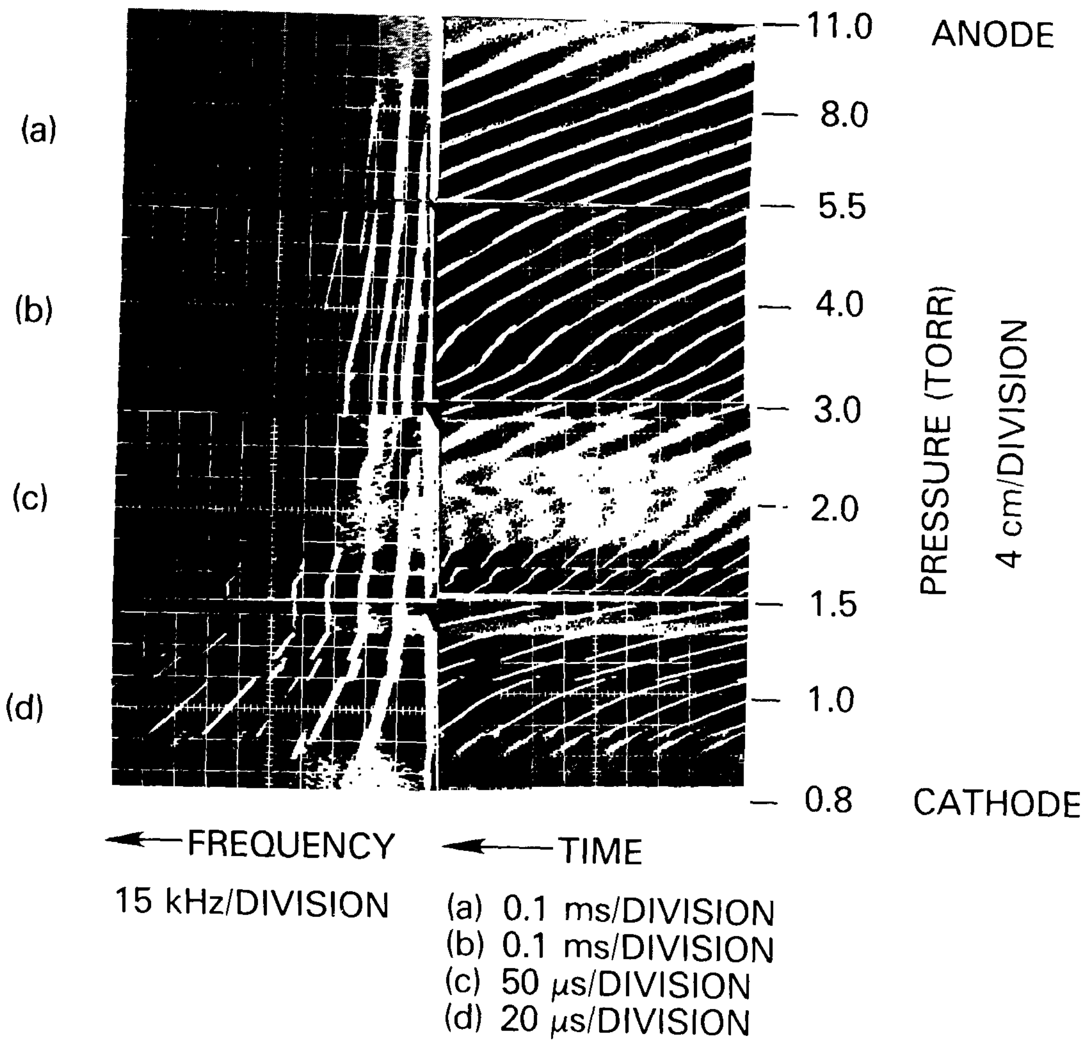

Fig. D44 — Current I = 25 mA, radius R = 0.5 cm, and I/R = 50 mA/cm

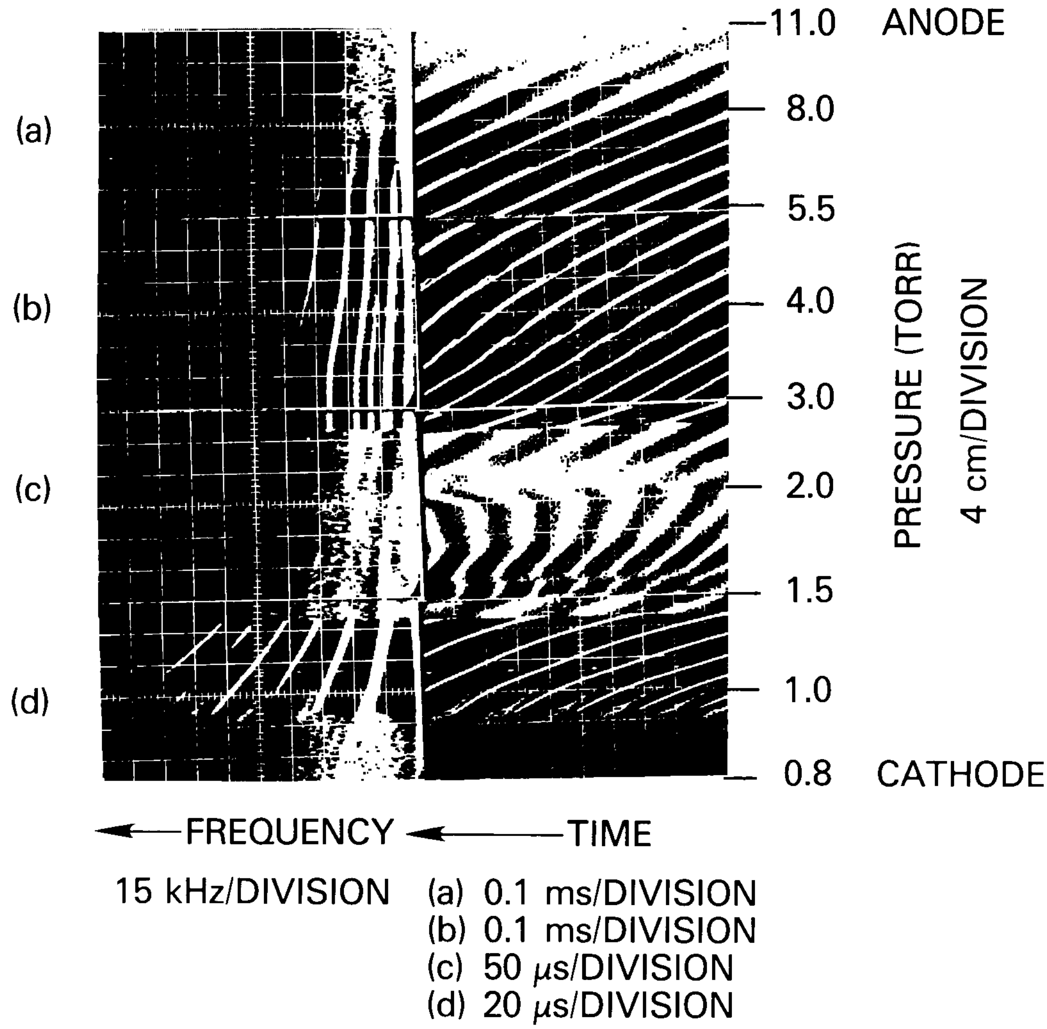

Fig. D45 — Current I = 30 mA, radius R = 0.5 cm, and I/R = 60 mA/cm

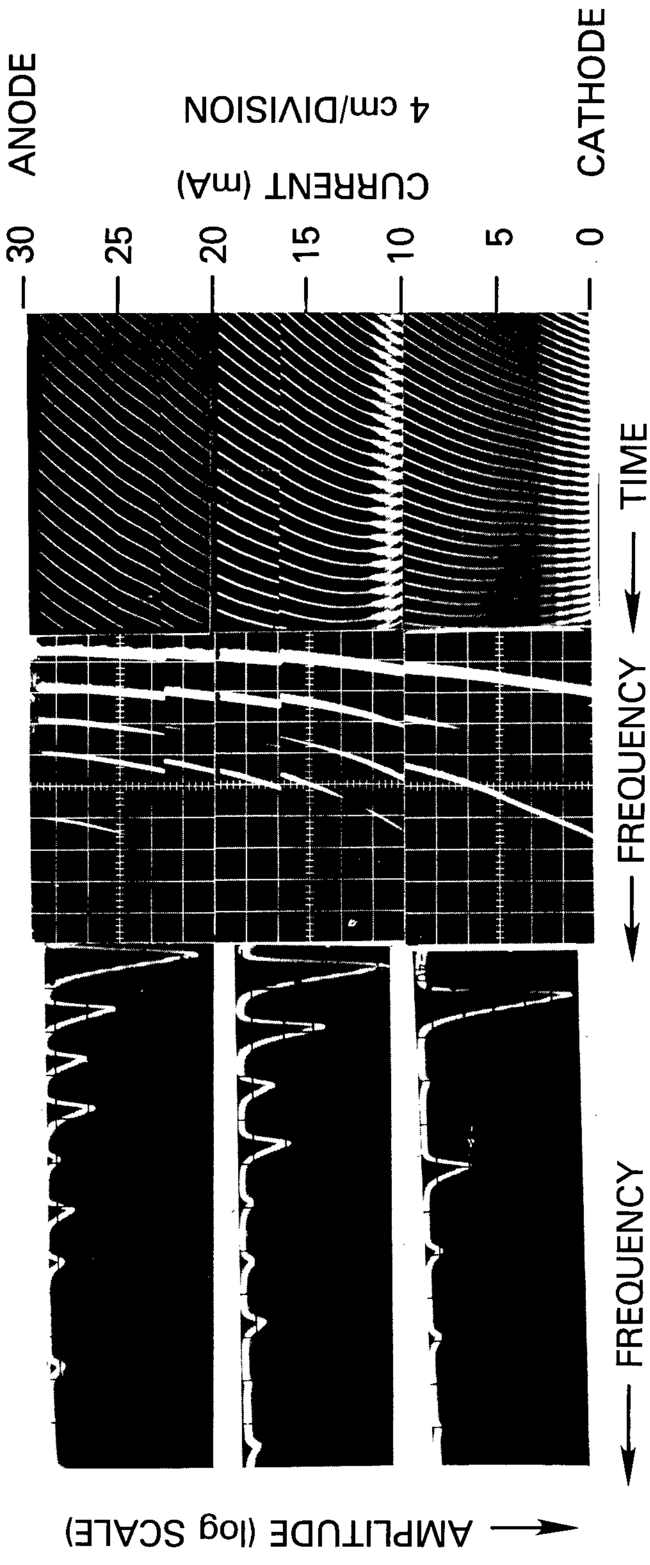

Fig. D46 — Pressure p = 1.3 torr, radius R = 0.5 cm, and pR = 0.65 torr-cm

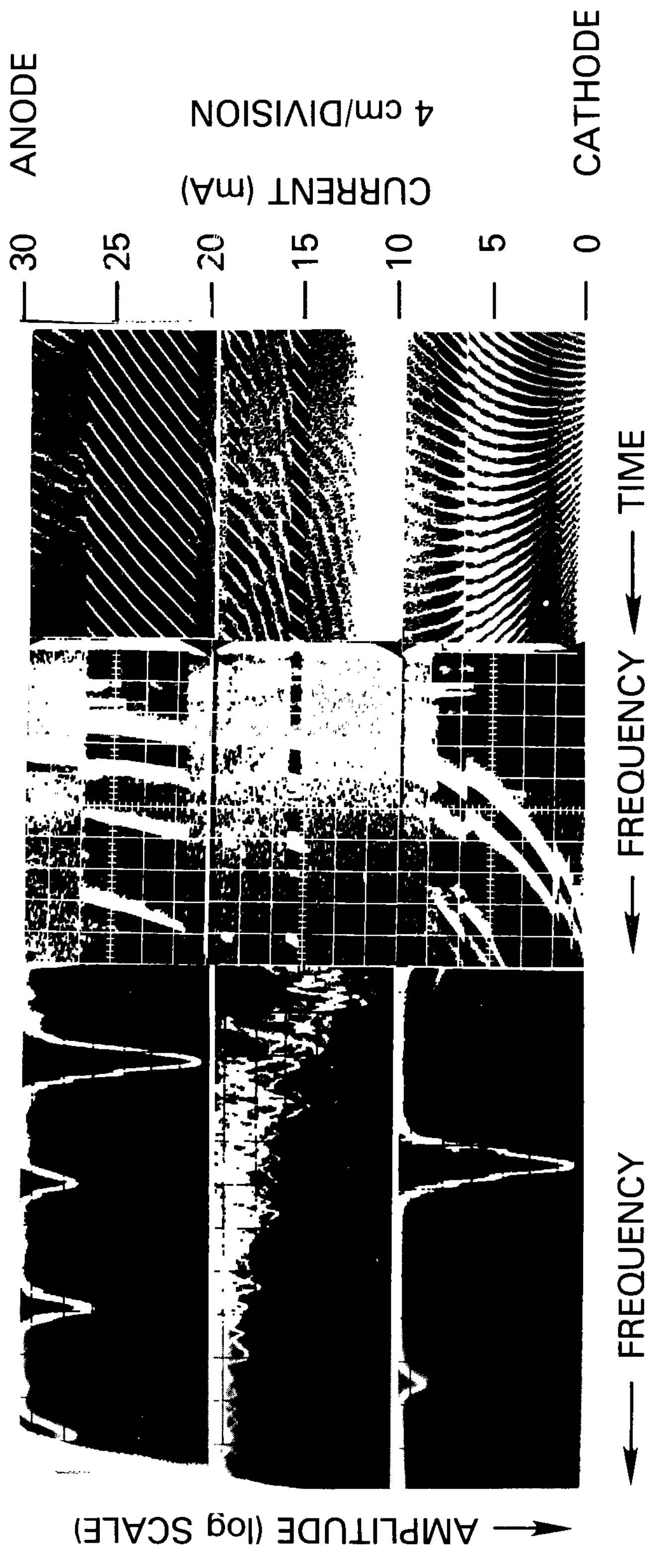

Fig. D47 — Pressure $p = 1.5$ torr, radius $R = 0.5$ cm, and $pR = 0.75$ torr-cm

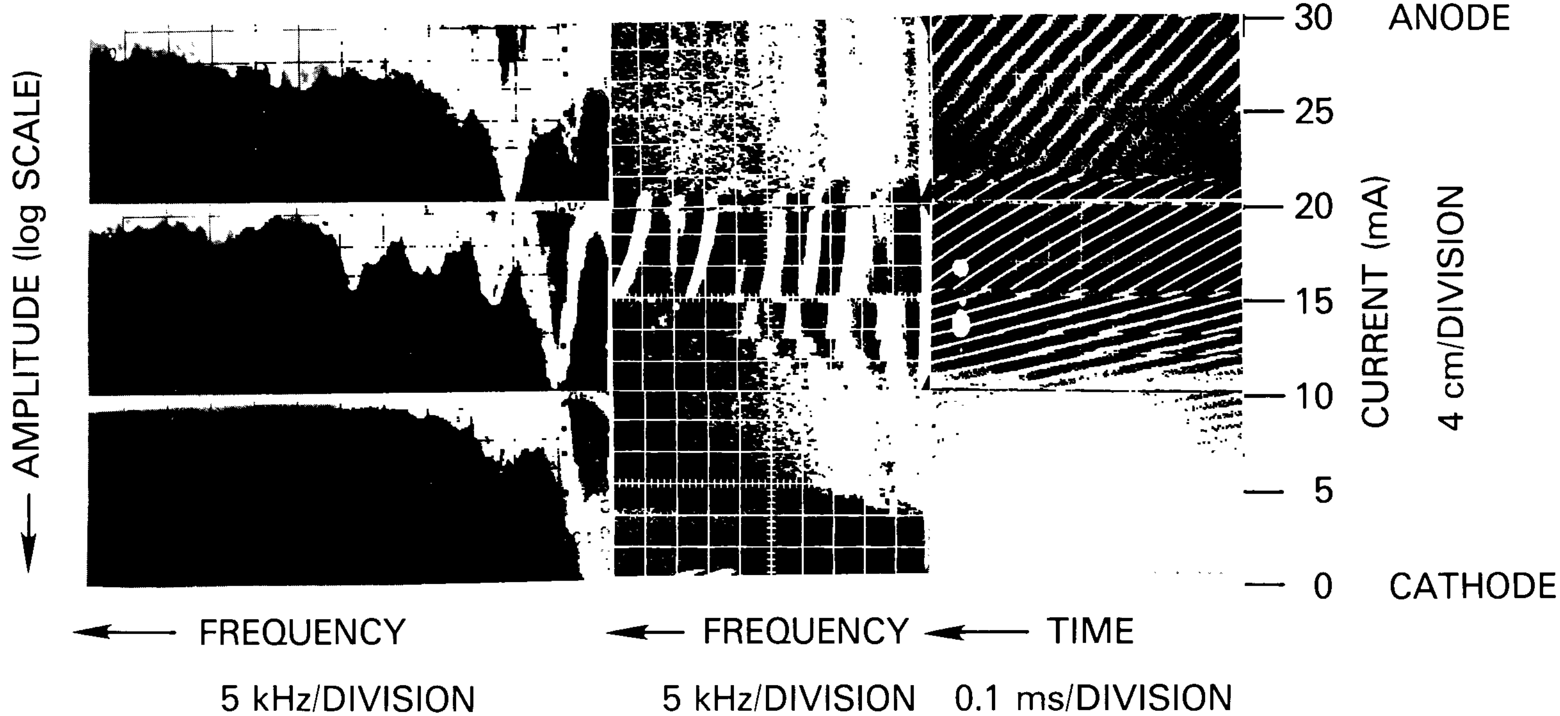

Fig. D48 — Pressure $p = 2.0$ torr, radius $R = 0.5$ cm, and $pR = 1.0$ torr-cm

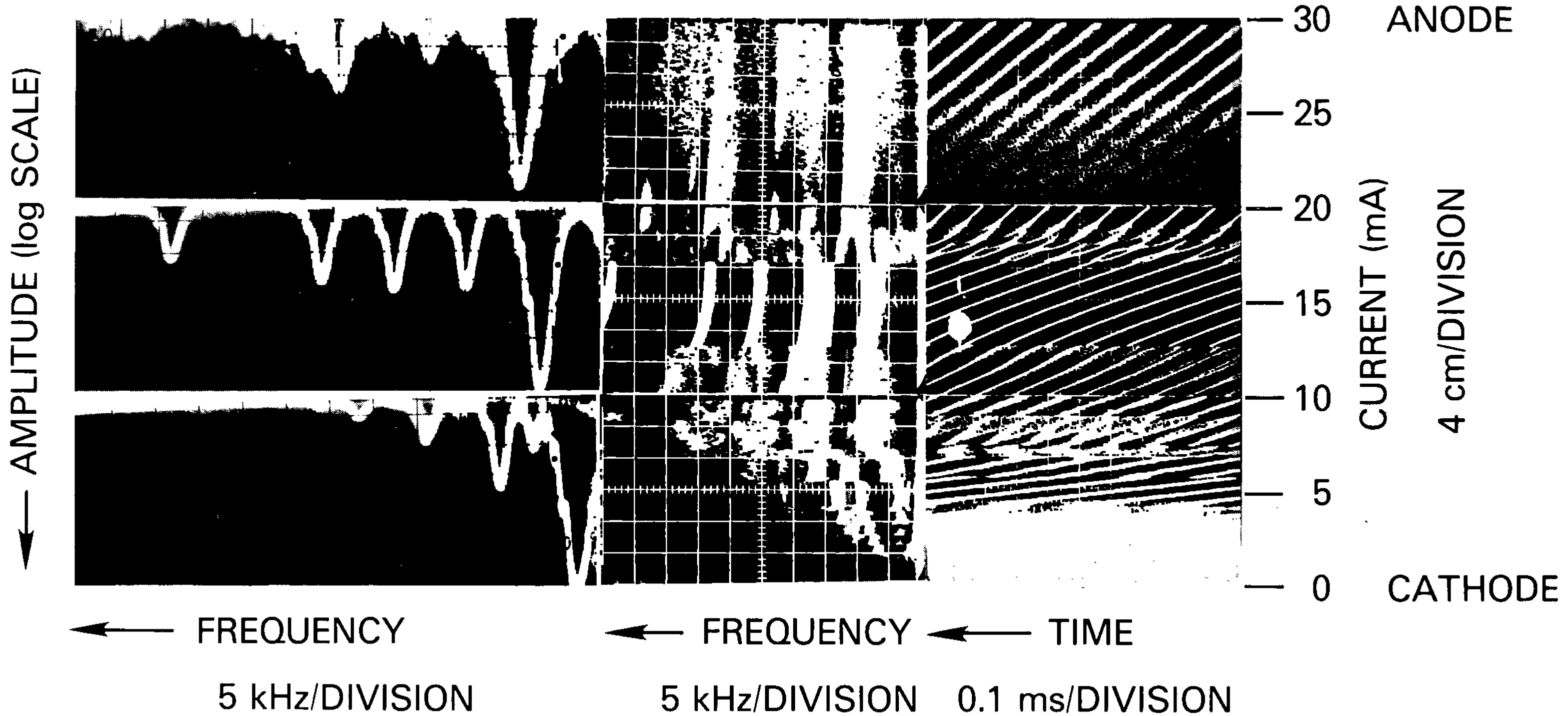

Fig. D49 — Pressure p = 2.5 torr, radius R = 0.5 cm, and pR = 1.25 torr-cm

UNCLASSIFIED

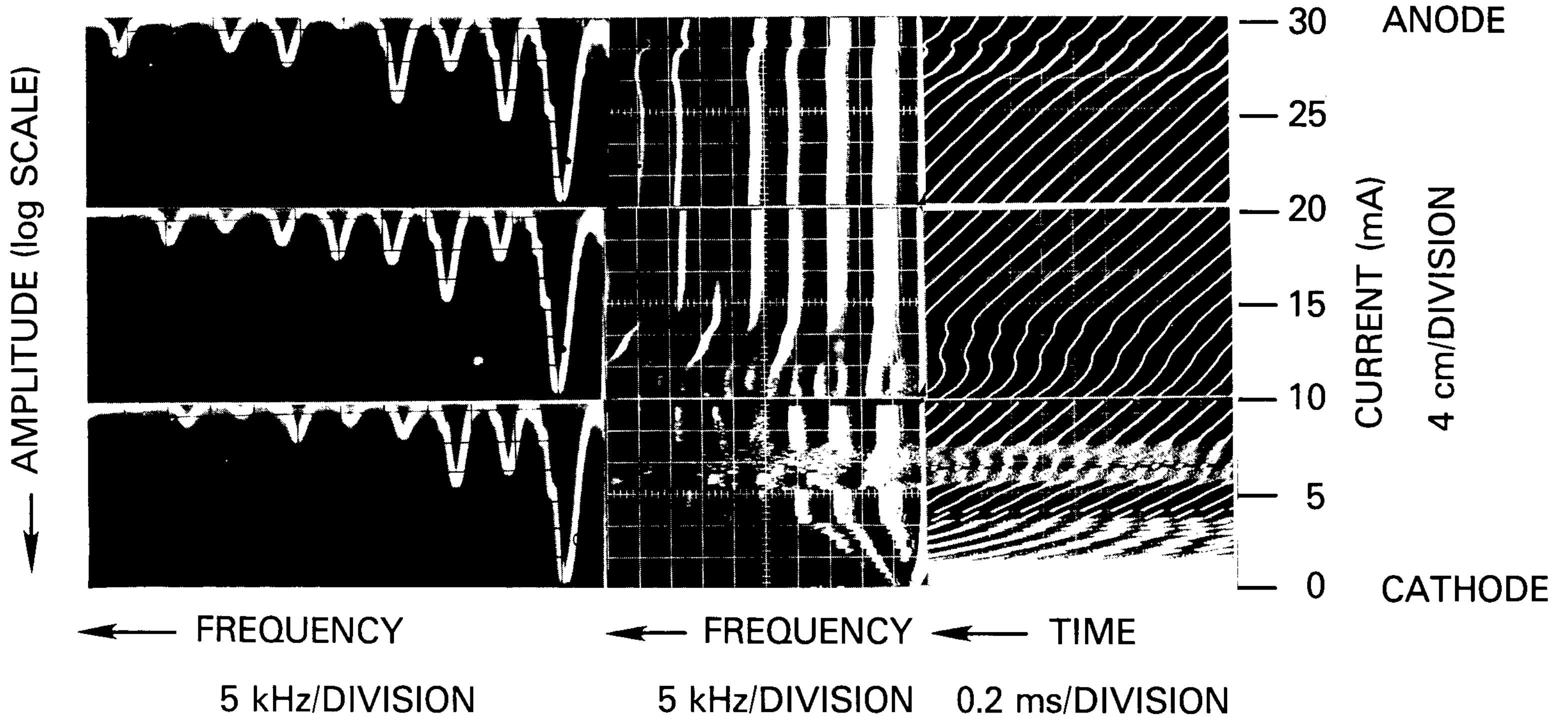

Fig. D50 — Pressure $p = 4.0$ torr, radius $R = 0.5$ cm, and $pR = 2.0$ torr-cm

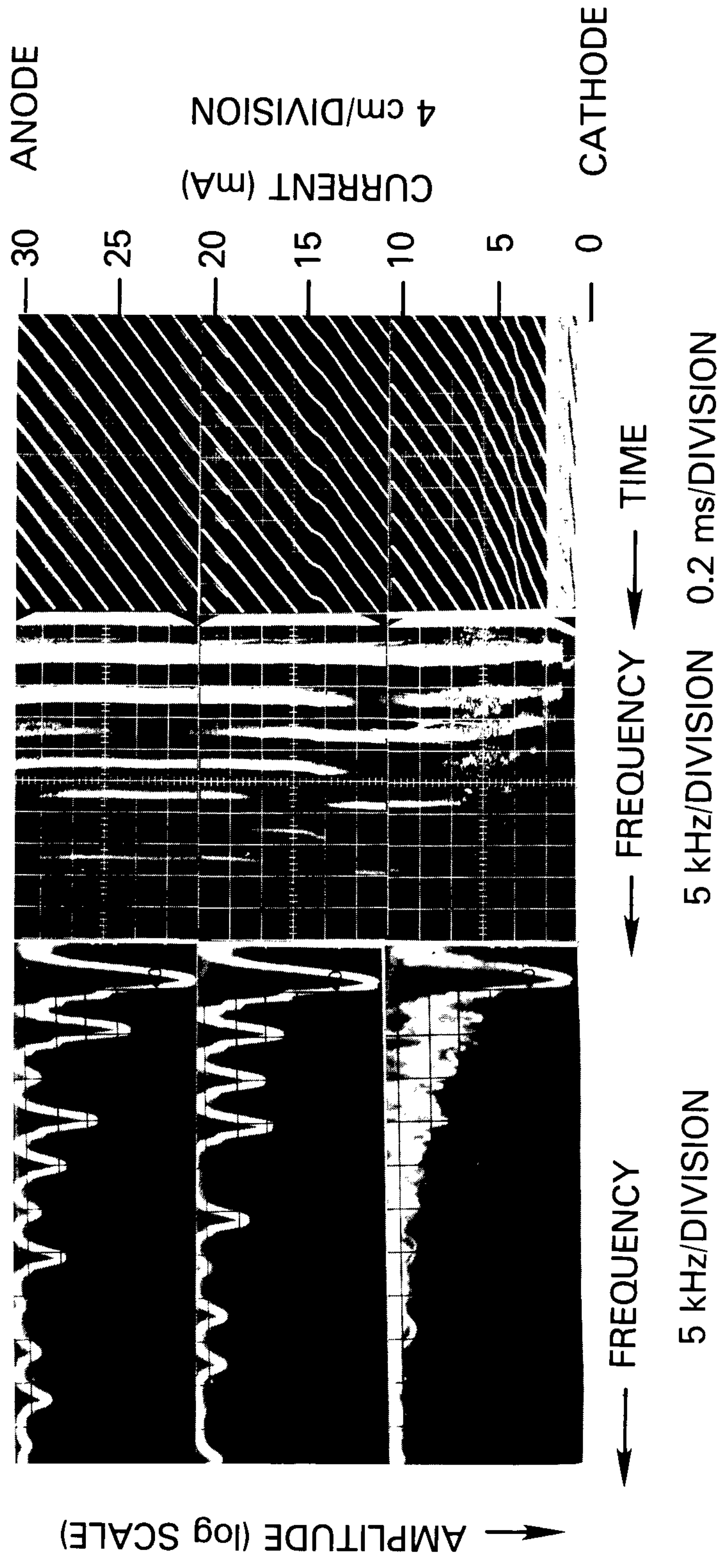

Fig. D51 — Pressure p = 6.0 torr, radius R = 0.5 cm, and pR = 3.0 torr-cm

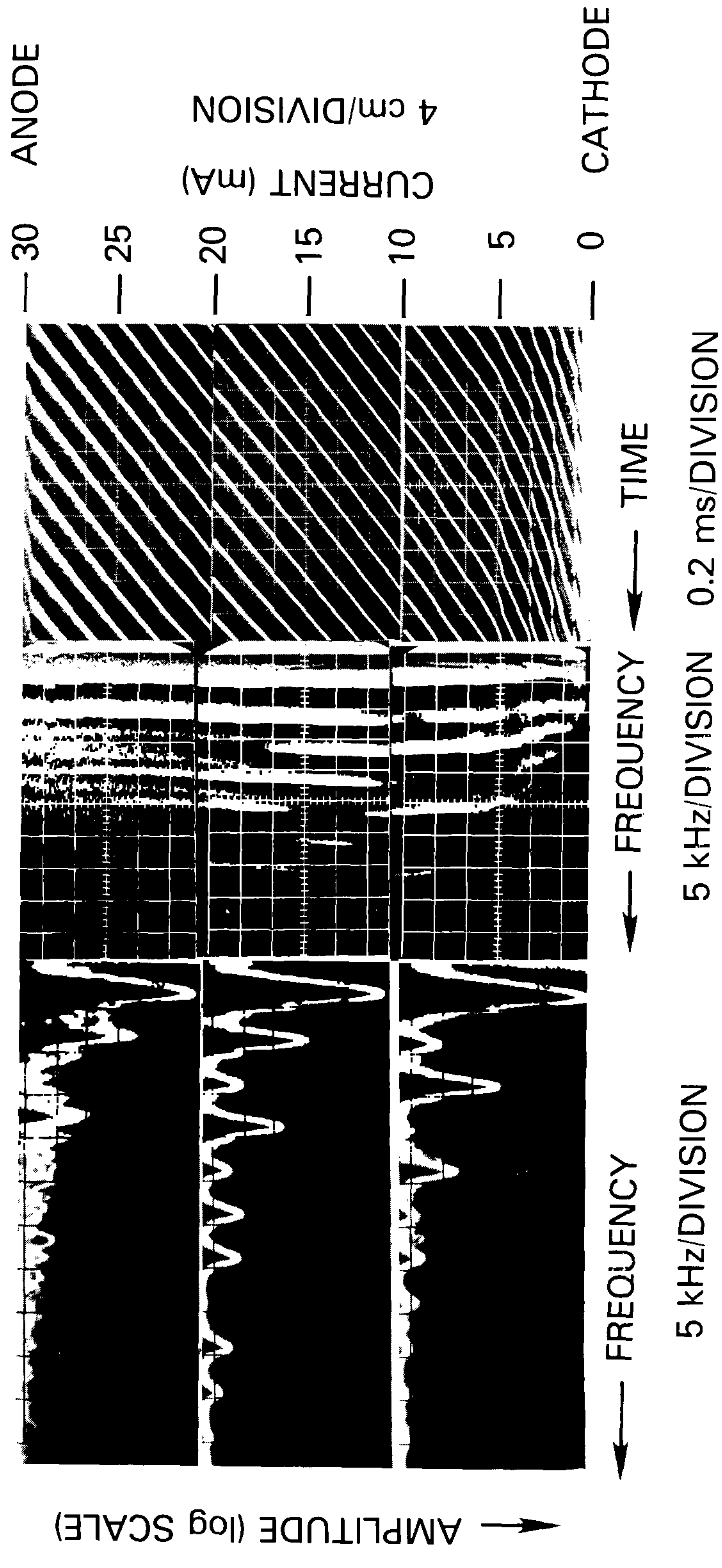

Fig. D52 – Pressure p = 8.0 torr, radius R = 0.5 cm, and pR = 4.0 torr-cm

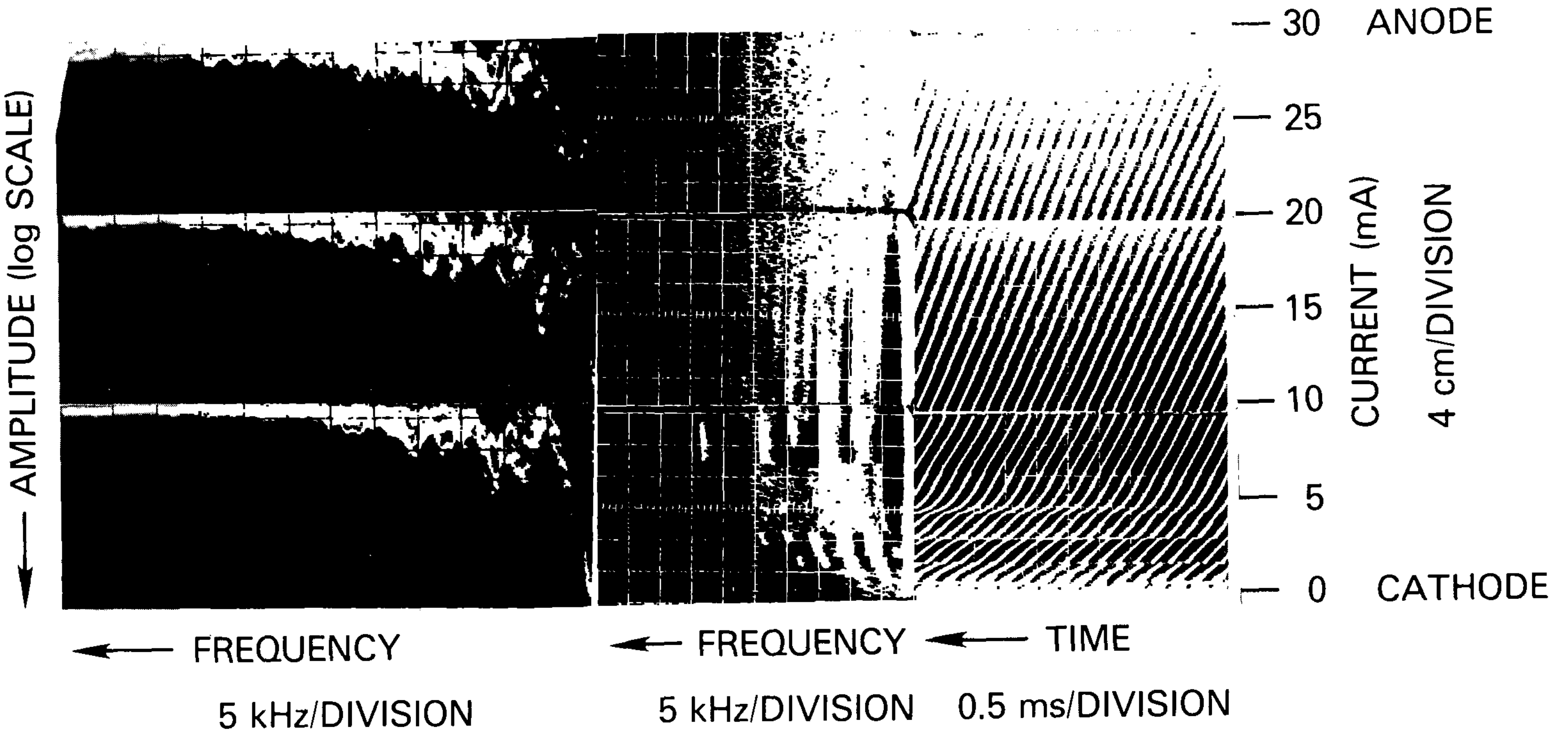

Fig. D53 — Pressure p = 10.0 torr, radius R = 0.5 cm, and pR = 5.0 torr-cm

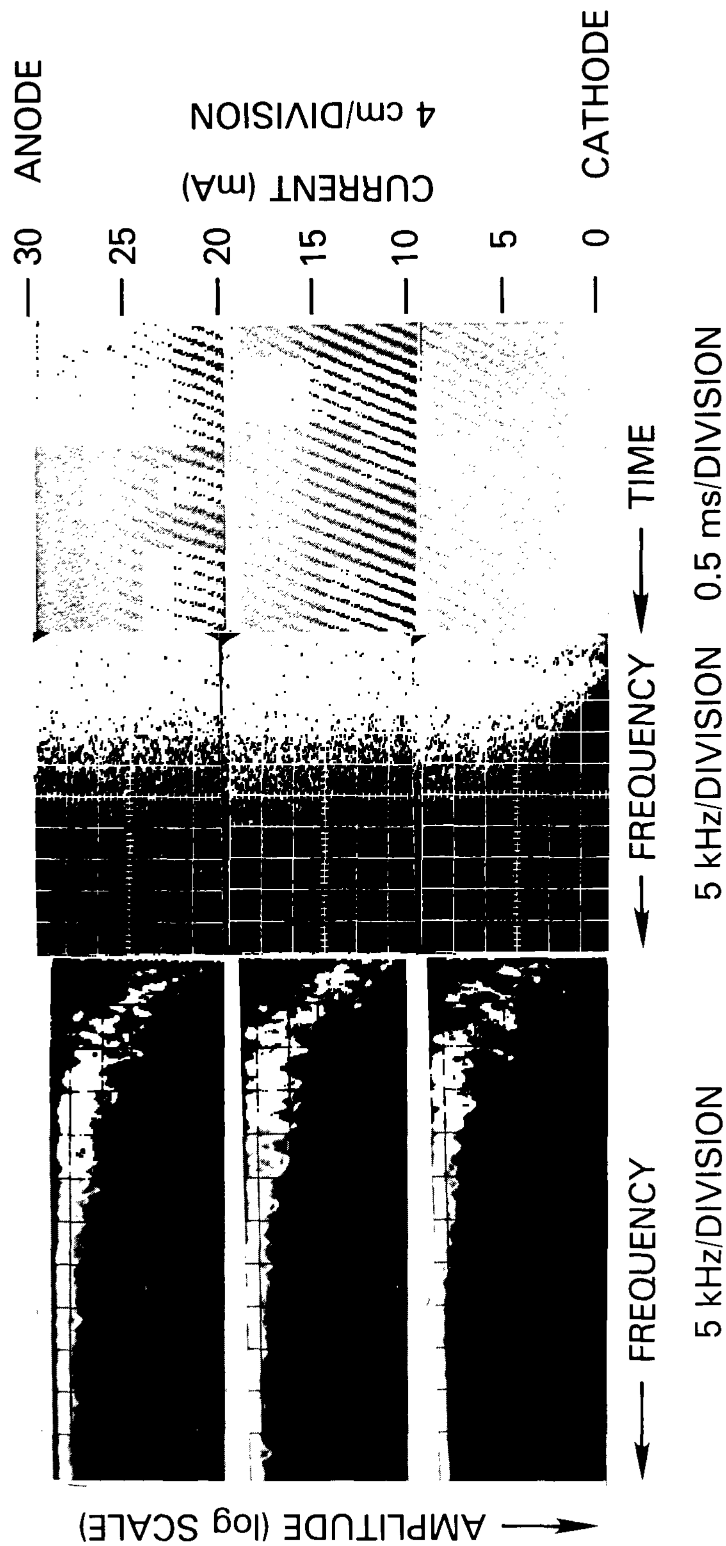

Fig. D54 — Pressure $p = 15.0$ torr, radius $R = 0.5$ cm, and $pR = 7.5$ torr-cm

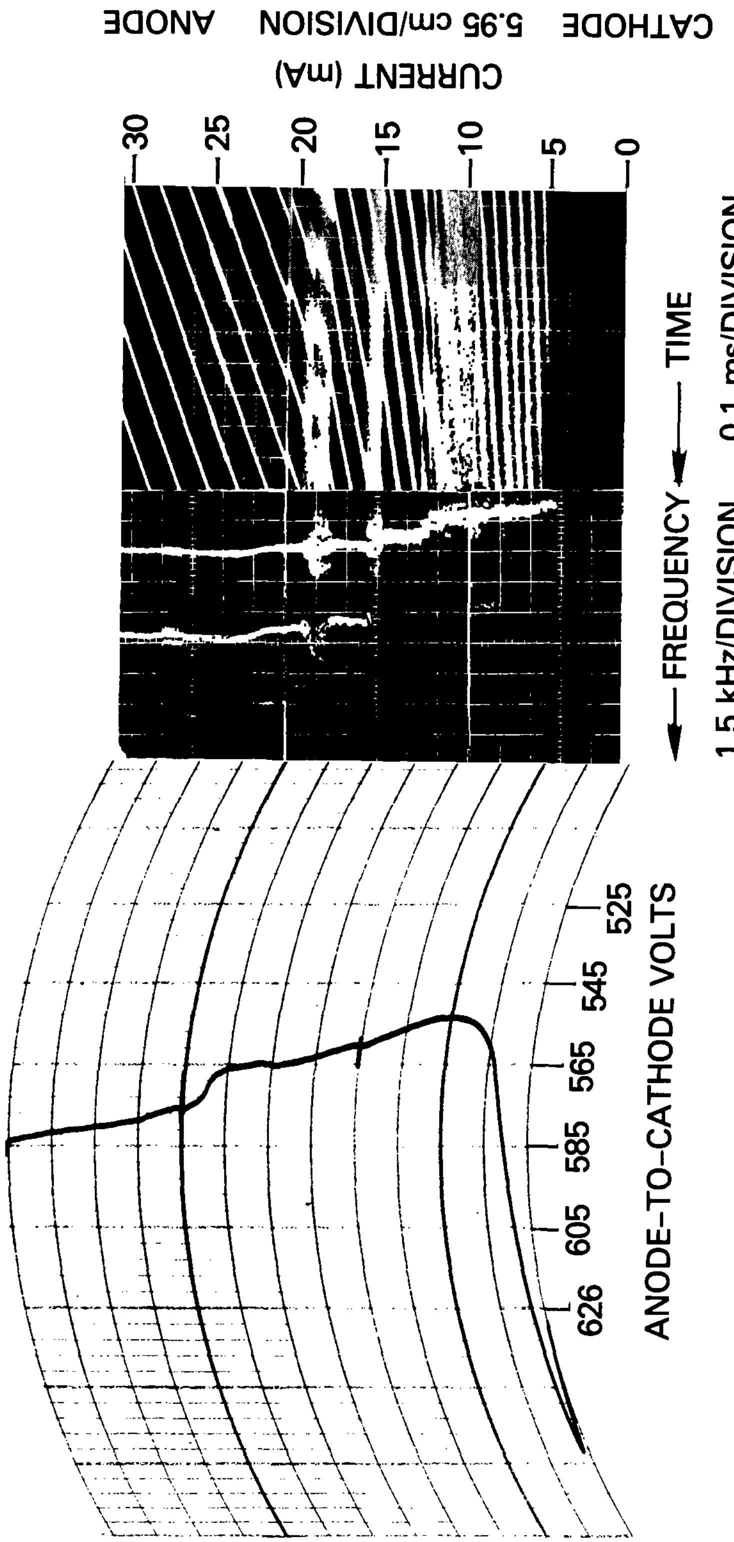

Fig. D55 — Pressure p = 1.5 torr, radius R = 0.95 cm, and 0% argon

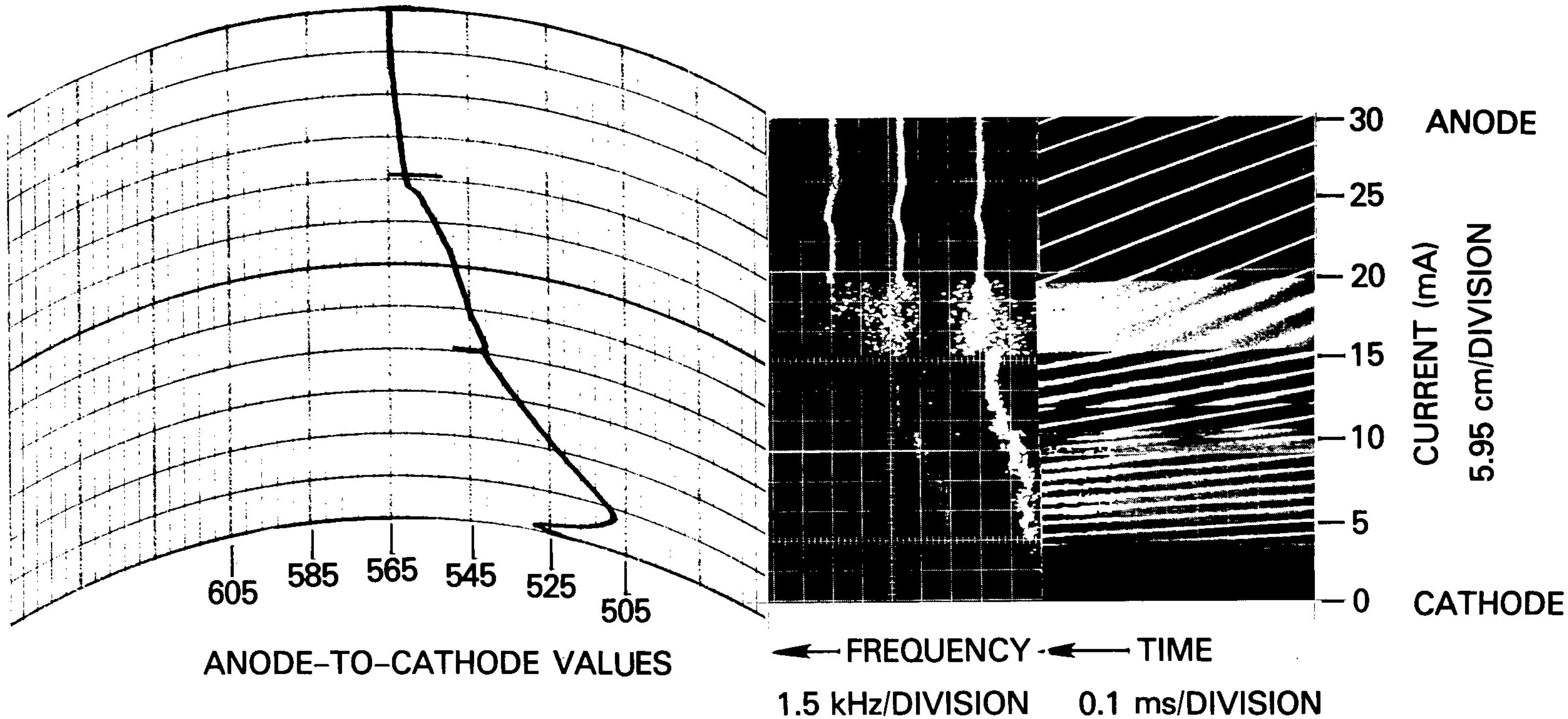

Fig. D56 — Pressure p = 1.5 torr, radius R = 0.95 cm, and 0.02% argon

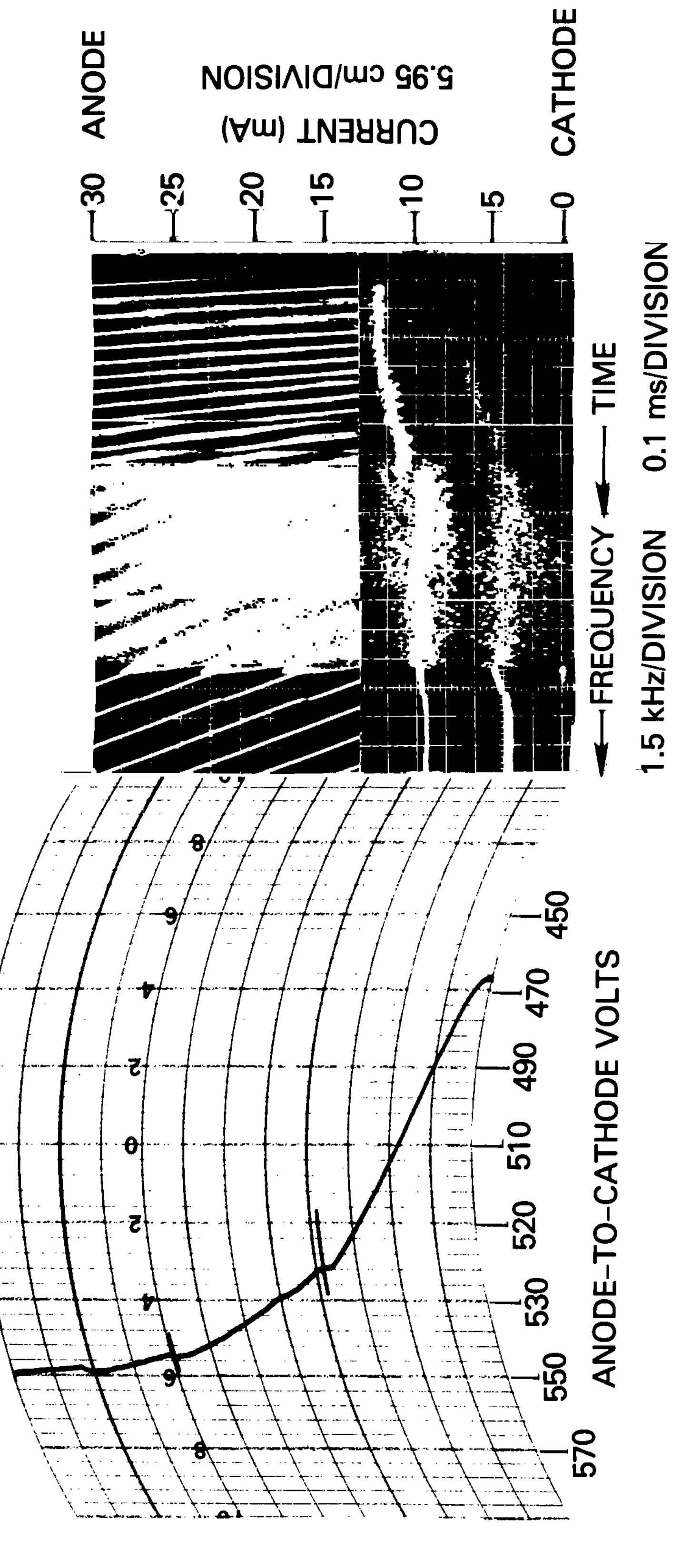

Fig. D57 — Pressure p = 1.5 torr, radius R = 0.95 cm, and 0.05% argon

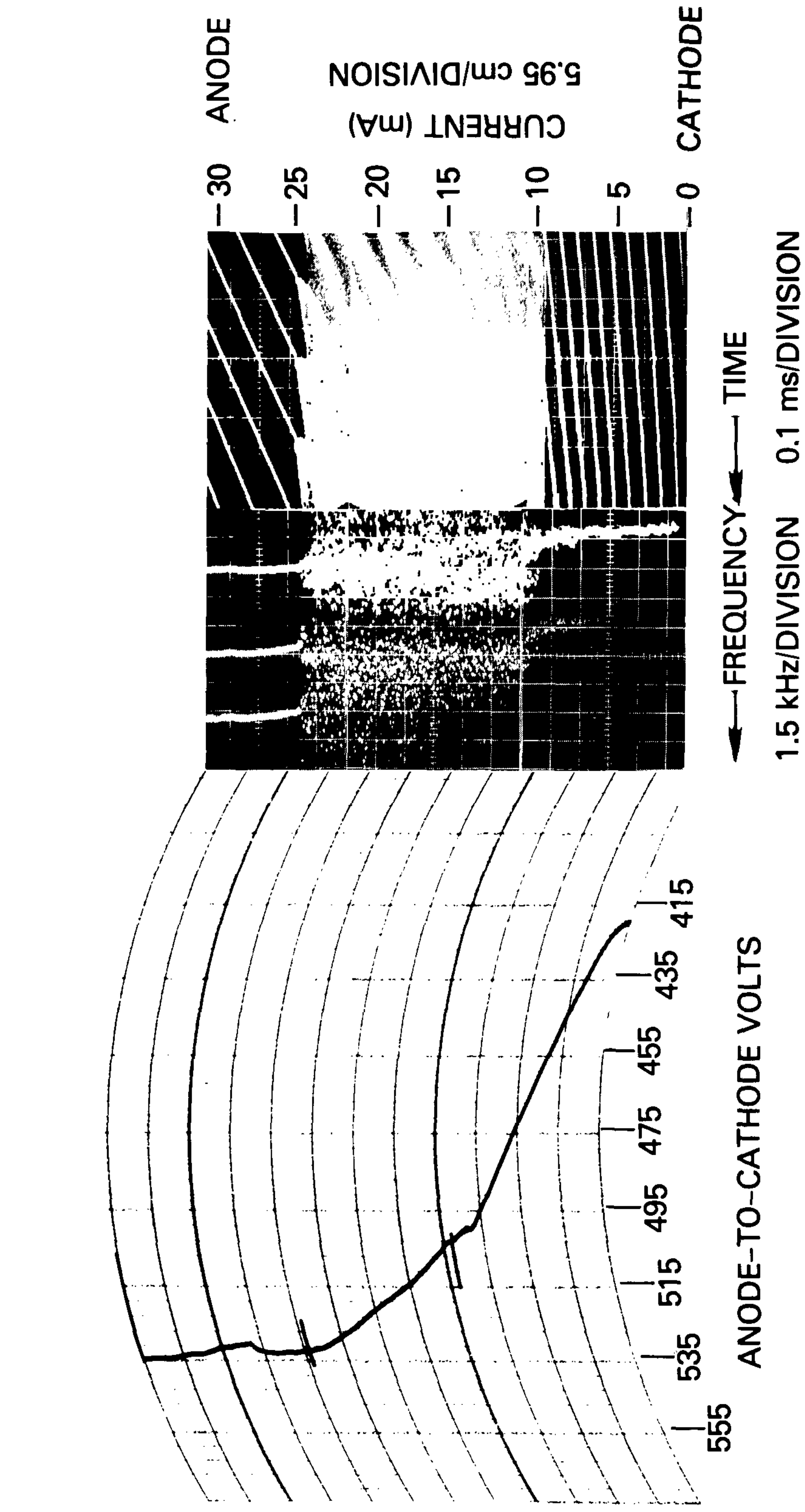

Fig. D58 — Pressure p = 1.5 torr, radius R = 0.95 cm, and 0.07% argon

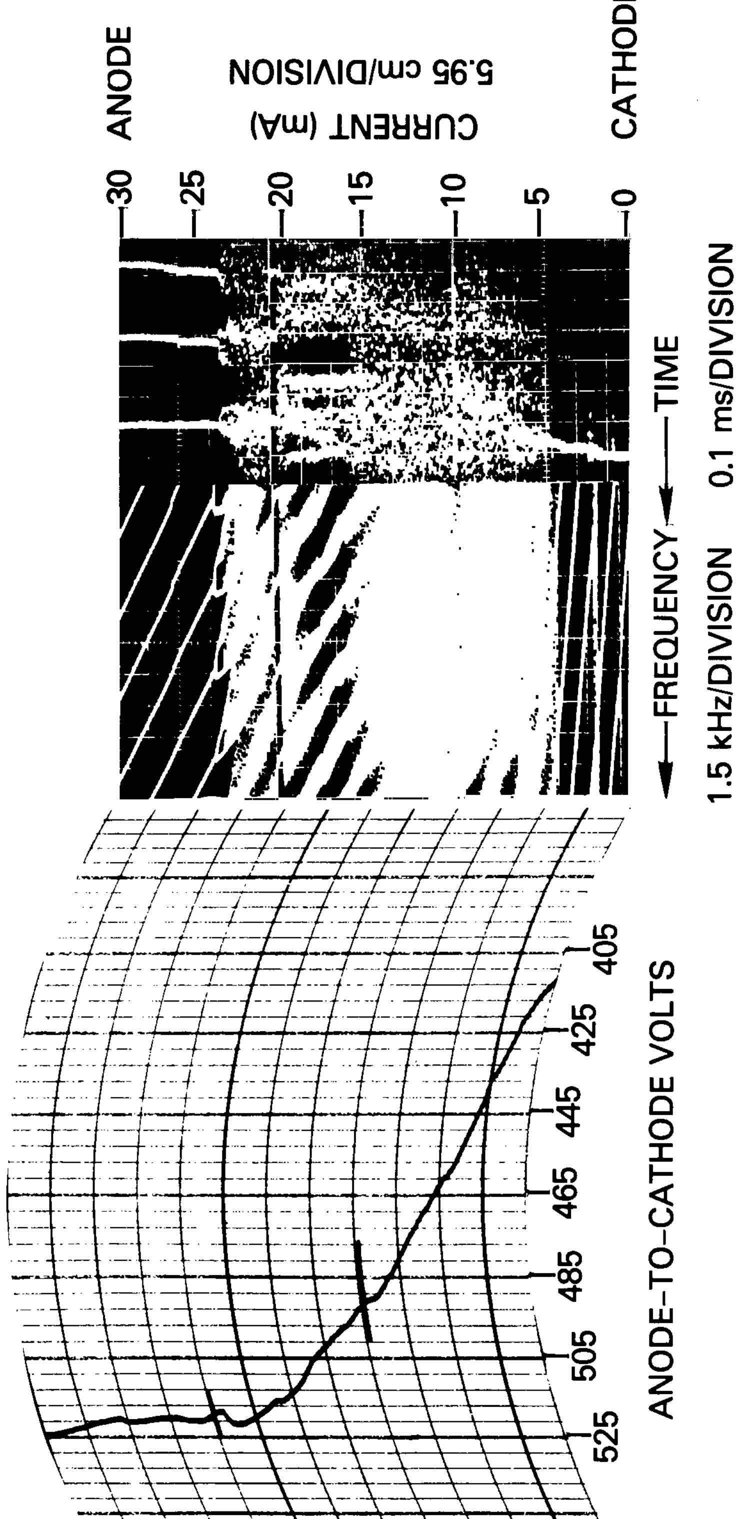

Fig. D59 — Pressure p = 1.5 torr, radius R = 0.95 cm, and 0.1% argon

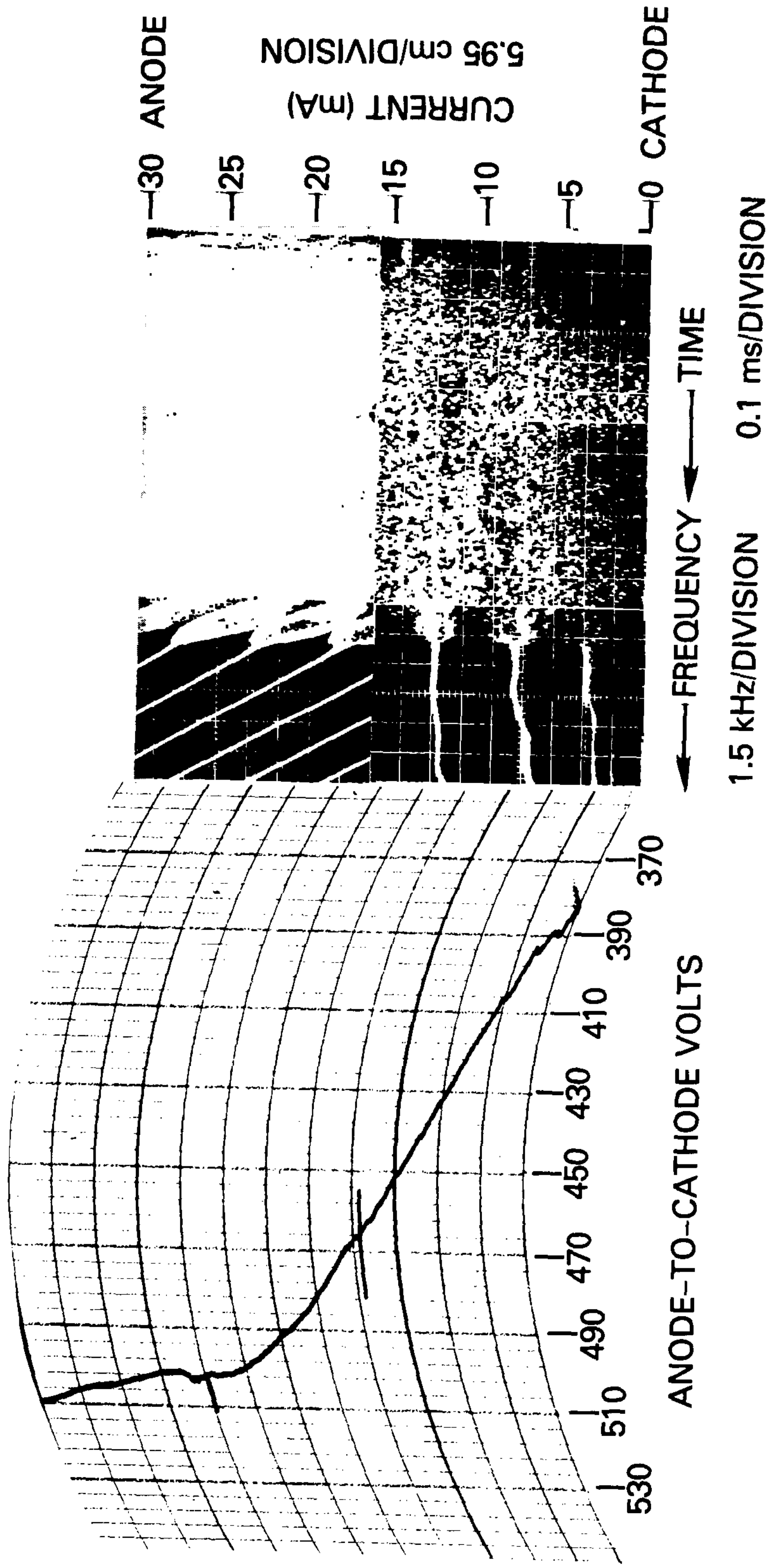

Fig. D60 — Pressure p = 1.5 torr, radius R = 0.95 cm, and 0.14% argon

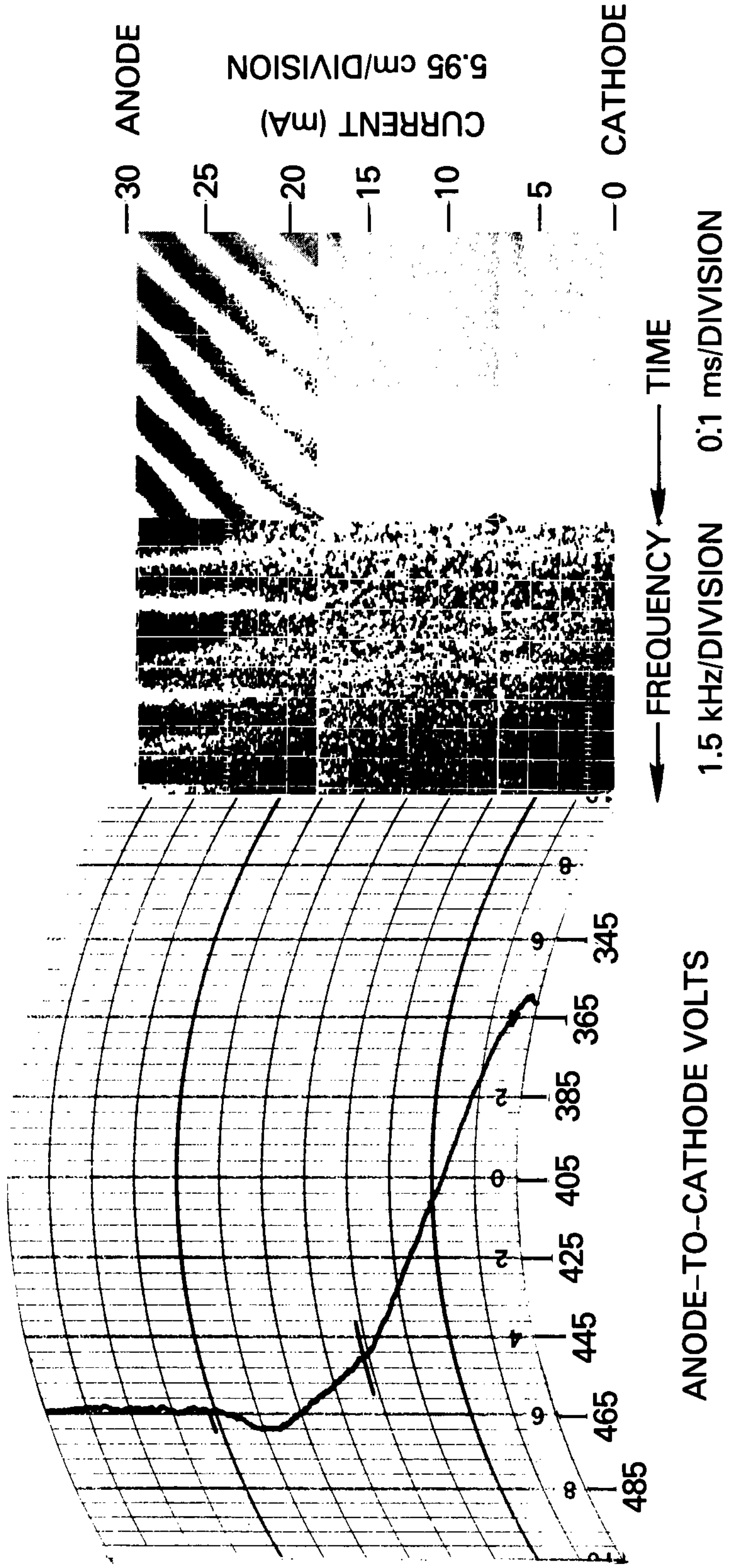

Fig. D61 — Pressure p = 1.5 torr, radius R = 0.95 cm, and 0.18% argon

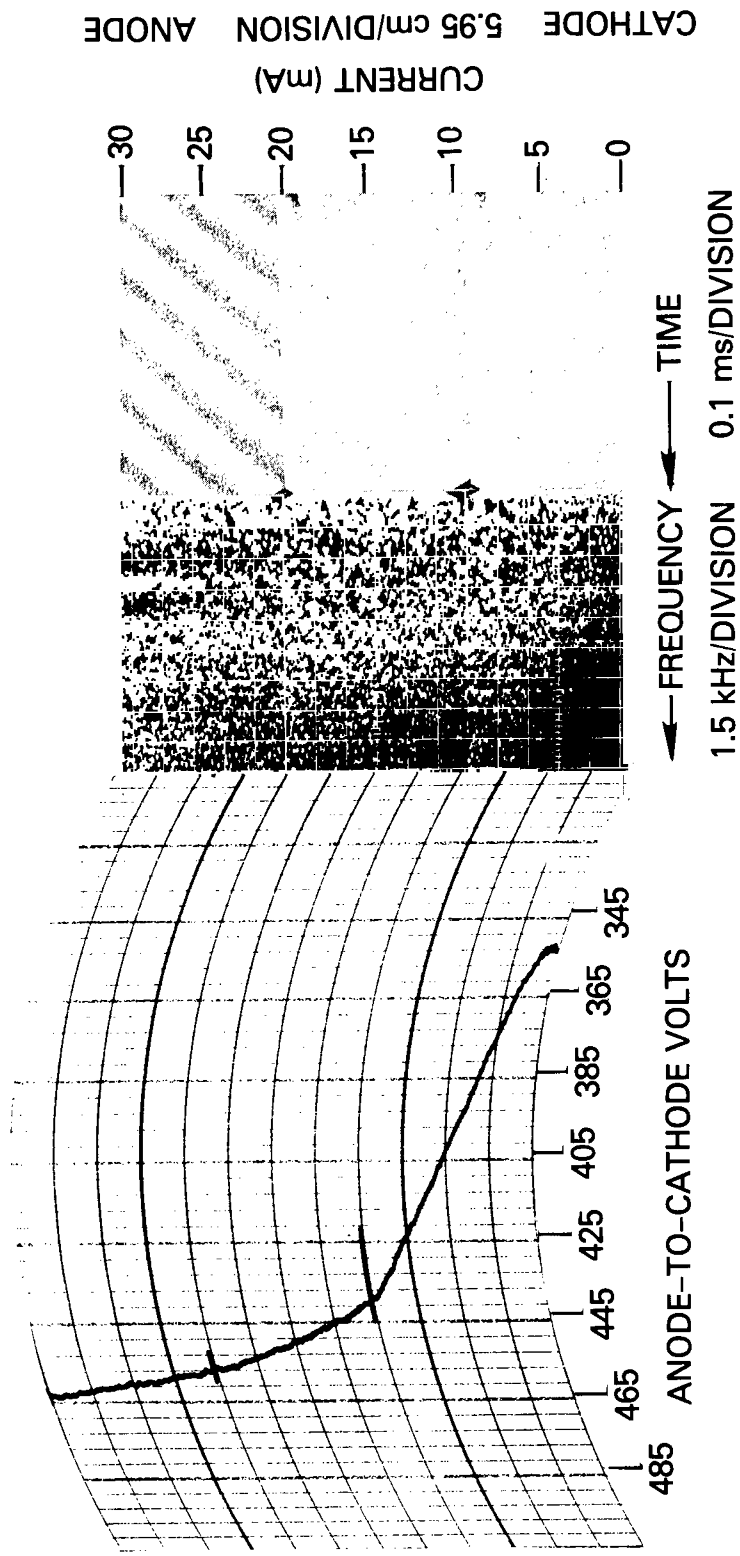

Fig. D62 — Pressure p = 1.5 torr, radius R = 0.95 cm, and 0.2% argon

REFERENCES

1. J.J. Thomson, Phil. Mag. **18**, 441 (1909).

2. J.J. Thomson and G.P. Thomson, *Conduction of Electricity Through Gases*, Cambridge University Press, London, 1933.

3. F.M. Penning, Z. Physik **41**, 769 (1926).

4. M.J. Druyvesteyn, Physica **1**, 273, 1003 (1934).

5. V. Ingard, Phys. Rev. **145**, 145 (1966).

6. L. Tonks and I. Langmuir, Phys. Rev. **33**, 195 (1929).

7. W.D. Jones and I. Alexeff, Phys. Rev. Lett. **15** 286 (1965).

8. L.B. Loeb, Phys. Rev. **76**, 255 (1949).

9. J.R.M. Coulter, N.H.K. Armstrong, and K.G. Emeleus, Proc. Phys. Soc. **77**, 476 (1960).

10. L. Pekarek, Czech. J. Phys. **4**, 221 (1954).

11. L. Pekarek and V. Krejci, Proc. 6th. Int. Conf. Phen. Ioniz. Gas., 1965 , p. 573.

12. L. Pekarek, Czech. J. Phys. **8**, 32 (1958).

13. L. Pekarek and V. Krejci, Czech. J. Phys. **B12**, 450 (1962).

14. L. Pekarek, Proc. 10th Int. Conf. Phen. Ioniz. Gas., p. 365, 1971.

15. W. Pupp, Phys. Z. **33**, 844 (1932); **35**, 705 (1934); **36**, 61 (1935).

16. L. Pekarek and V. Krejci, Czech. J. Phys. **B12**, 296 (1962).

17. D.A. Lee, P. Bletzinger, and A. Garscadden, J. Appl. Phys. **37**, 377 (1966).

18. H. Achterberg and J. Michel, Ann. Phys. **7**, 365 (1959).

19. A.W. Cooper, J. Appl. Phys. **35**, 2877 (1964).

20. M. Sicha and M.G. Drouet, Can. J. Phys. **46**, 2491 (1968).

21. M. Sicha and V. Rezacova, Czeck J. Phys. **B20**, 356 (1970); **B20**, 770 (1970).

22. A. Rutscher and S. Pfau, Proc. 8th Int. Conf. Phen, Ioniz. Gas., 1967, Section 3.1.5.4.

23. J.M. Meek and J.D. Craggs *Electrical Breakdown in Gases*, Oxford Press, 1953, p. 48.

24. E.W. McDaniel and E.A. Mason, *The Mobility and Diffusion of Ions in Gases*, Wiely, 1973, p. 273.

25. A. Niehaus, Proc. 10th Int. Conf. Ioniz. Gas., 1970, p. 85.

26. A.V. Phelps, Phys. Rev., **99**, 1657 (1955).

27. Didlankis, Ann. Physik **5**, 221 (1930).

28. A. Dalgarno and R.A. Buckingham, Proc. Roy. Soc. A, **213**, 506 (1952).

29. E.W. Pike, Phys. Rev. **49**, 513 (1936).

30. K. Masek and V. Perina, Czech. J. Phys. **B18**, 363 (1968).

31. L. Spitzer, *Physics of Fully Ionized Gases*, New York, Interscience, 1962.

32. J. Freudenthal and J.M. Fluit, Proc. 8th Int. Conf. Ioniz. Gas., 1967, Section 3.1.10.2.

33. A. Garscadden and P. Bletzinger, J. Appl. Phys. **35**, 34432 (1964).

34. N.E. Breadbury and R.A. Nielsen, Phys. Rev. **49**, 338 (1936); **51**, 69 (1937).

35. J. Nakata, E. Takenaka, and T. Masutani, J. Phys. Soc. Japan **20**, 1698 (1965).

36. H. Lashinsky and R.E. Monblatt, Rev. Sci. Inst. **42**, 1413 (1971).

37. O. Stirand, V. Krezci, and L. Laska, Rev. Sci. Inst. **37**, 1481 (1966).

38. T. Ruzicka, Czech. J. Phys. **B18**, 928 (1968).